Diffusion of organic molecules with multiple substrate bonds: A density-functional theory study of 1,4-butanedithiol on Au surfaces

Dissertation
zur Erlangung des Doktorgrades
der Mathematisch-Naturwissenschaftlichen Fakultät
der Christian-Albrechts-Universität zu Kiel

vorgelegt von

Andreas Franke

Kiel, 2010

Referent:	Prof. Dr. Eckhard Pehlke
Koreferent:	Prof. Dr. Stefan Heinze
Tag der mündlichen Prüfung:	08.11.2010
Zum Druck genehmigt:	08.11.2010

gez. Prof. Dr. Lutz Kipp, Dekan

Contents

Abstract

The pursuit of miniaturization in technology has created a wide interest in functional nanostructures at metal-vacuum and metal-liquid interfaces making it one of the hot topics in modern surface science. Widely utilized and promising methods to achieve such a functionalization are the growth of organic molecular assemblies on metal surfaces and the manipulation of atomic structures via the tip of a scanning-tunneling microscope. Alkanedithiol molecules have adopted the role of model systems for the bonding of organic molecules on Au surfaces via two sulfur anchors and the formation of self-assembled monolayers. So far, however, little is known about the details of adsorption geometries and diffusion mechanisms of dithiol molecules on Au surfaces, especially in the presence of two S-Au bonds to the substrate surface.

In this work density-functional theory (DFT) calculations have been employed to investigate the adsorption and diffusion characteristics of an archetypical dithiol-metal model-system: 1,4-butanedithiol molecules, HS-$(CH_2)_4$-SH (BDTs), and 1,4-butanedithiol radicals, $\cdot$S-$(CH_2)_4$-S$\cdot$ (BDTRs), adsorbed on the unreconstructed Au(111) and Au(100) surfaces. It has been found that dissociation of BDT into H_2 in the gas phase and chemisorbed BDTR on the unreconstructed Au(111) and Au(100) surfaces is preferred over BDT adsorption for energetic and entropic reasons. BDTR forms two strong S-Au bonds, interconnected through an alkane chain, with the Au(111) and Au(100) surfaces. DFT calculations for low total-energy chemisorption geometries have revealed that the interplay between internal degrees of freedom and two S-Au bonds leads to a complicated multivalley potential energy surface (PES). Local total-energy minima within a few 100 meV of the ground state chemisorption geometry suggest that BDTR/Au diffusion characteristics should be more multifaceted than the diffusion of adatoms or simple molecules with only a single bond to the substrate surface.

Diffusion properties of BDTR/Au(100) have been studied by explicitly integrating a master equation for elementary BDTR diffusion hops between neighboring local total-energy minima on the PES. Notably, translational motion of BDTR occurs at a faster rate compared to rotations on the surface. This suggests that subsequent diffusion hops occur back and forth along the same direction on short time scales. If the diffusion of BDTR/Au can be monitored with sufficient temporal resolution, such correlated motion should be accessible to experiments. On longer time scales the numerical diffusion constant obeys an Arrhenius law. Similar diffusion characteristics are also suggested to occur for BDTR/Au(111).

Diffusion experiments on electrode surfaces in an electrochemical cell offer the unique feature of varying the electric field present at the solid-liquid interface through an applied external potential. A significant influence of an electric field on the PES has been discovered for BDTR on Au(111) and Au(100) surfaces within an approximative approach. It is suggested that this might render BDTR diffusion properties tunable to a certain degree via an applied external potential in an electrochemical cell. In particular, the diffusivity of BDTR/Au(111) has been estimated to decrease significantly at more positive applied potentials, which is in qualitative agreement with preliminary experimental results by Suto and Magnussen.

Beyond BDTR/Au diffusion, this work contains results from collaborations with the group of R. Berndt related to the unoccupied electronic structure of Ag adatoms and clusters on the Ag(111) surface and the group of O. M. Magnussen related to the reversal of c(2×2) Cl/Cu(100) subsurface buckling in an electrochemical environment.

Kurzfassung

Die fortschreitende Miniaturisierung von elektronischen Bauelementen hat zu einem breiten Forschungsinteresse an funktionalisierten Nanostrukturen an Metall-Vakuum sowie Metall-Flüssigkeits Grenzflächen geführt. Diese Bereiche bilden aktuelle Forschungsschwerpunkte der modernen Oberflächenwissenschaften. In diesem Zusammenhang betrachtet man die Adsorption von Dithiolmolekülen auf Goldoberflächen häufig als ein Modellsystem für die Adsorption von organischen Molekülen und Selbstorganisation auf Festkörperoberflächen. Jedoch ist wenig über die Adsorptionsgeometrien und Diffusionseigenschaften dieser Spezies bekannt. Dies gilt vor allem für Strukturen in denen Dithiolmoleküle über zwei S-Au Bindungen an das Substrat gebunden sind.

In dieser Arbeit sind Gesamtenergierechnungen mittels Dichtefunktionaltheorie (DFT) für ein charakteristisches Dithiol-Metall Modellsystem durchgeführt worden: Adsorption und Diffusion von 1,4-Butanditholmolekülen, HS-$(CH_2)_4$-SH (BDT), und Radikalen, $\cdot$S-$(CH_2)_4$-S$\cdot$ (BDTR), auf unrekonstruierten Au(111) und Au(100) Oberflächen. Ein Vergleich der Adsorption von BDT und BDTR im Gleichgewicht hat ergeben, daß BDT auf beiden Oberflächen aus energetischen und entropischen Gründen in gasförmiges H_2 und chemisorbiertes BDTR dissoziiert. Hierbei ist BDTR durch zwei starke S-Au Bindungen, welche über die Alkankette miteinander gekoppelt sind, auf der Oberfläche chemisorbiert. Das Zusammenspiel beider S-Au Bindungen mit den internen Freiheitsgraden des BDTR führt zu einer komplizierten Gesamtenergiefläche mit vielen lokalen Minima innerhalb von wenigen 100 meV oberhalb des Grundzustandes. Dieser Umstand ist bereits ein Indiz dafür, dass die Diffusion in dem vorliegenden Fall eine deutlich komplexere Dynamik zeigen sollte als die Diffusion von Adatomen und einfachen Molekülen auf Metalloberflächen.

Die Diffusion von BDTR/Au(100) wurde durch direkte Integration einer Mastergleichung für elementare Hüpfprozesse zwischen benachbarten lokalen Minima der Gesamtenergiefläche studiert. Insbesondere hat sich gezeigt, daß Translationen entlang ausgezeichneter Richtungen auf der Oberfläche eine niedrigere Diffusionsbarriere als Rotationen besitzen. Aufeinanderfolgende Hüpfprozesse sollten demnach entlang bevorzugter Richtungen erfolgen, was zu einer korrelierten Dynamik auf kurzen Zeitskalen führt. Falls diese Zeitskalen experimentell zugänglich sind, sollte sich diese Korrelation beobachten lassen. Auf längeren Zeitskalen folgt die numerisch bestimmte Diffusionskonstante für BDTR/Au(100) einem Arrheniusgesetz. Die DFT Resultate für die Diffusion von BDTR/Au(111) legen eine ähnliche Charakterisierung der Dynamik nahe. Ein Alleinstellungsmerkmal von Diffusionsexperimenten unter elektrochemischen Bedingungen ergibt sich aus der Möglichkeit, ein elektrisches Feld an der Festkörper-Flüssigkeits Grenzfläche durch eine äußere Spannung zu verändern. Modellrechnungen für BDTR/Au ergeben einen signifikanten Einfluss des elektrischen Feldes auf die Diffusion, wodurch die BDTR Dynamik in gewissen Grenzen extern beeinflussbar wird. Es lässt sich abschätzen, daß die BDTR/Au(111) Diffusion um so langsamer sein sollte, je positiver die angelegte Spannung ist. Dies ist konsistent mit vorläufigen Experimenten von Suto und Magnussen.

Über die BDTR/Au Diffusion hinaus enthält diese Arbeit Ergebnisse aus einer Kooperation mit der Gruppe von R. Berndt für die unbesetzte elektronische Struktur von Ag Adatomen und Clustern auf der Ag(111) Oberfläche und aus einer Kooperation mit der der Gruppe von O. M. Magnussen für die geometrische Struktur von c(2×2) Cl/Cu(100) an der Festkörper-Flüssigkeits Grenzfläche unter elektrochemischen Bedingungen.

Acronyms

Numbers indicate the page of first appearance in the document.

$E_{\mathbf{xc}}[n]$ exchange-correlation energy-functional. 49

AES Auger electron spectroscopy. 18

AQ 9,10-anthraquinone. 14

BDT 1,4-butanedithiol molecule, HS-$(CH_2)_4$-SH. 63

BDTR 1,4-butanedithiol radical, $\cdot$S-$(CH_2)_4$-S$\cdot$. 23

CI-NEB climbing-image nudged elastic band. 33

CPR conjugate peak refinement. 30

DFT density-functional theory. 17

DFT-D semi-empirical vdW-correction to DFT. 56

DHS Dewar, Healy and Stewart. 30

DMDS dimethyldisulfide, $(SCH_3)_2$. 17

DMDTA methylated 9,10-dithioanthracene. 43

DOS density of states. 28

DTA 9,10-dithioanthracene. 43

EAM embedded atom method. 36

EC electrochemical. 38

GGA generalized gradient approximation. 51

HOMO highest occupied molecular orbital. 64

HREELS high resolution electron energy loss spectroscopy. 17

LDA local density approximation. 50

LEAD low energy atom diffraction. 22

LUMO lowest unoccupied molecular orbital. 64

MD molecular dynamics. 30

MEP minimum energy path. 31

MGGA meta-GGA. 52

MT methanethiol, $HSCH_3$. 17

NEB nudged elastic band. 31

PAW projector augmented-wave. 61

PEEM photoemission electron microscope. 41

PES potential energy surface. 25

PTCDA perylene-3,4,9,10-tetracarboxylicdianhydride. 43

QM-QM quantum-mechanical-quantum-mechanical. 156

QMC Quantum Monte-Carlo. 47

RPA random phase approximation. 54

SAM self-assembled monolayer. 13

STM scanning tunneling microscope. 14

SXRD surface x-ray diffraction. 160

TATA triazatriangulenium. 15

TPD temperature-programmed desorption. 17

TST transition state theory. 27

UHV ultra high vacuum. 20

vdW van der Waals. 16

vdW-DF van der Waals density-functional. 55

XPS x-ray photoelectron spectroscopy. 17

1 Functionalization of metal surfaces

1.1 Tailoring molecular devices and functionalized surfaces

The commonly observed trend of miniaturization in many technological fields is a phenomenon which most people can relate to because they have personally witnessed it. Only a few decades ago, carrying around a cell phone may have required a small bag, while nowadays it is small enough to nicely fit into one's front pocket. Moreover, the increased capabilities of a modern cell phone, which may even compare to small computers, is not even reflected in a plain comparison of physical size. From a computational physicists point of view, the miniaturization mainly manifests itself in the doubling of computational power every few years. This empirical observation is known as Moore's law.[1] The traditional approach of increasing the computational power is a refinement of lithographic techniques, which allows for smaller and smaller structures on a computer chip. Even though this classical top-down approach still works, one might ask where the limitations are and what comes next. A possible end of traditional miniaturization has sparked an increased interest into ways of designing new devices in a bottom-up approach using single molecules and atoms as building blocks of functional nanostructures. In his ground-breaking speech "There's plenty of room at the bottom", Feynman already envisioned a development towards such true nanotechnology in 1959.[2]

A promising way to advance in the direction of a technology at the atomic scale might lie in the functionalization of solid surfaces. Molecules are considered suitable building blocks to achieve such a functionalization because they can be used as a *coating* of the surface. In addition, they have atomic scale dimensions by nature and their chemical and physical properties can be specifically tailored.[3] Many molecules have also been reported to self-organize into regular patterns on a solid or even liquid surface due to the interplay between molecule-substrate and molecule-molecule interactions.[4,5] The structure of the resulting self-assembled monolayers (SAMs) may be tuned by choosing suitable molecules such that patterns of functional units can be designed.[4]

A variety of surface functionalizations via tailored nanostructures aimed at different tasks have been demonstrated. E.g., molecules are envisioned to serve as cargo transporters on the surface. It has been shown that four C_{60} molecules can be connected such that the resulting compound looks like a nanocar with C_{60} wheels.[7] Upon adsorbing

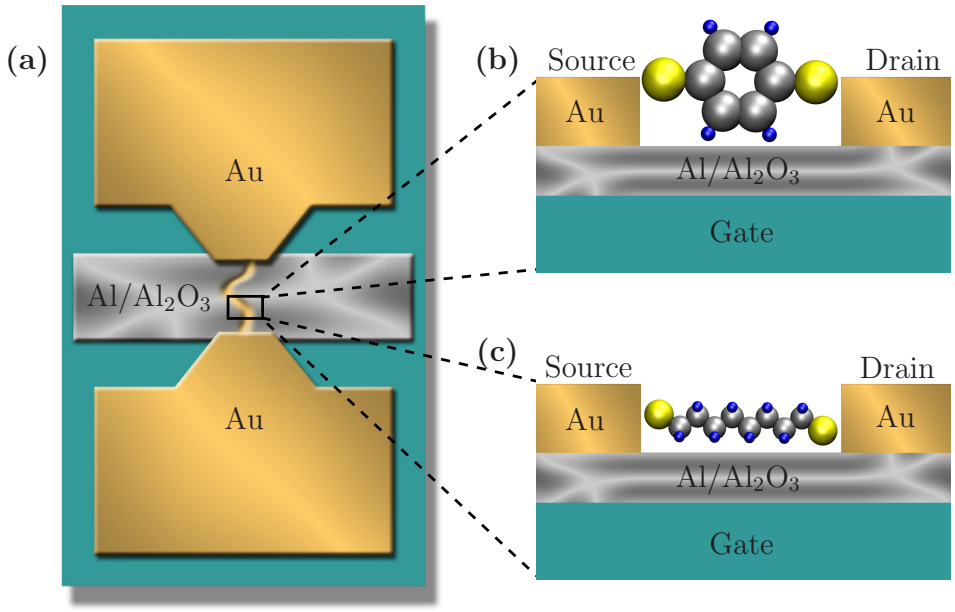

Figure 1.1: Schematic representation of a proposed single molecule transistor (a) as characterized by Song *et al.*[6] The molecular junctions have been assembled from dilute solutions of benzenedithiol molecules [HS-C_6H_4-SH] (b) or octanedithiol molecules [HS-$(C_2H_2)_8$-SH] (c). Yellow, gray, and blue spheres represent S, C, and H atoms, respectively.

the nanocar on a surface, it exhibits directional motion on the surface which is believed to occur via a rolling mechanism of the fullerene-wheels.[7] In a different study, Wong *et al.* have reported that 9,10-anthraquinone (AQ) molecules adsorbed on a Cu surface may act as a molecular carrier of CO_2 cargo molecules.[8] Surfaces may also be suited as highly sensitive chemical noses. Bohrer *et al.* have demonstrated that the conductance of thin films of metal-phthalocyanine molecules on a substrate changes when the device is exposed to gases.[9] Depending on the type of metal atom at the center of the phthalocyanine molecule, the sensors can detect different analytes in the gas phase.

Intense research effort is aimed at functionalized surfaces as a form of nanoelectronics. In this context molecules are envisioned to serve as wires,[10,11] transistors,[6] switches,[12–16] storage units,[12] or simply as insulating spacers.[17] Different research groups have demonstrated that (reversible) switching of molecules between different meta-stable states on a surface can be achieved.[12,13] Wang *et al.* have assembled multi-layers of Sn-phthalocyanine on a Ag(111) surface.[12] By controlled scanning tunneling microscope (STM) manipulation, the Sn atom can be switched between two meta-stable positions, one slightly above and one below the molecular plane of the phthalocyanine molecule. Sn-phthalocyanine units could be addressed individually within an array of four molecules. Hence, one might speculate about a molecular memory composed of such molecular ar-

rays. An alternative approach has been pursued by Baisch *et al.* who have assembled an array of switchable azobenzene molecules on a Au(111) surface.[13] In their approach the molecules are attached to the surface via platforms composed of TATA molecules. The platforms create the space between adjacent adsorbates and between the adsorbates and the substrate surface to facilitate reversible switching.

Molecules can serve as nanowires in an electrode/molecule/electrode set-up. Measuring the charge transport or the conductance of single molecules can be thought of as one of the primary tasks to pave the way for nanoelectronics. The fabrication of reproducible single-molecule conductance-measurements for different benzenedithiol or alkanedithiol molecules has been achieved through the use of mechanically controllable break junctions[18] or STM-based break junctions.[19] Obviously, the molecular conductance will depend starkly on the type of molecule in the junction. To get an impression of the order of magnitude of experimentally observed molecular conductances, a conductance of 0.0012 G_0[i] has been reported for 1,6-hexanedithiol molecules.[19] In this case, it has been found that the conductance varies exponentially with the length of the molecules which is indicative of a tunneling transport mechanism.[19] Further developments aim to gain control over the molecular geometry of the contacts which are usually not known precisely. It has been demonstrated that the contact geometry has a significant influence on the conductance properties.[11,20,21]

An integral part of modern electronic devices are transistors used to amplify electronic signals. As a result, many groups have sought after a true three-terminal molecular-device with source, drain, and gate electrode which has characteristic properties of a transistor. Recently, Song *et al.* have demonstrated a first realization of a three-terminal molecular-transistor which relies on electrostatic modulation of the molecular-orbital energy as the gate mechanism.[6] The Au-molecule-Au device is placed over an oxidized Al electrode which serves as the gate electrode, see Fig. 1.1. In between the Au electrodes 1,8-octanedithiol and 1,4-benzenedithiol molecules have been successfully assembled. Using transition-voltage and inelastic tunneling spectroscopy, the device has been characterized in an unprecedented manner uncovering the role of direct molecular-orbital gating for the modulation of charge carrier transport.

The search for new nanodevices composed of atoms and molecules, which could pave the way towards an ultimate miniaturization of functional units, has made considerable progress in recent years. Molecular switches and transistors have been assembled and characterized with great precision. Challenges in future work will be related to further tailoring, optimizing, and characterizing the manufactured devices. Finally, fabrication methods which have the potential to meet industrial standards have yet to be developed.

[i] $G_0 = e^2/h$ is the quantized unit of conductance. The measured conductance of molecules is usually much smaller than G_0 because the transmission into the conduction channel is not unity.

1.2 An archetypical model system: the thiol-gold interface

If one considers the huge number of possibilities to functionalize metal surfaces by self-assembling molecules, it comes at no surprise that model systems have been used to study basic principles and properties which may be transferable to more complex systems. Many of these model systems involve the self-assembly of organic molecules which bind to a Au surface or nanoparticle via sulfur anchors. In fact, these model systems may have certain functionalizing properties on their own part. Some prominent examples have been given in the previous Section. One of the most widely studied systems, which retains important aspects typical for SAMs, comprises alkane(di)thiol molecules adsorbed on a Au(111) surface. Alkanethiol-based molecules adsorbed on a Au(111) surface have emerged as prominent model systems because thiol groups have a high affinity towards formation of strong S-Au bonds, the molecules tend to self-assemble on a Au(111) surface, and standard deposition techniques can be used.[5,22] Furthermore, alkanethiols and Au samples are commercially available and Au is an inert metal, i.e. clean under almost all conditions.[22]

Self-assembled monolayers of alkanethiol molecules on Au(111)

Growth of alkanethiols, $HS(CH_2)_nCH_3$, on Au surfaces can be achieved by deposition from solution or gas phase.[5] The formation of SAMs on a Au(111) surface can involve multiple intermediate stages which will be discussed for gas phase deposition in the following, see Fig. 1.2.[23] An initial stage may involve physisorbed alkanethiol molecules above the surface in an ordered or disordered layer. In the following intermediate stages, the thiol molecules chemisorb on the surface forming strong S-Au bonds. This so called striped phase can be characterized by the appearance of ordered domains of lying-down alkanethiols. The alkane chains of the alkanethiols are oriented approximately parallel to the surface. If the impingement rate of molecules on the surface and with it the chemical potential of the gas phase molecules is further increased, the striped phase can be converted into an ordered standing-up phase in which the alkane chains become erected. The number of molecules per unit surface area has increased to saturation coverage upon completion of this transformation. This last stage completes the SAM formation. The orders of magnitude of the involved energy gains for the different phases amount to approximately 1-2 eV for the S-Au chemisorption bond formation,[24,25] 0.06 eV/CH_2-group for the van der Waals (vdW) interaction between the alkane chain of a physisorbed alkanethiol molecule and the Au(111) surface,[24] and 0.03 eV/CH_2-group for the vdW interaction between two alkane chains.[26,27]

There is strong evidence that most chemisorbed alkanethiol SAMs result from dissociative adsorption of gas phase alkanethiol molecules, $HS(CH_2)_nCH_3$, on the Au(111) surface via cleavage of the S-H bond of the thiol group.[28] The H atoms are believed to desorb from the surface as H_2 molecules.[28] Hence, this process leads to adsorbed alka-

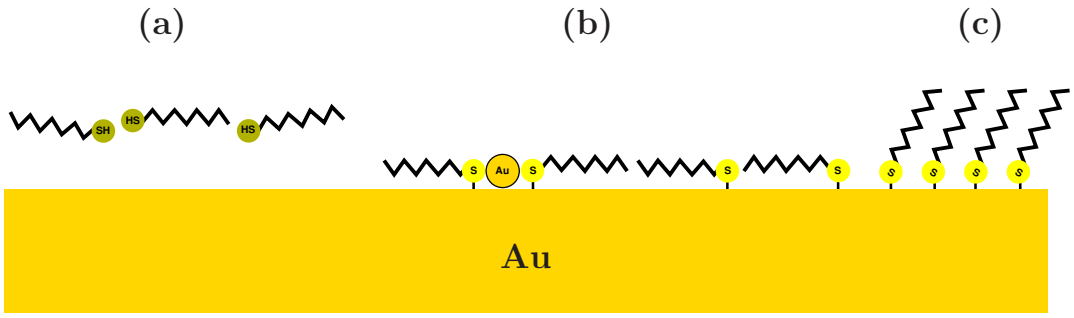

Figure 1.2: Schematic diagram of different stages during SAM growth of alkanethiol molecules from the gas phase: (a) physisorbed molecules, (b) striped phases of chemisorbed alkanethiol radicals, (c) standing-up chemisorbed phase.

nethiol radicals, $\cdot S(CH_2)_nCH_3$, on the Au(111) surface. A breaking of the S-H bond can be inferred from high resolution electron energy loss spectroscopy (HREELS).[29] The spectra show no vibrational peaks associated with S-H stretch modes at about 2600 cm^{-1}. Instead, soft modes attributed to S-Au bonds become visible in the spectra (200-300 cm^{-1}). Further evidence for S-H bond scission has been obtained from the adsorption of nitroaromatic thiols on a Au surface.[30] In this case the nitro groups, NO_2, are (partially) reduced to amino groups, NH_2, upon SAM formation.

Alternatively, SAMs can be formed from dialkyldisulfide molecules, $CH_3(CH_2)_nS$-$S(CH_2)_nCH_3$.[24] The dissociative adsorption of dimethyldisulfide, $(SCH_3)_2$ (DMDS), on a Au(111) surface through dissociation of the S-S bond has been reported in a temperature-programmed desorption (TPD) study by Roper and Jones.[31] Furthermore, Wang *et al.* have carried through density-functional theory (DFT) calculations for the dissociative adsorption of DMDS on a Au(111) surface.[32] Their calculations involved a large $(22\times\sqrt{3})$ surface unit cell with one additional Au atom in the first layer to capture the main characteristics of the Au(111) herringbone reconstruction. Above a coverage of approximately 8% SCH_3 units per Au surface atom, a process which involves a lifting of the surface reconstruction, dissociation of DMDS, and bonding of two SCH_3 units to a Au adatom has been reported to be endothermic.

Gas phase deposition from disulfides is especially important for short alkanethiol molecules (with only a few C atoms in the alkane chain). There have been doubts about a cleavage of the S-H bond upon adsorption of short alkanethiol molecules.[28,33] In particular, there has been a long standing controversy about whether methanethiol, $HSCH_3$ (MT), adsorbs dissociatively from the gas phase through S-H bond dissociation or merely physisorbs on the herringbone reconstruction of the Au(111) surface.[33] Dubois, Zegarski, and Nuzzo were the first to report in a combined TPD, HREELS, and x-ray photoelectron spectroscopy (XPS) study that MT does not form chemisorbed SAMs on Au(111).[34] On the other hand, Liu *et al.* have reported chemisorbed CH_3S/Au(111)

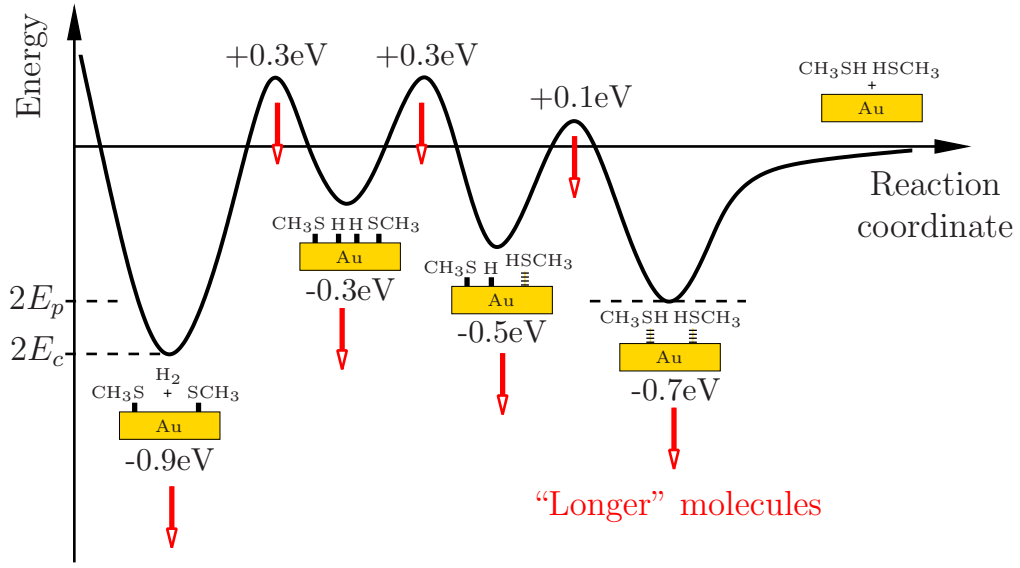

Figure 1.3: Schematic depiction of a (potential) dissociative adsorption mechanism for two methanethiol molecules, $HSCH_3$, in the gas phase above an unreconstructed Au(111) surface. Intermediate stages involve physisorption bonds (broken lines), S-H bond cleavage,[36] desorption of H_2,[37] and chemisorbed SCH_3 species (S-Au bonds: thick solid lines). The total energy of $HSCH_3$ molecules in the gas phase has been set to zero. E_p is the DFT-PW91 physisorption energy (this work) per $HSCH_3$ molecule on Au(111). The DFT-PW91 chemisorption energy (this work) per SCH_3 radical on Au(111) is denoted as E_c. The expected modification of the potential energy due to stabilizing vdW interactions is indicated by arrows (red).[28] The physisorption-to-chemisorption activation energy, ΔE, is estimated to be of the order of 0.8-1.0 eV.

from gas phase deposition of $HSCH_3$ in a TPD and XPS survey.[35] In a convincing TPD, Auger electron spectroscopy (AES), and low-temperature STM study, Rzeznicka *et al.* have shown that gas phase deposition of $HSCH_3$, $HS(CH_2)_2CH_3$, and their isotopomers on Au(111) results in weakly bonded physisorbed molecules only.[33] All in all, there appears to be general consensus that gas phase deposition of $HSCH_3$, $HS(CH_2)_2CH_3$, and possibly other short alkanethiol molecules on Au(111) does not result in S-H bond cleavage and formation of strong S-Au bonds.

This leaves the as yet unanswered question which mechanism is responsible for the chain length dependance of the chemisorption probability for incident alkanethiol molecules. Slightly different mechanisms have been proposed. These can be illustrated with the schematic potential energy diagram for a $HSCH_3$ molecule in front of a Au(111) surface, see Fig. 1.3. Let a molecule from a gas phase reservoir have two (locally) stable positions on the surface: a weakly bound physisorbed precursor state (binding energy E_p) and a chemisorbed state (binding energy E_c). Assume that dissociative chemisorption from the

precursor state is an activated process with a dissociation barrier ΔE. Dubois, Zegarski, and Nuzzo have proposed that ΔE is larger than the absolute value of E_p for short chain alkanethiols.[28] Furthermore, they have argued that ΔE is approximately independent of the alkane chain length, while E_p decreases with increasing alkane chain length.[28] Estimated values for ΔE and E_p amount to approximately 0.78 eV and -0.52 eV, respectively, in case of $HSCH_3$ and a Au(111) surface.[28] According to Dubois *et al.* the dependance of these values on the length of the alkane chain can be rationalized as follows. For longer alkanethiol molecules the physisorbed state is increasingly stabilized by attractive vdW interactions, which leads to a decrease of E_p. The dissociation barrier ΔE, on the other hand, is approximately independent of the chain length if it is assumed that the transition state to dissociation is stabilized to a comparable degree as the physisorbed state. Hence, there should be a critical alkane chain length from where on the absolute value of E_p becomes larger than ΔE. The important point is that in the picture proposed by Dubois, Zegarski, and Nuzzo the increase in sticking coefficient with increasing alkane chain length is related to the change in the branching ration between dissociative adsorption and desorption from the precursor state when the absolute value of E_p becomes larger than ΔE. Lavrich *et al.* have proposed a slightly different mechanism to explain the chain length dependance of the sticking coefficient.[24] First of all they have reported a value of $\Delta E = 0.3$ eV independent of the length of the alkanethiol molecule. ΔE has been measured from conversion rates of the precursor state to the chemisorbed state for different alkanethiols ranging from ethanethiol to decanethiol. By performing these measurement at different temperatures the physisorption-to-chemisorption energy barrier has been obtained from an Arrhenius plot of the data. In addition, they have measured the physisorption energy for a wide range of alkanethiols and have reported that the physisorption well depth increases with alkane chain length in accordance with Dubois *et al.* The value of E_p of ethanethiol obtained from their TPD measurements amounts to -0.59 eV and decreases by approximately 0.06 eV for every additional CH_2 unit for longer alkanethiols. From a linear extrapolation of the data to $HSCH_3$ a value of E_p = -0.53 eV has been obtained.[24] Note that the value for ΔE measured by Lavrich *et al.* is significantly smaller by approximately 0.4 eV than the value proposed by Dubois *et al.* Hence, there should be no sign change of $\Delta E + E_p$ as a function of the alkane chain length. This implies no cross over in the branching between chemisorption and desorption due to stabilizing vdW interactions for longer alkane chains as proposed by Dubois *et al.* Instead, Lavrich *et al.* have related the chain length dependance of the branching ration between chemisorption and desorption from the precursor state solely to an increase of the mean residence time in the precursor state close to the surface with increasing chain length of the molecule. It is not entirely clear whether this model can explain the absence of chemisorption from gas phase $HSCH_3$ and $HS(CH_2)_2CH_3$ molecules on the Au(111) surface reported by Rzeznicka *et al.*[33] Finally, there appears to be a certain degree of discrepancy between the model proposed by Lavrich *et al.* and recent DFT calculation for the dissociation of methanethiol molecules on the unreconstructed Au(111) surface. Lustemberger *et al.* have reported an activation barrier of 0.79

eV for the dissociative adsorption of physisorbed $HSCH_3$ to chemisorbed CH_3S/Au(111) and H/Au(111).[36] This value is significantly larger than the absolute value of the DFT physisorption energy of -0.38 eV for $HSCH_3$/Au(111) obtained by Lustemberger *et al.*[36] Hence, it is tempting to establish a qualitative agreement between the DFT calculations and the model proposed by Dubois *et al.* Taking into account the physisorption energy of $HSCH_3$/Au(111) (-0.35 eV) and the chemisorption energy of CH_3S/Au(111) (approximately -1.9 eV) as calculated in this work and the values for the dissociation energy barriers from the literature,[36,38] the dissociation of $HSCH_3$ on the unreconstructed Au(111) surface is energetically slightly favored by approximately -0.1 eV per SCH_3, see Fig. 1.3. If bonding of SCH_3 to Au adatoms is additionally taken into account, the dissociated equilibrium state is further stabilized by approximately -0.2 eV per SCH_3 radical.[39] However, there is a large dissociation energy barrier of approximately 0.8-1.0 eV. Therefore, the dissociated equilibrium state should not be accessible at temperatures below the $HSCH_3$/Au(111) desorption temperature of roughly 140-220 K.[33] It should be noted that the DFT calculations on which Fig. 1.3 has been based do not encompass contributions due to the reconstruction of the Au(111) surface, entropic effects, vibrational energies[ii] and vdW interactions apart from any spurious contributions included in standard DFT. These factors and a coverage dependance of the binding energies[39] might have a significant but at this point unpredictable impact on the total-energy barriers and total-energy differences in Fig. 1.3.

Considerable progress has been made in the characterization of self-assembly and the various (intermediate) phases involved in the adsorption of alkanethiol molecules on the Au(111) surface. Some questions concerning the kinetics involved in the transition from physisorption to chemisorption appear to leave room for future experimental as well as theoretical research. Moreover, little is known so far about the reactions involved in the formation of SAMs from solution or under electrochemical conditions, where ions of the electrolyte could be important. Less is known about the adsorption of alkanedithiols on a Au(111) surface. But the mechanism behind SAM formation are believed to be similar to the alkanethiol case.

Ordered structures of alkanethiols on Au(111)

Upon formation of ordered chemisorbed structures of alkanethiols on a Au(111) surface, the herringbone reconstruction, which is stable under ultra high vacuum (UHV) conditions, is lifted and the substrate surface exhibits a (1×1) translational symmetry [unreconstructed Au(111) surface].[23] Ordered physisorbed structures have also been reported in case of $HSCH_3$/Au(111) but in this case the herringbone reconstruction is not lifted.[33,40] In the following paragraphs the focus will be on ordered structures chemisorbed on the Au(111)-(1×1) substrate surface.

[ii] Note the large harmonic vibrational energy ($\hbar\omega \approx 0.3$ eV) associated with the S-H stretch mode. If this mode is not present at the transition state for dissociation, the assumptions leading from Eq. 2.9 to Eq. 2.10 of transition state theory might not be valid in this case.

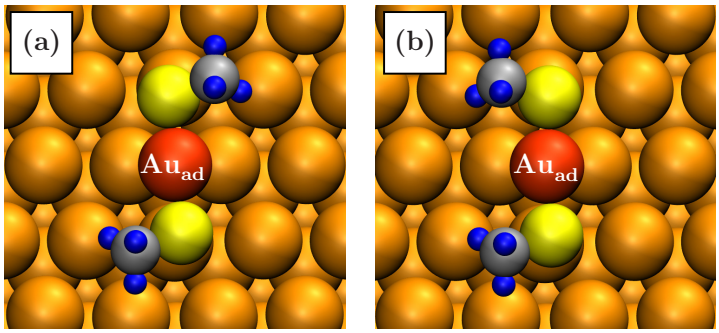

Figure 1.4: (a) Trans and (b) cis configuration of an $Au(SCH_3)_2$ complex on a Au(111) surface. The energy difference as calculated within DFT between the ground state configuration in (a) and (b) amounts to only a few 10 meV below saturation coverage.[39] S atoms: yellow, C atoms: gray, H atoms: blue, Au-adatom: red. The Figure has been taken from Ref. 39.

In case of a SAM at saturation coverage, alkanethiols are densely packed on the Au(111) surface in an upright manner (standing-up phase), i.e. the S atoms are bound to the substrate surface via S-Au bonds and the alkane chains take a typical average tilt angle with respect to the surface normal of about 30°.[5,23] The periodicity of the standing-up phase corresponds to a $(\sqrt{3} \times \sqrt{3})$R30°, or $(2\sqrt{3}\times3)$ rectangular surface unit mesh.[23,41] Both structures may coexist in different domains on the surface and external perturbations, e.g. temperature changes or sweeps with an STM tip, can easily induce switching between the two.[23] Hence, both structures are believed to be close in energy.[23] Strong evidence points towards one adsorbate per $(\sqrt{3} \times \sqrt{3})$ and four adsorbates per $(2\sqrt{3}\times3)$ unit cell, i.e. the saturation coverage corresponds to one adsorbed alkanethiol radical per three surface Au atoms ($\Theta = 1/3$).[23,41] The four adsorbates in the $(2\sqrt{3}\times3)$ structure are believed to adopt at least two inequivalent local configurations.[23,41] Detailed structural models of the adsorbates within each unit cell of these meshes, including the precise location and local bonding geometry of the S atom(s) with respect to the underlying Au(111) substrate surface, are a long standing controversy. Positions of the S atom(s) in the chemisorption configuration close to on top and fcc sites of the unreconstructed Au(111)-(1×1) surface have been discussed in the literature.[41] While there have been experimental reports consistent with one or the other of these local binding sites, almost all DFT calculations have favored adsorption near fcc or bridge sites of the Au(111) surface.[42–53] Molina and Hammer as well as Morikawa *et al.* have proposed that a reconstruction of the Au(111)-(1×1) surface might lead a way out of this dilemma.[54,55] Indeed, from a combined STM and DFT study Maksymovych *et al.* have suggested that SCH_3 radicals are bound to the Au(111)-(1×1) surface by incorporating Au adatoms in a dilute phase of $Au(SCH_3)_2$ complexes.[56] These complexes consist of a Au adatom at a bridge site of the Au(111)-(1×1) surface and two SCH_3 radicals each of which forms a bond to the Au adatom and a surface atom (on top),

see Fig. 1.4. The SCH_3 radicals in an $Au(SCH_3)_2$ complex may be aligned anti-parallel (trans ground state configuration) or parallel (cis configuration) with respect to each other.[39] Both trans and cis configurations have been observed in STM experiments.[57] Inspired by these results, experimental hints of Au adatoms have been identified to play a vital role for a variety of alkanethiol SAMs at saturation coverage.[58–62] The ground breaking work by Maksymovych *et al.* has lead to many new structural models for SAMs at saturation coverage involving Au adatoms and vacancies in the first atomic layer of the substrate surface.[23,41]

Significant progress has been made to resolve the local binding geometries of the alkanethiol/Au(111) adsorption structures at saturation coverage. Nevertheless, not all inconsistencies related to the interpretation of some experimental data and the relation to calculations have been resolved so far. In particular, a unifying structural model has not been agreed upon yet.

In case of intermediate adsorbate coverages, domains of densely-packed lying-down structures (alkane chains approximately parallel to the surface) have been identified on the Au(111) surface in STM and low energy atom diffraction (LEAD) experiments.[63] These structures can be characterized by molecules which are strongly bound to the surface via S-Au bonds and a chain length dependant contribution to the total binding energy from the vdW interaction between the alkane chain and the Au surface.[23,41] In this phase the adsorbates are ordered on the Au(111) surface with a periodicity corresponding to a rectangular (p$\times\sqrt{3}$) unit cell with p taking on integer or half-integer values.[23,41] Along the $\sqrt{3}$-direction, i.e. a $[11\bar{2}]$ direction of the substrate surface, the alkane chains of the alkanethiol adsorbates are aligned parallel to each other.[5] The alkane chains themselves are oriented parallel to the p-direction, i.e. a $[1\bar{1}0]$ direction of the substrate surface.[5] This can either be achieved in a head-to-head (S atoms closest to each other) or head-to-tail (S atoms closest to CH_3 groups) configuration, see Fig. 1.2.[5] The majority of the experiments aimed at identifying the position of the S atom with respect to the underlying Au(111) substrate surface favor a S-Au bonding close to on top sites of the surface.[41] A few studies have suggested a co-occupation of two distinct S atom sites with the possibility of S-S pairing.[41] Even though no unifying picture could be established so far, the $Au(SCH_3)_2$ complexes observed by Maksymovych *et al.* for a dilute adsorption phase could be able to explain the experimental evidence for S atoms residing atop Au surface atoms. In fact, these complexes have also been observed for low coverage phases of ethanethiol and propanethiol radicals.[41,57] This suggests that bonding of two alkanethiol radicals to a Au adatom could be a key structural property of the lying-down phase.

Ordered structures of alkanedithiols on Au(111)

In recent recent years an increasing interest into the adsorption of dithiol molecules, HS-$(CH_2)_n$-SH, has sparked several investigations of the adsorption structures of theses molecules on the Au(111) surface under UHV, ambient, as well as electrochemical condi-

tions.[64–78] Nevertheless, compared to alkanethiols far less is known about the adsorption of dithiol molecules on the Au(111) surface. The existence of two terminal thiol groups (-SH) has raised the question whether alkanedithiol molecules bind via one or two bonds to the Au surface.[23,24,66] Moreover, the fate of the H atoms of the thiol groups upon adsorption, which is important for the proposal of chemisorption structures, is a matter of debate.[23]

The adsorption of alkanedithiol molecules has been reported to result in domains of ordered phases of lying-down adsorbates (alkane chains approximately parallel to the surface) below surface coverages of one monolayer,[65–70,75,79,80] standing-up adsorbates at one monolayer coverage (erected molecules),[65,69,70,75,80,81] and multi-layers of adsorbates composed of erected molecules at larger coverages.[71–74,82,83] In a detailed experimental study employing complementary structural techniques (grazing-incidence x-ray diffraction (GIXD), LEAD, STM) Leung *et al.* have characterized the ordered structure of 1,6-hexanedithiol molecules on the Au(111) surface prepared by vapor phase deposition.[66] They have reported a lying-down phase of the adsorbates at a coverage below one monolayer, which exhibits an incommensurate surface mesh in the direction of the molecular axis with a (p$\times\sqrt{3}$) unit cell (p = 4.24 or 3×4.24). From this it follows that the two S atoms of each adsorbate can not occupy equivalent binding sites.[5,66] The STM images show elongated bright features which approximately line up along $\langle 11\bar{2}\rangle$ high symmetry directions of the Au(111) substrate surface. Theses features have been attributed to originate from neighboring S atoms of adjacent molecules. Note that simulated STM images calculated for a 1,4-butanedithiol radical, $\cdot$S-$(CH_2)_4$-S$\cdot$ (BDTR) on the Au(111) surface in this work suggest contributions from the alkane chain to elongated bright features visible in the images.[84] Leung and co-workers did not observe a transition to standing-up dithiols even after the dosing of gas phase molecules onto the surface was significantly increased. To investigate if the deposition procedure influences the appearance of an ordered monolayer of standing-up 1,6-hexanedithiol molecules, the investigations have been repeated for a solution grown sample. As a matter of fact, no evidence for an ordered standing-up phase could be found.

The adsorption of 1,4-butanedithiol, 1,6-hexanedithiol, and 1,9-nonanedithiol mol/-ecu/-les on a Au(111) surface has been analyzed based on reflection-adsorption infrared spectroscopy (RAIRS), electrochemistry, XPS, and time of flight direct recoil spectroscopy by Millone *et al.*[80] 1,4-butanedithiol molecules have been found to mainly adopt a lying-down configuration on the surface. One of the central results stated by Millone *et al.* is that with increasing alkane chain length the ratio between the number of standing-up to lying-down molecules increases sharply. DFT calculations have been reported to support this finding on the basis of thermodynamic considerations.[85] In contrast to Leung *et al.* a transition for 1,6-hexanedithiol/Au(111) from a lying-down to a standing-up configuration for solution grown samples has been observed. Moreover, Millone *et al.* have reported that the growth procedure has a significant influence on the formation of SAMs comprising standing-up dithiols, which might account for the discrepancy to the survey conducted by Leung *et al.*

From the structural investigations discussed so far, it can be inferred that alkanedithiols assemble in a lying-down structure below saturation coverage in which the alkane chain is oriented approximately parallel to the Au(111) surface. But what is known about the bonding of alkanedithiols to the Au(111) surface? Do the lying-down phases consist of ordered physisorbed or chemisorbed S-Au bonded entities? An inspection of the literature yields the impression that for the most part S-H bond cleavage and H_2 formation is implicitly assumed. Few experimental studies have addressed this issue and theoretical considerations are lacking altogether. Kobayashi *et al.* have carried through RAIRS experiments for the lying-down phase of 1,8-octanedithiol on the Au(111) surface.[67] The authors have speculated that the S-H bonds have been cleaved based on the observation that a peak at the characteristic frequency associated with the S-H bond stretch vibrations is missing. It should be noted, however, that the S-H signal is rather weak and might have been masked.[67] Finally, XPS experiments can be employed to gain information about the chemical bonds formed at the thiol-gold interface from inspection of S core levels and their intensities. Millone *et al.* have analyzed XPS data for the lying-down phase of 1,4-butanedithiol on Au(111). It has been concluded that 1,4-butanedithiol is chemisorbed on the surface via two S-Au bonds.[80] Hence, the S-H bonds should be cleaved. The DFT calculations carried through in this work, published in Ref. 84, support this finding in case of submonolayer coverages.

The determination of long-range order in alkanedithiol SAMs on the Au(111) surface at a coverage which corresponds to one monolayer (standing-up configuration) appears to be significantly more difficult compared to the case of alkanethiol SAMs. STM images with atomic resolution of $(\sqrt{3} \times \sqrt{3})$ ordered domains of standing-up alkanedithiols are rare which has been attributed to a large degree of disorder and a strong interaction between the STM tip and the terminal SH groups.[85] There have been speculations that the disorder of the alkanedithiol monolayer might be related to S-S dimerization of the terminal SH groups of adjacent alkanedithiols in the SAM.[65]

Compared to SAMs of alkanethiol molecules on a Au(111) surface, far less is known about SAMs of alkanedithiol molecules especially for monolayers consisting of standing-up adsorbates. In recent years much more research effort has been devoted to these systems and SAMs of lying-down dithiols with two S-Au bonds have been partially characterized in experiments. The body of theoretical data available for this system[77,85] is very modest and will be detailed and, if reasonable, compared to the data presented in this work in Sec. 4.2.

2 Diffusion

Diffusion of atoms or molecules on solid surfaces is a key element in many surface processes which involve mass transport. For example, a prerequisite for surface equilibration and growth of thin films is the transport of adsorbates or adatoms across the surface. Catalytic properties of surfaces, which are indispensable in many industrial applications, would not be accessible if the reaction partners could not diffuse on the surface. Furthermore, the surface diffusion of molecules plays a vital role for self-assembly and the formation of nanostructures to which intense and ongoing research is devoted. This effort arises from a pursuit to further miniaturization in fields such as microelectronics and biosensor technology. A detailed insight into the diffusion properties of the molecular building-blocks on the surface should contribute to further the development in these fields.

2.1 Theoretical approach

2.1.1 Transition state theory

An assessment of diffusion from a theoretical and experimental point of view requires a quantitative framework on which a discussion of the matter can be based. One such framework, often applied to describe diffusion processes, is transition state theory (TST). The basic TST concepts and terminology introduced in this Section are at the heart of the discussion throughout this work.

An adsorbate which is bonded to a substrate surface experiences a change of its binding energy with lateral position above the surface as a result of the atomic substrate-lattice. The total-energy of the electronic ground-state of an adsorbate-substrate system or, equivalently, the binding energy between the adsorbate and the substrate, as a function of all atomic positions is called the potential energy surface (PES). Global minima on the PES are referred to as adsorption configurations. The lateral position of the adsorbate above a surface in the adsorption configuration is called adsorption site.[i] Classical diffusion of an adsorbate across a substrate surface from one adsorption configuration to another inevitably involves intermediate, i.e. energetically less favorable, configurations. The minimum energy barrier between adsorption configurations is called the diffusion

[i] If the adsorbate is an extended object, e.g. a molecule, the adsorption site could be defined as the center-of-mass of the object.

energy barrier, ΔE_d, and the saddle-point configuration at the top of the diffusion energy barrier is referred to as the transition state.

Adsorbate diffusion across a surface is a thermally-driven stochastic-motion arising from the coupling of the adsorbate and the substrate phonon bath. If the diffusion energy barrier is smaller or comparable to the thermal energy, $k_\mathrm{B}T \gtrapprox \Delta E_d$, the adsorbate will follow a Brownian motion. In this case the adsorbate is not confined to a specific adsorption site but moves rather freely on the surface.[86] Assuming the condition $k_\mathrm{B}T \ll \Delta E_d$, the adsorbate motion can be ascribed to hops across diffusion energy barriers between different adsorption configurations.[86] In between subsequent hops the adsorbate thermalizes and is hence confined to the basin of attraction associated with a certain adsorption site on the surface.[86] Hence, subsequent hops can be considered independent and the definition of a mean hopping rate Γ or mean residence time $1/\Gamma$ becomes meaningful.[86] The following discussion focuses on hopping diffusion in a regime where $k_\mathrm{B}T \ll \Delta E_d$. According to Barth the hopping diffusion model and, thus, the results of TST should be valid as long as $5k_\mathrm{B}T \lessapprox \Delta E_d$ holds, i.e. for diffusion energy barriers not much smaller than 0.13 eV at room temperature.[86]

In the adsorbate hopping model the stochastic motion of the adsorbate corresponds to a random walk, which can be characterized by the mean square displacement $\langle[\Delta\boldsymbol{r}(t)]^2\rangle$ of the adsorbate at time t. Consider an adsorbate which diffuses isotropically on a two dimensional square lattice with lattice vectors $a\hat{\boldsymbol{e}}_x$ and $a\hat{\boldsymbol{e}}_y$. Let the mean hopping rate for a translation in one of the $\pm x$ and $\pm y$ directions be Γ. If the adsorbate performs only nearest neighbor hops, the mean square displacement is:[86]

$$\langle[\Delta\boldsymbol{r}(t)]^2\rangle = \langle[\boldsymbol{r}(t) - \boldsymbol{r}(0)]^2\rangle = 4\Gamma a^2 t \tag{2.1}$$

It is straightforward to extend this expression to other substrate symmetries and non-isotropic hopping rates.[86] The two dimensional tracer diffusion constant D is a common experimental and theoretical measure for the diffusivity of adsorbates on substrate surfaces and is given by:[86]

$$D = \lim_{t\to\infty} = \frac{\langle[\Delta\boldsymbol{r}(t)]^2\rangle}{4t} = \Gamma a^2 \tag{2.2}$$

The quantity responsible for the diffusion properties on long time scales is the mean hopping rate Γ. Within TST an approximate expression for Γ can be derived if quantum effects such a as tunneling diffusion can be neglected. This is illustrated by considering the PES, V, of a model system which could, for example, correspond to an adsorbate atom on a substrate surface, see Fig. 2.1. If the substrate consists of N atoms, V is a function of $3N$ atomic coordinates of the substrate $\boldsymbol{q} = (q_i)_{i=1\ldots3N}$ and three atomic coordinates of the adsorbate (x, y, z). The $3N+3$ dimensional configuration space of the coupled adsorbate-substrate system is $\boldsymbol{R} = (\boldsymbol{q}, x, y, z)$. Let the PES have two minima labeled A and B. As a result, at least one point, call it ts, has to exist which is a saddle point of V. Consequently, there are continuous paths in configuration space which lead

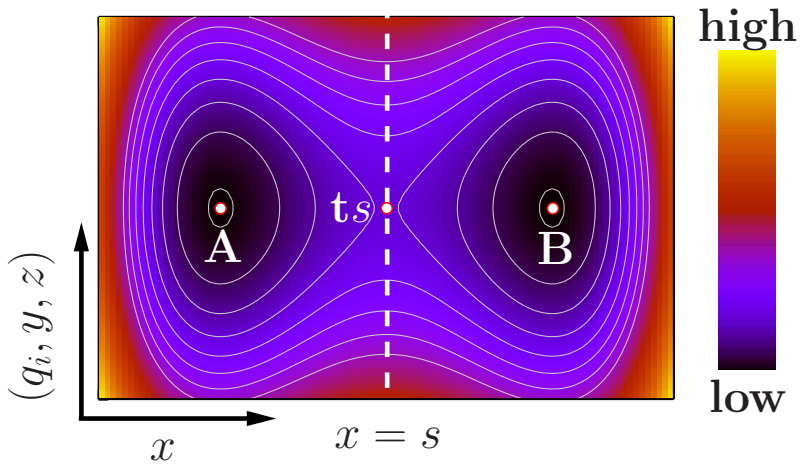

Figure 2.1: Cut through a $3N + 3$ dimensional PES with coordinate labels $(q_i, x, y, z)_{i=1\ldots3N}$. The minima of the PES are labeled A and B and the transition state for a hop from A to B is labeled ts. Constant potential-energy hyper-surfaces are denoted by grey lines. The broken white line is a $3N + 2$ dimensional hyper-surface Σ_{ts} given by the condition $x = s$. Σ_{ts} separates the basins of attraction associated with the minima A and B.

from A (initial configuration) via ts (transition state) to B (final configuration). Among all such paths the minimum energy barrier which needs to be surmounted for a hop from A to B is the diffusion energy barrier $\Delta E_d = V(\boldsymbol{R}_{ts}) - V(\boldsymbol{R}_A)$. Another important aspect is the definition of a dividing plane in configuration space. It is defined as the $3N + 2$ dimensional hyper-plane in configuration space, call it Σ_{ts}, which contains the transition state ts, is orthogonal to the unstable mode at ts and is orthogonal to all constant V hyper-surfaces every where else.[87] Without loss of generality, Σ_{ts} shall be given by the condition $x = s$ as illustrated in Fig. 2.1. It will henceforth be assumed that every configuration on Σ_{ts} with a positive velocity component perpendicular to Σ_{ts} leads to a diffusion event from A to B. Configuration space paths which involve re-crossings of Σ_{ts} are neglected. Consequently, the TST hopping rate will be an upper bound to the true hopping rate.[88] In transition state theory the hopping rate $\Gamma_{\mathrm{TST}}^{\mathrm{A} \to \mathrm{B}}$ can thus be defined via an ensemble average denoted as $\langle \ldots \rangle$:[89]

$$\Gamma_{\mathrm{TST}}^{\mathrm{A} \to \mathrm{B}} := \frac{\langle v_x \Theta(v_x) \delta(x - s) \rangle}{\langle \Theta(s - x) \rangle}. \tag{2.3}$$

The velocity of a configuration along x is v_x and Θ is the Heaviside function. Let $Z_{\Sigma_{ts}}$ be the constrained partition function of all points restricted to lie on Σ_{ts}, and let Z_{A} be the constrained partition function of all points which belong to the basin of attraction around A ($x < s$). By evaluating the ensemble averages in Eq. 2.3, the hopping rate can

be cast into:[89]

$$\Gamma_{\mathrm{TST}}^{\mathrm{A}\rightarrow\mathrm{B}} = \frac{k_{\mathrm{B}}T}{h}\frac{Z_{\Sigma_{ts}}}{Z_{\mathrm{A}}} \tag{2.4}$$

$$= \frac{k_{\mathrm{B}}T}{h}e^{-\Delta F/k_{\mathrm{B}}T} \tag{2.5}$$

where the thermodynamic relation $F = -\beta\ln(Z)$ has been used. In the harmonic approximation the expression for the free energy can be further evaluated to give:[89]

$$\Delta F = \Delta E_d + \Delta F_{\mathrm{vib}} \tag{2.6}$$

$$= \Delta E_d + k_{\mathrm{B}}T\int_0^\infty d\nu\,\ln(2\sinh(\frac{h\nu}{2k_{\mathrm{B}}T}))\Delta n(\nu) \tag{2.7}$$

$$\int_0^\infty d\nu\Delta n(\nu) = \int_0^\infty d\nu(n_{\mathrm{ts}}(\nu) - n_{\mathrm{A}}(\nu)) = -1 \tag{2.8}$$

where ΔE_d is the diffusion energy barrier obtained from the total energy of the static system. The density of states (DOS), n, of the harmonic frequencies can be calculated from the dynamic matrix in A and ts. The DOS is zero for $\nu > \nu_{\max}$, where $\nu_{\max}$ is the largest eigenvalue of the dynamic matrix. At the transition state ts one eigenvector of the dynamic matrix is oriented along the direction of descend (unstable mode), which corresponds to one negative eigenvalue of the dynamic matrix. This mode is not include in the DOS n_{ts}, which leads to Eq. 2.8.

In the classical limit, i.e. at high temperatures where $h\nu/k_{\mathrm{B}}T \ll 1$ holds for all $\nu \leq \nu_{\max}$ or at least for those stable eigenmodes which significantly differ between the minimum and the transition state, $\Gamma_{\mathrm{TST}}^{\mathrm{A}\rightarrow\mathrm{B}}$ can be written as:[89]

$$\Gamma_{\mathrm{TST}}^{\mathrm{A}\rightarrow\mathrm{B}} = 2\frac{k_{\mathrm{B}}T}{h}\frac{\prod_{i=1}^{3N}\sinh(\frac{h\nu_i^{\min}}{2k_{\mathrm{B}}T})}{\prod_{j=1}^{3N-1}\sinh(\frac{h\nu_j^{\mathrm{ts}}}{2k_{\mathrm{B}}T})}e^{-\Delta E_d/k_{\mathrm{B}}T} \tag{2.9}$$

$$\xrightarrow{T\gg h\nu/k_{\mathrm{B}}} \frac{\prod_{i=1}^{3N}\nu_i^{\min}}{\prod_{j=1}^{3N-1}\nu_j^{\mathrm{ts}}}e^{-\Delta E_d/k_{\mathrm{B}}T} = \nu_0 e^{-\Delta E_d/k_{\mathrm{B}}T} \tag{2.10}$$

where the total number of stable modes with non-zero eigenfrequency is $3N$ at the minimum and $3N-1$ at the transition state. Three modes with $\nu = 0$ s^{-1} ($\lambda \rightarrow \infty$) which promote a translation of the entire system have been omitted. The prefactor ν_0 is commonly referred to as the Vineyard attempt frequency.[87]

Eq. 2.10 is the well known expression for the TST hopping rate. It is instructive to recall the assumptions on which the TST result is based:

- Adsorbate hopping is a Markov process ($k_\mathrm{B}T \ll \Delta E_d$)
- No re-crossing of the dividing surface is taken into account (the transition state is a point of no return)
- Quantum effects are not significant (no tunneling diffusion and $h\nu/k_\mathrm{B}T \ll 1$ for all $\nu \leq \nu_\mathrm{max}$)
- The harmonic approximation of the lattice dynamics is valid

Γ_TST and D obey an Arrhenius law with a prefactor ν_0 which depends on the eigenmodes of the adsorbate-substrate system. Hence, ν_0 is generally considered to be comparable in magnitude to typical phonon frequencies, i.e. $\nu_0 \approx 10^{11}$-10^{13} s^{-1}. Note, however, that prefactors which differ from this rule of thumb by many order of magnitude have been reported, e.g. see Ref. 86. What renders the approximate expression for the hopping rate in Eq. 2.10 appealing is that the prefactor ν_0 and the diffusion energy barrier ΔE_d can be obtained from calculated or measured diffusion constants D at different temperatures. If the hopping rate obeys an Arrhenius law, a linear fit of D versus $1/k_\mathrm{B}T$ yields ν_0 and ΔE_d (Arrhenius plot: $\ln(D/a^2) = \ln(\nu_0) - \Delta E_d/k_\mathrm{B}T$). Alternatively, both the prefactor ν_0 and the diffusion energy barrier ΔE_d can be calculated from first principles. For example, ΔE_d is the difference between the DFT total energies of the transition state configuration and the ground state configuration. ν_0 can be calculated by diagonalizing the dynamic matrix in A and ts. In practice, a calculation of ν_0 might not be feasible due to numerical errors which can easily be of the order of a phonon frequency (10^{12} s^{-1} requires an accuracy of ≈ 4 meV). In addition, the computational cost associated with a calculation of the dynamic matrix can be prohibitive. However, it might not be necessary to calculate ν_0 at all for many purposes as long as scaled quantities (Γ/ν_0, D/ν_0) are reported.

In the low temperature limit, which is mentioned just for the sake of completeness, the overall diffusion energy barrier is the sum of a zero-point energy ΔE_zp and the static diffusion energy barrier ΔE_d:[89]

$$\Gamma_\mathrm{TST}^{\mathrm{A}\,\rightarrow\,\mathrm{B}} \xrightarrow{T\rightarrow 0K} \frac{k_\mathrm{B}T}{h} e^{-(\Delta E_d - \Delta E_\mathrm{zp})/k_\mathrm{B}T} \tag{2.11}$$

$$\Delta E_\mathrm{zp} = \sum_{i=1}^{3N} \frac{h\nu_i^\mathrm{A}}{2} - \sum_{i=1}^{3N-1} \frac{h\nu_i^\mathrm{ts}}{2} \tag{2.12}$$

Note that below a critical temperature T_c, given by the Goldanskii criterion $T_c = \hbar|\omega_i|/2\pi k_\mathrm{B}$, quantum effects such as tunneling diffusion should be significant (ω_i is the unstable mode at ts).[88,90] Hence, the rate according to Eq. 2.11 is not necessarily an accurate approximation of the true rate for very low temperatures. A quantum transition state theory is more appropriate in this case.[91,92]

2.1.2 The nudged elastic-band method

The calculation of the TST hopping rate between two minima of the PES can be accomplished by a determination of the transition state on a configuration space path connecting the minima. This task is far from trivial due to the fact that a transition state is a saddle point of the PES. Consequently, there is no basin of attraction in the vicinity of a transition state. A simple steepest-descend search would follow the unstable mode at the saddle point and converge to a minimum of the PES (unless the search is started exactly at the transition state). Many different iterative algorithms have been proposed to search for transition states on a PES. Most algorithms can be assigned to two main categories: single-state and multiple-state transition-state searches.

The single-state search-algorithms only require knowledge of the initial minimum from which a transition state search is started. The employed strategies are either based on uphill-climb approaches or ab initio molecular dynamics (MD). Uphill-climb approaches, which rely on the calculation and diagonalization of the full Hessian or dynamic matrix, have been developed especially for small molecular systems.[93,94] However, both the calculation as well as the diagonalization of the full Hessian matrix at every transition-state search-step may involve a prohibitive computational cost for large systems.[94] Hence, approaches which only require the calculation of first derivatives like the dimer[95] or the lanczos[96] method have been proposed.[94] These methods are referred to as min-mode following methods because they make use of the direction of slowest ascend starting from a configuration near the minimum, i.e. only the smallest eigenvector and eigenvalue of the Hessian matrix are needed.[94] Min-mode following methods can be used to calculate all accessible transitions starting from an initial minimum by using stochastically perturbed coordinates of the minimum as starting points. In this case a very large number of independent transition state calculations for each minimum is required.[95] Finally, ab initio MD simulations can be used to model rare events such as diffusion dynamics on substrate surfaces. The diffusion constant can be directly computed from the mean square displacements. The Vineyard attempt frequency as well as the overall diffusion barrier can be obtained from an Arrhenius plot of the calculated diffusion constants at different temperatures. However, MD simulations can be rather inefficient in this respect.[97] If the energy barriers are large compared to $k_{\mathrm{B}}T$, the transition state region is only rarely visited and most of the computing time is spent on the dynamics at the well bottom. To bridge the gap to longer timescales, accelerated or restricted molecular dynamics techniques have been developed.[97–100]

The second class of transition-state search-algorithms comprises multiple-state methods. These require the *a priori* knowledge of the initial and final state of a diffusion event. In the course of an iterative saddle point search, these algorithms use intermediate configurations somewhere between the initial and final state to locate a transition state. Examples of algorithms in this category are the drag-method, the step-and-slide method,[101] the ridge-method,[101] transition-path-sampling,[102] the DHS method,[101] the CPR method,[101] and chain-of-states methods.[103]

Today, the most frequently employed transition-state search-method for diffusion events on substrate surfaces is a special chain-of-states method called nudged elastic band (NEB).[103] By means of the NEB method a discrete approximation of the reaction path or minimum energy path (MEP) can be calculated in addition to the transition state configuration, and with it, the diffusion energy barrier. A MEP is a path in configuration space such that the force perpendicular to the tangent on the path acting on every point of the MEP is zero. The NEB method is the algorithm of choice to determine diffusion energy barriers, transition states, and reaction paths in this work. A NEB calculation starts with an initial and final minimum of the PES and a certain number of intermediate configurations. A reasonable starting set-up can usually be obtained from a straight line interpolation in configuration space between the minima. Note that in general there could be multiple MEPs with different transition states between two minima. In such a situation the final result can depend on the choice of the initial chain-of-states guess.

In the following, the NEB method is introduced step-by-step starting from a simple elastic-band scheme which introduces artificial spring forces $\boldsymbol{F}_{\text{spring}}$ between adjacent intermediate states to keep them from relaxing to one of the minima. Let the number of intermediate states be N and the spring constant be k. The resulting *elastic-band* total energy E_{EB} of all coupled states on the PES, V, and the force F_i^{EB} on intermediate configuration i are given by:

$$E_{\text{EB}} = \sum_{i=0}^{N+1} V(\boldsymbol{R}_i) + \sum_{i=0}^{N} \frac{k}{2}(\boldsymbol{R}_i - \boldsymbol{R}_{i+1})^2 \tag{2.13}$$

$$i = 1...N: \quad \boldsymbol{F}_i^{\text{EB}} = -\boldsymbol{\nabla} V(\boldsymbol{R}_i) + \boldsymbol{F}_{\text{spring},i} \tag{2.14}$$

$$= -\boldsymbol{\nabla} V(\boldsymbol{R}_i) - k(\boldsymbol{R}_i - \boldsymbol{R}_{i+1}) + k(\boldsymbol{R}_{i-1} - \boldsymbol{R}_i) \tag{2.15}$$

Even though this elastic-band scheme already provides a reasonable estimate of the MEP and the transition state configuration, the deviations can be largest in a region of configuration space where it matters the most, i.e. near the transition state.[103] Intermediate states in this scheme tend to *cut-the-corner* when the MEP is curved due to components of the spring forces tangential to the MEP, or they slide away from the barrier region due to a non-zero gradient of the PES along the MEP.[103] In addition, the results can significantly depend on the value for the spring constant.[103] These deficiencies can be overcome by a procedure called *nudging* in which the components of the total force responsible for corner cutting and down-sliding are set to zero.[103] The forces in the original NEB method are given by:[101,103]

$$\begin{aligned} i = 1...N: \quad \boldsymbol{F}_i^{\text{NEB}} &= -\boldsymbol{\nabla}^{\perp} V(\boldsymbol{R}_i) + \boldsymbol{F}_{\text{spring},i}^{\parallel} \\ &= -(\boldsymbol{\nabla} V(\boldsymbol{R}_i) - \boldsymbol{\nabla} V(\boldsymbol{R}_i) \cdot \hat{\boldsymbol{\tau}}_i) + (\boldsymbol{F}_{\text{spring},i} \cdot \hat{\boldsymbol{\tau}}_i)\hat{\boldsymbol{\tau}}_i \end{aligned} \tag{2.16}$$

where $\hat{\boldsymbol{\tau}}_i$ is the tangent unit vector to the path at $\boldsymbol{R}_i$.

The definition of a tangent vector for a discrete set of intermediate states is certainly an issue especially if the path is only sampled by a few states. The tangent vector $\hat{\boldsymbol{\tau}}_i$ was originally calculated from a bisection of two line segments:[104]

$$i = 1...N: \quad \hat{\boldsymbol{\tau}}_i = \boldsymbol{\tau}_i / \|\boldsymbol{\tau}_i\| \quad \text{with} \qquad \boldsymbol{\tau}_i = \frac{\boldsymbol{R}_i - \boldsymbol{R}_{i-1}}{\|\boldsymbol{R}_i - \boldsymbol{R}_{i-1}\|} + \frac{\boldsymbol{R}_{i+1} - \boldsymbol{R}_i}{||\boldsymbol{R}_{i+1} - \boldsymbol{R}_i||}. \tag{2.17}$$

It turned out that in regions where the reaction path is curved this definition can lead to kinky approximate MEPs even if a large number of states is used.[104] A way to circumvent this issue has been put forward by Henkelman and Jonsson. They have proposed to calculate an approximate tangent vector for intermediate states which are not at a local extremum by:[104]

$$\boldsymbol{\tau}_i = \begin{cases} \boldsymbol{\tau}_i^+ = \boldsymbol{R}_{i+1} - \boldsymbol{R}_i & \text{if} \quad V_{i+1} > V_i > V_{i-1} \\ \boldsymbol{\tau}_i^- = \boldsymbol{R}_i - \boldsymbol{R}_{i-1} & \text{if} \quad V_{i+1} < V_i < V_{i-1} \end{cases} \tag{2.18}$$

where V_i is the potential energy at $\boldsymbol{R}_i$. For states which are at an extremum, e.g. near a local minimum or transition state, an approximate tangent is calculated from a weighted average of $\boldsymbol{\tau}_i^-$ and $\boldsymbol{\tau}_i^+$ which switches smoothly between the two. If the potential energy sequence of the two states adjacent to i is either $V_{i-1} < V_i > V_{i+1}$ or $V_{i-1} > V_i < V_{i+1}$, the approximate tangent vector is calculated as:[104]

$$\begin{aligned} \boldsymbol{\tau}_i &= \begin{cases} \boldsymbol{\tau}_i^+ \Delta V_i^{\max} + \boldsymbol{\tau}_i^- \Delta V_i^{\min} & \text{if} \quad V_{i+1} > V_{i-1} \\ \boldsymbol{\tau}_i^- \Delta V_i^{\min} + \boldsymbol{\tau}_i^- \Delta V_i^{\max} & \text{if} \quad V_{i+1} < V_{i-1} \end{cases} \\ \text{with} \quad \Delta V_i^{\max} &= \max\{|V_{i+1} - V_i|, |V_{i-1} - V_i|\} \\ \text{and} \quad \Delta V_i^{\min} &= \min\{|V_{i+1} - V_i|, |V_{i-1} - V_i|\}. \end{aligned} \tag{2.19}$$

With this definition of the approximate tangent vector a rigorous and well behaved convergence of the nudged elastic band can be achieved if a sufficient number of intermediate states is introduced.[104]

A slight change to the original NEB forces in Eq. 2.16 has been proposed by Henkelman and Jonsson. They have modified the spring forces parallel to the tangent vector to ensure that in the converged elastic band all intermediate states are equally spaced along the MEP:[104]

$$\begin{aligned} i = 1...N: \quad \boldsymbol{F}_i^{\text{NEB}} &= -\boldsymbol{\nabla}^{\perp} V(\boldsymbol{R}_i) + \boldsymbol{F}_{\text{spring},i}^{\parallel} \\ \boldsymbol{F}_{\text{spring},i} &= k(\|\boldsymbol{R}_i - \boldsymbol{R}_{i+1}\| - \|\boldsymbol{R}_{i-1} - \boldsymbol{R}_i\|)\hat{\boldsymbol{\tau}}_i \end{aligned} \tag{2.20}$$

An equally spaced elastic band allows for a systematic improvement of the sampling density along the MEP by adding more intermediate states. However, the region around

a transition state may only be a small fraction of the entire MEP. Hence, a brute-force improvement of the transition state configuration by adding more states to the elastic band can significantly increase the computational cost, which often renders such an approach impracticable. A very elegant way of converging the highest-energy state of the elastic band to the transition state configuration without the need for a higher sampling density is the *climbing-image* variant of the NEB method called climbing-image nudged elastic band (CI-NEB).[105] If state i is the highest-energy state along the elastic band, i.e. if $V_j < V_i$ for all $j \neq i$, then the CI-NEB force acting on state i is given by:[105]

$$\begin{aligned} \boldsymbol{F}_i^{\text{CI-NEB}} &= -\boldsymbol{\nabla}^{\perp} V(\boldsymbol{R}_i) + \boldsymbol{\nabla}^{\parallel} V(\boldsymbol{R}_i) \\ \text{with} \quad \boldsymbol{\nabla}^{\parallel} V(\boldsymbol{R}_i) &= (\boldsymbol{\nabla} V(\boldsymbol{R}_i) \cdot \hat{\boldsymbol{\tau}}_i)\hat{\boldsymbol{\tau}}_i. \end{aligned} \tag{2.21}$$

Replacing the NEB spring force by the negative physical force tangential to the MEP, leads to an uphill climb of state i. As an aside, it is advisable to pre-converge all intermediate states using the regular NEB scheme before attempting a CI-NEB calculation.

The transition-state searches employing the NEB scheme reported in this work use Eq. 2.20 to calculate the NEB forces with a spring constant of 5 eV/Å^2 and Eq. 2.18 and 2.19 to obtain an approximate tangent unit vector. If the CI-NEB scheme is applied, it has been initialized with a pre-converged chain of states from a regular NEB calculation.

2.2 Metal substrate surfaces

Equilibrium structures and growth kinetics of atoms or molecules on metal substrates are at the heart of intensive research activities motivated by possible technological applications as well as fundamental physical interest. In a first step, establishing a thorough understanding of adsorbate diffusion is a key element in this respect as the diffusivity greatly influences, e.g. epitaxial growth and self-assembly of nanostructures.[106] Beyond the properties of single objects on substrate surfaces, adsorbate-adsorbate interactions can have great ramifications on long-range order at high adsorbate coverages.[4]

Atoms or molecules can be rather mobile on metal surfaces as adsorbate-metal bonds tend to be less localized compared to covalent bonds at non-metallic surfaces. For example, diffusion energy barriers of H/Si(100) have been reported to be as large as 1.68 eV for H[107] and 1.95 eV for paired H[108] compared to energy barriers of the order of a few 100 meV for H on metal surfaces.[86] Non-metallic substrates are an interesting subject on its own, but they are beyond the scope of the present work.

This Section is dedicated to reviewing some of the timely aspects of diffusion discussed in the literature. To do so, it is instructive to climb up the ladder of complexity starting with the diffusion of single atoms before dealing with complex systems such as the diffusion of molecules. It is obviously in the nature of things that only a selection of topics can be presented with a focus on aspects relevant to this work. For a comprehensive overview, the reader is referred to reviews available in the literature.[86,109,110]

2.2.1 Atoms

Metal adatom diffusion

Upon adsorbing on a surface an incident atom loses its kinetic energy acquired in the attractive potential in front of the surface on a picosecond timescale by thermalizing with the substrate phonon bath.[86] During thermalization the adsorbate atom can move across the surface. Such a process is called transient mobility.[86] Once the kinetic energy acquired during adsorption has dissipated, the adatom may diffuse on the surface by a thermally activated stochastic process. Considering a metal adatom on a metal surface, different diffusion channels can be identified, see Fig. 2.2.[111] Generally the diffusion channel with the lowest diffusion energy barrier dominates. On a flat terrace an adatom may hop from one adsorption site to the next (not necessarily nearest neighbor sites)[112] by crossing over energetically unfavorable locations.[113–115] In this case the surface diffusivity can be quite large with diffusion energy barriers ranging from a few 10 meV to a few 100 meV, see Tab. 2.1. Or, it may diffuse by an atom exchange process involving one or more atoms of the first atomic layer of the substrate.[95,115,116] Reported diffusion energy barriers for exchange diffusion range from approximately 100 meV to more than 1 eV.[95,115,116] Note that the diffusion rate for the hopping channel can be smaller than the rate of the atom exchange process which might appear counterintuitive at first site.[95,115] In the presence of steps, adislands, or other adatoms the diffusion properties can be altered and the variety of diffusion channels may increase. When an adatom approaches a straight step, e.g. at the boundary of an adisland on the surface, it may either diffuse across the step or along the step edge. In both cases diffusion may occur via hopping across the step or an exchange mechanism at the step edge.[89,117] Diffusion across a step may require a higher activation energy compared to diffusion on the flat adisland or terrace (Ehrlich-Schwoebel barrier),[118,119] and this can have important ramifications on crystal growth for certain temperatures (three dimensional or layer-by-layer).[89,106] The details of the adatom diffusivity along adisland boundaries (edges, kinks), on the other hand, will determine equilibrium adisland shapes.[89,106] Several adatoms can also unite to form stable dimers, trimers, or larger clusters which may subsequently diffuse as an entity.[120–122] Evidently, the more atoms comprise a cluster the more diffusion modes could be thought of which may lead to very complex diffusion.[122,123] On a general note, it has been reported that the diffusivity of clusters decreases with size.[124]

An aspect of adatom diffusion on metal surfaces which has caused quite some controversy in the literature is the order of magnitude of the exponential prefactor (or attempt frequency) which enters the diffusion constant, see Eqs. 2.2 and 2.10. There is general believe that typical attempt frequencies should be of the order of phonon frequencies (approximately 0.1 THz to 10 THz).[86] However, Barth *et al.* have reported very low attempt frequencies between 10^9 s^{-1} and 10^3 s^{-1} for adsorbate-substrate systems with a weakly corrugated PES (ΔE_d of the order of a few 10 meV).[128] Such a reduction (increase) of the attempt frequency with a reduced (increased) corrugation of the PES is

Table 2.1: Adatom diffusion data for metal substrate-surfaces. ΔE_d is the diffusion energy barrier. D_0 is the exponential prefactor, i.e. the diffusion constant is $D_0 e^{-\Delta E_d/k_\mathrm{B}T}$. ν_0 is an effective attempt frequency given by $D_0{=}\nu_0 a^2/4$ (a: surface lattice constant). An asterisk is synonymic for "*see references in ...*". See the main text for a critical discussion. (*STM*: scanning-tunneling microscope, *FIM*: field ion microscopy)

	ΔE_d (meV)	D_0 (cm^2/s)	ν_0 (s^{-1})	Method	Reference
			Experiment		
Al/Au(111)	30	$5\cdot10^{-13}$	$2\cdot10^{3}$	STM, nucleation theory	125
Cu/Cu(111)	37	$8\cdot10^{-3}$	$5\cdot10^{13}$	STM	126
Cu/Cu(111)	40	$8\cdot10^{-4}$	$5\cdot10^{12}$		127
Al/Al(111)	42	$2\cdot10^{-9}$	$8\cdot10^{6}$	STM, nucleation theory	128
Al/Al(111)	60	$2\cdot10^{-5}$	$1\cdot10^{11}$	STM, nucleation theory	129
Ag/1ML Ag-Ag(111)	60	$2\cdot10^{-7}$	$1\cdot10^{9}$	STM, nucleation theory	130
Ag/Ag(111)	97	$4\cdot10^{-5}$	$2\cdot10^{11}$	STM, nucleation theory	130
Pt/Pt(111)	260		$5\cdot10^{12}$	STM, nucleation theory	131
Ir/Ir(111)	289	$3.5\cdot10^{-4}$	$2.1\cdot10^{12}$	FIM	(∗) 128
Cu/Cu(100)	280-400		10^{11-12}	Helium atom scattering	(∗) 132
Pt/Pt(100)	470	$1\cdot10^{-3}$	$5\cdot10^{12}$	FIM	(∗) 128
Rh/Rh(100)	880	$1\cdot10^{-3}$	$6\cdot10^{12}$	FIM	(∗) 128
			Theory		
Cu/Cu(111)	41		$1.1\cdot10^{12}$	Embedded atom method	121
Al/Al(111)	42		$4\cdot10^{12}$	DFT	133
Ag/Ag(111) strained	60		$1.3\cdot10^{12}$	DFT	114
Ag/1ML-Ag/Pt(111)	60		$5.9\cdot10^{12}$	DFT	114
Ag/Ag(111)	82		$8.2\cdot10^{11}$	DFT	114
Al/Au(111)	120		$7\cdot10^{12}$	DFT	133
Al/Al(110)	390		$1.980\cdot10^{12}$	DFT	134
Cu/Cu(111) along steps	235-312		$7.4\text{-}8.5\cdot10^{12}$	Embedded atom method	89

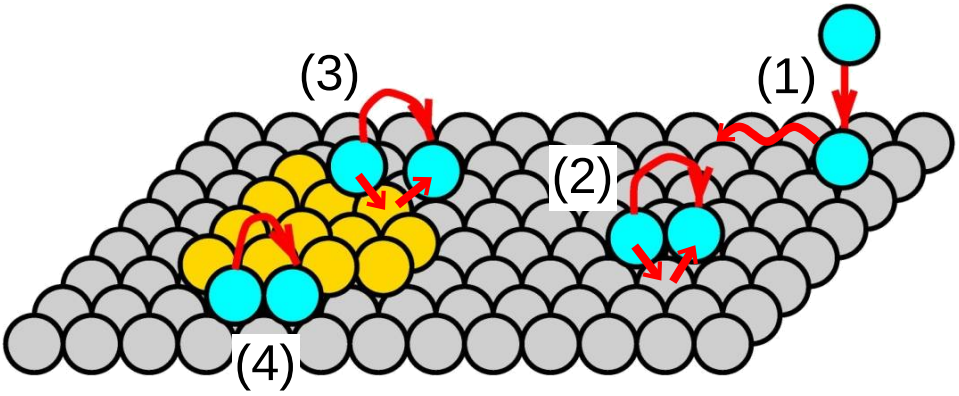

Figure 2.2: Excerpt of diffusion channels for adatoms on a solid surface (schematic diagram): adsorption dynamics and transient diffusivity (1), hopping or exchange process on a terrace (2) or across a step edge (3), and diffusion along a step edge (4).

commonly referred to as the Meyer-Neldel rule.[135] Barth *et al.* determined the attempt frequencies for Al adatom diffusion on the Al(111) surface from STM experiments.[128] They have measured the density of Al adislands and have related this quantity to the diffusion constant by means of nucleation theory. However, doubts about the interpretation of the experiments have been raised. Michely *et al.* have argued that the experimental conditions used by Barth *et al.* have lead to significant co-adsorption of impurities which alter the results compared to a clean growth system.[129] Repeating the STM experiment for Al/Al(111), Michely *et al.* have reported a much higher attempt frequency of 10^{11} s^{-1} in accordance with the expected order of magnitude. They also noted that independent STM experiments for self-diffusion of Pt/Pt(111) show a similar significant dependance of the results with experimental conditions.[129] Notably, the reported higher attempt frequencies and diffusion energy barriers measured by Michely *et al.* are in agreement with DFT calculations for Al/Al(111) diffusion.[133] Both Fichthorn and Scheffler as well as Ovesson *et al.* have reasoned that the exceptionally low prefactors observed in some experiments can be understood when adsorbate-adsorbate interactions are correctly taken into account.[133,136] For isolated adsorbates, however, the typical range for attempt frequencies should remain valid.[136]

Finally, Boisvert *et al.* have assessed the correlation between attempt frequencies and PES corrugation (Meyer-Neldel rule) for a variety of adsorbate-substrate systems using the embedded atom method (EAM).[135] Their results support the validity of the Meyer-Neldel rule. Reported attempt frequencies approximately fall in a range from 10^{11} s^{-1} to 10^{15} s^{-1}. The highest attempt frequency has been calculated for exchange self-diffusion of Ni/Ni(100). At this point the validity of the Ni/Ni(100) EAM results could be challenged because the EAM diffusion energy barrier is at variance with recent DFT calculations.[115,137] First of all, the DFT value for ΔE_d exhibits a significant dependance on adatom coverage. The ΔE_d value for the lowest reported coverage is about 40%

smaller than the EAM result.[115,137] Secondly, the EAM results favor a hopping diffusion mechanism while the DFT diffusion energy barrier for an exchange process is lower than that for the hopping mechanism.[115,137] The consequences from this argument for the attempt frequency are hard to judge from a distance but if the Meyer-Neldel rule holds, the frequency could be lower than what has been reported. Kürpick has also assessed the Meyer-Neldel rule using the EAM.[138] The observed variation in exponential prefactors with PES corrugation has been reported to be small. The results are consistent with attempt frequencies of the usual order of magnitude (0.1-10 THz).

Attempt frequencies for isolated adatom diffusion on metal surfaces can be considered to approximately lie in a universal range between 0.1-10 THz. No undisputed evidence which contradicts this observation has been reported so far. Unless large adatom clusters are considered, the diffusion channels of (metal) adatoms on metal substrates can be considered well understood owing to the comparatively simple PES.

Sulfur atom diffusion

One of the workhorse model-systems for bonding of non-metal atoms and organic molecules on metal substrate-surfaces is the sulfur-metal bond. S atoms are strongly bound to metal surfaces with binding energies, E_b, of several eV, see Tab. 2.2. In low-energy adsorption configurations S atoms occupy hollow-sites of (111) or (100) substrate metal surface at low S coverage. The strong adsorbate-substrate interaction can be taken as an indication of a large corrugation of the PES.[86,139] Indeed, the energy barriers, ΔE_d, for jump diffusion of atomic S on unreconstructed (111) and (100) metal surfaces come out between 0.17 eV and 0.94 eV, see Tab. 2.2. In the transition state geometry the S atom resides approximately above a bridge site of the (111) or (100) substrate surfaces in case of S/Cu(100), S/Ag(100), S/Pt(111), and S/Pt(100).[140,141]

Nilekar *et al.* have proposed a general rule-of-thumb for the relation between the bond strength and the corrugation of the PES for non-metallic adsorbates on transition metal substrate-surfaces [(111) or (0001) surfaces].[139] The proposed general relation is $\Delta E_d \approx 0.12 E_b$ obtained from a linear fit to the adsorption-diffusion data. Notably, the scatter of the data is significant.[139] E_b for different metal substrates is plotted versus corresponding ΔE_d values in Fig. 2.3 for a coverage of $\Theta = 1/4$. Overall, there appears to be a correlation between E_b and ΔE_d (irrespective of the two surface orientations) but any underlying relation does not seem to be strictly monotonic. Following Nilekar *et al.* , if the DFT values for E_b and ΔE_d in Fig. 2.3 are fitted with a straight line, the slope is approximately 0.18 [(111) only: 0.20, (100) only: 0.27]. Unfortunately, a robust conclusion can not be drawn from experiment alone because not enough data is available. It is speculated that the differences between the results within this work and Nilekar *et al.* originate from a different set-up of their calculations, e.g. Nilekar *et al.* use only three atomic layers to model the substrate-surface, the substrate atomic positions are fixed at ideal bulk positions, and various non-metallic elements are studied as adsorbates. Furthermore, the data reported by Nilekar *et al.* has been obtained at a

slightly lower coverage which can be an issue for certain system, see Tab. 2.2. In view of the above, the rule-of-thumb proposed in Ref. 139 should be considered as such, which may certainly give useful guidance. However, if a precision of the order of 100 meV or better is required, a detailed system-specific assessment seems indispensable.

In view of the controversy about the order of magnitude of the metal-adatom attempt-frequencies, a review of available data for S diffusion on metal surfaces is certainly of interest. The few experimental attempt frequencies or exponential prefactors reported in the literature are of the expected order of magnitude ($\nu_0 \approx$ 0.1-10 THz), see Tab. 2.2. The DFT attempt frequencies are all of the order of 10^{12} s^{-1}. Hence, the experimental as well as theoretical data for available substrates is consistent with the general expectation that attempt frequencies are approximately of the order of THz.

Thus far, the discussion of S diffusion has been focused on the metal-vacuum interface. Diffusion can also be studied in an electrochemical (EC) environment at a solid-liquid interface, which is an important interface for technological applications like batteries or fuel-cells. In addition, surface reconstructions like Au(100)-(1×1) or Au(111)-(1×1) are only stable under certain EC conditions.[151] A detailed analysis of diffusion characteristics at the solid-liquid interface requires the development of techniques with a high spacial resolution at the interface like a video-STM capable of operating in an EC cell. Such an instrument has been developed in the group of O. M. Magnussen.[148] Using the video-STM technique, Tansel and Magnussen have characterized the diffusion of S atoms at the interface of a Cu(100) metal surface and 0.01 M HCl solution.[148] In a certain range of the external potential, applied to the working electrode with respect to a reference, dissolved Cl^- ions adsorb on the Cu substrate surface forming a c(2×2) adlayer.[148] Individual S atoms can be incorporated into the adlayer most probably by substituting single Cl adsorbates.[140,148] The diffusion properties of these S atoms have been monitored at different temperatures and applied potentials. The S atom motion can be characterized by nearest neighbor hops to adjacent sites of the c(2×2) adlayer lattice for the majority of diffusion events [jump length $\sqrt{2}$ times the surface lattice constant of Cu(100)].[148] From measurements at different temperatures the attempt frequency and diffusion energy barrier can be deduced. What makes the diffusion under EC conditions unique is that for certain systems the PES landscape can be tuned by varying the applied external potential, ϕ, between the working electrode surface and a reference electrode in the EC cell. It has been suggested that this effect is related to the coupling of the adsorbate dipole moment (intrinsic or induced) to the electric field at the interface.[148,152] Tansel and Magnussen have measured the relation between the diffusion energy barrier and the applied potential. The potential dependance of the barrier is significant and follows a relation $\Delta E_d = 0.94\ \text{eV} + 0.50\ \text{eV}\phi/V_{\text{SCE}}$.[148] Notably, the attempt frequency, $2.35 \cdot 10^{12}$ s^{-1}, is of the order of typical phonon frequencies and is independent of the applied potential.[148]

Stremme has carried through DFT calculations for the adsorption and diffusion of S atoms on the Cu(100) surface with a c(2×2) Cl adlayer.[140] The calculations have been carried through for the solid-vacuum interface, i.e. the electrolyte solution was

Table 2.2: Adsorption/diffusion data for sulfur-metal systems. ΔE_d is the diffusion energy barrier. If no NEB calculation is available, ΔE_d is estimated from the total-energy difference between an S atom at a hollow-site and a bridge-site of the surface. E_b is the binding energy per S atom without a zero-point energy-correction (theory) or the desorption energy (experiment). D_0 is the exponential prefactor of the diffusion constant D. ν_0 is an effective attempt frequency (D_0=$\nu_0 a^2/4$ with surface lattice constant a). The coverage θ is the number of S atoms per substrate-surface atom. (*STM*: scanning-tunneling microscope, *FIM*: field ion microscopy, *QHAS*: quasi-elastic helium atom scattering, *TDS*: thermo desorption spectroscopy)

	ΔE_d (eV)	E_b (eV)	D_0 (cm^2/s)	ν_0 (s^{-1})	θ	Method	Reference
				Theory			
S/Ag(111)	0.17	−3.64			1/4	DFT, NEB	142
S/Ag(111)	0.18	−3.61	$\approx 3\cdot 10^{-3}$	$\approx 3\cdot 10^{12}$	1/9	DFT, NEB	this work
S/Cu(111)	0.21	−4.43			1/4	DFT, NEB	142
S/Cu(111)	0.23	−4.2[a]		$2.8\cdot 10^{12}$	1/8	DFT, NEB	139
S/Pd(111)	0.37	−4.85			1/4	DFT, NEB	142
S/Ni(111)	0.37	−5.0[a]		$3.4\cdot 10^{12}$	1/8	DFT, NEB	139
S/Au(111)	0.43	−3.83[b]			1/4	DFT	143
S/Pt(111)	0.54	−5.0[a]		$3.9\cdot 10^{12}$	1/8	DFT, NEB	139
S/Pt(111)	0.67	−5.14			1/4	DFT	144
S/Au(100)	0.46	−3.77			1/9	DFT	this work
S/Au(100)	0.58	−3.81			1/4	DFT	this work
S/Ag(100)	0.84	−4.06			1/4	DFT, NEB	this work
S/Cu(100)	0.94	−4.93			1/4	DFT, NEB	140
S/Re(0001)	0.46	−5.7[a]		$3.6\cdot 10^{12}$	1/8	DFT, NEB	139
S/Ru(0001)	0.55	−5.6[a]		$3.5\cdot 10^{12}$	1/8	DFT, NEB	139
				Experiment			
S/Pt(111)	0.57		$4\cdot 10^{-5}$	$2\cdot 10^{11}$	Atom	STM, T=185-200 K	86
S/Ni(111)[c]	0.29	−2.6	$2.2\cdot 10^{-4}$	$1\cdot 10^{12}$	Atom	FIM, T=105-115 K, TDS	145,146
S/Cu(111)[d]			$\{5.5\cdot 10^{-4}\}$	$\{3\cdot 10^{12}\}$	< 0.16	QHAS, T=820 K	147
S/Cl-Cu(100)[e]				$2.35\cdot 10^{12}$	Atom	Video STM, T=277-296 K	148
S/Re(0001)	0.79	−4.2			≈ 0.25	STM, T=300 K, TDS	149,150

[a] Including zero-point energy-correction. E_b estimated from Fig. 2 of Ref. 139.

[b] This work: -3.52 eV (64 k-points in the BZ) and -3.82 eV (25 k-points as in Ref. 143).

[c] No Arrhenius plot, D_0 from general considerations.

[d] Diffusion constant D=$2.9\cdot 10^{-5}$ cm^2/s, DFT-ΔE_d=0.21 eV to calc. D_0 and ν_0 from D

[e] Solid-liquid interface, Cl-c(2x2) adlayer, ΔE_d/eV=0.94+0.50 ϕ_{SCE}/V (potential dep.)

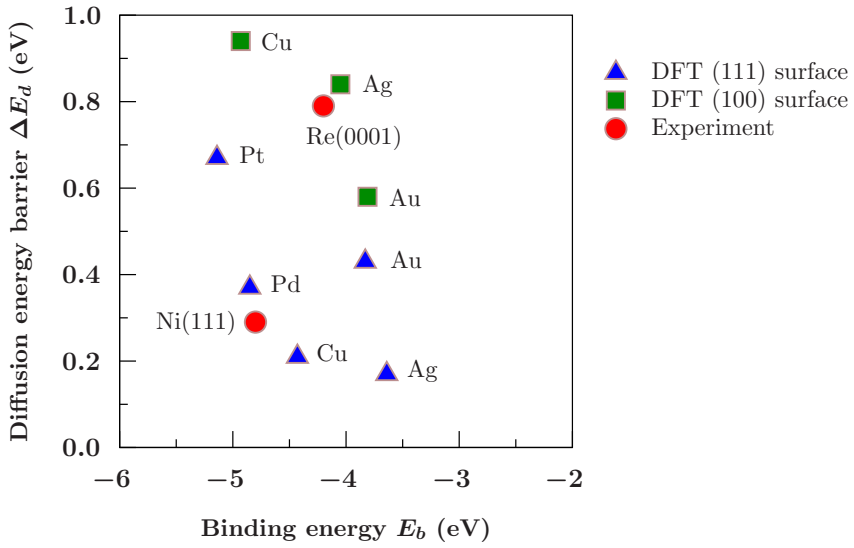

Figure 2.3: Diffusion energy barrier of an S atom on different metal substrates versus binding energy (theory, no zero-point energy-correction) or desorption energy (experiment). DFT values for the (111) (blue) and (100) (green) substrate surfaces as well as experimental data (red) are taken from Tab. 2.2. The S coverage is 1/4 for the DFT data.

not treated explicitly. These calculations may provide a starting point for an atomistic view of the system under EC conditions. The results suggest that an S atom adsorbs on the Cl-covered Cu-surface by replacing one Cl atom of the adlayer. An atomistic view of the S hopping mechanism could, in principle, involve different diffusion channels. E.g. diffusion could occur via an S-Cl exchange process, or it could be promoted by Cl vacancies adjacent to an adsorbed S atom.[140] Candidates for such diffusion channels have been analyzed from first principles, which is a truly formidable task due to the many degrees of freedom involved in the interplay between the S atom and the Cl adlayer.[140] Before a conclusion can be drawn from a comparison of the different diffusion channels, an assessment of the energetics behind Cl vacancy formation would be needed. This piece of the puzzle has not been added because the chemical potential of Cl^- ions in solution is rather difficult to obtain from DFT calculations. A very interesting result of Stremme's work is related to the potential dependance of the diffusion energy barriers. From the DFT calculations a change of the overall dipole moment of the system along the diffusion paths can be deduced from work function changes.[140] If only the non-self-consistent electrostatic contribution to the coupling of the dipole moment and an electric field at the interface is considered, the change of the diffusion energy barriers with potential has the same sign as has been observed by Tansel and Magnussen.[140,148] In

addition, the order of magnitude of the potential dependance seems to be approximately in the right ballpark.[140] Note, however, that this conjecture depends sensitively on the value assumed for the electric field at the interface, which is a difficult issue to assess. Furthermore, the influence on the diffusion paths of the ionic solution through induced surface charges, screening effects, or co-adsorption of water molecules has not been characterized. An improved atomistic description, which explicitly includes the solid-liquid interface in the calculation, would be required to assess the importance of such effects for diffusion under EC conditions.

2.2.2 Molecules

The diffusion properties of single molecules on substrate surfaces may differ substantially from simple jump diffusion of isolated adatoms. Rotations, conformational changes, distortions, re-orientations, and the possibility to form multiple molecule-surface bonds may increase the complexity of the diffusion characteristics.

Small molecules - few internal degrees of freedom

Diffusion of small molecules, which only possess a very limited number of conformational degrees of freedom relevant for diffusion like diatomic molecules, CH_4, or SCH_3, belong to simpler molecular adsorbate-substrate systems. If the molecule is covalently bonded to the surface with a well defined anchor atom, the main elementary diffusion modes should in principle be composed of relocations of the molecule-surface anchor, variations of molecular tilt and azimuthal angles, and rotations around covalent bonds (internal or molecule-surface).

CO is one of the archetypical model system for diffusion of small diatomic molecules on metal surfaces. The CO diffusivity has been extensively studied on many different metal substrates using various experimental techniques.[86] Despite these intense efforts a consistent picture could not be established so far and many experimental results remain contradictory.[86] Especially the origin of the reported range for the order of magnitude of attempt frequencies (10^8 s^{-1} to 10^{16} s^{-1}) is a matter of debate. From photoemission electron microscope (PEEM) experiments of CO diffusion at finite coverage on a Pd(111) substrate surface, diffusion energy barriers of 520 meV and 175 meV as well as exponential prefactors of 10^0 cm^2s^{-1} and 10^{-3} cm^2s^{-1} have been inferred.[86] For isolated CO molecules, a diffusion energy barrier of 118 meV and an exponential prefactor of 10^{-4} cm^2s^{-1} (attempt frequency $\approx 10^{12}$ s^{-1}) have been measured by means of a STM.[153] The authors of Ref. 153 speculate that the surface coverage of CO molecules has a significant influence on the results and may be responsible for the substantial differences between the experimental findings. There does not seem to be any published theoretical work related to an atomistic understanding of the diffusion of CO molecules on metal surfaces. In view of the expected simple diffusion properties, this might seem puzzling at first sight. However, it has been noted that standard DFT calculations of CO on metal

surfaces may lead to an energetical order of local minima of the PES which is inconsistent with experiments.[154] This deems any standard DFT calculation of CO diffusion on a metal substrate surface quite speculative.

In view of the great importance and model character of the S-Au bond, the diffusion of methanethiol radicals, SCH_3, on Au substrate surfaces is certainly a timely topic. An isolated SCH_3 radical binds to the unreconstructed Au(111) surface via an S-Au anchor.[39,50] In the lowest-energy configuration the S atom is located between a bridge and hollow site of the substrate surface (fcc-bridge or hcp-bridge configurations).[39,50] The S-C bond is tilted with respect to the surface normal by approximately 50°.[39,50] For a depiction of an SCH_3/Au(111) fcc-bridge configuration, see Fig. 4.2. The main elementary diffusion modes comprise a relocation of the S atom on the surface, and a change of the S-C tilt and azimuth angle.[39,50] Different reports concerning the diffusion properties (transition state and diffusion energy barrier) for SCH_3 radicals on the unreconstructed Au(111) surface can be found in the literature. Cometto *et al.* conducted cluster calculations for SCH_3 on Au(111) in which they position the radical over the rigid surface keeping the S atom at a constant height.[48] Within this cut through the PES, the authors of Ref. 48 consider a local maximum for SCH_3 with an energy of 0.76 eV above the adsorption minimum as the transition state for diffusion on the surface. However, a local maximum is by definition not a transition state. Ford *et al.* reported that no barrier to diffusion at the bridge site exists at all.[155] They have interpreted the corrugation of the PES between the adsorption configuration and a configuration in which the S atom is located on top of a Au surface atom as the diffusion energy barrier ($\Delta E_d = 0.36$ eV). A minimum requirement for a diffusion path on the PES is the continuity of the path. Unfortunately, it appears that the path in configuration space chosen by Ford *et al.* is not continuous. A systematic assessment of a possible diffusion path can be found in a report by Maksymovych *et al.*[50] They have calculated an energy barrier of 0.23 eV using the NEB transition state search algorithm for a relocation of the S atom from an fcc-bridge configuration to an adjacent hcp-bridge configuration. Because Maksymovych *et al.* were not interested in SCH_3 translations on the surface, the initial and final SCH_3 configuration are inequivalent. Hence, the published calculations only comprise part of a diffusion path. The results published by Maksymovych *et al.* are in agreement with the DFT calculations carried through in this work, see Sec. 4.1.

Maksymovych *et al.* have reported that SCH_3 radicals form $Au(SCH_3)_2$ complexes on the Au(111) surface at room temperature.[56] The diffusion of these complexes has been studied in this work, see Sec. 4.1.[39] Jiang and Dai have also published a diffusion study of $Au(SCH_3)_2$ on the Au(111) surface at the same time.[156,157] A comparison to their results and a summary of the published $Au(SCH_3)_2$ diffusion characteristics[39] will be given in Sec. 4.1.

Larger molecules - few internal degrees of freedom

This class of molecular adsorbates comprises large molecules with only few low-energy excitable internal degrees of freedom which are relevant for diffusion. Polycyclic-aromatic hydrocarbon-based molecules could be ascribed to this category like, e.g., the quasi-

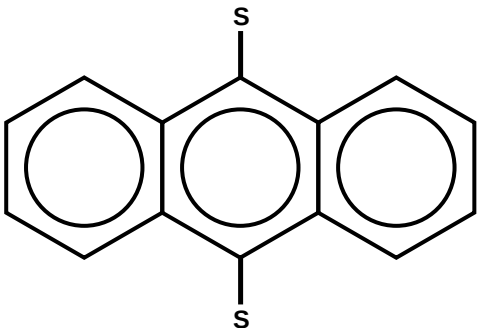

Figure 2.4: Schematic representation of a DTA radical. Hydrocarbon rings are abbreviated in the usual manner. In a DTA molecule both S atoms are saturated with H atoms forming thiol groups (-SH).

planar molecules PTCDA or anthracene. The dynamics of quasi-planar molecules on metal surfaces has attracted considerable attention due to their intriguing diffusion properties. Kwon *et al.* have characterized the motion of 9,10-dithioanthracene (DTA) radicals on the Cu(111) surface by STM experiments and DFT calculations.[158] DTA consists of an anthracene backbone and two S atoms attached to one of the carbon rings of anthracene, see Fig. 2.4. The radical adsorbs on the Cu(111) surface with the anthracene plane approximately parallel to the surface. Both S atoms form S-Cu bonds and serve as molecule-substrate anchors.[158] The internal degrees of freedom of DTA adsorbed on a metal surface are most probably restricted to distortions, i.e. bending and shearing. As a result of the interplay between the adsorbate-substrate interaction and the restrictions imposed by the anthracene backbone (internal degrees of freedom), DTA diffusion can be described as bipedal locomotion resembling the human walking motion.[158] Notably no rotation of DTA on the surface has been witnessed in experiment. The diffusion of DTA has been described as purely one dimensional along high-symmetry directions of the substrate-surface.[158] Strictly speaking, this means that the energy barrier for rotations is significantly larger than the energy barrier for translations on a scale of typical thermal energies. The DTA diffusion energy barrier and attempt frequency obtained from an Arrhenius plot are 130 meV and 0.004 THz, respectively.[158] In addition, the diffusion of individual DTA radicals has been modified by attaching two methyl groups to one end of the anthracene backbone.[159] Retaining the overall characteristic one-dimensional bipedal-locomotion, the diffusivity of methylated 9,10-dithioanthracene (DMDTA) compared to DTA is significantly reduced. The diffusion energy barrier and attempt frequency of DMDTA have been reported to be 210 meV and 2 THz, respectively.[159]

A further anthracene derived molecule with intriguing diffusion characteristics is AQ. The motion of AQ adsorbed on a Cu(111) substrate surface has been analyzed using a STM.[8] The only difference between an AQ molecule and a DTA radical is that both S atoms of DTA are replaced by O atoms. Compared to DTA, the surface diffusivity of

AQ is about three orders of magnitude higher with a diffusion energy barrier of approximately 0.02 eV and an extraordinarily low attempt frequency in the kHz regime.[8] The tiny diffusion energy barrier might be an indication of a weaker molecule-substrate interaction of AQ/Cu(111) compared to DTA/Cu(111). Analogous to DTA, the diffusion properties of AQ can be described as one-dimensional bipedal-locomotion.[8] What renders AQ diffusion special beyond what has been said, is that one or two CO_2 molecules attach to AQ either by STM manipulation or spontaneous clustering.[8] Hence, it serves as a molecular carrier, which turns isotropic CO_2 diffusion into a quasi one dimensional CO_2 molecule transport on the surface.[8] Attaching CO_2 to AQ leads to an increase of the overall diffusion energy barrier roughly by a factor of two to three.[8]

As has been described above for DTA, the diffusivity of a molecule can be altered by attaching functional units to it. A different route of tuning the diffusivity of molecules has been taken by Otero *et al.* for a violet lander molecule on Cu(110) and Miwa *et al.*[160,161] for azobenzene on Cu(110). Both groups exploit the possibility that molecules may adopt metastable adsorption configurations which possess a large barrier for returning to the ground state configuration. It has been reported that the surface diffusivity of a molecule in an excited state can be substantially increased with respect to a molecule in the ground state configuration (diffusivity enhancement factor $\gtrapprox 100$ Otero *et al.*[160], ≈ 6 Miwa *et al.*[161]). Note that, on average, this implies that the excited molecules did not return to their ground state configuration during the observation period of the diffusion process.

One aspect of molecular diffusion which lacks a thorough understanding to this day is the fact that the range of reported attempt frequencies for diffusion of large molecules spans approximately 11 orders of magnitude. At the low frequency end resides AQ/Cu(111) with a reported attempt frequency of the order of 10^3 s^{-1}.[8] At the high end an attempt frequency of $10^{13.9\pm0.7}$ s^{-1} and $10^{13.5\pm0.4}$ s^{-1} has been reported by Schunack *et al.* for decacyclene/Cu(110) and hexa-tert-butyl-decacyclene/Cu(110), respectively.[162] Furthermore, Weckesser *et al.* have reported an attempt frequency of $10^{14.4\pm0.4}$ s^{-1} for the diffusion of C_{60} on Pd(110).[163] Other attempt frequencies are in between these extremes (DTA:[159] $4 \cdot 10^9$ s^{-1}, DMTA:[159] $2 \cdot 10^{12}$ s^{-1}, PVBA:[164] $10^{10.3}$ s^{-1}). Finally, Ikonomov *et al.* have reported exponential prefactors, D_0, for PTCDA and Cu-phthalocyanine on the Ag(100) surface to be $10^{-7.9\pm0.7}$ cm^2s^{-1} and $10^{-8.4\pm0.4}$ cm^2s^{-1}, respectively.[165] Using a standard conversion factor between D_0 and ν_0 ($D_0/a_0^2 \approx \nu_0$, a_0: surface lattice constant ≈ 3 Å), the attempt frequencies come out approximately in the range 10^6-10^9 s^{-1}.

Alkane-based molecules - multiple conformational degrees of freedom

For most planar and rather stiff molecules, like the ones discussed in the previous paragraph, the relevant molecular degrees of freedom for diffusion are related to molecular distortions (bond lengths, bond angles). On the other hand alkane-based molecules, e.g. n-alkanes [H_3C-$(CH_2)_n$-CH_3], n-alkanethiols [HS-$(CH_2)_n$-CH_3], and n-alkanedithiols [HS-$(CH_2)_n$-SH], exhibit a greater flexibility due to their conformational degrees of freedom. Such conformations of single n-alkane chains may be characterized as internal

rotations around C-C bond axes. Hence, the number of internal degrees of freedom (conformations, bond lengths, bond angles) starkly increases for longer n-alkane based molecules, which may translate into an increased complexity of the PES for n-alkane based molecules on metal surfaces.

A systematic experimental study of the diffusion of n-alkanes with different chain lengths on the Ru(001) surface reported a linear relationship between the diffusion energy barrier and the alkane chain length.[86,166] The large exponential prefactor (order of 0.1 cm^2s^{-1}) was found to be independent of the chain length.[86,166]

Cohen and Zeiri have performed MD simulations, using empirical model potentials to describe the atom-atom interactions, for the adsorption and diffusion of different n-alkanes (# of C atoms = 3, 6, 10, 20) on a W(100) substrate at temperatures from 300-1000 K.[167] The reported qualitative picture is the following: (i) the diffusion constants follow an Arrhenius law as a function of temperature, (ii) the exponential prefactors are independent of alkane chain length and are close to the universal value of 10^{-3} cm^2s^{-1}, (iii) the diffusion energy barriers are proportional to the square root of the chain length, and (iv) the diffusion modes can be described as compositions of subsequent rotations of segments of the n-alkanes around C-C bond axes.[167]

Fichthorn *et al.* have carried through MD simulations (T = 15-350 K) and calculations of diffusion paths (MEPs) for short chain n-alkanes on the Pt(111) substrate surface (# of C atoms = 2, 4, 6, 8, 10).[168–170] They have used empirical potentials of the Lennard-Jones type to describe the atom-atom interactions. In their study, Fichthorn *et al.* have found that the considered n-alkanes adsorb on the surface in an *all-trans* configuration with all C-C-C planes approximately parallel to the surface.[169] For ethane through octane the diffusion energy barriers increase with the alkane chain length. The diffusive motion of ethane through octane can be described as rigid rode translations and rotations across the surface. No out-of-plane motion involving rotations around C-C bond axes has been reported.[168,169] In case of decane the diffusion consisted of bond bending and flexing and was not purely rigid-rod like anymore. It was concluded that there may exist a critical chain length above which internal conformations become more important and the diffusion modes resemble the alkane-segment rotations described by Cohen and Zeiri.[167–169] Moreover, the fact that rigid-rod motion prevails for the adsorbate-substrate systems considered by Fichthorn *et al.* might be related to the weak corrugation of the PES (order of 50 meV) which is less than the energy needed to excite internal conformations (order of 100-200 meV). The calculated attempt frequencies for n-alkane diffusion on Pt(111) are reported to be of the order of $10^{12}s^{-1}$. Fichthorn *et al.* have revealed unique molecular features of n-alkane diffusion from a calculation of the individual diffusion processes using systematic transition state search methods.[170] In particular, they could show that multiple-local minima exist on the PES especially for longer alkanes.[170] Furthermore, Fichthorn *et al.* have concluded that a directional anisotropy of the diffusion could be induced by the molecular orientation on the surface.[170]

Flexible molecules which strongly bind to a metal surface via two or more covalent bonds might be ideal model systems to study the impact of internal degrees of freedom and multiple molecule-surface bonds on the molecule's diffusivity. One such class of molecules are alkanedithiols, which may bind to the surface via two sulfur anchors.

Indeed, first steps towards a systematic diffusion study of BDTRs, under EC conditions have been undertaken by Suto and Magnussen at the University of Kiel.[171] It has been shown that low coverages (1-2% of a monolayer) of BDTRs adsorbed on a Au(111) surface can be prepared in 0.1 M $HClO_4$ solution in a regime of the applied external potential which stabilizes an unreconstructed Au(111) surface.[171] The adsorbed molecules can be monitored with a video-STM capable of taking up to 30 images per second.[171] BDTR adsorbates appeared as protrusions in the STM images, which reveal first hints of intriguing diffusion properties. It has been suggested that the protrusions originate from chemisorbed BDTRs, which bind to the Au(111) via two S-Au bonds. This could indeed be affirmed by DFT calculations for the solid-vacuum interface carried through in this work. Notably, the diffusion of BDTR in experiment is sufficiently low such that their dynamics should be accessible.[171] Images acquired at time intervals of 67-100 ms show protrusions of different shapes (elongated or almost circular) some of which are translated or have changed their orientation from image to image while others can be considered stationary.[171] This might be taken as an indication of translational and rotational BDTR diffusion channels. Note, however, that under the employed experimental conditions the surface diffusivity of BDTR was high enough for the adsorbates to move during image recording which might lead to distorted protrusions and artefacts.[171] A unique feature of experiments under EC conditions is that the applied external potential can be tuned. Interestingly, Suto and Magnussen observed a strongly decreasing diffusivity of BDTR on the Au(111) surface with increasing applied potential.[171] Furthermore, the adsorbate motion could be noticeably slowed down by cooling to 10 °C.[171] Activation energies or attempt frequencies have not been reported so far.

The diffusion of molecules on metal surfaces is a fascinating and active research field as can be witnessed by the many publications in the field. Many new and unexpected diffusion phenomena, which are unique to molecular diffusion, have been discovered. Especially the interplay between internal degrees of freedom and the molecule-surface interactions for molecules with more than one surface anchor may lead to new and unexpected diffusion characteristics. E.g. a molecule may preferentially diffuse in certain directions on a surface (at least on short time scales) depending on the prepared initial orientation of the molecule. This is a manifestation that internal degrees of freedom play an important role for the diffusion characteristics. A promising model system for molecular diffusion are alkanedithiols on metal surfaces. In a pioneering work, the accessibility of local information of BDTR diffusion processes on a Au(111) surface has been demonstrated in a video-STM study under EC conditions.[171] An atomistic understanding of the BDTR/Au diffusion mechanisms is presented in following Sections of this work. Finally, the reported range of attempt frequencies for molecular diffusion on metal surfaces, which spans 11 orders of magnitude, is highly unexpected and should trigger further investigations.

3 Density-functional theory

3.1 Basic framework

DFT is the state-of-art method to computationally investigate ground-state properties of extended systems in theoretical solid-state and surface physics today. As it provides the framework for all calculations in this work, the basic ideas and theorems are briefly introduced.

Hohenberg-Kohn theorems

In principle, the main task in theoretical chemistry and solid-state physics is to solve the many-body Schrödinger Equation for interacting electrons in a given external potential caused by the nuclei.[i] However, a general explicit solution to this problem is not available. Different strategies have been devised which allow for approximate solutions. For example, Greens-function based methods have been developed to determine physical properties in a perturbative manner.[173] Quantum chemical methods like configuration interaction focus on approximations to the many-body wave function which is represented in a span of slater determinants for the ground state and excited states. In addition, Quantum Monte-Carlo (QMC) techniques like variational QMC, diffusion QMC, and path-integral QMC represent accurate tools to determine ground-state expectation values.[174,175] However, a common draw back of these methods is the prohibitive computational cost for extended systems like molecular adsorbates on substrate surfaces.

Accurate and practicable calculations for large systems containing thousands of electrons have become practicable through the development of DFT which is an exact reformulation of the many-body problem for the ground state. Hohenberg and Kohn have shown that all ground state properties, in particular the total energy, are unique functionals of the electron density.[176,177] Hence, the intractable many-body wave function can be replaced by the electron density. The theorems derived by Hohenberg and Kohn for a non-degenerate ground-state constitute the fundamental basis of DFT. They have later been generalized to degenerate ground-states, spin-densities and finite temperature, see Ref. 177 and references therein.

Consider a system which is described by the Hamiltonian $\hat{H} = \hat{T} + \hat{W} + \hat{V}$ composed of the kinetic energy operator $\hat{T}$, the two-particle interaction $\hat{W}$, and the external potential

[i] The Born-Oppenheimer approximation[172] separates the time scales for the motion of the nuclei and the electrons which is a common approximation.

$\hat{V}$. In case of atoms, molecules, or solids, $\hat{W}$ equals the Coulomb interaction and $\hat{V}$ is the external potential caused by the nuclei. The first Hohenberg-Kohn theorem reads:[176]

Hohenberg-Kohn theorem 1. *The ground-state energy E_0 is a unique functional of the ground-state electron-density $n(\boldsymbol{r})$.*

In other words, there is a one-to-one mapping of the external potential to the ground-state electron density.[ii] As a consequence one can define the Hohenberg-Kohn functional F_{HK}:[176–178]

$$F_{\mathrm{HK}}[n] \;:=\; E_0[n] - \int n(\boldsymbol{r})\, v([n],\boldsymbol{r})\, d\boldsymbol{r}. \tag{3.1}$$

$v([n],\boldsymbol{r})$ denotes the external potential corresponding to the density $n(\boldsymbol{r})$. Notably, F_{HK} is a unique functional of the electron density for non-degenerate and degenerate ground-states.[177] This allows for a definition of an energy functional in which the external potential and the density are independent quantities:[176]

$$E_v[n] := F_{\mathrm{HK}}[n] + \int n(\boldsymbol{r})\, v(\boldsymbol{r})\, d\boldsymbol{r}\ . \tag{3.2}$$

Using this functional the second Hohenberg-Kohn theorem can be formulated:

Hohenberg-Kohn theorem 2. *Let n_0 be the ground-state electron-density corresponding to the external potential v_0. For every density $n(\boldsymbol{r})$ in the domain of $E_v[n]$ the following inequality holds:*

$$E_0[n_0] = E_{v_0}[n_0] \leq E_{v_0}[n]. \tag{3.3}$$

Hence, Hohenberg and Kohn have cast the determination of the electronic ground state of the interacting many-body system into a minimization of an energy functional which depends on the electron density alone.

Kohn-Sham equations

The Hohenberg-Kohn theorems do not make a statement about how to achieve a minimization of the energy functional. However, Kohn and Sham have derived a self-consistency scheme based on the Hohenberg-Kohn theorems by which the ground-state density of the interacting many-body system can be calculated.[179] The result is an exact mapping of the interacting many-body system onto a system of ficticious, non-interacting Kohn-Sham fermions in an effective external potential. Most importantly, the ground-state density of the Kohn-Sham system equals the electron density which minimizes the total-energy functional of the interacting system.

[ii] This equivalent formulation is actually closer to the wording in the original Hohenberg-Kohn paper.[176]

Let $T_{\rm KS}[n]$ denote the kinetic energy of the non-interacting system. Then the total-energy functional can be recast into the form:

$$E_v[n] = T_{\rm KS}[n] + \int v(\boldsymbol{r}) n(\boldsymbol{r}) d\boldsymbol{r} + \frac{1}{2} \int \int \frac{n(\boldsymbol{r}) n(\boldsymbol{r}')}{|\boldsymbol{r} - \boldsymbol{r}'|} d\boldsymbol{r}' d\boldsymbol{r} + E_{\rm xc}[n]$$

In this expression the exchange-correlation energy-functional ($E_{\rm xc}[n]$) represents all parts of the total-energy which can not be calculated explicitly. In particular, it contains the exchange-correlation energy of the interacting electrons plus the difference in kinetic energy between the interacting system and the non-interacting Kohn-Sham system. Hence, the whole intricacy of the interacting system has been summed up in $E_{\rm xc}[n]$.

The following theorem by Kohn and Sham represents a self-consistency cycle for the solution of the non-interacting Kohn-Sham system whose ground-state density equals the electron density of the interacting system.[179]

Kohn-Sham equations. *The ground-state electron-density $n(\boldsymbol{r})$ of an interacting many-body system containing N electrons equals the self-consistent solution of:*

$$-\frac{1}{2}\nabla^2 \phi_i(\boldsymbol{r}) + v_{\mathit{eff}}(\boldsymbol{r}) \phi_i(\boldsymbol{r}) = \varepsilon_i \phi_i(\boldsymbol{r}) \quad \textit{with} \quad \varepsilon_1 \leq \varepsilon_2 \leq \ldots$$

The effective one-body potential is defined as

$$\begin{aligned} v_{\rm eff}(\boldsymbol{r}) &= v(\boldsymbol{r}) + v_{\rm H}(\boldsymbol{r}) + v_{\rm XC}(\boldsymbol{r}) \\ v_{\rm H}(\boldsymbol{r}) &= \int \frac{n(\boldsymbol{r'})}{|\boldsymbol{r} - \boldsymbol{r}'|} d\boldsymbol{r}' \\ v_{\rm xc}(\boldsymbol{r}) &= \frac{\delta E_{\rm xc}\,[n]}{\delta n(\boldsymbol{r})} \end{aligned}$$

and the density is calculated as

$$n(\boldsymbol{r}) = \sum_i f_i \left|\phi_i(\boldsymbol{r})\right|^2 \quad \text{with}$$

$$f_i = \begin{cases} 2 & : \varepsilon_i < \mu \\ 0 \leq f_i \leq 2 & : \varepsilon_i = \mu \\ 0 & : \varepsilon_i > \mu \end{cases} \quad \text{and} \quad \sum_i f_i = N\,.$$

The factor of two in the expression for the occupation numbers takes the degeneracy of spin-up and spin-down fermions into account. For an extension of the above theorems to spin-polarized systems, see Ref. 177.

To a large extent the success of DFT can be attributed to the formulation of the Kohn-Sham equations together with successful approximations to the exact $E_{\rm xc}[n]$.

3.2 Approximate exchange-correlation energy-functionals

Because the whole complexity of the interacting electrons has been condensed into the unknown exchange-correlation energy-functional, it is necessary to propose approximations to $E_{\mathrm{xc}}[n]$. In principle, this step is the accuracy determining factor in the calculation. Many different approximate functionals have been put forward and have been applied successfully in solid-state physics and chemistry over the last decades. The approximations available today, however, still suffer from deficiencies, e.g. to accurately describe systems in which long-range vdW interactions play a significant role.[180] Consequently, intense research effort is devoted to the development of new approximations to the exact $E_{\mathrm{xc}}[n]$. This poses an highly active and timely research area.

3.2.1 Local and semi-local functionals

The local density approximation

In the local density approximation (LDA) the approximate $E_{\mathrm{xc}}[n]$ is based on the exchange-correlation energy per particle of the homogenous electron gas $\varepsilon_{\mathrm{xc}}^{\mathrm{hom}}$:

$$E_{\mathrm{xc}}^{\mathrm{LDA}}[n] = \int n(\boldsymbol{r})\varepsilon_{\mathrm{xc}}^{\mathrm{hom}}(n(\boldsymbol{r}))d\boldsymbol{r}. \tag{3.4}$$

$\varepsilon_{\mathrm{xc}}^{\mathrm{hom}}$ has been calculated by means of QMC calculations by Ceperley and Alder[181], and the parameterization of their results by Perdew and Zunger[182] has been used in LDA test calculations in this work. The LDA is a local functional in the sense that the energy density $\varepsilon_{\mathrm{xc}}^{\mathrm{hom}}$ at position $\boldsymbol{r}$ is determined from the electron density at position $\boldsymbol{r}$.[183]

A general assessment of the accuracy of LDA calculations is not available. Yet, despite the simplicity of this approximate E_{xc} functional, the LDA has been successfully applied in numerous calculations for atoms, molecules, and solid-state materials to this day. For example, the bulk lattice constants for many solids come out only slightly smaller than the experimental value (error: a few percent).[184,185] Bulk moduli on the other hand have been calculated to be somewhat too large with a relative error of the order of 10-20%.[184,185] Note, however, that the error in the bulk moduli are related to the error in the lattice constants. If this is taken into account, the corrected bulk moduli come out only about 5% too large.[184] However, as far as cohesive energies of solids are concerned, the LDA values are found to be significantly too negative, i.e. the LDA over-binds. Errors for the theoretical cohesive energies are reported to be of the order of 15% with respect to the experimental values.[184,185] On an absolute scale, the mean error of the cohesive energies for a set of test calculations of solids as reported in Ref. 184 amounts to 0.7 eV/atom. Furthermore, atomization energies of a test set of molecules in the gas

phase come out roughly 22% too negative with an absolute mean error of approximately 1.4 eV.[183] For a different set of molecules the mean absolute error amounts to as much as 4 eV.[186] Finally, one of the most prominent shortcomings of the LDA is the prediction of a non-magnetic ground state for iron.[187]

The generalized gradient approximation

Approximate exchange-correlation energy-functionals within the generalized gradient approximation (GGA) belong to the class of semi-local functionals. The GGA poses an improvement over the LDA with respect to accuracy for a variety of physical properties of atoms, molecules, and solids. This has lead to an increased popularity and use of DFT calculations. In contrast to the LDA and apart from different parameterizations, many different flavors of GGA exchange-correlation energy-functionals have been proposed.[188] This is due to the fact that there is no unique way to define $E_{\mathrm{xc}}^{\mathrm{GGA}}$. Within a GGA, the exchange-correlation energy per particle $\varepsilon_{\mathrm{xc}}^{\mathrm{GGA}}$ depends not only on the electron density at position $\boldsymbol{r}$ but also on the density in an infinitesimal region around $\boldsymbol{r}$ (semi-locality):[183]

$$E_{\mathrm{xc}}^{\mathrm{GGA}}[n] = \int n(\boldsymbol{r})\varepsilon_{\mathrm{xc}}^{\mathrm{GGA}}(n(\boldsymbol{r}), |\nabla n(\boldsymbol{r})|)d\boldsymbol{r}. \tag{3.5}$$

For all calculations in this work the parameter-free GGA by Perdew and Wang (PW91) has been used.[189] The PW91-GGA as well as other GGA functionals[iii] have been extensively used by many groups over the last decades. GGAs are state-of-the-art functionals in calculations of extended systems to this day because they mark an excellent compromise between accuracy and computational costs.

As is the case for the LDA, a general prediction of the accuracy is not available but many calculations illustrate which properties can be accurately described and where the limits of applicability are. Within a GGA, the calculated bulk lattice constants of many solids come out approximately as accurate as within the LDA.[183–185] Notably, a GGA tends to give theoretical lattice constants which are smaller than the experimental values in contrast to the LDA which results in larger values.[183–185] A slight statistical improvement for the mean relative error of bulk moduli has been reported for a range of solids (error: ≈7%).[183,184] However, if the lattice constant error is corrected in a bulk modulus calculation, bulk moduli within LDA and GGA seem to be of comparable accuracy.[184] The wide spread use of GGAs in DFT calculations can be attributed to a significant (average) improvement of atomization energies of molecules,[183,186] cohesive energies of solids,[184,185] magnetic properties[187] and activation energy barriers for diffusion[194] and chemical reactions[111,195,196] in comparison to the LDA. For example, the mean relative GGA error of the atomization energies of selected molecules amounts to approximately 7.4% (LDA: 21.7%).[183] The mean relative error of cohesive energies of selected bulk

[iii] Excerpt of proposed GGA functionals: PBE,[190] RPBE,[191] revPBE,[192] PBEsol.[193]

materials amounts to approximately 2.4% (LDA: 14.4%) within a GGA.[184] While the GGA improves the accuracy of calculated DFT properties in many cases, it still lacks accuracy in other areas. One prominent example is the failure of both GGA and LDA to predict the lowest-energy binding site of CO on most $4d$ and $5d$ metal surfaces.[154] The lowest-energy adsorption site of CO on Cu(111), e.g. is predicted to be an fcc-hollow position of the substrate surface while experimentally adsorption at on top sites of Cu(111) has been reported.[154,197] On the other hand, the PBE-GGA predicts the correct binding site of CO on the Cu(100) surface.[198] The flawed adsorption site on Cu(111) has been reported to be due to the lack of long-range correlation in GGA and LDA.[154] Furthermore, just like the LDA, it fails to predict correct band gaps of semiconductors[199] and does not systematically account for vdW interactions.[200]

Beyond the generalized gradient approximation

The development of exchange-correlation energy-functionals, which go beyond a GGA, is an highly active research field. A road map of possible ways to go beyond a GGA has been introduced by Perdew *et al.* and is referred to as *Jacob's ladder*.[201] The LDA and GGA are on the first and second rung of *Jacob's ladder*, respectively. The third rung is a systematic extrapolation of the first two rungs and can be summarized for spin-unpolarized systems as:[201,202]

$$E_{\mathrm{xc}}^{\text{meta-GGA}}[n] = \int n(\boldsymbol{r})\, \varepsilon_{\mathrm{xc}}^{\text{meta-GGA}}(n(\boldsymbol{r}), \nabla n(\boldsymbol{r}), \tau(\boldsymbol{r}), \nabla^2 n(\boldsymbol{r}))d\boldsymbol{r} \tag{3.6}$$

$$\tau(\boldsymbol{r}) = -\frac{1}{2}\sum_{i}^{\mathrm{occ}} |\nabla \phi_i(\boldsymbol{r})|^2. \tag{3.7}$$

Here, τ is the kinetic energy density calculated from the occupied Kohn-Sham orbitals. Exchange-correlation energy-functionals of this type are referred to as meta-GGA (MGGA) functionals.[201] In principle, they can be constructed in a way that all constraints satisfied by the LDA and GGA are preserved.[184] The TPSS functional is the first example of a non-empirical, i.e. parameter-free, MGGA functional.[201]. Recently, a revised version (revTPSS) intended to be the workhorse for solid-state physics and quantum-chemistry has been proposed.[203] The average accuracy of the revTPSS functional improves upon GGAs and the TPSS functional for solids by approximately 50% (lattice constants, cohesive energies, jellium surface energies).[203] In addition, an improved accuracy over GGAs for selected test sets of molecules by a factor of roughly 3-10 has been reported (atomization energies, formation enthalpies).[203] For a large set of test molecules the TPSS and revTPSS functionals have been reported to be approximately as accurate as the B3LYP exchange-correlation energy-functional, todays workhorse functional in quantum-chemistry.[204] The improved accuracy for some of these small test systems goes hand-in-hand with an increased computational cost of about 30%.[203] An

assessment of the accuracy for extended systems, e.g. a calculation of adatom adsorption energies on substrate surfaces, has apparently not been published to this day. Most importantly, MGGA functionals can not improve upon the LDA or GGAs in every respect, e.g. MGGAs can not correctly account for vdW interactions.[180,204]

MGGA functionals belong to a wider class of exchange-correlation energy-functionals which are referred to as orbital-dependant density-functionals.[188] Other members of this class are exact-exchange methods,[205] hybrid functionals,[206] fully non-local functionals (hyper-GGA[202] on the forth rung and the generalized random-phase-approximation[202] on the fifth rung of *Jacob's ladder*), self-interaction correction,[207,208] and LDA+U approaches.[209] A comprehensive review of orbital-dependant density-functionals has been given in Ref. 188 by Kümmel and Kronik.

3.2.2 The van der Waals interaction: a current challenge

One of the most difficult challenges for DFT and the community, which develops approximate expressions for $E_{\mathrm{xc}}[n]$, is the inclusion of a consistent description of vdW interactions. Speaking in terms of Perdews's *Jacob's ladder*,[201] the physics behind vdW interactions could only be accounted for consistently on the fifth rung (generalized random-phase-approximation).[202]

VdW interactions are the dominant long-range interaction between fragments which do not possess any permanent electrostatic multipole moments, e.g. two distant rare gas atoms or benzene molecules. The vdW interaction is non-local because it arises from the correlated motion of the electrons of these fragments even if their electron densities have only negligible or no overlap.[210] Hence, local and semi-local exchange-correlation energy-functionals can not properly encompass such interactions. This poses a serious problem for DFT-GGA calculations of many weakly bonded systems. Dion *et al.* have demonstrated this by a comparison of the interaction energy of two benzene molecules calculated with a PW91-GGA and a highly accurate quantum-chemistry method.[210] Use of the PW91-GGA results in negligible binding[iv] (absolute value of the binding energy only a few meV). The quantum-chemistry calculation, on the other hand, yields a binding energy of the order of 70-80 meV.[210,211] VdW interactions may also play an important role for the adsorption of molecules on metal surfaces. McNellis *et al.* have calculated the adsorption of a benzene molecule on (111) coinage metal surfaces within DFT using a PBE-GGA.[212] The absolute values of the DFT-PBE binding energies are of the order of 50 meV which is approximately an order of magnitude smaller than the experimental binding energies.[212]

A contribution of vdW interactions to the binding energy of butanedithiol molecules on the Au substrate surface will be touched in the discussion of Sec. 4.2 and the corresponding publication in Ref. 84. Therefore, a brief review of current efforts to account for vdW interactions in DFT calculations is given below including the semi-empirical approach adopted in this work.

[iv] A small spurious attraction is an artefact of the exchange part of the PW91-GGA.[200,210]

As stated above, vdW interactions arise from the correlated motion of electrons which is fully accounted for by the exact but unknown $E_{\mathrm{xc}}[n]$. If the exchange (Hartree-Fock) part of the functional is evaluated using Kohn-Sham orbitals,[v] the exact correlation energy can be written as:[213,214]

$$E_{\mathrm{c}} = -\int_0^\infty \frac{d\omega}{2\pi} \int_0^1 d\lambda \, \mathrm{tr}[v\chi^\lambda(i\omega) - v\chi^0(i\omega)]. \tag{3.8}$$

Here, v is the Coulomb interaction and χ^λ and χ^0 are the response functions with Coulomb interaction λv and the Kohn-Sham system (λ=0), respectively. Deriving approximations for E_{c} starting from the exact correlation energy in Eq. 3.8 is regarded a promising pathway to arrive at improved approximate E_{xc} functionals including vdW interaction effects.

Harl *et al.* have evaluated the correlation energy using the random phase approximation (RPA) for the response function of the interacting system χ^λ.[214] They have reported RPA lattice constants and RPA cohesive energies of various solids to be about as accurate, in comparison to experiment, as the corresponding PBE-GGA values.[215] In case of vdW bonded rare gas solids, the RPA methods results in improved lattice constants and cohesive energies compared to a semi-local GGA.[214] A significant improvement has also been reported for the diamond and graphite bulk phase of C. Within the RPA, they are approximately degenerate whereas the diamond structure is incorrectly predicted to be more stable in a DFT-GGA calculation.[214] Moreover, the interlayer separation, d, of vdW bonded graphite layers shows the correct $1/d^4$ scaling within the RPA.[214]

Lu *et al.* have calculated a vdW bonded benzene molecular crystal within the RPA approach.[216] The calculated equilibrium volume per molecule, the cohesive energy, and the bulk modulus are in agreement with experiment to within 1-20%.

Only a few very demanding RPA calculations for adsorbate-substrate systems have been published so far. Harl *et al.* have reported that the lowest-energy adsorption site of a CO molecule on Cu(111) is the on top site of the surface in agreement with experiment whereas semi-local GGA functionals favor adsorption at the fcc-hollow site of the surface.[215] An approximate assessment of the adsorption energy and height above the surface for Xe/Ag(111) and PTCDA/Ag(111) has been presented by Rohlfing and Bredow.[217] An improvement over both LDA and GGA results has been reported.[217]

On the downside, the RPA method has been reported to introduce unphysical maxima to the total energy of two alkaline-earth atoms for large separations especially in case of Be_2.[218] Additional major drawbacks of this approach are: structural optimizations can not be performed since forces are unavailable yet,[214] the computationally very costly evaluation of the response function scales unfavorably with system size N ($\approx N^3$-N^4),[214] and extensive tests for the accuracy in case of extended systems, e.g. adsorption phenomena on metal surfaces, are not available to this day.

[v] This is referred to as *exact exchange*.

The long range interaction between fragments of a system (atoms, molecules, surfaces) can be attributed in many cases to vdW interactions. In this spirit, Rydberg *et al.* have devised an approximation to the exact $E_{\rm xc}$ functional. They have treated the exchange part within a GGA and seamlessly separate the correlation energy into an LDA part and a non-local longe-range vdW part.[210,219–221] The LDA part dominates at shorter ranges where the long-range part vanishes by construction.[220,221] What renders this approach appealing is that the long-range part is less sensitive to the details of the system's dielectric response such that very simple approximations for this part can be made.[220] The general form of the non-local, long-range correlation energy involves a six dimensional integration and depends on the electron density n and an integration kernel ϕ:[210]

$$E_{\rm c}^{\rm nl} = \frac{1}{2}\int\int d\boldsymbol{r}d\boldsymbol{r}' n(\boldsymbol{r})\phi(\boldsymbol{r},\boldsymbol{r}')n(\boldsymbol{r}'). \tag{3.9}$$

An approximate non-empiric van der Waals density-functional (vdW-DF) based on this approach has been proposed by Dion *et al.*[210] It has been applied in DFT calculations for a wide variety of systems (atoms, molecules, bulk solids, adsorption on surfaces, DNA).[vi] A comprehensive review of the various systems it has been applied to can be found in Ref. 221. The overall performance of this vdW-DF for systems where non-local correlations are important is a significant improvement over standard GGA functionals.[221] In most cases the vdW-DF is only applied in a post-processing manner, i.e. the total energy is recalculated using the charge density from a GGA or LDA calculation.[200,210] Notably, the adsorption of vdW bonded molecules on metal or semiconductor surfaces can be calculated with reasonable accuracy.[200,221,223–227] For the few available calculations, the adsorption energy error with respect to experiment is of the order of only 20% for most cases.[200,221,223–225] Bond lengths and adsorbate-substrate separations appear to come out slightly too large (under-binding) when the vdW-DF results are compared to high-level quantum-chemistry calculations or experiment.[221,223–225] Mura *et al.* have reported that a fully self-consistent implementation,[228] i.e. including a self-consistent potential, charge density and Hellmann-Feynman forces, improves structural data and leads to a better agreement between a vdW-DF calculation and experiments.[223] Cooper has noted that the under-binding could result from an overestimate of the exchange repulsion of the employed GGA in the calculation.[229] He has improved the accuracy of the vdW-DF by a modification of the GGA behind the exchange part of the vdW-DF.[229] A tough benchmark system for the vdW-DF approach could be bonding at metal surfaces for systems where both covalent and vdW interactions are important (e.g. see Refs. 84,154,212). In such cases the separation into short- and long-range correlation and the employed approximation for the dielectric function could be challenged.

A vdW-DF calculation for fixed atomic coordinates is rather expensive if large su-

[vi] An alternative vdW-DF scheme has been proposed by Vydorov and Voorhis.[222] It mainly differs from Dion's functional[210] in the model dielectric function and introduces a few empiric parameters.[222]

percells are involved and if the six dimensional integration in Eq. 3.9 is evaluated on a real space grid.[223,230] Structural optimization will be even more demanding since a typical fully self-consistent calculation involves many evaluations of the total energy plus a calculation of the Hellmann-Feynman forces. Recently, computationally efficient techniques have been proposed to make calculation for large systems feasible. Gulans *et al.* have performed calculations using a liner-scaling self-consistent implementation of the vdW-DF[231] and Guillermo and Soler have proposed an efficient way to perform vdW-DF calculations based on fast Fourier transforms.[232] Finally, Ambosch-Draxl *et al.* have used Monte-Carlo integration techniques to efficiently implement the double integral in Eq. 3.9.[233] These developments could pave the way for future vdW-DF calculations of large extended systems.[223]

The approaches discussed so far all resort to explicit approximations of the non-local exact $E_{\mathrm{xc}}[n]$ making these methods rather costly in terms of CPU time. As an alternative, computationally very efficient semi-empirical approaches have been developed. These approaches focuses solely on the long-range part of the vdW interaction, which can be approximated by means of perturbation theory.

Consider a situation in which two neutral, spherical atoms A and B are far away from each other (atomic radius small compared to atom-atom separation R_{AB}). It can be shown that the second-order perturbation-correction to the energy, $\Delta E^{(2)}$, is the leading term in the perturbation series and that it asymptotically, i.e. for large R_{AB}, behaves as:[234–236]

$$\Delta E^{(2)} = \frac{1}{R_{\mathrm{AB}}^{-6}} \frac{3}{\pi} \int_0^\infty \alpha_{\mathrm{A}}(i\omega)\alpha_{\mathrm{B}}(i\omega)d\omega = -\frac{C_6^{\mathrm{AB}}}{R_{\mathrm{AB}}^{-6}}. \tag{3.10}$$

The frequency-dependant atomic polarizabilities of atom A and B are α_{A} and α_{B}, respectively. Zaremba and Kohn have derived a similar expression for an atom in front of a solid surface.[235] For very large distances of the order of 100 Å retardation effects come into play and the asymptotic fall-off is $\Delta E^{(2)} \propto 1/R_{\mathrm{AB}}^{-7}$ (Casimir forces).[228,236,237] The expression for the C_6 coefficient in Eq. 3.10 can be approximated as (London dispersion formula):[238,239]

$$C_6^{\mathrm{AB}} \approx \frac{3}{2}\alpha_{\mathrm{A}}\alpha_{\mathrm{B}}\frac{I_{\mathrm{A}}I_{\mathrm{B}}}{I_{\mathrm{A}}+I_{\mathrm{B}}}. \tag{3.11}$$

Here, I_{A} and I_{B} are the ionization energies of atom A and B, respectively.

Based on the above perturbative treatment of the leading long-range part of the vdW interaction between two atoms, a widely employed semi-empirical vdW-correction to DFT (DFT-D)[vii] has been proposed. The method is aimed at correcting local or semi-local DFT calculations of atoms and molecules by the leading long-range vdW contribution in an easy to implement and computationally very efficient way. Within

[vii] VdW interactions are also referred to as dispersion (D) interactions.

the DFT-D approach the total energy is defined as:[238–240]

$$E_{\text{DFT-D}} = E_{\text{DFT-xc}} + E_{\text{vdW}} = E_{\text{DFT-xc}} - \frac{s_6}{2} \sum_{\substack{i,j \\ i \neq j}} f(R_{i,j}, r_i^{\text{vdW}}, r_j^{\text{vdW}}) \frac{C_6^{i,j}}{R_{i,j}^{-6}}. \quad (3.12)$$

$E_{\text{DFT-xc}}$ is the total energy obtained from a self-consistent DFT calculation using an approximate $E_{\text{xc}}[n]$. E_{vdW} is a sum over all atom pairs (i, j) each of which contributes $f(R_{i,j}, r_i^{\text{vdW}}, r_j^{\text{vdW}}) C_6^{i,j} / R_{i,j}^{-6}$ to the vdW interaction energy. The interaction between any two atoms is artificially truncated at short distances derived from the vdW-radii r_i^{vdW} and r_j^{vdW} of the interacting atoms via an empirical cutoff function f.[238–241] f tends to unity for large separation $R_{i,j}$. Depending on the approximate E_{xc} functional used in the DFT part of the calculation, different values for the semi-empirical scaling factor s_6 have been proposed in the literature.[238,240,241] This parameter is usually obtained by minimizing the statistical deviation of calculated physical properties with respect to reference data.[238,240,241] By taking the derivative of Eq. 3.12 with respect to the atomic coordinates, a semi-empirical vdW correction to the Hellmann-Feynman forces acting on the atoms is readily available.

The main issue of the DFT-D method is the ambiguous choice of the C_6 coefficients, the cutoff function f, the atomic vdW radii and the s_6 constant. This work follows Ortmann *et al.*[239] for the choice of the C_6 coefficients, which have been calculated from the London formula (Eq. 3.11) using experimental atomic polarizabilities and ionization energies.[84] The functional form of the cutoff function, f, is a Fermi function chosen according to the work by Grimme[240,242] using experimental atomic vdW radii.[84] The semi-empirical constant s_6 is taken to be 0.75. Grimme has reported this to be optimum value for the PBE-GGA which behaves very similar to the PW91-GGA used here. Alternative choices for the C_6 coefficients, the cutoff function, the vdW radii, and E_{xc} dependant scaling factors can be found in Refs. 238–241. Tkatchenko *et al.*[238] and Grimme *et al.*[241] have recently proposed atomic C_6 coefficients which depend on the chemical environment of each atom, i.e. different C_6 values can be assigned to the same element in different bonding situations within the same molecule. Grimme *et al.* have additionally introduced an extension of the DFT-D scheme which encompasses three-body interactions and a higher order vdW interaction term which falls of as $C_8^{i,j} / R_{i,j}^{-8}$.[241] There is a debate about whether or not C_6 coefficients of metal atoms should be utilized in a calculation of a metal surface.[212,243] In all likelihood, the dielectric response of an electron gas in a metal will differ from that of a single metal atom. Tonigold and Groß have introduced a method of estimating C_6 coefficients for metal atoms in a cluster from a comparison of DFT-D and accurate quantum-chemical cluster-calculations.[243]

The DFT-D scheme, with all its variants discussed above, has been extensively applied to molecular systems (heats of formation, chemical reactions and barriers), complexes, clusters, and graphene.[238–242,244] Overall, the DFT-D scheme results in a general im-

provement over DFT calculations using semi-local approximate E_{xc} functionals. For many molecular test systems the DFT-D approaches can yield values within approximately 30% of high-level benchmark-calculations or experimental values.[238–241] In other cases, especially for chemical reaction barriers, the approach yields rather poor values on an absolute scale.[240] Note that often the performance may depend heavily on the GGA used in the DFT part of the calculation.[240,241,244] To further improve performance, Goerik and Grimme have attempted to re-parameterize various GGA and MGGA functionals by minimizing the average statistical differences between a DFT-D calculation and a very large molecular benchmark set.[244] Despite the fact that a slight improvement has been achieved based on a statistical mean for a very large test set of molecules, they have found that the performance significantly worsened for certain molecular subsets.[244] The emergent general picture for weakly-bonded molecular-systems is that the DFT-D approach can improve upon semi-local DFT-GGA calculations based on a statistical measure of the error. However, a given DFT-D scheme of reasonable accuracy for certain benchmarks is generally not transferable to other systems.

In the context of this work the relevant question is whether the DFT-D method can be transfered to extended systems and improve DFT adsorption energies and configurations where usual DFT-GGA calculations yield rather poor results. A vdW correction is certainly necessary for DFT-GGA calculations of large organic molecules interacting solely via delocalized electrons with a substrate surface.[212,217,227,243,245–248] Whether a vdW correction is necessary for a description of BDTR/Au diffusion will be discussed in following Sections.

Small π-conjugated aromatic molecules like benzene, pyridine, pyrazine, and thiophene adsorbed on coinage metal surfaces have emerged as widely studied model systems because vdW interactions should be their dominant molecule-surface bonding-mechanism.[212,227,241,243] If a semi-empirical vdW correction is applied to, e.g. benzene adsorption, the overall common is that (i) the molecule-surface bond strengthens, (ii) the average molecule-surface separation shortens, and (iii) the adsorption energies improve upon the GGA results but a significant dependance on the semi-empirical parameters is observed.[84,212,241,243] The impact of the semi-empirical vdW correction can be quite dramatic on an absolute scale. This has been consistently reported in Refs. 212,227,241,243. E.g., McNellis *et al.* have reported DFT-D binding energies for benzene and azobenzene on the Cu(111), Ag(111), and Au(111) surfaces.[212] Within the PBE-GGA, the benzene binding energies on these surfaces are of the order of -0.05 eV compared to an experimental value of approximately -0.6 eV.[212] The reported DFT-D binding energy values range from -0.5 eV to -1.0 eV depending on the metal surface and construction scheme of the vdW correction (C_6 coefficients, cutoff function, vdW radii).[212] The molecule-surface separation decreases compared to the PBE-GGA values by 0.3-1 Å.[212] McNellis *et al.* cautiously conclude that the semi-empirical scheme merely provides a correction which could be in the right ballbark with a slight tendency to result in too strong binding.[212] They have proposed that a better assessment of the accuracy of the DFT-D approach and the various construction schemes could be reached by a careful comparison with

experiment.[212]

Mercurio *et al.* have recently studied the adsorption of azobenzene molecules on the Ag(111) surface using normal-incidence x-ray standing waves, TPD, and DFT with semi-empirical vdW corrections.[248] The experimental value for the desorption energy has been reported to be -1.0±0.1 eV. As a key structural parameter the authors have measured an N-Ag distance of 3.07±0.02 Å. A DFT-GGA calculation (no vdW correction) yields approximately -0.2 eV for the binding energy and 3.64 Å for the N-Ag distance. Mercurio *et al.* have adopted two different semi-empirical vdW corrections, one following the ideas of Tkatchenko and Scheffler[238] and the other following the ideas of Grimme.[240] Using the Grimme scheme[240] they have calculated a binding energy of -2.16 eV and an N-Ag distance of 2.75 Å. The Tkatchenko scheme[238] yields a binding energy of -1.71 eV and an N-Ag distance of 2.98 Å. In addition, Mercurio *et al.* have proposed that electronic screening effects due to the metal surface can be roughly accounted for if the vdW interactions are restricted to act between the molecule and the atoms of the first substrate layer. In case of the Tkatchenko scheme[238] such a procedure is reported to result in a binding energy of approximately -1.4 eV while the N-Ag distance remains almost unaffected. Thus, they have concluded that the available DFT-D schemes are not suitable to capture the molecular adsorption energetics at metal surfaces with sufficient accuracy because the tendency to over-bind is significant. On the other hand, structural information from a DFT-D calculation could be useful as a starting point for higher level calculations.[248]

Finally, Toyoda *et al.* have recently published a DFT study of pentacene adsorption on the Cu(111), Ag(111), and Au(111) surfaces.[224] They have compared adsorption energies and molecule-surface separations obtained from DFT PBE-GGA, semi-empirical DFT-D,[240] and non-self-consistent vdW-DF calculations[210] to experiments. Note that no zero-point energy-correction has been applied to the calculated data. In case of the Cu(111) surface both the DFT-D and vdW-DF approaches yield similar binding energies in close agreement with experimental data (residual differences less than 0.13 eV). On Ag(111) and Au(111) the DFT-D approach yields significantly lower binding energies than the vdW-DF calculation and the experiment. Compared to experiment the DFT-D calculations yield an over-binding of 0.78 eV and 1.41 eV for Ag(111) and Au(111), respectively. The vdW-DF calculation, on the other hand, yields binding energies closer to experimental data. The vdW-DF binding energies are 0.12 eV and 0.56 eV more negative than experimental adsorption energies for Ag(111) and Au(111), respectively. Calculated molecule-surface separations come out 0.5-1.3 Å smaller within DFT-D than within vdW-DF on all three considered surfaces. For the Cu(111) surface the DFT-D value is in agreement with experiment. No experimental data has been cited for the Au and Ag surfaces. Note that the error of the reported non-self-consistent vdW-DF structural data appears to be significant in light of the reported shallow adsorption minima.

The DFT-D approaches have been successfully applied to various systems consisting of weakly interacting atoms and molecules. Despite this success the transferability of the available approaches to extended systems remains arguable. There appears to be

consensus in the literature that DFT-D consistently results in considerable over-binding for adsorbates on metal surfaces. This is consistent with the data presented in this work for the adsorption of butanedithiol on Au(111), see Sec. 4.2 and Ref. 84. In addition, the results tend to depend sensitively on the available construction schemes of the semi-empirical parameters within DFT-D. This comes as little surprise because most of these schemes have been designed for atomic or molecular systems and a reliable extension, e.g. to metal surfaces, has yet to be devised. Despite the tendency to over-bind, the DFT-D approach has been reported to give reasonable structural information but the results again depend on the particular DFT-D. Moreover, a general assessment including comparison to experiment for different systems has not been carried through. Even if proper C_6 coefficients for metal surface atoms could be found, a proper cutoff function at short atom-atom separations would still be needed. In cases where atom-atom separations between the adsorbate and the surface are of the order of the cutoff length (sum of the vdW radii), the chosen cutoff function will dominate the vdW correction of the total energy and the forces acting on the atoms. As an example, consider the work by Sony *et al.* who have reported DFT-GGA and vdW-DF total-energy data for thiophene/Cu(110) as a function of the adsorbate-surface separation.[200] As a matter of fact, the adsorbate-surface spacing of the vdW-DF method is significantly larger than the value obtained in a GGA calculation (0.4 Å increase). Sony *et al.* have estimated an experimental adsorbate-surface separation which is also slightly larger than the GGA value. Hence, a semi-empirical vdW correction, which Sony *et al.* have not applied, would have to be repulsive by means of the cutoff function to improve on the GGA result. Such a dependance on the cutoff function further adds to the extend of DFT-D empiricism.

In consideration of the above, the DFT-D method seems to be appropriate to obtain an order of magnitude estimate of the vdW interaction effect. To this purpose, different construction schemes should be taken into account.

3.3 The Vienna Ab Initio Simulation Package - VASP

All DFT calculations in this work have been carried through with the Vienna Ab Initio Simulation Package (VASP) developed at the Institut für Materialphysik der Universität Wien.[249–252] VASP is among the most efficient, widely used and well tested DFT programs available today. It has been applied in many key areas of modern solid-state physics and chemistry.[253] The program performs ab-initio quantum-mechanical molecular dynamics simulations based on DFT for systems containing up to a few thousand electrons.[253] For a full list of all capabilities see the program manual.[254] In particular, VASP can be applied to minimize the total energy functional by self-consistently solving the Kohn-Sham equations and calculate the total energy of the electronic ground state.

Detailed reviews of the all algorithms implemented in VASP have been published in Ref. 255. Here, only the basic idea behind the employed self-consistency cycle involved

in a ground state calculation for a given external potential (atomic coordinates) shall be summarized.[255] Each iteration starts with a trial charge density n_{in} and trial Kohn-Sham wave functions. These input quantities are either obtained from a previous iteration or they represent an initial guess, if a calculation is started from scratch.[viii] After the effective potential[ix] has been calculated from n_{in}, the Kohn-Sham wave functions and eigenvalues are iteratively improved. The algorithm of choice to update the Kohn-Sham wave functions, especially for large systems, is the residual-minimization method with direct-inversion-in-iterative-subspace (RMM-DIIS). From the improved Kohn-Sham wave functions and eigenvalues the single-particle occupancies, the total energy, and a charge density n_{out} are calculated. A self-consistent solution of the Kohn-Sham equations demands that the norm of the charge-density residual-vector $R[n_{\text{in}}] = n_{\text{out}}[n_{\text{in}}] - n_{\text{in}}$ is zero. A quasi-Newton method proposed by Pulay (Pulay mixing) is employed to (approximately) obtain the minimum of $||R[n_{\text{in}}]||$. The Pulay mixing scheme provides the new input charge density for the next iteration by adding a certain part of the residual vector $R[n_{\text{in}}]$ to the old input charge density n_{in}. The subsequent iteration starts with the improved (trial) wave functions and charge density until the change in total energy and band structure energy[x] between successive iterations is below a threshold which is typically of the order of 10^{-5}-10^{-7} eV. The computational cost of the self-consistency cycle scales with the size N of the system approximately like N^3.

Once a self-consistent solution is reached for a given set of atomic coordinates, the Hellmann-Feynman forces on the atoms can be calculated. This allows for an iterative optimization of the atomic geometry until the residual forces have fallen below a threshold which is typically of the order of 0.005-0.001 eV/Å. Different algorithms to optimize the atomic positions are implemented in the VASP code. In this work a damped second-order equation of motion has been used.

The electron-ion interaction, which enters the Kohn-Sham equations, has been treated within the projector augmented-wave (PAW) method introduced by Blöchl.[256] Calculations using the PAW method are compatible in accuracy with a true all-electron treatment. In fact, the PAW method is an all-electron approach as it allows to reconstruct the all-electron (valence) wave functions from corresponding pseudo wave functions by a linear transform.[253,256,257] To improve calculational efficiency, a set of strongly bound and chemically inert core-electrons has not been treated explicitly (frozen-core approximation).[xi] This is a legitimate approximation for most calculations.[258] Besides its high accuracy the PAW method also yields smoother pseudo wave functions compared to norm-conserving pseudopotentials. This improves the computational efficiency because

[viii] The charge density is calculated from overlapping atomic charge densities, and the wave functions are initialized with random numbers. The charge density should not be updated for a few iterations to pre-converge the Kohn-Sham wave functions.

[ix] Unless noted otherwise, the exchange-correlation energy-functional is approximated with a PW91-GGA in this work, see Sec. 3.2.1.

[x] Sum of the Kohn-Sham eigenvalues multiplied by the partial occupancies.

[xi] Marsman and Kresse have proposed a relaxed-core PAW method to incorporate core-relaxation effects.[258]

the required number of plane waves used to expand the Kohn-Sham wave functions is reduced. For all chemical elements the PAW potentials from the VASP database maintained by Kresse *et al.* has been used unless noted otherwise.[259]

Atomic structures have been set up in a periodic super-cell approach, which allows for an efficient calculation of physical bulk and surface properties. The three basis vectors defining the unit cell (super-cell) of the super-lattice plus the positions of all atoms within a super-cell have to be provided for every calculation as input parameters. Such a periodic set-up has several important advantages:[253] the wave functions can be expanded in a plane-wave basis-set, the charge density can be represented as an integral over the first Brillouin zone of the super-lattice, the Hellmann-Feynman forces acting on the atoms can be calculated directly, and an efficient fast-Fourier transform can be used to switch between real-space (potential-energy operator diagonal) and momentum-space (kinetic-energy operator diagonal). VASP uses plane waves as a basis to represent the wave functions. Consequently, the required size of the plane-wave basis-set can be systematically determined, i.e. the highest-energy plane-wave in the expansion controlled by the cutoff energy parameter can be increased until convergence of a desired physical quantity is reached. Finally, the Brillouin zone integration to calculate the charge density has to be approximated by a sum over special k-points in the first Brillouin zone. Monkhorst and Pack have provided a scheme by which an efficient sampling can be achieved.[260] Again the total number of k-points can be systematically increased until convergence is reached. The k-point convergence in case of metallic systems can be further improved if a smoothening of the drop in occupation numbers near the Fermi energy at T=0 K is applied.[255] Different schemes to replace the step function at the Fermi energy are implemented in VASP. The most common schemes to define partial occupancies are a finite-temperature Fermi-Dirac function or an expansion of the step function in a complete orthonormal set of functions (Methfessel-Paxton method).[261] This ruse introduces an artificial entropy contribution to the total (free) energy. The total energy at T=0 K is calculated from an accurate extrapolation to zero-smoothing.[255]

A detailed description of the main computational parameters and a summary of systematic convergence tests (dimension of the super-cell, cutoff energy, k-point sampling, force convergence threshold) are given in the Sections or publications where the calculations are discussed. If not noted otherwise, partial occupancies near the Fermi-energy have been calculated with a first-order Methfessel-Paxton method using a broadening parameter of 0.4 eV.

The reliability of the used PAW potentials from the VASP database[259] has been tested. Calculations of Au bulk properties (lattice parameter 4.174 Å, bulk modulus 1.33 Mbar),[xii] surface energies of the the unreconstructed Au(111) (45 meV/Å^2) and Au(100) (54 meV/Å^2) surfaces,[xiii] as well as molecular properties of $HSCH_3$, SCH_3, CH_3S-SCH_3, and CH_4 are in agreement with published all-electron and DFT-PAW studies.

[xii] Ref. 262: lattice parameter 4.175 Å, bulk modulus 1.32 Mbar.
[xiii] Ref. 262: Au(111) 45 meV/Å^2, Au(100) 54 meV/Å^2.

4 Adsorption and diffusion of sulfur bonded molecules on Au surfaces: survey of publications and related work

4.1 Adsorption and diffusion of SCH_3 radicals and $Au(SCH_3)_2$ complexes on the unreconstructed Au(111) surface in the submonolayer coverage regime (published)

4.1.1 Synopsis

Alkanethiols and alkanedithiols have adopted the role of model systems for the bonding of organic molecules on metal surfaces via sulfur anchors and the formation of self-assembled monolayers (SAMs). So far, however, little is known about the detailed diffusion mechanisms of such molecules on the surface especially if two S-Au bonds to the substrate surface are involved. Therefore, the overall goal of the presented work is to investigate the adsorption and diffusion characteristics of an archetypical model system. The model and benchmark system chosen here comprises 1,4-butanedithiol molecules, HS-$(CH_2)_4$-SH (BDTs), and 1,4-butanedithiol radicals, $\cdot$S-$(CH_2)_4$-S$\cdot$ (BDTRs), adsorbed on the unreconstructed Au(111) and Au(100) surfaces. Before engaging density-functional theory (DFT) calculations for BDT on a Au substrate surface, it is instructive to survey important bonding and diffusion mechanisms on a simpler system, which retains important aspects of BDT/Au. As will be shown in a following Section, BDT dissociatively adsorbs as a BDTR, on the unreconstructed Au(111) and Au(100) surface by cleavage of both S-H bonds and formation of two strong S-Au bonds. Hence, methanethiol radicals, SCH_3, adsorbed on an unreconstructed Au(111) and Au(100) surface are a suitable model system because SCH_3 binds via its S atom to the Au surface and it closely resembles one of the two S-C "legs" of BDTR. Moreover, the diffusion of SCH_3 on a Au surface yields important information about low energy pathways for S bonded molecules on the surface. A further benefit of the CH_3S/Au system is that reference data for the chemisorption geometry and chemisorption energy

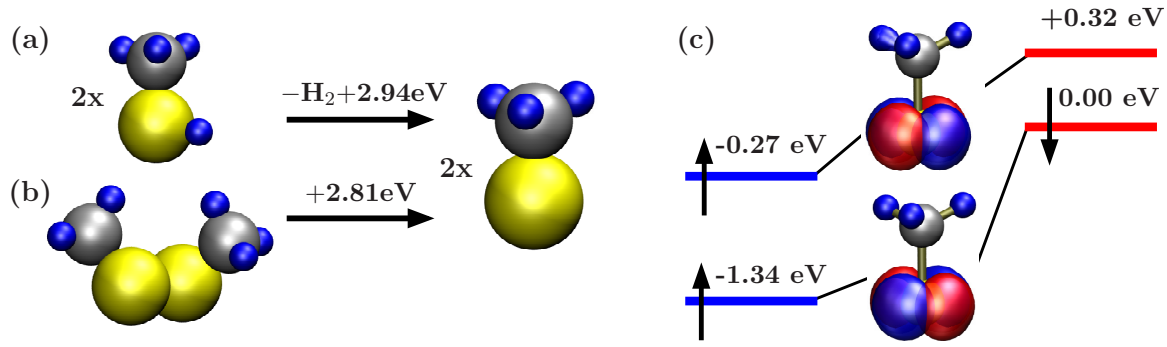

Figure 4.1: Dissociation reactions (including zero-point energy corrections) of methanethiol, $HSCH_3$, (a) and dimethyldisulfide, $(SCH_3)_2$, (b) to form SCH_3 in the gas phase. (c) Electronic structure of a spin-polarized SCH_3 radical. The energy eigenvalues of molecular orbitals within at least ±3.5 eV of the HOMO are presented. The energy-zero is set to the eigenvalue of the HOMO. Contours of constant spin density of the molecular Kohn-Sham orbitals are depicted for spin-majority (blue) and spin-minority states (red).

are available in the literature, which allows for a valuable comparison of results. Finally, the adsorption and diffusion of $Au(SCH_3)_2$ complexes on the unreconstructed Au(111) surface has been studied. These complexes bond to the Au(111) surface via two S atoms which enclose a central Au adatom. One may therefore use these complexes to get a first impression of the diffusion properties of such simple bipedal adsorbates. But it is not only for academic purposes that the properties of $Au(SCH_3)_2$ on Au(111) are of interest, they also allow to get in contact with experiments in which these complexes have been observed. Maksymovych *et al.* have reported that these complexes represent a stable structure of SCH_3 on Au(111) at dilute and intermediate coverages in a joined scanning tunneling microscope (STM) and DFT study.[56] In addition, the existence of similar complexes has been reported following the ground breaking work by Maksymovych *et al.* for ethanethiol, propanethiol, and benzenthiol.[41,57,263] The DFT results within this work concerning the adsorption and diffusion of SCH_3 and $Au(SCH_3)_2$ on the unreconstructed Au(111) surface have been published in Ref. 39. The main results are summarized in the following paragraphs.

Methanethiol radicals may be deposited on the Au(111) surface either via dissociative adsorption of dimethyldisulfide molecules or STM induced dissociation of physisorbed methanethiol.[56] The binding energies associated with a cleavage of the S-H bond of the methanethiol molecule or S-S bond cleavage of the dimethyldisulfide molecule are summarized in Fig. 4.1. Considering the electronic structure of a free SCH_3 radical already yields important information about the bonding mechanism behind the S-Au bond of an adsorbed radical. The (spin-minority) highest occupied molecular orbital (HOMO) and lowest unoccupied molecular orbital (LUMO) states of an SCH_3 radical

are depicted in Fig. 4.1. The HOMO and LUMO orbitals are located at the S atom and have a dominant S 3*p* character. The orientation of the orbitals can be best described as being perpendicular to the S-C bond direction. Upon adsorption on the Au(111) surface, the S-Au bond will mainly arise from a hybridization of these orbitals and orbitals of the Au substrate surface. Therefore, the SCH_3 radical is likely to adsorb in a tilted geometry on a Au surface such that the molecular orbitals located at the S atom may point approximately in the direction of one or more atoms of the upper most layer of surface Au atoms. Indeed, DFT calculations of the chemisorption of SCH_3 on the unreconstructed Au(111) surface yield a ground state configuration in which the S atom is located in between an fcc hollow and a bridge site of the surface and the S-C bond is tilted by approximately 53° to the surface normal, see Fig. 4.2.[39] The SCH_3 radical is strongly bound to the Au surface with an S-Au bond strength of approximately -1.9 eV with respect to the unreconstructed Au(111) surface and a ground state SCH_3 radical in vacuum.[39] The SCH_3 coverage corresponds to one radical per 9 Au surface atoms in this case. The tilted SCH_3 configurations compete with upright configurations on the Au(111) surface in which the S-C bond is oriented along the surface normal and the S atom is located above a hollow site of the substrate surface.[39] Note the pronounced coverage dependance of the DFT chemisorption energy as discussed in Ref. 39.

Keeping in mind that the SCH_3 radical may be used as a model system for one "S-C leg" of BDTR, what is the lesson to be learned from such an analysis? First of all, low total-energy configurations of CH_3S/Au(111) comprise both tilted and upright S-C bond configurations. Moreover, the position of the S atom in these cases may either be in the proximity of hollow or bridge sites of the substrate surface. This may be further illustrated by a survey of the diffusion properties of CH_3S/Au(111), which yields a sliding motion of SCH_3 across the surface with a diffusion energy barrier of 0.26 eV.[39] The (unstable) configurations along the respective minimum energy path (MEP) yield information about low total-energy SCH_3 positions on the surface.[39] This important information will be incorporated into a strategy to search for low total energy adsorption configurations and diffusion paths of BDTR/Au(111).

To complement the DFT survey of CH_3S/Au(111), calculations of adsorption configurations of $Au(SCH_3)_2$ complexes on the unreconstructed Au(111) surface have been carried through. The results of these calculations affirm the observations by Maksymovych *et al.* that adsorption in a $Au(SCH_3)_2$ geometry is energetically preferred over adsorption as a single SCH_3 radical. In its ground state on Au(111), both SCH_3 radicals of the complex form a bond with the central Au adatom and two surface Au atoms, see Fig. 4.2. The S atoms are located approximately on top of surface Au atoms. The DFT binding energy per SCH_3 radical on Au(111) in the $Au(SCH_3)_2$ ground state configuration amounts to approximately -2.1 eV.[39] Comparing this value to the -1.9 eV in case of a single SCH_3 radical on Au(111) illustrates the energetical preference for $Au(SCH_3)_2$. What makes $Au(SCH_3)_2$ complexes bonded to Au(111) such an interesting system to study, apart from the fact that they have been observed experimentally, is that $Au(SCH_3)_2$ complexes exhibit two bonds to the Au(111) surface. This feature

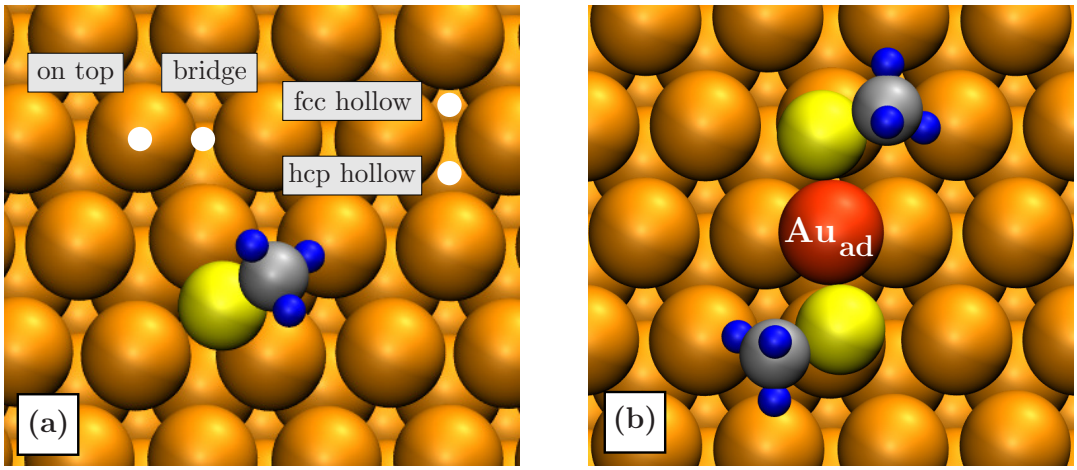

Figure 4.2: The fcc-bridge configuration of an SCH_3 radical (a) and the trans-bridge ground state configuration of an $Au(SCH_3)_2$ complex (b) on the Au(111)-(1×1) surface. High-symmetry sites of the Au(111)-(1×1) surface are denoted by white circles in (a). S atoms: yellow, C atoms: gray, H atoms: blue, Au-adatom: red. The Figures have been taken from Ref. 39.

hints towards interesting diffusion characteristics. Indeed, the motion of the $Au(SCH_3)_2$ complexes consists of translations and rotations on the Au(111) surface with different diffusion energy barriers of 0.37 eV and 0.44 eV, respectively.[39] The diffusion may be characterized as a bipedal locomotion on the surface, i.e. only one of the involved S-Au bonds is broken at a time.[39] Due to the different barriers for translations and rotations, short time correlations between subsequent diffusion hops might develop and subsequent hops can occur back and forth along the same direction. Theses points are again very valuable to aid the characterization of BDTR/Au diffusion, which indicates the true model character of this work.

Jiang and Dai have reported diffusion properties of $Au(SCH_3)_2$ complexes on the unreconstructed Au(111) surface in two separate DFT studies.[156,157] Their work has been submitted and published approximately at the same time as this work (Ref. 156 submitted 26.11.2008 and published 09.02.2009, Ref. 157 submitted 12.02.2009 and published 27.07.2009, this work, Ref. 39, submitted 23.01.2009 and published 29.06.2009). They have calculated a diffusion energy barrier for $Au(SCH_3)_2$ translations of 0.51 eV and an energy barrier for a cis-to-trans $Au(SCH_3)_2$ transition (see Fig. 1.4 in Sec. 1.2) of 0.5 eV. Jiang and Dai have only reported a translational diffusion path, i.e. they have not published $Au(SCH_3)_2$ rotational modes. The diffusion energy barrier calculated in this work for $Au(SCH_3)_2$ translations (0.44 eV) is lower than the the value reported by the authors of Ref. 156. This arises in part from the fact that Jiang and Dai do not consider $Au(SCH_3)_2$ rotations on the surface and a sequence of partial rotations leads to a more efficient diffusion channel. Moreover, it is speculated that the geometries on

the MEP presented in Ref. 156 are not well converged for the following reasons: (i) the convergence criterion for geometry optimization is ten times less stringent compared to this work, (ii) the MEP presented by Jiang and Dai exhibits characteristic kinks which might be a sign that the sampling density along the MEP is not sufficient, and (iii) the diffusion mode proposed in Ref. 156 has been considered in this work (prior to publication) and it has been found that it converges to the MEPs published in this work.[39] The energy barrier for a cis-to-trans $Au(SCH_3)_2$ transition has been calculated to be approximately 0.56 eV in this work.[39] The energy barrier comes out slightly larger compared to Ref. 157. In this case, however, the transition state geometry published by Jiang and Dai looks very similar to the respective one presented here.[39] It is speculated that the residual small difference of 0.06 eV is related to the use of a different surface unit cell and different convergence parameters in the calculations.

4.1.2 Publication Physical Review B 79, 235441 (2009), Copyright (2009) by the American Physical Society

Adsorption and diffusion of SCH_3 radicals and $Au(SCH_3)_2$ complexes on the unreconstructed Au(111) surface in the submonolayer coverage regime

Andreas Franke* and Eckhard Pehlke
Institut für Theoretische Physik und Astrophysik, Christian-Albrechts-Universität zu Kiel, 24098 Kiel, Germany
(Received 23 January 2009; revised manuscript received 4 May 2009; published 29 June 2009)

We study the adsorption and diffusion of $Au(SCH_3)_2$ complexes as well as bare SCH_3 radicals on the unreconstructed Au(111) surface using density-functional theory. Maksymovych *et al.* observed these complexes at the Au(111) surface by scanning tunneling microscopy. In accordance with previous density-functional theory studies by other groups, we find a slight energetical preference for the bonding of SCH_3 on the surface in $Au(SCH_3)_2$ complexes. The net energy gain accounting for the creation of one Au adatom amounts to approximately 0.2 eV per SCH_3 radical. The diffusive motion of these complexes includes rotational and translational diffusion steps with energy barriers of 0.44 eV and 0.37 eV, respectively. We speculate whether this may result in a correlation of the direction of consecutive diffusion events. In case of bare SCH_3 radicals we calculate a diffusion barrier of 0.26 eV.

DOI: 10.1103/PhysRevB.79.235441 PACS number(s): 68.43.Jk, 68.43.Bc, 68.43.Fg

I. INTRODUCTION

The formation and structure of self-assembled monolayers (SAMs) of alkanethiol molecules adsorbed at noble-metal surfaces has attracted great interest during the past two decades. This is due to the wide variety of promising applications that have been proposed, ranging from molecular electronics and nanolithographic techniques to biofunctionalized surfaces and biosensoring devices.[1–10] Moreover, alkanethiols are regarded as a model system for organic molecules that bind to a substrate surface via sulfur anchors.[1–4,6–10] The most often considered substrate in this respect is the Au(111) surface,[9] which is also studied in this work. Despite intense efforts both from experiment and theory, the details of the adsorption mechanism and the equilibrium structures at different coverages and alkanethiol chain lengths are still controversial. For a recent review see, e.g., Ref. 11 and references therein.

In case of the shortest alkanethiol $HSCH_3$, adsorption at the Au(111) surface may or may not involve H-S bond cleavage depending on the occurrence of surface defects (e.g., created by ion bombardment prior to adsorption).[9,12,13] The low desorption temperature ($\approx$140 K–220 K) of $HSCH_3$ on defect free Au(111) (Ref. 12) is indicative of a rather weak molecule-surface bond.[14] As a result, only small amounts of strongly bound methanethiol radicals SCH_3 are formed on the surface at room temperature (RT).[12,15] However, dosing of dimethyl disulfide CH_3S-SCH_3 at RT is found to result in cleavage of the S-S bond leaving methanethiol radicals SCH_3 adsorbed at the Au(111) surface, which form strong Au-S bonds.[12,16] At saturation coverage (one radical per three Au atoms), a $(\sqrt{3}\times\sqrt{3})$R30° equilibrium phase has been identified.[17–20] There is an experimental report that this phase can be transformed into a $(3\times2\sqrt{3})$ structure by thermal annealing[18] [also referred to as a $c(4\times2)$ structure]. Both of these structures are also found for longer chains (see, e.g., Refs. 4, 7, and 21). There have been contradictory experimental reports about what the exact binding configuration within the $(\sqrt{3}\times\sqrt{3})$R30° structure is.[19,20,22–24] Both on top as well as hollow-bridge adsorption have been discussed. This was in contrast to almost all *ab initio* density-functional theory (DFT) studies which favored adsorption at hollow or hollow-bridge sites on defect free unreconstructed Au(111).[22,25–35] Molina *et al.* and Morikawa *et al.* considered adsorbate induced vacancy formation or surface reconstruction as a way out.[36,37] A combined experimental photoelectron diffraction, grazing incidence x-ray diffraction and DFT study conducted by Mazzarello *et al.* suggests that the $(\sqrt{3}\times\sqrt{3})$R30° periodicity evolves from a dynamic equilibrium between hollow-bridge site adsorption and a structure in which two SCH_3 radicals bind on top to surface atoms and additionally to one Au adatom which is lifted from the surface.[33,38] Recently, an adsorption model was proposed for the $(3\times2\sqrt{3})$ structure of longer alkanethiol chains which also involves gold adatoms.[34] Even at submonolayer coverages Maksymovych *et al.* suggested by means of scanning tunneling microscopy (STM) experiments and DFT calculations that methanethiol radicals are bound to the surface in a $Au(SCH_3)_2$ complex in which both sulfur atoms form a bond with a central Au atom and two surface atoms (on top).[39] DFT calculations conducted by other groups corroborate their result.[35,40] Furthermore, Kautz *et al.* confirmed the incorporation of Au adatoms into monolayers of octanethiol resulting in an adatom-thiol ratio of 1:2,[41] which is consistent with the above mentioned structure model proposed in Ref. 39.

The focus of our work is to study and compare single SCH_3 radicals and $Au(SCH_3)_2$ complexes by means of DFT calculations as an archetypical model system for molecular diffusion in which one or two sulfur bonds to the underlying substrate exist. Since $Au(SCH_3)_2$ complexes are stable under UHV conditions on the unreconstructed Au(111) surface,[39,40] they can be studied without having to consider the $(22\times\sqrt{3})$ herringbone reconstruction of Au(111). Furthermore, adsorption properties and diffusion of bare SCH_3 radicals would be relevant in case of electrochemical environments[42] where a lifting of the herringbone reconstruction induced by an electric potential can be achieved.[43] So far, however, little is known about the detailed diffusion mechanisms for such sulfur bonded assemblies from *ab initio* calculations.[32,44–46]

This knowledge is essential in order to obtain a detailed understanding of self-assembly and growth processes of alkanethiols and other organic molecules.[47–50] Moreover, diffusion of molecules with one or more bonds to the surface is of fundamental interest since it can differ substantially from diffusion of single atoms.[45,51–60] Apart from this, diffusion characteristics also play an important role for possible future applications.[5,59] The experimental accessibility of diffusion barriers, paths or constants has been demonstrated via STM and video STM studies.[53,54,56,59,61,62]

II. CALCULATIONAL METHOD

The total energy of the electronic ground state has been calculated using the Vienna *ab initio* simulation program (VASP) (Refs. 63–66) developed at the Institut für Materialphysik of the Universität Wien which is based on density-functional theory. The generalized gradient approximation (GGA) by Perdew and Wang (PW91) (Ref. 67) is applied to the exchange-correlation functional and the electron-ion interaction is treated within the framework of Blöchl's projector augmented wave method (PAW).[68] The potentials for VASP from the database are used.[69] The adsorption configurations are modeled in a slab geometry comprising six layers of gold and a $(\sqrt{3}\times\sqrt{3})$, (3×3), (4×4), or (6×6) surface unit cell. Perpendicular to the surface the periodically repeated gold slabs are separated by a vacuum region of approximately 15 Å, which has been subject to convergence tests and proved to be sufficient. Asymmetric slabs have been chosen, i.e., the adsorbed molecules bind to a single side of the slab only. A dipole correction is applied perpendicular to the surface in order to account for the dipole moment due to the asymmetry of the slabs. For the adsorption geometries the Kohn-Sham wave functions are expanded in a plane-wave basis set with a cutoff energy of 340 eV. Plane waves up to an energy of 1000 eV are used to represent the augmentation charges. The integrals over the Brillouin zone are approximated by sums over special **k**-points[70] using meshes consisting of 49, 16, 9, and 4 **k**-points in the complete first Brillouin zone of the $(\sqrt{3}\times\sqrt{3})$, (3×3), (4×4), and (6×6) surface unit cell, respectively. For optimum comparability of the calculated total energies, the **k**-point meshes of the (3×3), (4×4), and (6×6) unit cells have been chosen equivalent.

The diffusion paths and transition states reported below have been calculated in a (3×3) surface unit cell for the SCH_3 radical, and in a (4×4) surface unit cell for the configurations involving a Au adatom. The slab geometries consist of six and four layers of gold, respectively. Due to the increased computational costs we have chosen less stringent convergence parameters in case of the large (4×4) cell. The Kohn-Sham wave functions are expanded in a plane-wave basis-set up to a cutoff energy of 250 eV (augmentation charge: 750 eV). Calculations done in the (3×3) cell include 16 **k**-points to approximate the integrals over the Brillouin zone. 4 **k**-points were used for the (4×4) surface unit cell.

The gold atoms of the outermost three layers on one side of the slab as well as the adsorbed molecule(s) are allowed to relax without constraints until the residual force per atom is smaller than 0.005 eV/Å. The remaining layers of the slab are kept fixed at their ideal bulk positions. All slabs have been set up using the theoretical lattice constant, which is calculated to be 4.18 Å. The slight overestimate compared to the experimental value of 4.08 Å is consistent with other density-functional calculations, e.g., for noble metals using GGA functionals.[71]

The calculational parameters cutoff energy, **k**-point sampling, number of relaxed and total substrate layers have been subject to systematic convergence tests as reported in the Appendix A. In summary, the overall error of the reported binding energies with respect to these parameters amounts to approximately 100 meV. The calculated energy barriers are less sensitive. Errors related to the use of the approximate PW91 exchange-correlation functional are not included in this estimate. There is a coverage dependence of the binding energies (corresponding to different sizes of the surface unit cell), which will be detailed below.

III. RESULTS AND DISCUSSION

In order to compare diffusion of SCH_3 radicals and dimethanethiol radical complexes $Au(SCH_3)_2$ on the Au(111) surface, it is essential to first gain insight into the adsorption geometries and binding energies. After the minima on the potential-energy surface (PES) have been localized, one can proceed with the calculation of the reaction paths connecting these minima and shed light on the relevant transition states and energy barriers. The following sections are organized along this line.

A. Adsorption

1. *Single* SCH_3 *radicals*

We have calculated stable adsorption sites and binding energies of bare SCH_3 methanethiol radicals on the unreconstructed Au(111) surface. We compare to results from previous DFT studies in the Appendix B. Two stable adsorption positions have been identified for the (3×3) surface unit cell. In these configurations the sulfur atom bonds to the Au surface close to the bridge site, slightly shifted toward either the fcc-hollow or hcp-hollow site. The shift amounts to 0.26 and 0.34 Å, respectively. In both cases, the S-C bond is tilted toward the nearest bridge site (fcc: 53° and hcp: 56° with respect to the surface normal; see Fig. 1). The CH_3 group is oriented in such a way that one of the hydrogen atoms is directed toward the surface whereas the other two are pointing away from the surface (see Fig. 2). However, the energy changes only slightly ($\leq$20 meV) when the CH_3 group is rotated around the S-C bond. Throughout this work we will refer to these configurations as fcc-bridge and hcp-bridge. Configurations in which the sulfur atom resides exactly at the bridge site or on top a gold surface atom were not stable in our calculations. All initial configurations that were chosen relaxed to either the fcc-bridge or hcp-bridge site in case of the (3×3) surface unit cell.

The strength of the involved S-Au bond has been evaluated as the difference in total energy between the adsorbate-substrate system and the sum of the total energies of the

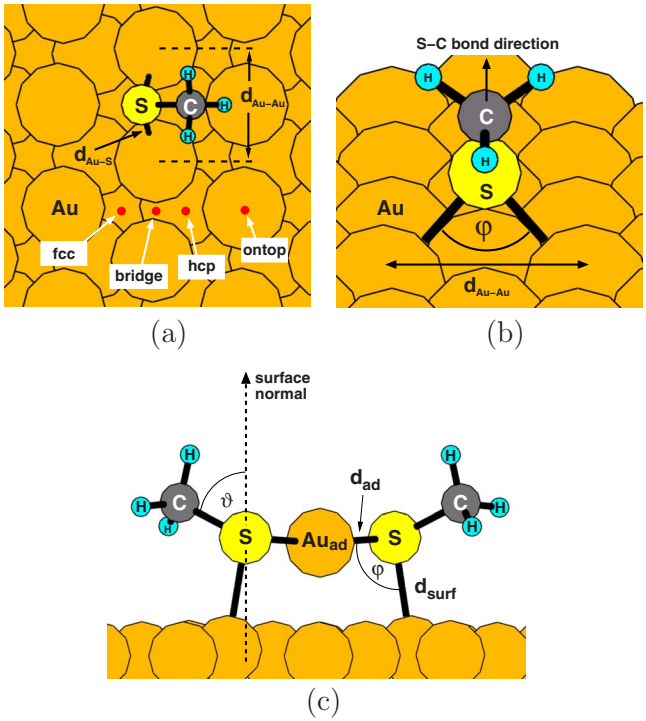

FIG. 1. (Color online) Definition of the structural parameters in a schematic representation of the calculated adsorption configurations for a bare SCH_3 radical (a) top view, (b) side view and the $Au(SCH_3)_2$ complex, (c) side view. The bond angle φ refers to the angle between the sulfur atom and the gold atoms it binds to. ϑ refers to the angle between the surface normal and the S-C bond for all configurations considered.

Au(111) surface and the spin-polarized SCH_3 radical in the gas phase:

$$E_{\text{bind}} = E_{\text{total}}\{CH_3S/Au(111)\} - E_{\text{total}}\{Au(111)\} - E^{\text{spin}}_{\text{total}}\{CH_3S\}. \quad (1)$$

In Table I the binding energies for a bare SCH_3 methanethiol radical on the unreconstructed Au(111) surface are summarized.

For comparison, the binding energy of two SCH_3 radicals forming a dimethyl disulfide molecule amounts to two times −1.5 eV. Zero point vibration energies are not included, but should be added before comparison to experimental dimethyl-disulfide dissociation energies. At a coverage of one SCH_3 radical per 9 Au surface atoms the CH_3S-Au binding energy amounts to −1.86 eV for the fcc-bridge configuration and −1.83 eV for the hcp-bridge configuration. In view of the uncertainty of approximately 100 meV for the computed binding energies, both adsorption sites should be considered approximately isoenergetic. In addition, the energy difference between these two configurations becomes even smaller for larger unit cells (see Table I). As the coverage decreases to one SCH_3 radical per 36 Au surface atoms the binding energy tends to increase to −1.99 eV for the fcc-bridge configuration. Hayashi *et al.* observed the same tendency noting that they had difficulties to obtain converged results for similar coverages.[22] In view of the large relaxation of the Au substrate, we attribute the increase in binding energy to substrate mediated, elastic adsorbate-adsorbate interactions. Due to the high computational cost of calculations with large supercells, we were not able to obtain results reflecting the properties of individual SCH_3 radicals on the Au(111) surface, i.e., the limit $\Theta \to 0$ could not be reached.

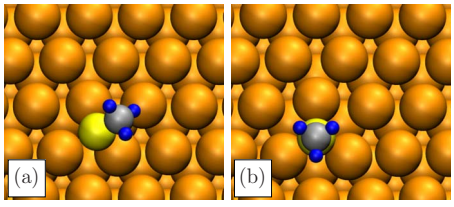

FIG. 2. (Color online) Top views of selected configurations for bare SCH_3 radicals: (a) fcc-bridge and (b) fcc-upright.

Calculations for an upright configuration with a tilt angle of 0° in which the sulfur atom resides directly above a fcc-site (or hcp-site) result in a CH_3S-Au binding energy of −1.72 eV (or −1.59 eV) for a (3×3) surface unit cell. At lower coverages the substrate relaxations increase (see $d_{\text{Au-Au}}$ in Table I). For the (4×4) and (6×6) surface unit cell we find that the upright fcc position becomes energetically favored over the tilted fcc-bridge configuration by 0.04 and 0.15 eV, respectively. To confirm these values, we increased the number of **k**-points to 64 for the (4×4) and 36 for the (6×6) surface unit cell, which yields values for these energy differences of 0.01 eV and 0.12 eV, respectively. The tendency in our calculations to favor upright configurations at small coverage is attributed to strong adsorbate induced relaxations of the unreconstructed Au(111) substrate. As a result of this relaxation the S atom moves deeper into the Au surface (see $d_{\text{S-Au},z}$ in Table I). Hence it binds stronger to the Au substrate in the upright configuration. The energy cost for expanding the hollow site with increasing cell size is overcompensated by a gain in binding energy and a relaxation of the tensile surface stress of the unreconstructed Au(111) surface. We consider this effect to be an artifact of the unreconstructed Au(111) surface as opposed to the $(22\times\sqrt{3})$ reconstruction stable under UHV conditions. In case of the reconstructed Au(111) surface, the surface stress is partially relaxed by incorporating additional gold atoms into the surface, which effectively reduces the average Au-Au distance within the first layer of atoms by approximately 5%.[40,72] In a very crude model calculation we have tried to simulate this higher density of Au surface atoms within the first layer by compressing the slab with the unreconstructed Au(111) surface in the $[1\bar{1}0]$ direction by 5%. When adsorbing the SCH_3 radical on this unreconstructed, but compressed Au(111) surface, the tilted fcc-bridge configuration remains energetically favored over the upright configuration by 0.21 eV. Even though this is certainly a very rough estimate, we speculate that the tendency to favor the tilted structure over the upright structure even at low coverage should prevail for the reconstructed Au(111) surface.

The herringbone reconstruction of Au(111) can be lifted under electrochemical conditions. Which configuration will be observed in case of bare SCH_3 radicals adsorbed on the

TABLE I. Calculated adsorption geometries for SCH_3 radicals on unreconstructed Au(111). Full coverage ($\Theta=1$) refers to one SCH_3 per three gold surface atoms, i.e., the experimentally observed saturation coverage (Ref. 17). $d_{S\text{-}Au,z}$ is the average vertical distance between the S atom and the Au atom it binds to. $d_{Au\text{-}Au}$ refers to the distance between the Au atoms of the hollow position in which the radical is adsorbed. All other structural parameters are defined in Fig. 1.

Configuration	Cell size	Coverage Θ	E_{bind} (eV)	ϑ	φ	$d_{S\text{-}Au}$ (Å)	$d_{S\text{-}Au,z}$ (Å)	$d_{Au\text{-}Au}$ (Å)
fcc-bridge	$(\sqrt{3}\times\sqrt{3})$	1	−1.79	52°	79°	2.48	1.88	3.15
fcc-bridge	(3×3)	0.33	−1.86	53°	80°	2.47	1.86	3.17
fcc-bridge	(4×4)	0.19	−1.92	50°	83°	2.46	1.80	3.26
fcc-bridge	(6×6)	0.08	−1.99	48°	86°	2.45	1.71	3.34
hcp-bridge	(3×3)	0.33	−1.83	56°	79°	2.48	1.90	3.14
hcp-bridge	(4×4)	0.19	−1.88	54°	81°	2.47	1.85	3.18
fcc-upright	(3×3)	0.33	−1.72	0°	85°	2.47	1.55	3.33
fcc-upright	(4×4)	0.19	−1.95	0°	91°	2.44	1.38	3.50
fcc-upright	(6×6)	0.08	−2.14	0°	96°	2.45	1.27	3.63

unreconstructed Au(111) surface under such electrochemical conditions is not yet clear to us. The answer might depend on the coverage of specifically coadsorbed ions from the electrolyte or other effects stabilizing the unreconstructed Au(111) surface.[73] Similar to the neighboring thiol radicals, the coadsorbed ions may tend to stabilize the unreconstructed surface.

2. $Au(SCH_3)_2$ *complexes*

In the submonolayer coverage regime the binding energy per SCH_3 radical is found to be further lowered when adsorbing two of the radicals alongside a gold adatom as depicted in Fig. 3. This has been reported by Maksymovych *et al.* based on their STM experiments[39] and DFT calculations.[35,39,40] As the creation of $Au(SCH_3)_2$ complexes at the surface is linked to a dereconstruction of the Au(111) surface,[39,40] the following analysis of the adsorption and diffusion properties of $Au(SCH_3)_2$ complexes on the unreconstructed Au(111) surface has significance for experiments under UHV and electrochemical conditions.

We have carried out a detailed analysis of the stable adsorption positions and binding energies of such a phase of $Au(SCH_3)_2$ complexes on unreconstructed Au(111) at intermediate coverage. Starting from the defect free Au(111) surface, a process is considered in which one gold adatom is added to the surface, which binds to a fcc site. Then two SCH_3 radicals are put onto the substrate, forming bonds with both the Au surface atoms and the Au adatom. The binding energy per methanethiol radical relative to the adatom covered surface plus the free radicals is

$$E_{bind(1)} = \frac{1}{2}(E_{total}\{Au(SCH_3)_2/Au(111)\} - E_{total}\{Au_{ad}/Au(111)\} - 2E^{spin}_{total}\{SCH_3\}). \quad (2)$$

To account for adatom formation, we calculate the energy of an Au adatom at the fcc position on the surface with respect to its bulk chemical potential

$$E_{ad} = E_{total}\{Au_{ad}/Au(111)\} - E_{total}\{Au(111)\} - E^{bulk}_{total}\{Au\}. \quad (3)$$

The Au chemical potential equals the energy per bulk atom $E^{bulk}_{total}\{Au\}$. Hence the binding energy per methanethiol radical as compared to the defect-free unreconstructed Au(111) surface is

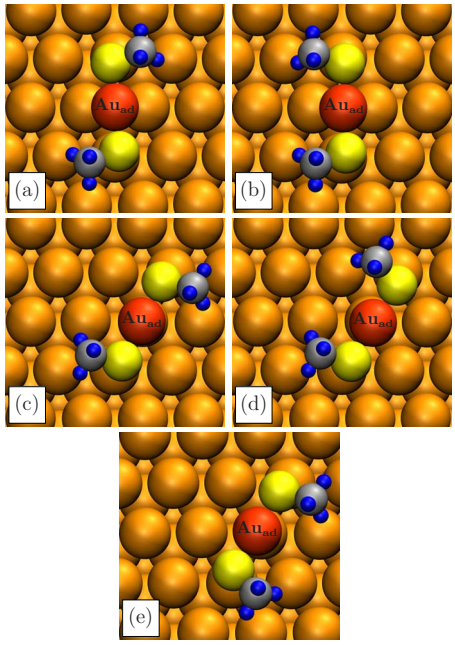

FIG. 3. (Color online) Top views of the calculated configurations for $Au(SCH_3)_2$ complexes on the unreconstructed Au(111) surface: (a) trans-bridge, (b) cis-bridge, (c) trans-on-top, (d) cis-on-top 1, (e) cis-on-top 2. For transisomers the SCH_3 group is pointing in different directions while for cisisomers they are pointing in the same direction. cis-on-top 1 and 2 differ in the way the SCH_3 groups are oriented with respect to the underlying surface.

TABLE II. Calculated adsorption geometries for $Au(SCH_3)_2$ complexes on Au(111). Full coverage ($\Theta=1$) refers to one SCH_3 per three gold surface atoms, i.e., the experimentally observed saturation coverage (Ref. 17). The structural parameters are defined in Fig. 1. The formation energy for one adatom at a fcc-hollow site has been calculated within the same supercell as the $Au(SCH_3)_2$ binding energy.

Configuration	Cell size	Coverage Θ	$E_{\mathrm{bind}(1)}$ (eV)	E_{ad} (eV)	$E_{\mathrm{bind}(2)}$ (eV)	ϑ	φ	d_{ad} (Å)	$d_{\mathrm{S\text{-}Au}}$ (Å)
trans-bridge	(4×4)	0.38	−2.37	+0.59	−2.08	66°	94°	2.33	2.50
trans-bridge	(6×6)	0.17	−2.40	+0.57	−2.12	65°	94°	2.33	2.48
cis-bridge	(4×4)	0.38	−2.36	+0.59	−2.07	67°	94°	2.34	2.50
trans-on-top	(4×4)	0.38	−2.27	+0.59	−1.98	66°	103°	2.34	2.53
cis-on-top 1	(4×4)	0.38	−2.27	+0.59	−1.98	65°	103°	2.34	2.53
cis-on-top 2	(4×4)	0.38	−2.27	+0.59	−1.98	65°	103°	2.34	2.53

$$E_{\mathrm{bind}(2)} = E_{\mathrm{bind}(1)} + \frac{1}{2}E_{\mathrm{ad}}. \tag{4}$$

$E_{\mathrm{bind}(2)}$ includes the energy expense necessary for adatom formation. Therefore this quantity can be compared to the binding energies of SCH_3 radicals presented in the previous subsection.

In order to identify stable adsorption configurations, we considered the proposed structure by Maksymovich *et al.*[39] as a starting point. We have relaxed several initial configurations to a nearest local energy minimum. The initial configurations are characterized by positioning the sulfur atom either above hollow or on top sites and parallel (trans) or antiparallel (cis) S-C bond orientations. Rotating the CH_3-group around the S-C bond directions is expected to yield energy changes similar to those found for a single SCH_3 radical at the Au(111) surface.

Altogether a total of five stable adsorption positions have been calculated, with binding energies $E_{\mathrm{bind}(1)}$ per SCH_3 radical between −2.37 and −2.27 eV. These data refer to a coverage of one complex, i.e., two SCH_3 radicals, per 16 Au surface atoms. The structures are depicted in Fig. 3. Taking into account the energy needed to create one Au adatom (see Table II), adsorption as $Au(SCH_3)_2$ complexes is energetically favorable compared to adsorption at the defect free (111) surface. The net energy gain per SCH_3 radical due to the formation of $Au(SCH_3)_2$ complexes amounts to 0.22 eV for a coverage of $\Theta\approx0.38$ and 0.20 eV for a coverage of $\Theta\approx0.17$.

The binding energies, together with characteristic structural parameters, are listed in Table II. The binding energy for the trans-bridge configuration is in agreement with the value of $E_{\mathrm{bind}(1)}=-2.4$ eV and $E_{\mathrm{bind}(2)}=-1.95$ eV reported in Refs. 35 and 39, respectively.

The sulfur atoms reside atop Au surface atoms, while the Au adatom is either found in a bridgelike or on top position. We will denote these configurations as trans-bridge, cis-bridge, trans-on-top, and cis-on-top, depending on the location of the adatom and the orientation of the SCH_3 radicals. In case of the energetically most favorable trans-bridge configuration, both S-atoms bond to two Au atoms with Au_{surf}-S-Au_{ad} bond angles of 93° and 94°. The SCH_3 radicals are tilted toward the gold surface with an average tilt angle between the surface normal and the S-C bond of 66°.

B. Diffusion

We investigate diffusion of the above described adsorption species on the unreconstructed Au(111) surface within the framework of harmonic transition state theory.[74] Minimum energy paths (MEP) between local minima of the PES are calculated.[75] To this purpose the climbing image nudged elastic band scheme (CI-NEB) (Refs. 75–77) is applied.[78] First, intermediate configurations between the respective two local minima need to be specified. They serve as an initial guess for the reaction path. In this work, we have chosen a linear interpolation in high dimensional configuration space connecting the two local minima. Subsequently, all intermediate configurations are relaxed to a MEP by using the CI-NEB scheme quoted above. The configuration along the path that is highest in energy converges to a (local) transition state.

1. $Au(SCH_3)_2$ *complexes*

Minimum energy paths, (local) transition states, and energy barriers for the diffusion of the $Au(SCH_3)_2$ complex on Au(111) are summarized in Fig. 4. We will refer to the highest energy barrier along the MEP leading from one configuration to a symmetrically equivalent (and hence isoenergetic) configuration as the diffusion barrier ΔE_{diff}. For a sequence of rotations around S-Au bonds resulting in a net translational motion across the surface, ΔE_{diff} is calculated to be 0.37 eV [calculated within a (4×4) surface unit cell]. In addition, a purely rotational motion without translating the complex across the surface is found to yield a diffusion barrier of 0.44 eV. The latter energy barrier has to be surmounted in order to achieve an arbitrary large rotation of the complex on the surface. The slightly smaller diffusion barrier height for translation as compared to rotation of the complex leads us to speculate that, at some suitably chosen temperature, a correlation between the directions of subsequent diffusion events might occur. Subsequent diffusion hops could preferentially occur back or forth along the same crystallographic direction on the surface (i.e., the $[1\bar{1}0]$ direction or a direction equivalent by symmetry). Such anisotropic diffu-

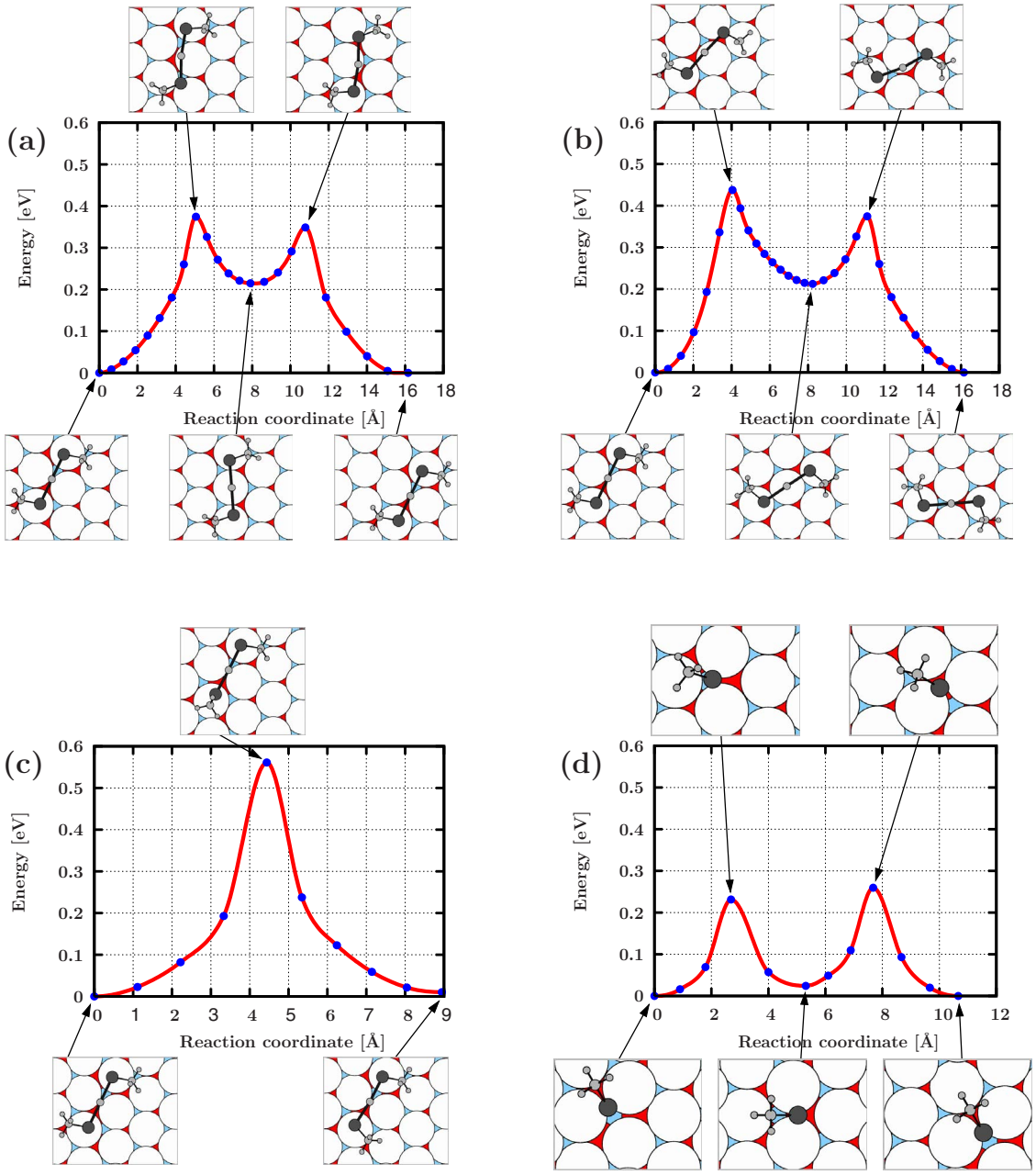

FIG. 4. (Color online) MEPs for the $Au(SCH_3)_2$ complex and a bare SCH_3 radical. Dots correspond to calculated intermediate configurations. The spline interpolation is a guide to the eyes. Configurations are depicted schematically: Au atoms large white circles (first layer), dark gray or red (second layer), light gray or blue (third layer); S atoms small black circles; Au adatom small light gray circle; CH_3 small light gray circles. (a): Translation of the $Au(SCH_3)_2$ complex. MEP from a trans-bridge configuration to a tran-sbridge configuration via a trans-on-top geometry (local minimum). (b) Rotation of the $Au(SCH_3)_2$ complex. MEP from a trans-bridge configuration to a rotated trans-bridge configuration via a trans-on-top geometry (local minimum). (c) Conformational change of the $Au(SCH_3)_2$ complex. MEP from the trans-bridge to the cis-bridge configuration. At the transition state one nearly upright SCH_3 group resides on top a gold surface atom. (d) Translation of a bare SCH_3 radical. MEP for a translation from a fcc-bridge position via the hcp-bridge position to a fcc-bridge position.

sion has been observed for large molecules that sustain more than one bond to the underlying substrate on anisotropic[53,55–57] as well as isotropic substrates.[45,52,60]

We have also considered the energy barrier for a conformational transformation, i.e., a flip of one of the SCH_3 groups of the adsorbed $Au(SCH_3)_2$ complex. The energy barrier that has to be overcome to obtain a transition from the trans-bridge to the cis-bridge configuration amounts to 0.56 eV; see Fig. 4(c). This barrier is larger than both the energy barriers toward rotation and translation, which points toward a certain relative stability of different $Au(SCH_3)_2$ conformations at the Au(111) surface against such conformation flips.

The vibrational frequencies have been determined for the transbridge configuration and the transition state for translations using a finite difference approach as implemented in VASP. All atoms of the SCH_3 radicals and the Au adatom are

displaced by 0.025 Å in each direction of the Cartesian coordinate system. The other Au atoms are kept fixed. Diagonalization of the resulting approximation for the Hessian matrix yields the vibrational frequencies and the corresponding vibrational eigenmodes. Within the harmonic transition state theory the (classical) attempt frequency ν_0 for the diffusion process can be deduced from the vibrational frequencies at the minimum and the transition state,[74]

$$\nu_0 = \frac{\prod_{i=1}^{N} \nu_i^{\min}}{\prod_{j=1}^{N-1} \nu_j^{\mathrm{ts}}}. \tag{5}$$

Together with the energy barrier height $\Delta E_{\mathrm{diff}} = E^{\mathrm{ts}} - E^{\min}$ it determines the hopping rate with respect to the particular transition state,[74]

$$k^{\mathrm{hTST}} = \nu_0 e^{-\Delta E_{\mathrm{diff}}/k_b T}. \tag{6}$$

We obtain an attempt frequency $\nu_0 = 8 \times 10^{12}$ s^{-1} for the translational diffusion event of $Au(SCH_3)_2$ shown in Fig. 4(a), which is of the same order of magnitude found also for other diffusing species on various substrates.[54] For the hopping rate across the first barrier in Fig. 4(a) we thus arrive at a hTST-value on the order of 10^6 s^{-1} at 293 K. We find one imaginary frequency at the saddle point with a magnitude of ≈ 0.01 eV. Sometimes a zero-point energy correction is applied to the (classical) energy barrier ΔE_{diff} for low temperatures,[79]

$$\delta E_{\mathrm{zero}} = \sum_{i=1}^{N} \frac{h}{2} \nu_i^{\min} - \sum_{j=1}^{N-1} \frac{h}{2} \nu_j^{\mathrm{ts}}. \tag{7}$$

In our case, the zero-point energy correction is rather small and amounts to ≈ 15 meV, which is below the accuracy of the calculated DFT energy barriers. Additional temperature-dependent quantum corrections such as the Wigner correction[79] need not be considered here.

A characteristic common feature of the calculated diffusion paths is that only one of the two involved S-Au_{surf} bonds is broken at a time. The second S atom stays in the vicinity of the Au surface atom to which it was initially bound in the minimum-energy configuration. The other atoms in the complex rotate about the nearly fixed S-Au_{surf} bond. To check the validity of this observation, we have performed additional NEB calculations in which the initial configuration is both rotated and translated about the surface to a symmetrically equivalent final geometry. As a matter of fact, the calculation converged to a MEP which consisted of two subsequent pure rotations of the complex around fixed S-Au_{surf} bonds. This corroborates our assertion.

Finally, we consider the possibility that the $Au(SCH_3)_2$ complex dissociates into $AuSCH_3$ and a bare SCH_3 radical, which diffuse separately and then recombine. To this purpose, we compare the energy of an adsorbed $Au(SCH_3)_2$ complex with the energy of an $AuSCH_3$ complex and a SCH_3 radical adsorbed independently at the Au(111) surface. Due to different substrate relaxations, these energies depend sensitively on the size of the surface supercell used in the calculations. This translates into an uncertainty of the dissociation energy. Nevertheless, our values come out greater or at worst equal to the largest of the energy barriers considered in Fig. 4 corresponding to the conformational flip. Thus we conclude that dissociation of a SCH_3 radical from the $Au(SCH_3)_2$ complex is of minor importance compared to the diffusion processes described above.

2. *Single* SCH_3 *radicals*

In order to get into contact with previous work and to complete the physical picture of SCH_3 diffusion mechanisms on Au(111), we present calculated minimum-energy paths for bare SCH_3 radicals on the unreconstructed Au(111) surface. We point out that the dependence on coverage (or, equivalently, the dependence on surface unit-cell size) of the SCH_3 binding energies will translate into a corresponding sensitivity of the diffusion barrier heights on coverage. Energy barrier values quoted below are for a (3×3) surface unit cell.

We have found two local transition states for crossing a bridge site with energy barriers relative to the fcc-bridge adsorption minimum of 0.23 and 0.26 eV; see Fig. 4(d). For both transition states the sulfur atom of the radical is located near the bridge site and the S-C bond is tilted toward the surface normal by 48° and 52°, respectively. In addition to these translations, the radical can also rotate from one fcc-bridge position via a fcc-upright configuration to a symmetrically equivalent fcc-bridge position. The barrier for this rotation is found to be 0.13 eV (corresponding MEP not shown). We obtain an attempt frequency of 12×10^{12} s^{-1} for the transition states with an energy barrier to translation of 0.26 eV. The imaginary frequency at the saddle point is approximately 0.01 eV and the zero-point energy correction amounts to 14 meV.

Different reports concerning the transition state and the diffusion barrier for SCH_3 radicals on Au(111) can be found in the literature. Cometto *et al.* conducted cluster calculations for SCH_3 on Au(111) in which they position the radical over the rigid surface keeping the S atom at a constant height.[30] Within the cut through the PES considered in Ref. 30, the authors find a local maximum for a SCH_3 radical in an upright configuration at the bridge site with an energy of 0.76 eV above the adsorption minimum. On the other hand, Ford *et al.* report no barrier to diffusion at the bridge site. They found the corrugation of the PES to be 0.36 eV between the fcc-bridge and a tilted on top position. Maksymovych *et al.*[32] calculated a diffusion barrier of 0.23 eV using the NEB transition state search algorithm. The barrier height as well as the transition state geometry is in agreement with the transition state reported here.

Altogether, the calculated diffusion barriers of $Au(SCH_3)_2$ are 40% higher compared to bare methanethiol radicals. On the reconstructed gold surface this tendency is likely to increase further, since the bare SCH_3 adsorption minima are shallower in this case, which could lead to even lower diffusion barriers.

The relative stability of the $Au(SCH_3)_2$ complexes is in qualitative agreement with the STM experiments carried through by Maksymovych *et al.*[39] Even though no actual diffusion rates were measured, they found the $Au(SCH_3)_2$ complex to be much more stable under high tunneling currents and voltages than SCH_3 radicals or dimethyldisulfide

(CH_3S-SCH_3) at 5 K. Thus, our calculations tend to corroborate the results of Ref. 39.

IV. SUMMARY

We present results from *ab initio* DFT calculations for the adsorption and diffusion properties of single SCH_3 radicals and $Au(SCH_3)_2$ complexes on the unreconstructed Au(111) surface. Previous STM experiments and DFT calculations have suggested that these complexes form at the Au(111) surface at submonolayer coverages.[35,39,40] Our calculations corroborate this finding, in particular we also obtain an energetical preference for the formation of $Au(SCH_3)_2$ complexes as compared to independently chemisorbed SCH_3 radicals at not too low coverages on the unreconstructed Au(111) surface.

Besides other contributions to the bonding, there are two Au-S bonds between the complex and the underlying Au substrate atoms. This makes $Au(SCH_3)_2$/Au(111) a model system for complex molecular diffusion with few internal degrees of freedom of the diffusing object.

Diffusion paths in configuration space with maximum statistical weight, so-called minimum-energy paths, have been calculated using the nudged elastic band algorithm. The diffusion rates have been estimated within harmonic transition state theory. One translational and one purely rotational diffusion event have been identified with energy barriers of 0.37 and 0.44 eV, respectively. The attempt frequency for translations $\nu_0 = 8 \times 10^{12}$ s^{-1} has been estimated using finite differences and the frozen phonon approach.

Translations of $Au(SCH_3)_2$ are found to consist of subsequent rotations around one of the two Au-S bonds resembling a "walking" motion. A similar diffusion characteristic was found by Kwon *et al.* for a larger organic molecule with two sulfur bonds to the surface and multiple internal degrees of freedom.[45,60] This indicates the model character of our study. We contemplate that diffusion mechanisms, which consists of multiple steps with only one broken sulfur-substrate bond at a time, may be of a more general validity.[45,52,57,60]

The sequence of energy barrier heights is $\Delta E_{\text{translation}} < \Delta E_{\text{rotation}} < \Delta E_{\text{cis}\leftrightarrow\text{trans}}$. We speculate that this might result in a correlation between the direction of subsequent diffusion hops.

ACKNOWLEDGMENTS

We thank the Deutsche Forschungsgemeinschaft (DFG) for financial support within Project No. Pe497/4-1. Calculations have been carried through at the Rechenzentrum der Universität Kiel.

APPENDIX A: CONVERGENCE TESTS

In this appendix we quantify the convergence of the reported binding energies and diffusion barriers with respect to the parameters used in our calculations. The parameters used in the main part of this work are marked with an asterisk (*). In order to obtain a measure of the uncertainty related to the exchange-correlation functional $E_{xc}[n]$, we compare to results calculated within the local-density approximation (LDA) (Refs. 80 and 81) for $E_{xc}[n]$.

TABLE III. Convergence of the binding energy per SCH_3 radical (fcc-bridge configuration unless noted otherwise).

	Cell size	E_{cutoff} (eV)	N_{kpt}	N_{layer}	E_{bind} (eV)
	Plane wave cutoff energy E_{cutoff}				
	$(\sqrt{3}\times\sqrt{3})$	250	49	6	−1.76
(*)	$(\sqrt{3}\times\sqrt{3})$	340	49	6	−1.79
	$(\sqrt{3}\times\sqrt{3})$	420	49	6	−1.79
	$(\sqrt{3}\times\sqrt{3})$	520	49	6	−1.80
	Number of Au layers N_{layer}				
	$(\sqrt{3}\times\sqrt{3})$	340	49	4	−1.77
(*)	$(\sqrt{3}\times\sqrt{3})$	340	49	6	−1.79
	$(\sqrt{3}\times\sqrt{3})$	340	49	12	−1.83
	$(\sqrt{3}\times\sqrt{3})$	340	49	15	−1.80
	$(\sqrt{3}\times\sqrt{3})$	340	49	18	−1.79
	Number of **k**-points N_{kpt}				
(*)	(3×3)	340	16	6	−1.86
	(3×3)	340	25	6	−1.84
	(3×3)	340	64	6	−1.83
	(3×3)	340	100	6	−1.82
(*)	(6×6) fcc-upright	340	4	6	−2.14
	(6×6) fcc-upright	340	16	6	−2.09
	(6×6) fcc-upright	340	36	6	−2.06

1. (1) SCH_3

The binding energies of one SCH_3 radical calculated for different computational parameters are summarized in Table III. The convergence with respect to the cutoff energy for the Kohn-Sham wave functions and the number of layers in the slab geometry has been evaluated at a coverage of one SCH_3 radical per $(\sqrt{3}\times\sqrt{3})$ surface unit cell and 49 **k**-points in the complete first Brillouin zone.

The **k**-point sampling has been tested for a configuration involving one SCH_3 radical per (3×3) and (6×6) surface unit cell to ensure an equivalent **k**-point mesh as in the calculations of the main part of this work. The **k**-point sampling appears to be the most sensitive parameter. The fcc-bridge binding energy changes by approximately 40 meV for the (3×3) surface unit cell. For the fcc-upright configuration we calculated a change of 80 meV for the (6×6) surface unit cell. Upon increasing the number of **k**-points from 16 to 36 for the (6×6) surface unit cell, the total energy of the calculated slab geometry changed by less than 100 meV.

Relaxing the top most four layers [one SCH_3 radical per (3×3) unit cell] and increasing the vacuum region by ≈ 5 Å changed the calculated binding energy by 1 and 3 meV, respectively. Altogether, we arrive at an estimate for the binding-energy error of approximately 100 meV.

Convergence tests for the diffusion barrier for a transition from a fcc-bridge to a hcp-bridge configuration [left barrier

TABLE IV. Convergence test for the binding energy $E_{bind(1)}$ per SCH_3 radical in the trans-bridge configuration of the $Au(SCH_3)_2$ complex. Note that the value of $E_{bind(1)}=-2.37$ eV in Table II has been calculated at a cutoff energy of 340 eV.

	Cell size	E_{cutoff} (eV)	N_{kpt}	N_{layer}	$E_{bind(1)}$ (eV)
		Number of **k**-points N_{kpt}			
(*)	(6×6)	340	4	6	−2.40
	(6×6)	340	16	6	−2.39
		Number of Au layers N_{layer}			
	(4×4)	250	4	4	−2.30
	(4×4)	250	4	6	−2.28
	(4×4)	250	4	9	−2.28
	(4×4)	250	4	12	−2.31
	(4×4)	250	4	15	−2.31

in Fig. 4(d)] indicate a convergence to within a few 10 meV (see Table V). This suggests that the energy barriers converge faster than the binding energy.

2. (2) $Au(SCH_3)_2$

Table IV summarizes the dependence on calculational parameters of the binding energy per SCH_3 radical for the $Au(SCH_3)_2$ complex. The convergence seems to be at least as good as for the bare SCH_3 radical. For the $Au(SCH_3)_2$ complexes we use less stringent convergence parameters to calculate the MEPs (250 eV cutoff, 4 **k**-points, 4 Au layers). Table V summarizes the convergence behavior of the translational diffusion barrier. As for the bare SCH_3 radical, convergence to within a few 10 meV of the diffusion barrier is found. Furthermore, the translational motion has a lower diffusion barrier compared to rotations for both exchange-correlation energy functionals under consideration (see Table VI). The effect of the LDA on the barrier height is on the order of 0.1–0.2 eV.

APPENDIX B: COMPARISON TO OTHER DFT STUDIES

In Table VII we compare to DFT studies of the SCH_3 binding energy on the unreconstructed Au(111) surface by other authors. From the many studies we found in the literature, we include mainly those that we feel are closest to our work in terms of the computational method and the SCH_3 coverage. The binding energies depend on the choice of the reference configuration. In our work the reference has been chosen as a spin polarized, C_{1v} symmetric SCH_3 radical in vacuum. A spin-polarized SCH_3 radical has also been taken as the energy reference in Refs. 31 and 32. In case of the other calculations cited in Table VII, the spin polarization of the reference configuration has not been stated explicitly to our knowledge. The energy difference between the spin unpolarized and the spin-polarized SCH_3 radical in vacuum amounts to approximately 0.3 eV.

In Refs. 31 and 82 (first and second row of Table VII) the authors report an SCH_3 binding energy at saturation coverage of −1.76 and −1.62 eV, respectively. Both values were obtained using the VASP code with similar computational parameters as were used in our work. Our value of −1.79 eV is in agreement with the work in Ref. 31. In Ref. 82 substrate relaxations were not taken into account. Excluding substrate relaxations we obtain a binding energy of −1.63 eV in agreement with the −1.62 eV from Ref. 82.

TABLE V. Convergence test for the translational diffusion barrier of the $Au(SCH_3)_2$ complex and the fcc-bridge to hcp-bridge SCH_3 diffusion barrier.

	E_{cutoff} (eV)	N_{kpt}	N_{layer}	ΔE_{diff} (eV)
		$Au(SCH_3)_2$ complex		
		Number of **k**-points N_{kpt}		
(*)	250	4	4	0.37
	250	16	4	0.38
		Plane-wave cutoff energy E_{cutoff}		
(*)	250	4	4	0.37
	340	4	4	0.37
		Number of Au layer N_{layer}		
	250	4	4	0.37
(*)	250	4	6	0.36
	250	4	9	0.35
	250	4	12	0.36
	250	4	15	0.36
		SCH_3		
		Number of **k**-points N_{kpt}		
(*)	340	16	6	0.23
	340	25	6	0.24
	340	64	6	0.23
		Plane-wave cutoff energy E_{cutoff}		
(*)	340	16	6	0.23
	420	16	6	0.23

TABLE VI. Bare SCH_3 binding energy and diffusion barriers for different approximations to the exchange-correlation functional. In case of the SCH_3 radical a transition from fcc-bridge to hcp-bridge and translational and rotational diffusion barriers are considered for the $Au(SCH_3)_2$ complex.

	E_{XC}	Lattice constant from	$E_{bind}^{fcc\text{-}brg}$ (eV)	ΔE_{diff} (eV)
SCH_3	GGA-PW91	GGA	−1.86	0.23
	LDA	LDA	−2.64	0.25
	LDA	GGA	−2.83	0.31
Ref. 34	LDA		−2.79	
$Au(SCH_3)_2$	GGA-PW91	GGA		0.37
Translation	LDA	GGA		0.49
$Au(SCH_3)_2$	GGA-PW91	GGA		0.44
Rotation	LDA	GGA		0.66

TABLE VII. Overview of calculated binding energies for SCH_3 radicals on unreconstructed Au(111) from other DFT studies. A coverage of $\Theta=1$ refers to one SCH_3 per three gold surface atoms (saturation coverage) (Ref. 17). Structural parameters are defined in Fig. 1. A summary of the computational details is given (USPP: ultrasoft pseudopotentials, NCPP: norm conserving pseudopotentials). The number of **k**-points and the cutoff energy for the plane-wave expansion are given. The number in parentheses after the layer thickness of the slab refers to the number of relaxed topmost layers.

Configuration	Coverage Θ	E_{bind} (eV)	ϑ	$d_{S\text{-}Au}$ (Å)	Computational details
fcc-bridge[a]	1	−1.76	50°	2.47	VASP, GGA-PW91, PAW, 500 eV, 81 **k**, 7 (2) layers
fcc-bridge[b]	1	−1.62	56°		VASP, GGA-PW91, USPP, 320 eV, 81 **k**, 3 (0) layers
fcc-bridge[c]	1	−1.71	52.8°	2.49	GGA-PBE, USPP, 25 Ry, 64 **k**, 6 (2) layers
fcc-bridge[d]	1	−1.72			GGA-PBE, NCPP, 45 Ry, 64 **k**, 6 (unknown) layers
fcc-bridge[e]	1	−1.92	50.8°	2.49	GGA-PBE, USPP, 22 Ry, 36 **k**, 4 (3) layers
fcc-bridge[f]	1	−1.67			GGA-PW91, USPP, 25 Ry, 54 **k**, 5 (3) layers
fcc-bridge[g]	0.33	−1.77	53.7°	2.45	
fcc-bridge[g]	0.20	−1.88	52.9°	2.46	
fcc-upright[g]	0.33	−1.61	0°	2.44	VASP, GGA-PW91, PAW, 400 eV, 4 **k**, 4 (2) layers
fcc-upright[g]	0.20	−1.82	0°	2.45	
hcp-bridge[g]	0.33	−1.75	55.9°	2.45	
hcp-bridge[g]	0.20	−1.84	56.9°	2.57	

[a]Reference 31.
[b]Reference 82.
[c]Reference 35.
[d]Reference 33.
[e]Reference 30.
[f]Reference 37.
[g]Reference 32.

In Refs. 33 and 35 (third and fourth row of Table VII) the reported bond strength is 80 and 60 meV smaller than our value at $\Theta=1$. The main difference to our calculation is the different gradient corrected approximation to the exchange-correlation functional and the use of norm conserving and ultrasoft pseudopotentials. Together with the accuracy of our calculation of approximately 100 meV, the result reported in our work is in agreement with Refs. 33 and 35.

In the fifth and sixth row of Table VII we summarize calculated SCH_3 binding energies at $\Theta=1$ from Ref. 30 (−1.92 eV) and Ref. 37 (−1.67 eV). These values are 130 meV smaller and 120 meV larger than our result, respectively, which is only slightly larger than our error bar of approximately 100 meV.

In Ref. 32 (seventh to 13th row of Table VII) Maksymovych *et al.* calculate SCH_3 binding energies at coverages of 1/3 and 1/5 of a monolayer using VASP. Compared to our results, the reported bond strengths agree within the accuracy of our calculations. The difference in bond strength lies in the range of 40 meV (fcc-/hcp-bridge) to 130 meV (fcc-upright). We speculate whether the residual small difference is due to a different **k**-point set and number of layers.

*franke@theo-physik.uni-kiel.de

[1] L. H. Dubois and R. H. Nuzzo, Annu. Rev. Phys. Chem. **43**, 437 (1992).
[2] A. Ulman, Chem. Rev. **96**, 1533 (1996).
[3] G. Poirier, Chem. Rev. **97**, 1117 (1997).
[4] F. Schreiber, Prog. Surf. Sci. **65**, 151 (2000).
[5] P. E. Sheehan and L. J. Whitman, Phys. Rev. Lett. **88**, 156104 (2002).
[6] F. Schreiber, J. Phys.: Condens. Matter **16**, R881 (2004).
[7] C. Vericat, M. Vela, and R. Salvarezza, Phys. Chem. Chem. Phys. **7**, 3258 (2005).
[8] J. Love, L. Estroff, J. Kriebel, R. Nuzzo, and G. Whitesides, Chem. Rev. **105**, 1103 (2005).
[9] C. Vericat, M. E. Vela, G. A. Benitez, J. A. M. Gago, X. Torrelles, R. C. Salvarezza, J. Phys.: Condens. Matter **18**, R867 (2006).
[10] L. Grill, J. Phys.: Condens. Matter **20**, 053001 (2008).
[11] D. P. Woodruff, Phys. Chem. Chem. Phys. **10**, 7211 (2008).
[12] I. I. Rzeznicka, J. Lee, P. Maksymovych, and J. T. Yates, J. Phys. Chem. B **109**, 15992 (2005).
[13] J.-G. Zhou and F. Hagelberg, Phys. Rev. Lett. **97**, 045505 (2006).
[14] P. Maksymovych, D. C. Sorescu, D. Dougherty, and J. T. Yates, J. Phys. Chem. B **109**, 22463 (2005).

[15] P. G. Lustemberg, M. L. Martiarena, A. E. Martinez, and H. F. Busnengo, Langmuir **24**, 3274 (2008).
[16] M. G. Roper and R. G. Jones, Phys. Chem. Chem. Phys. **10**, 1336 (2008).
[17] L. H. Dubois, B. R. Zegarski, and R. H. Nuzzo, J. Chem. Phys. **98**, 678 (1993).
[18] M. Danisman, L. Casalis, G. Bracco, and G. Scoles, J. Phys. Chem. B **106**, 11771 (2002).
[19] H. Kondoh, M. Iwasaki, T. Shimada, K. Amemiya, T. Yokoyama, T. Ohta, M. Shimomura, and S. Kono, Phys. Rev. Lett. **90**, 066102 (2003).
[20] M. G. Roper, M. P. Skegg, C. J. Fisher, J. J. Lee, V. R. Dhanak, D. P. Woodruff, and R. G. Jones, Chem. Phys. Lett. **389**, 87 (2004).
[21] X. Torrelles, C. Vericat, M. Vela, M. Fonticelli, M. Daza Millone, R. Felici, T.-L. Lee, J. Zegenhagen, G. Munoz, J. Martin-Gago, and Roberto C. Salvarezza, J. Phys. Chem. B **110**, 5586 (2006).
[22] T. Hayashi, Y. Morikawa, and H. Nozoye, J. Chem. Phys. **114**, 7615 (2001).
[23] M. Yu, N. Bovet, C. J. Satterley, S. Bengió, K. R. J. Lovelock, P. K. Milligan, R. G. Jones, D. P. Woodruff, and V. Dhanak, Phys. Rev. Lett. **97**, 166102 (2006).
[24] D. P. Woodruff, Surf. Sci. **254**, 76 (2007).
[25] H. Grönbeck, A. Curioni, and W. Andreoni, J. Am. Chem. Soc. **122**, 3839 (2000).
[26] M. C. Vargas, P. Giannozzi, A. Selloni, and G. Scoles, J. Phys. Chem. B **105**, 9509 (2001).
[27] Y. Yourdshahyan, H. K. Zhang, and A. M. Rappe, Phys. Rev. B **63**, 081405(R) (2001).
[28] J. Gottschalck and B. Hammer, J. Chem. Phys. **116**, 784 (2002).
[29] Y. Yourdshahyan and A. M. Rappe, J. Chem. Phys. **117**, 825 (2002).
[30] F. P. Cometto, P. Paredes-Olivera, V. A. Macagno, and E. M. Patrito, J. Phys. Chem. B **109**, 21737 (2005).
[31] N. Gonzalez, N. Lorente, and A. Arnau, Surf. Sci. **600**, 4039 (2006).
[32] P. Maksymovych, D. C. Sorescu, and J. T. Yates, J. Phys. Chem. B **110**, 21161 (2006).
[33] R. Mazzarello, A. Cossaro, A. Verdini, R. Rousseau, L. Casalis, M. F. Danisman, L. Floreano, S. Scandolo, A. Morgante, and G. Scoles, Phys. Rev. Lett. **98**, 016102 (2007).
[34] J. Wang and A. Selloni, J. Phys. Chem. C **111**, 12149 (2007).
[35] A. Nagoya and Y. Morikawa, J. Phys.: Condens. Matter **19**, 365245 (2007).
[36] Y. Morikawa, C. C. Liew, and H. Nozoye, Surf. Sci. **514**, 389 (2002).
[37] L. M. Molina and B. Hammer, Chem. Phys. Lett. **360**, 264 (2002).
[38] A. Cossaro, R. Mazzarello, R. Rousseau, L. Casalis, A. Verdini, A. Kohlmeyer, L. Floreano, S. Scandolo, A. Morgante, M. L. Klein, and G. Scoles, Science **321**, 943 (2008).
[39] P. Maksymovych, D. C. Sorescu, and J. T. Yates, Phys. Rev. Lett. **97**, 146103 (2006).
[40] Y. Wang, N. S. Hush, and J. R. Reimers, J. Am. Chem. Soc. **129**, 14532 (2007).
[41] N. A. Kautz and S. A. Kandel, J. Am. Chem. Soc. **130**, 6908 (2008).
[42] C. Vericat, G. Andreasen, M. E. Vela, H. Martin, and R. C. Salvarezza, J. Chem. Phys. **115**, 6672 (2001).
[43] M. Schneeweiss, H. Hagenström, M. Esplandi, and D. Kolb, Appl. Phys. A: Mater. Sci. Process. **69**, 537 (1999).
[44] R. Mahaffy, R. Bhatia, and B. J. Garrison, J. Phys. Chem. B **101**, 771 (1997).
[45] K.-Y. Kwon, K. L. Wong, G. Pawin, L. Bartels, S. Stolbov, and T. S. Rahman, Phys. Rev. Lett. **95**, 166101 (2005).
[46] M. J. Ford, R. C. Hoft, and J. D. Gale, Mol. Simul. **32**, 1219 (2006).
[47] G. E. Poirier and E. D. Pylant, Science **272**, 1145 (1996).
[48] I. Doudevski, W. A. Hayes, and D. K. Schwartz, Phys. Rev. Lett. **81**, 4927 (1998).
[49] H. Kondoh, C. Kodama, H. Sumida, and H. Nozoye, J. Chem. Phys. **111**, 1175 (1999).
[50] D. K. Schwartz, Annu. Rev. Phys. Chem. **52**, 107 (2001).
[51] S. J. Stranick, M. M. Kamna, and P. S. Weiss, Science **266**, 99 (1994).
[52] J. S. Raut and K. A. Fichthorn, J. Chem. Phys. **108**, 1626 (1998).
[53] J. Weckesser, J. V. Barth, and K. Kern, J. Chem. Phys. **110**, 5351 (1999).
[54] J. V. Barth, Surf. Sci. Rep. **40**, 75 (2000).
[55] J. Weckesser, J. V. Barth, and K. Kern, Phys. Rev. B **64**, 161403(R) (2001).
[56] M. Schunack, T. R. Linderoth, F. Rosei, E. Lægsgaard, I. Stensgaard, and F. Besenbacher, Phys. Rev. Lett. **88**, 156102 (2002).
[57] R. Otero, F. Hümmelink, F. Sato, S. B. Legoas, P. Thostrup, E. Laegsgaard, I. Stensgaard, D. S. Galvao, and F. Besenbacher, Nature Mater. **3**, 779 (2004).
[58] S. Subramanian and J.-C. Wang, J. Chem. Phys. **123**, 014706 (2005).
[59] J. V. Barth, Annu. Rev. Phys. Chem. **58**, 375 (2007).
[60] G. Pawin, K. L. Wong, K.-Y. Kwon, R. J. Frisbee, T. S. Rahman, and L. Bartels, J. Am. Chem. Soc. **130**, 15244 (2008).
[61] R. Otero, F. Rosei, and F. Besenbacher, Annu. Rev. Phys. Chem. **57**, 497 (2006).
[62] T. Tansel and O. M. Magnussen, Phys. Rev. Lett. **96**, 026101 (2006).
[63] G. Kresse and J. Hafner, Phys. Rev. B **47**, 558 (1993).
[64] G. Kresse and J. Hafner, Phys. Rev. B **49**, 14251 (1994).
[65] G. Kresse and J. Furthmüller, Comput. Mater. Sci. **6**, 15 (1996).
[66] G. Kresse and J. Furthmüller, Phys. Rev. B **54**, 11169 (1996).
[67] J. P. Perdew, J. A. Chevary, S. H. Vosko, K. A. Jackson, M. R. Pederson, D. J. Singh, and C. Fiolhais, Phys. Rev. B **46**, 6671 (1992).
[68] P. E. Blöchl, Phys. Rev. B **50**, 17953 (1994).
[69] G. Kresse and D. Joubert, Phys. Rev. B **59**, 1758 (1999).
[70] H. J. Monkhorst and J. D. Pack, Phys. Rev. B **13**, 5188 (1976).
[71] M. Fuchs, M. Bockstedte, E. Pehlke, and M. Scheffler, Phys. Rev. B **57**, 2134 (1998).
[72] Y. Wang, N. S. Hush, and J. R. Reimers, Phys. Rev. B **75**, 233416 (2007).
[73] C. E. Bach, M. Giesen, H. Ibach, and T. L. Einstein, Phys. Rev. Lett. **78**, 4225 (1997).
[74] G. H. Vineyard, J. Phys. Chem. Solids **3**, 121 (1957).
[75] H. Jónsson, G. Mills, and K. W. Jacobsen, *Classical and Quantum Dynamics in Condensed Phase Simulations* (World Scientific Press, Singapore, 1998), Chap. Nudged Elastic Band Method for Finding Minimum Energy Paths of Transitions, p. 385.
[76] G. Henkelman, B. Uberuaga, and H. Jónsson, J. Chem. Phys. **113**, 9901 (2000).

[77] G. Henkelman and H. Jónsson, J. Chem. Phys. **113**, 9978 (2000).
[78] The implementation of the CI-NEB scheme and other transition state search algorithms into the VASP program has been done by several people who were in or are associated with H. Jónssons group and G. Henkelmans group. The source code is available under http://theory.cm.utexas.edu/henkelman.
[79] G. Henkelman, A. Arnaldsson, and H. Jónsson, J. Chem. Phys. **124**, 044706 (2006).
[80] D. M. Ceperley and B. J. Alder, Phys. Rev. Lett. **45**, 566 (1980).
[81] J. P. Perdew and A. Zunger, Phys. Rev. B **23**, 5048 (1981).
[82] Y. Cao, Q. Ge, D. J. Dyer, and L. Wang, J. Phys. Chem. B **107**, 3803 (2003).

4.2 First-principles study of 1,4-butanedithiol molecules and radicals adsorbed on unreconstructed Au(111) and Au(100) (published)

4.2.1 Synopsis

Many experimental research projects have been conducted to further the understanding of sulfur bonded molecules like alkanedithiols on metal surfaces. In experiment adsorption phases of alkanedithiols at different adsorbate coverages on the Au(111) surface have been analyzed: a saturation coverage phase comprised of a full monolayer of standing-up alkanedithiols with one S-Au bond and a submonolayer coverage phase of lying-down adsorbates with two S-Au bonds, see Sec. 1.2. Alkanedithiols with two bonds to a metal substrate surface may serve as model systems for molecular diffusion. The diffusion characteristics of molecules with two bonds to the substrate have been found to differ substantially from simple adatom hopping models, see Sec. 2.2.2. An important prerequisite to unravel the diffusion properties of molecules on surfaces is to study their low total-energy adsorption configurations. So far, however little is known about the details of alkanedithiol adsorption on Au surfaces from a theoretical standpoint. Here, BDTRs bonded to the unreconstructed Au(111) and Au(100) surfaces have been studied as a model system for molecular adsorption and as a precursor study for diffusion. The results have been published in Ref. 84.

Before the results for the adsorption of BDTs and BDTs on unreconstructed Au(111) and Au(100) surfaces are summarized, it is instructive to review free BDT and BDTR. In vacuum the ground state geometries of BDT and BDTR are planar structures, in which the S and C atoms are located (approximately) on a common plane, see Fig. 4.3. The calculated ground state is consistent with theoretical results published in the NIST database.[264] When BDT or BDTR adsorb on a Au surface, the planar structure will most probably not be conserved. Instead, both the molecule and the radical will be distorted. Such distortions comprise, e.g. conformational changes of BDT and BDTR. The change in total energy with respect to the planar ground state structure due to rotations of one part of BDT around C-C bond axes are depicted in Fig. 4.4. Depending on the relative orientation of the different atoms within the molecule, the BDT total energy changes as a function of the internal rotational angle and increases by as much as approximately 0.2 eV for a 180° rotation. The change in total energy associated with such conformational changes is approximately independent of the particular choice of the C-C bond rotational axis. Furthermore, it appears intuitive to suggest that a conformation change of BDTR, which has not been calculated, will result in a similar change of the total energy.

Deposition of BDT from the gas phase or dilute solution on the Au(111) and Au(100)

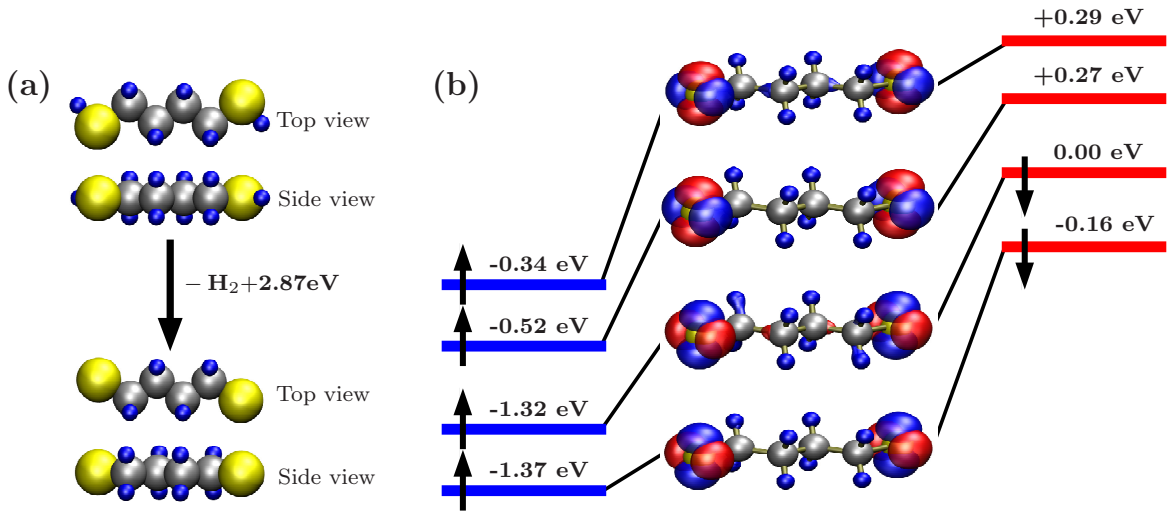

Figure 4.3: Dissociation reaction (including zero-point energy corrections) of BDT, HS-$(CH_2)_4$-SH, to form a BDTR, $\cdot$S-$(CH_2)_4$-S$\cdot$, in the gas phase. (b) Electronic structure of a spin-polarized butanedithiol radical. The energy eigenvalues of molecular orbitals within at least ± 2.4 eV of the HOMO are presented. The energy-zero has been set to the eigenvalue of the HOMO. Contours of constant spin density of the molecular Kohn-Sham orbitals are depicted for spin-majority (blue) and spin-minority states (red).

surfaces calls for a discussion of the fate of the thiol groups (HS-) upon adsorption. In particular, the question arises whether or not the strong S-H bonds are cleaved and chemisorbed BDTR is the predominant adsorbate on the surface. From a comparison of BDT and BDTR adsorption on the Au(111) and Au(100) surfaces within a lattice gas model, which includes entropic contributions, it has been found that at all considered submonolayer coverages BDTR should be the dominant species on the Au(111) and Au(100) surfaces in thermodynamic equilibrium.

The potential energy surface (PES) of chemisorbed BDTR on Au(111) and Au(100) surfaces results from the interplay between internal degrees of freedom and the formation of two strong S-Au chemisorption bonds. An analysis of the HOMO and LUMO states of BDTR yields important information about the prevailing bonding mechanism behind the S-Au bonds, see Fig. 4.3. Similar to gas phase SCH_3 discussed in the previous Section, the HOMO and LUMO are located at the S atoms and mainly derive from $3p$ orbitals of the S atoms. The HOMO and LUMO are both oriented in a direction perpendicular to the S-C axes. Hence, upon adsorption of BDTR on Au(111) and Au(100) surfaces, the S-C bonds will either adopt a tilt angle with respect to the surface normal or adopt an upright configuration similar to low total energy adsorption configurations of single SCH_3 radicals. In this way the reactive molecular orbitals may point approximately in the direction of Au surface atoms. This in turn will induce distortions of the BDTR due to the coexistence of two S-Au chemisorption bonds. In case of BDT molecules

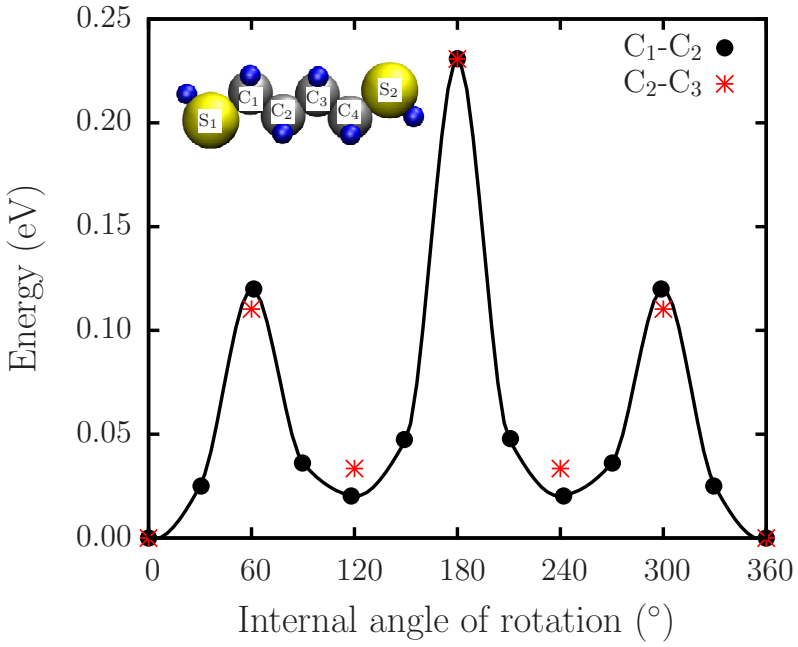

Figure 4.4: Change of the total energy versus the internal angle of rotation of conformational changes of a BDT molecule. The inset depicts the labeling of the atomic groups within the molecule. The data for an internal rotation of the S_1 and C_1 groups around the C_1-C_2 axis (black dots) have been obtained from a DFT CI-NEB calculation. The rotation of the S_1, C_1, and C_2 groups around the C_2-C_3 axis has been obtained from a DFT NEB calculation. The spline interpolation of the data is a guide to the eyes.

the S atom derived LUMO orbitals are saturated by H atoms forming strong S-H thiol bonds (see Fig. 4.3) and non-dissociative adsorption of BDT/Au is most probably best described in terms of weak physisorption.

The survey of BDT and BDTR adsorption on the unreconstructed Au(111) and Au(100) surfaces has been aimed at addressing a set of key issues. As a prerequisite for a survey of the diffusion properties of BDTR/Au (local) total energy minima on the PES have been identified. It has been found that chemisorption of BDTR differs fundamentally from chemisorption of short alkane(mono)thiols on both considered Au surfaces. Low total-energy chemisorption configurations comprise lying-down BDTR with two S-Au bonds and an alkane chain which is oriented approximately parallel to the surface, see Fig. 4.5. The chemisorption energies for the ground state geometries on the Au(111) and Au(100) surface amount to approximately -3.3 eV and -4.0 eV, respectively, in case of a coverage of one BDTR per (4×3) surface unit cell.[84] The value of the binding energy depends significantly on the adsorbate coverage. The presence of a

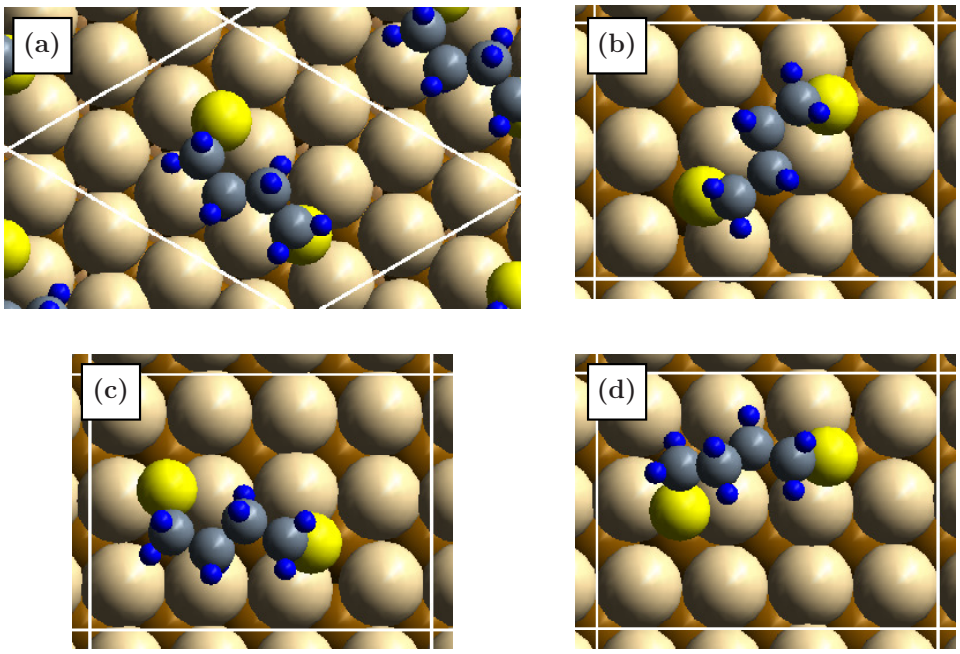

Figure 4.5: Calculated lowest-energy configurations for BDTR on the unreconstructed Au(111) (a) and Au(100) (b)-(d) surfaces. The configurations (b), (c), and (d) are considered to be energetically degenerate due to very small total energy differences between them. The chemisorption energies amount to approximately -3.3 eV for configuration (a) and -4.0 eV for the configurations (b)-(d). Au atoms of the first layer: light brown, second layer: dark brown, third layer: brown, S atoms: yellow, C atoms: gray, H atoms: blue. The Figures have been taken from Ref. 84.

second adsorbate-substrate bond together with internal conformational degrees of freedom leads to a complicated multivalley PES. The PESs on Au(111) and Au(100) exhibit many local minima which are only within a few 100 meV of the lowest total energy configuration.[84] In particular on the Au(100) surface, the three energetically most favorable chemisorption configurations are degenerate to within the accuracy of the calculations. These results suggest BDTR/Au diffusion characteristics which are much more multifaceted than the diffusion of SCH_3 radicals and $Au(SCH_3)_2$ complexes described in the previous Section.

In a recent publication (Ref. 85 published 16.04.2010, this work Ref. 84 published 08.02.2010) Carro *et al.* have studied the adsorption of BDTR on the unreconstructed Au(111) surface for densely packed lying-down adsorbates. The considered coverage of 1/8 (one BDTR per eight Au surface atoms) is higher than the coverages ($<1/12$) in this work. Carro *et al.* have reported a ground state chemisorption geometry of BDTR/Au(111) which differs from the ground state geometry obtained in this work mainly by an internal rotation of the alkane chain and a slight shift of the S atoms.

By re-calculating the geometry suggested by Carro *et al.* for a coverage of 1/16 it has been found that the ground state geometry calculated in this work (see Fig. 4.5) is approximately 0.1 eV more favorable. For densely packed BDTR adsorbates in the configuration suggested by Carro *et al.* , the geometry suggested by the authors of Ref. 85 is energetically only very slightly more favorable compared to Fig. 4.5a by approximately 0.01 eV.

Finally, constant current and constant height STM images have been simulated for BDTR/Au(111) within the Tersoff-Hamann model to be able to get into contact with future experiments. The images show elongated bright features at the position of the alkane chain. The long axis of these features is slightly tilted with respect to $\langle 1\bar{1}0 \rangle$ directions on the surface. In a publication by Leung *et al.* the lying-down striped phase of 1,6-hexanedithiol on a Au(111) surface has been characterized by STM measurements and complementing experimental techniques.[66] They have suggested that the adsorbates line up along high symmetry directions of the Au(111) surface and that the C-C-C planes of the adsorbates are approximately parallel to the substrate. The long axis of the bright protrusion in the STM images point approximately in $\langle 1\bar{1}0 \rangle$ directions. It is suggested that these protrusions originate from rows of S-atoms of two adjacent molecules in the densely packed structure. In view of the simulated STM images of BDTR/Au(111), this interpretation might have to be reconsidered. Even though Leung *et al.* have studied a slightly longer alkanedithiol, it is encouraging that their result concerning the orientation of the alkanedithiol on the surface is compatible with the DFT result for BDTR/Au(111) presented here.

4.2.2 Publication Physical Review B 81, 075409 (2010), Copyright (2010) by the American Physical Society

First-principles study of 1,4-butanedithiol molecules and radicals adsorbed on unreconstructed Au(111) and Au(100)

A. Franke* and E. Pehlke

Institut für Theoretische Physik und Astrophysik, Christian-Albrechts-Universität zu Kiel, 24098 Kiel, Germany

(Received 15 September 2009; revised manuscript received 5 January 2010; published 8 February 2010)

Ongoing experimental research effort is devoted to further the understanding of the adsorption of dithiol molecules on gold surfaces with promising technological applications. To elucidate the subject from a theoretical perspective, we study the submonolayer adsorption of 1,4-butanedithiol molecules and radicals on the unreconstructed Au(111) and Au(100) surfaces using density-functional theory. From the calculated local energy minima the lowest-energy configurations are selected. The alkane chains are roughly parallel to the surface, such that two sulfur-gold adsorbate-substrate bonds can form. On the unreconstructed Au(100) surface dissociation of butanedithiol molecules into H_2 in the gas phase and butanedithiol radicals chemisorbed on the surface is energetically preferred. The two sulfur atoms of the radical adopt hollow-bridge-like positions. On the unreconstructed Au(111) surface the S-H bonds are predicted to be cleaved due to entropic effects. In the ground-state configuration the two sulfur atoms of the butanedithiol radical adopt an fcc hollow and an fcc hollow-bridge position on the surface. Hence, we expect butanedithiol radicals to be the prevailing adsorbed species on both investigated gold surfaces. STM-images of the ground-state configuration of butanedithiol radicals chemisorbed on Au(111) have been simulated within the Tersoff-Hamann model. They show elongated bright features above the location of the alkane chain. The long axis is slightly tilted with respect to the $\langle 1\bar{1}0\rangle$ directions. Finally, a semiempirical approach has been evaluated to investigate the effect of van der Waals interactions to the binding energies calculated within GGA-DFT.

DOI: 10.1103/PhysRevB.81.075409 PACS number(s): 68.43.Bc, 68.43.Fg, 82.65.+r, 64.75.Yz

I. INTRODUCTION

The pursuit of miniaturization in fields such as microelectronics and biosensor technology has lead to an increased interest in functionalized metal or semiconductor surfaces.[1] The synthesis of organic molecular assemblies at the surface is a widely utilized method to achieve such a functionalization.[1,2] Organic molecules offer the prospect of tailor-made functionalizations by choosing specific end groups of the adsorbates.[2] Prominent examples include the fabrication of switchable molecular assemblies on the surface.[3–11]

Among the most widely studied systems are self-assembled monolayers (SAMs) of sulfur bonded thiol molecules at Au surfaces. In particular, SAMs of alkanedithiols in which one of the thiol groups is adsorbed on the surface while the other is pointing away from the surface, are considered promising building blocks of future nanodevices.[12–15] The thiol group at the top of the alkane chain offers the possibility to serve, e.g., as an anchor for cadmium-selenide nanocrystals in single electron transistors (Ref. 12), metal contacts in molecular dithiol junctions (Refs. 13, 14, and 16–20), metal and metal-oxide clusters (Ref. 21–28), as well as metallic thin films (Refs. 29 and 30). From a fundamental point of view, alkanedithiols are regarded as an important model system for organic sulfur bonded molecules.[2,15]

In recent years intense experimental research effort is devoted to the adsorption of different dithiol molecules on the Au(111) surface under ultra high vacuum (UHV), ambient as well as electrochemical (EC) conditions.[19,31–41] However, the details of metastable adsorption phases and equilibrium structures remains controversial. The existence of two thiol groups within the molecule raises the question whether dithiol molecules bind via one (upright configuration) or two (lying-down configuration) Au-S bonds to the surface. In case of the most common deposition methods either from the gas phase or from solution both upright (Refs. 19, 32, 36, 37, and 42) and lying-down configurations (Refs. 19, 32–37, and 43) were observed. It was reported that dithiol molecules can polymerize upon adsorption on the surface forming multilayers of molecules connected through S-S bonds.[38–41,44,45] Furthermore, butanedithiol adsorbates have been observed in video scanning tunneling microscopy experiments at low and saturation coverages under EC conditions on the unreconstructed Au(111) surface.[46]

The adsorption configurations of upright and lying-down alkanedithiol molecules at Au surfaces thus call for detailed density-functional studies. The focus of our present work is to compare the adsorption of 1,4-butanedithiol molecules [BDT: HS-$(CH_2)_4$-SH] and BDT radicals [BDTR: ·S-$(CH_2)_4$-S·] at submonolayer coverages on the unreconstructed Au(111) and Au(100) surfaces. Polymerization of BDT molecules or radicals is beyond the scope of the present work. Adsorption properties on unreconstructed Au surfaces are relevant in case of EC conditions, where a potential-induced lifting of the Au(111) and Au(100) surface reconstructions can be achieved.[47,48]

The BDT and BDTR adsorption configurations on Au(111) and Au(100) surfaces reported below currently serve as a starting point for the investigation of the BDT and BDTR diffusion dynamics. In our view, this knowledge is indispensable to a deeper understanding of self assembly at Au surfaces and the diffusion of molecular adsorbates with one or two sulfur bonds to the Au surface.[49–63]

The present paper is organized in the following manner. Section II summarizes the calculational details of our work.

In Secs. III A 1 and III A 2 we present adsorption configurations of the BDT molecule and radical on the unreconstructed Au(111) surface. Adsorption of BDT molecules and radicals on the Au(100) surface is discussed in Secs. III B 1 and III B 2. In order to assess the importance of surface defects, we consider the adsorption of BDT radicals in the presence of adatoms and vacancies on the Au(111) surface in Sec. III A 3 and on the Au(100) surface in Sec. III B 3. Sections III A 4 and III B 3 are devoted to the question whether BDT adsorbs as molecules or radicals on the Au(111) and Au(100) surface. Simulated scanning tunneling microscopy (STM) images are reported in Sec. III A 5.

II. CALCULATIONAL METHOD

Relaxed adsorption configurations for BDT and BDTR on the unreconstructed Au(111) and Au(100) surfaces have been calculated within density-functional theory using slab geometries. First we choose a set of initial configurations, which are relaxed to local chemisorption energy minima. The initial configurations differ by the positions of the two sulfur atoms with respect to the underlying substrate and the conformation of the adsorbed BDT molecule or radical. To reduce computational costs, the convergence criteria have been alleviated for this survey. We select the lowest-energy structures from this survey and recalculate the total energies for frozen-in atomic coordinates at increased values for plane-wave cutoff energy, number of **k** points, and number of bulklike Au layers in the slab. We have verified that the ordering with respect to chemisorption energy is not affected (see Appendix C).

The total energy of the electronic ground state has been calculated using the Vienna *ab initio* simulation program (VASP) (Refs. 64–67) developed at the Institut für Materialphysik of the Universität Wien which is based on density-functional theory. The generalized gradient approximation (GGA) by Perdew and Wang (PW91) (Ref. 68) is applied to the exchange-correlation functional and the electron-ion interaction is treated within the framework of Blöchl's projector augmented wave method (PAW).[69,70] The potentials for VASP from the database are used.[70]

The periodically repeated gold slabs are separated by a vacuum region of at least 12 Å. Asymmetric slabs have been chosen, i.e., the adsorbate binds to a single side of the slab only. A dipole correction is applied in order to account for the work function difference between the opposite surfaces of the slab.

The initial survey has been carried through with slabs comprising 4 layers of gold and a (4×3) or (4×4) surface unit cell. The Kohn-Sham wave functions are expanded in a plane-wave basis set with a cutoff energy of 250 eV. Plane waves up to an energy of 750 eV are used to represent the augmentation charges. The integrals over the Brillouin zone are approximated by sums over special **k** points (Ref. 71) using meshes consisting of 12 and 9 **k** points in the complete first Brillouin zone of the (4×3) and (4×4) surface unit cell, respectively. The **k**-point meshes are equivalent.

The gold atoms in the outermost three layers on the adsorbate side of the slab as well as all adsorbate atoms are relaxed without constraints until the residual force per atom is smaller than 0.005 eV/Å. The remaining layers of the slab are kept fixed at their ideal bulk positions. All slabs have been set up using a theoretical lattice constant of 4.18 Å. The slight overestimate compared to the experimental value of 4.08 Å is consistent with other density-functional calculations, e. g., for noble metals using GGA functionals.[72,73]

The final absolute chemisorption energies of BDT or BDTR configurations on Au(111) are calculated for a slab geometry comprising 9 layers of gold and a (4×3), (4×4), (4×6), (6×3), or (6×6) surface unit cell. The **k**-point meshes in the complete first Brillouin zone comprise 48, 36, 24, 32, and 16 special **k** points, respectively.[71] In case of BDT or BDTR on Au(100), the slab comprises 12 atomic layers and a (4×3), (4×4), or (6×6) surface unit cell. The **k**-point meshes in the complete first Brillouin zone comprise 48, 36, and 16 special **k** points, respectively. In both cases, the Kohn-Sham wave functions are expanded in a plane-wave basis set with a cutoff energy of 340 eV, and 1000 eV cutoff for the augmentation charge.

The convergence with respect to cutoff energy, **k**-point sampling, number of relaxed substrate layers and total number of substrate layers has been subject to systematic convergence tests as reported in Appendix C. In summary, the overall error of the reported absolute values of the binding energies with respect to these convergence parameters amounts to approximately 0.1 eV. The total-energy differences between chemisorption configurations are less susceptible to the choice of these parameters. The error induced by the use of the approximate PW91 exchange-correlation energy functional is not included in this estimate. The coverage dependence of the BDT or BDTR chemisorption energies (corresponding to different sizes of the surface unit cell) depends on surface orientation and will be detailed in Appendix B.

The program P4VASP (Ref. 74) has been used to visualize all atomic configurations and STM-images calculated within the Tersoff-Hamann approach.[75]

Finally, we have applied semi-empirical dispersion corrections in order to investigate the effect of van der Waals (vdW) corrections to the binding energies calculated within PW91-DFT.[76–78] Exchange-correlation functionals accounting for dispersion-interactions[79] are beyond the scope of the present paper. The semiempirical vdW correction is cut off at short range using a Fermi-function while the long range vdW interaction of atoms i and j is described by $s_6 C_{6,ij}/R_{ij}^6$.[77] In the literature s_6 has been chosen differently for different exchange-correlation functionals.[77] Here we have taken $s_6=0.75$, which is the value suggested by Grimme[77] in case of the closely related PBE exchange-correlation functional. The C_6 parameters are calculated from experimental atomic polarizabilities and ionization energies[108] by means of the London formula.[78,80] Experimental vdW-radii[109] are used to define a scale for the interatomic distances that enter the Fermi cutoff function.[81,82]

How to obtain an appropriate choice of above constants for the vdW interaction is certainly an issue, apart from the question how well the approach is suitable for metal surfaces. Recently Tkatchenko *et al.* proposed a method of deriving C_6 coefficients and vdW radii for atoms in molecules,

which results in smaller values for the C_6 coefficients and larger vdW radii.[76] To obtain a rough impression of the effect associated with such a variation of the parameters that control the vdW interaction, we artificially decreased the C_6 coefficients by approximately 20% and concomitantly increased the vdW radii between 20% and 50%. The variation of the vdW correction with respect to these parameter changes will be discussed in the main part of this work. To test the consistency of our vdW parameters we have applied them to the case of benzene adsorbed on Au(111). We found the adsorption energies for our original parameter set, and the scaled parameter set described above, to vary over about the same range of adsorption energies as the data presented by McNellis *et al.*.[83]

III. RESULTS AND DISCUSSION

A. Adsorption on Au(111)

The search for the ground-state adsorption configurations of BDT molecules and radicals is an important and indispensable prerequisite for any investigation concerning the growth properties of the adsorbed species. Beyond that, a detailed knowledge of competing configurations which are within a few k_bT of the ground state is almost equally important to facilitate a thorough study of diffusion.

In order to assess whether adsorbed BDT binds to the Au(111) surface as molecules or dissociates into BDTR and H_2, the chemisorption energy and ground-state configuration of both BDT and BDTR need to be calculated. Hence, in the following sections we discuss the submonolayer adsorption of BDT molecules and radicals on the defect-free, unreconstructed Au(111) surface. As previous DFT-studies of monothiol adsorption have revealed the importance of surface defects (Refs. 84–86), we present calculations for adsorbed BDT radicals in the presence of Au adatoms or surface vacancies.

1. Adsorption of BDT molecules on defect-free Au(111)

Local total-energy minima and the corresponding binding energies have been calculated for BDT adsorbed on the unreconstructed, but relaxed, Au(111) surface. A set of five initial configurations has been relaxed to local energy minima. The initial configurations differ by the number of S-Au bonds, which can be either one or two in case of BDT lying parallel to the surface, and the choice of the Au surface atoms to which the S atoms bind on top. Bonding to Au(111) hollow sites is expected to be of minor importance. A DFT-study conducted by Maksymovich *et al.* has shown that the HS-Au bond strength of methanethiol molecules $HSCH_3$ at Au(111) hollow sites is at least 0.24 eV less favorable compared to bonding atop Au surface atoms.[87]

The strength of the molecule-surface bond has been calculated as the difference between the total energy of the adsorbate-substrate system and the sum of the total energies of the unreconstructed Au(111) surface and BDT in the gas phase,

$$E_b = E_{\text{total}}\{\text{BDT/Au(111)}\} - E_{\text{total}}\{\text{Au(111)}\} - E_{\text{total}}\{\text{BDT}\}. \quad (1)$$

In the energetically most favorable adsorption geometry for one molecule per (4×3) surface unit cell, the BDT adopts a lying-down configuration in which the alkane chain is slightly bent and the C-C-C planes of the molecule are oriented approximately parallel to the surface, see Figs. 1(a) and 1(b). Both sulfur atoms are close to Au on-top positions. The molecule-surface DFT-PW91 binding energy is calculated to be $E_b=-0.45$ eV. The zero-point energy correction is not included. Relaxed structural parameters of BDT are summarized in Table I.

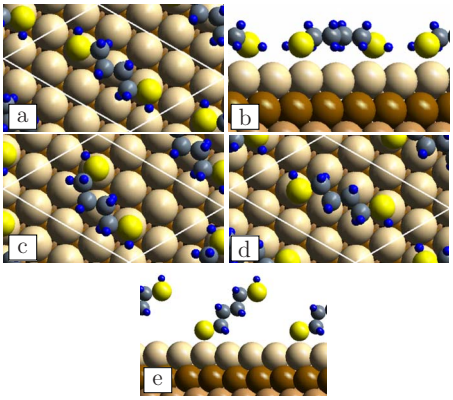

FIG. 1. (Color online) Top view (a) and side view (b) of the BDT ground-state configuration with the lowest calculated energy per (4×3) surface unit cell on the unreconstructed Au(111) surface (DFT-PW91 binding energy $E_b=-0.45$ eV). Competing stable configurations are shown for comparison: (c) $E_b=-0.40$ eV, (d) $E_b=-0.38$ eV, and (e) $E_b=-0.35$ eV. The surface unit cell is indicated by white lines.

Energetically slightly less favorable configurations with the alkane chain oriented parallel to the surface are shown in Figs. 1(c) and 1(d) for comparison. The energy difference with respect to the structure with the lowest calculated energy amounts to only 0.05 and 0.07 eV, respectively.

The semiempirical vdW correction to the binding energy at a coverage of one BDT per (4×3) surface unit cell amounts to −1.43, −1.36, and −1.33 eV for the configurations depicted in Figs. 1(a), 1(c), and 1(d), respectively. Using the artificially scaled vdW-radii together with the smaller C_6 coefficients, we obtain vdW corrections of −0.71 eV almost equal for all three configurations. If the intermolecular contribution to the vdW interaction is omitted from the summation, above semiempirical vdW correction to the binding energy amounts to −1.07, −1.03, and −1.09 eV in case of the original vdW parameters. These data indicate the range of values obtained for the vdW interaction when the empirical approach is applied. Most importantly, we note that the ground-state configuration does not change when the vdW energy is added to the DFT total energy.

We point out that, based on comparison to experiment, we distrust the absolute value of the vdW correction to the binding energy. Lavrich *et al.* conducted TDS experiments for adsorbed alkanethiols and alkanedithiols with varying alkane chain lengths on the Au(111) surface.[88] They observe two peaks in the TDS spectrum for BDT. The peak at lower desorption temperature is attributed to physisorbed BDT molecules, with a desorption energy barrier of 0.85 eV. Neglecting the small zero-point corrections, our estimated binding energy including semiempirical vdW corrections of −1.9 eV

TABLE I. Structural parameters and binding energies for BDT configurations on the unreconstructed Au(111) surface as depicted in Fig. 1. E_b is the DFT-PW91 binding energy per molecule defined in Eq. (1), $d_{S\text{-}S}$ is the distance between the S atoms, $d_{S\text{-}Au}$ are the S-Au bond lengths, and $d_{Au\text{-}Au}$ is the distance between the Au atoms to which the BDT binds. The value in parenthesis is the equilibrium distance between the respective Au atoms on the surface.

Configuration	Cell size	E_b (eV)	$d_{S\text{-}S}$ (Å)	$d_{S\text{-}Au}$ (Å)	$d_{Au\text{-}Au}$ (Å)
a	(4×4)	−0.50	6.67	2.75, 2.75	5.91 (5.91)
a	(4×3)	−0.45	6.68	2.78, 2.79	5.92 (5.91)
c	(4×3)	−0.40	5.48	2.76, 2.80	5.08 (5.12)
d	(4×3)	−0.38	6.87	3.00, 2.93	7.74 (7.81)
e	(4×3)	−0.35	6.95	2.67	
BDT (gas)			6.89		

(−1.2 eV in case of the artificially scaled vdW parameters) is substantially larger than above experimental desorption energy barrier. Apparently, the semiempirical equation overestimates the vdW correction in case of BDT/Au. Furthermore, Lavrich *et al.* estimated the contribution to the binding energy per CH_2-group of the alkane chain to yield approximately −64 meV.[88] We arrive at a vdW contribution to the binding energy of −0.2 eV (about −0.1 eV in case of the artificially scaled vdW parameters) per CH_2 group of the BDT molecule, which is considerably larger than the experimental estimate. Again, the vdW correction appears to be overestimated by the present semiempirical approach. The issue of the contribution from the vdW interaction to the binding energy is still an open question for molecules with alkane chains on metal surfaces. For clarity we will henceforth quote the unaltered DFT-PW91 binding energies in this paper.

Besides lying-down configurations an upright configuration has been calculated in which the alkane chain and one of the HS groups are pointing away from the surface [see Fig. 1(e)]. In this configuration only one S atom is located atop a Au surface atom forming an HS-Au bond with a binding energy of E_b=−0.35 eV. The tilt angle of the S-S axis with respect to the surface normal amounts to 56°. A rotation of the molecule around the surface normal through the S-Au bond has not been calculated because we expect the variation of the total energy with azimuthal angle to be insignificant. This we conclude from the work by Maksymovich *et al.* who considered the rotation of $HSCH_3$ molecules that bind to Au(111) in an atop configuration and who found an energy variation with azimuthal angle on the order of only 5 meV.[87] We will refer to the configuration shown in Fig. 1(e) as on-top upright.

We are not aware of other theoretical studies of adsorbed BDT molecules on Au(111) that we could directly compare to. There are, however, DFT calculations for the adsorption of methanethiol molecules $HSCH_3$ on Au(111).[87] The authors of Ref. 87 report an adsorption geometry for the $HSCH_3$ molecule that is similar to the on-top upright configuration of the BDT molecule with respect to the positions of the corresponding H, S, and C atoms. For the energetically most favorable structure, the calculated binding energy per $HSCH_3$ molecule is reported to be −0.37 eV and the S-Au bond length is reported to be 2.668 Å.[87] Within the accuracy of our calculations, both quantities agree with the respective values for the on top-upright configuration (see Table I). Lavrich *et al.* estimate the universal contribution of the SH group to the binding enthalpy for alkanethiols with varying lengths to be −0.35 eV from TDS experiments.[88] Neglecting zero-point corrections and omitting the semi-empirical vdW contributions to the HS-Au bond, this value is consistent with the calculated HS-Au bond strength from Ref. 87 and our bond strength for BDT in the on-top upright configuration.

2. Adsorption of BDT radicals on defect-free Au(111)

We calculate the adsorption of BDTR on the Au(111) surface in the absence of surface defects. The search for the ground-state configuration is complicated by intramolecular conformational degrees of freedom and the availability of two S-Au bonding sites which can result in many stable configurations being close-by in energy. Therefore, as many as 20 initial configurations have been relaxed to local total-energy minima. Since it is well established within DFT that the sulfur atoms of alkanethiol-radicals bind to the defect-free, unreconstructed Au(111) surface in the vicinity of Au(111) hollow sites (Refs. 60, 61, and 89–100), the initial configurations have been chosen such that both sulfur atoms are located either close to fcc-or hcp-hollow sites. This approach is supported by the fact that a configuration with both S atoms at Au(111) on-top sites proved to be unstable. For the majority of configurations the C atoms of the alkane chain are approximately located in a plane parallel to the Au(111) surface. This corresponds to the energetically most favorable conformation of free BDTR. In addition, three initial configurations with other conformations of BDTR have been chosen. Throughout this section the spin-polarized ground state of BDTR in vacuum is chosen as the energy reference $E_{total}^{spin}\{BDTR\}$ [see Eq. (1)].

Finally, a configuration with an inclined alkane chain and with only a single S-Au bond was calculated. The S atom is located at an fcc-bridge position. After relaxation, the binding energy amounts to −1.9 eV. This is consistent with the binding energy for adsorbed SCH_3 radicals on the unreconstructed Au(111) surface.[61]

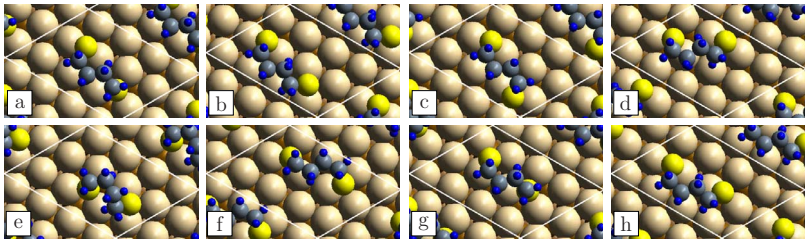

FIG. 2. (Color online) Top view of BDTR on the unreconstructed Au(111) surface. (a) Ground-state configuration with the lowest calculated binding energy (E_b=−3.26 eV) for the (4×3) and (4×4) surface unit cell. (b)–(h) Competing stable configurations with smaller absolute values of the binding energies, see Table II. The surface unit cell is indicated by white lines.

For a coverage of one BDTR per (4×3) and (4×4) surface unit cell the adsorption geometry in Fig. 2(a) yields the lowest total energy. The binding energy is E_b=−3.26 eV and E_b=−3.45 eV in case of the (4×3) and (4×4) surface unit cell, respectively. Evidently, the bond strength between BDTR and the Au(111) surface increases substantially as the coverage is decreased. We were not able to obtain the binding energy of an individual adsorbed BDTR even in case of a large (6×6) surface unit cell. This coverage dependence is attributed to strong substrate-mediated, adsorbate-adsorbate interactions, which we conclude from the data presented in Appendix B.

In the ground-state configuration both sulfur atoms bind to the substrate in the vicinity of fcc-hollow sites of Au(111). One of the S atoms is shifted by 0.57 Å toward a nearby bridge site, thus adopting a fcc-bridge position. The corresponding S-C bond is tilted with respect to the surface normal by 50°. The other sulfur atom binds at an fcc-site experiencing only a small shift of 0.06 Å toward a bridge site and a tilt of 13° of the S-C bond. Both S atoms adopt positions with respect to the substrate which resemble S-atom positions and S-C tilt angles of low adsorption-energy configurations of the SCH_3 radical on the Au(111) surface.[61]

In order to gain a deeper insight in to the nature of the BDTR-Au bond, we resort to the charge density difference $\Delta\rho(\mathbf{r})=\rho_{\mathrm{BDTR/Au(111)}}(\mathbf{r})-\rho_{\mathrm{BDTR}}(\mathbf{r})-\rho_{\mathrm{Au(111)}}(\mathbf{r})$. A distinct charge accumulation in the region between the S atoms and neighboring Au atoms is revealed which is indicative of the covalent S-Au bond formed upon adsorption. The partially filled HOMO orbitals of free BDTR are located at the S atoms and have a dominant $3p$ character. These p orbitals are oriented nearly perpendicular to the S-C bond, which favors tilted S-C bond orientations. From this we conclude, that the adsorbate-surface bond primarily originates from a hybridization of sulfur $3p$ states and substrate Au states.

The calculations reveal that the potential energy surface involves many local minima within a range of only a few 100 meV. This multivalley potential-energy landscape originates from the interplay between two S-Au adsorbate-surface bonds and the internal conformational degrees of freedom of BDTR. It differs fundamentally from the comparatively simple potential energy surface of a single SCH_3 radical which only form one S-Au bond with the Au(111) surface. An excerpt of competing stable configurations is depicted in Figs. 2(b)–2(h) and corresponding structural information is summarized in Table II. Among the calculated configurations, (a)–(f) represent the lowest-energy configurations. Interestingly, while (g) and (h) appear to have similar geometries as low-energy configurations, the absolute value of the binding energy is at least 0.18 eV smaller than for the ground-state configuration (a). A general characteristic of all calculated stable configurations is that both sulfur atoms bind to the substrate close to hollow or hollow-bridge sites.

Since it is a difficult task to locate the global minimum on a complicated potential energy surface, we provide an estimate for a lower bound of the global BDTR/Au(111) chemisorption energy in Appendix A. Altogether, we are confident that the configuration in Fig. 2(a) constitutes the ground state for submonolayer coverages of BDTR on the unreconstructed Au(111) surface. At worst, we expect it to be within a few k_BT of the global minimum at room temperature.

The semiempirical vdW correction is calculated in order to asses its impact on the conclusions drawn from relative binding energies of BDT molecules and radicals in Sec. III A 4. For the binding energy of the ground-state geometry in Fig. 2(a) it amounts to −1.33 and −1.37 eV in case of the (4×3) and (4×4) surface unit cell, respectively. Decreasing the C_6 coefficients and increasing the vdW radii as described in Sec. II yields a vdW correction of −0.68 and −0.70 eV. Notably, for both parameter sets the semiempirical vdW corrections for the BDT molecule and the BDT radical differ by less than 0.1 eV. Thus, the results presented in Sec. III A 4 based on binding energy differences between BDT molecules and BDT radicals are unaffected by the semiempirical vdW correction employed here. The same conclusions can be drawn in case of the Au(100) surface considered in Sec. III B. In order to quantify the effect of changes in bond distances due to vdW interactions on the STM-images, additional relaxations have been carried through. The ground-state configurations for BDT and BDTR on the Au(111) surface have been relaxed until the residual force per atom including the semiempirical vdW correction was smaller

TABLE II. Structural parameters and binding energies for an excerpt of calculated configurations of BDTR on the unreconstructed Au(111) surface as depicted in Fig. 2. E_b is the DFT-PW91 binding energy per radical as defined in Eq. (1) and $d_{S\text{-}S}$ refers to the distance between the S atoms. The approximate bonding sites of both S atoms are described in the last column.

Configuration	Cell size	E_b (eV)	$d_{S\text{-}S}$ (Å)	S-atom sites
a	(4×3)	−3.26	4.85	fcc-bridge, fcc
b	(4×3)	−3.25	5.48	fcc-, hcp-bridge
c	(4×3)	−3.24	5.44	fcc-, hcp-bridge
d	(4×3)	−3.23	4.81	fcc, fcc-bridge
e	(4×3)	−3.21	4.10	fcc, hcp-bridge
f	(4×3)	−3.19	5.41	fcc, fcc-bridge
g	(4×3)	−3.08	4.58	hcp, fcc
h	(4×3)	−3.05	5.28	fcc-, fcc-bridge

than 0.01 eV/Å. We observe no significant change of the calculated STM images.

3. Adsorption of BDT radicals in the presence of surface defects on Au(111)

In case of the adsorption of SCH_3 radicals on the unreconstructed Au(111) surface, geometries involving Au adatoms are found to be energetically favored compared to geometries without adatoms.[61,100–102] Furthermore, it has been reported that adsorption of $HSCH_3$ molecules at surface vacancies leads to a cleavage of the H-S bond and the formation of adsorbed alkanethiol radicals.[84–86] This has motivated us to investigate similar configurations in case of BDTR.

To assess the role of surface defects for the adsorption of BDTR, we calculate adsorption geometries involving one Au adatom and one or two surface vacancies per surface unit cell. The number of defects will be denoted by n. The binding energy per BDTR relative to the defect covered surface and a free radical is defined as

$$E_{b1} = E_{total}\{\text{BDTR}/n \cdot \text{defect/Au(111)}\} - E_{total}\{n \cdot \text{defect/Au(111)}\} - E^{spin}_{total}\{\text{BDTR}\}. \quad (2)$$

To account for defect formation, we calculate the energy of n defects at the surface,

$$E_{defect} = E_{total}\{n \cdot \text{defect/Au(111)}\} - E_{total}\{\text{Au(111)}\} - n \cdot E^{bulk}_{total}\{\text{Au}\}. \quad (3)$$

The Au chemical potential equals the energy per bulk atom $E^{bulk}_{total}\{\text{Au}\}$. Hence the binding energy per BDTR as compared to the defect-free unreconstructed Au(111) surface is

$$E_{b2} = E_{b1} + E_{defect}. \quad (4)$$

E_{b2} includes the energy expense necessary for defect formation and can be compared to the binding energies of BDTR presented in the previous subsection.

a. Adatoms. We consider a configuration in which a Au adatom is initially bound to the unreconstructed Au(111) surface at a fcc-site. A BDTR is added such that both S atoms form a bond with both the adatom and the surface. Adsorption geometries in which only one S atom binds to the adatom are energetically less favorable. Two stable configurations were calculated with the Au adatom either above a fcc-hollow or a bridge site of the Au(111) surface. The energetically most favorable configuration with the adatom above the fcc-hollow site is depicted in Fig. 3(a). The DFT-PW91 binding energy for one BDTR per (4×3) surface unit cell amounts to $E_{b1}=-3.85$ eV with respect to the adatom covered surface and $E_{b2}=-3.21$ eV with respect to the defect-free surface. Decreasing the coverage to one radical per (4×4) surface unit cell results in a slight increase of the bond strength to $E_{b1}=-3.87$ eV and $E_{b2}=-3.26$ eV. The energetical preference for adsorption at the defect-free surface amounts to 0.05 and 0.19 eV in case of the (4×3) and (4×4) surface unit cell, respectively. Hence, Au adatoms are of minor importance for submonolayer chemisorption of BDTR on the unreconstructed Au(111) surface.

b. Vacancies. The position of Au atoms which have been removed from the surface in order to create one or two vacancies are labeled 1–4 in Fig. 3(b). The depicted initial configuration of BDTR prior to relaxation corresponds to its ground-state configuration.

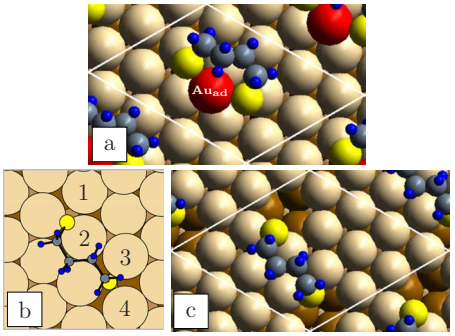

FIG. 3. (Color online) (a) Adsorption of BDTR at a Au adatom (red or dark gray) above a fcc-hollow site of the Au(111) surface ($E_{b2}=-3.21$ eV). Au atoms of the first layer: light gray or light brown, Au atoms of the second layer: dark gray or dark brown, and Au atoms of the third layer: gray or brown. (b) Schematic view of BDTR on the Au(111) surface in the ground-state configuration. Considered vacancy positions are labeled 1–4. (c) BDTR configuration with two surface vacancies at positions 1 and 4 ($E_{b2}=-3.15$ eV). The surface unit cells are indicated by white lines.

Among the considered geometries with only one vacancy, the energetically most favorable vacancy position is position 1. The DFT-PW91 binding energy as calculated in a (4×3) surface unit cell amounts to $E_{b1}=-3.81$ eV and $E_{b2}=-3.23$ eV. In case of the (4×4) surface unit cell, the binding energies are $E_{b1}=-3.88$ eV and $E_{b2}=-3.29$ eV.

BDTR configurations involving two vacancies have been calculated in a (4×4) surface unit cell in order to avoid that any two vacancies are located at nearest neighbor sites. The considered surface vacancy positions are (2,3) and (1,4). The largest absolute value of the binding energy per BDTR is obtained for vacancies at positions (1,4) as depicted in Fig. 3(c), with $E_{b1}=-4.35$ eV and $E_{b2}=-3.15$ eV.

Adsorption configurations involving one or two surface vacancies per (4×4) surface unit cell are energetically less favorable compared to adsorption at the defect-free Au(111) surface by at least 0.16 eV. Therefore, we expect that vacancies are not relevant for the submonolayer chemisorption of BDTR on the unreconstructed Au(111) surface.

4. S-H bond cleavage

The next section is devoted to the issue of BDT molecule dissociation via SH-bond cleavage and H_2 desorption into the gas phase. We make use of the DFT-PW91 binding energies of the optimum adsorption configurations of BDT and BDTR on the Au(111) surface. Thermodynamic equilibrium between BDT molecules, radicals, and hydrogen molecules in the gas phase is assumed. Metastable molecular chemisorption is not considered here.

In equilibrium, the relative abundance $p(\text{BDTR})/p(\text{BDT})$ of BDT radicals with respect to BDT molecules on the Au(111) surface is governed by the free energy difference,

$$\Delta f = [E_b\{\mathrm{BDTR}\} + f_{\mathrm{vib}}\{\mathrm{BDTR}\}] - [E_b\{\mathrm{BDT}\} + f_{\mathrm{vib}}\{\mathrm{BDT}\}] + E_{\mathrm{diss}}^{\mathrm{vac}} + [\mu_{\mathrm{H}_2}(T,p) - E_{\mathrm{total}}\{\mathrm{H}_2\}]. \quad (5)$$

$E_{\mathrm{total}}\{\mathrm{H}_2\}$ is the DFT total energy of an isolated hydrogen molecule. The dissociation of a free BDT into a BDTR and an H_2 molecule is endothermic by

$$E_{\mathrm{diss}}^{\mathrm{vac}} = E_{\mathrm{total}}\{\mathrm{BDTR}\} + E_{\mathrm{total}}\{\mathrm{H}_2\} - E_{\mathrm{total}}\{\mathrm{BDT}\}. \quad (6)$$

f_{vib} denotes the contribution per molecule to the vibrational free energy of a BDT molecule or radical adsorbed on the Au(111) surface. We approximate the difference $f_{\mathrm{vib}}\{\mathrm{BDT}\} - f_{\mathrm{vib}}\{\mathrm{BDTR}\}$ by the difference of zero-point energies of the BDT molecule and the BDT radical.

Vibrational frequencies have been determined using a finite difference approach as implemented in VASP. Atoms of the molecule are displaced by 0.025 Å in each direction of the Cartesian coordinate system. Diagonalization of the resulting approximation for the Hessian matrix yields the vibrational frequencies and the corresponding vibrational eigenmodes. For the H_2 molecule we obtain a zero-point energy of $\hbar\omega_{\mathrm{H}_2}/2 = 0.26$ eV. The difference of the zero-point energies between BDT and BDTR amounts to 0.55 eV.

The energy needed to break both S-H bonds of a free BDT is calculated to be 7.15 eV and the formation energy of H_2 amounts to −4.28 eV. In both cases zero-point energy-corrections are included. Thus, the dissociation of the free BDT molecule into a BDT radical and an H_2 molecule is endothermic by $E_{\mathrm{diss,zpc}}^{\mathrm{vac}} = 2.87$ eV including zero-point energies.

With the binding energies $E_b\{\mathrm{BDT}\} = -0.45$ eV and $E_b\{\mathrm{BDTR}\} = -3.26$ eV for a coverage of one BDT or BDTR per (4×3) surface unit cell, the free energy difference amounts to

$$\Delta f = 0.06 \text{ eV} + \left[\mu_{\mathrm{H}_2}(T,p) - E_{\mathrm{total}}\{\mathrm{H}_2\} - \frac{1}{2}\hbar\omega_{\mathrm{H}_2}\right]. \quad (7)$$

If the hydrogen reservoir is treated as an ideal gas, the chemical potential expression takes the form

$$\mu_{\mathrm{H}_2}(T,p) - E_{\mathrm{total}}\{\mathrm{H}_2\} - \frac{1}{2}\hbar\omega_{\mathrm{H}_2} = \tilde{\mu}_{\mathrm{H}_2}(T,p^0) + k_B T \ln(p/p^0). \quad (8)$$

p^0 is the reference pressure of 0.1 MPa. The temperature dependence of the chemical potential $\tilde{\mu}_{\mathrm{H}_2}(T,p^0)$ of hydrogen in the gas phase is taken from the thermodynamic tables of the CRC Handbook.[80] A similar logarithmic dependence is obtained in case of dilute solutions of H_2 in an electrolyte. At room temperature, the thermal energy $k_B T$ is only a factor of two to three smaller than the energy difference 0.06 eV in the above expression. Hence, the sign of Δf will change in favor of BDTR adsorption on the Au(111) surface at sufficiently small H_2 partial pressure. E.g., at a temperature of $T = 300$ K, and a hydrogen partial pressure as large as $p = 0.1$ MPa, adsorption of BDTR is still favorable compared to adsorbed BDT by approximately 0.26 eV. Thus, our calculations indicate that at submonolayer coverage the S-H bonds would be cleaved due to entropic reasons.

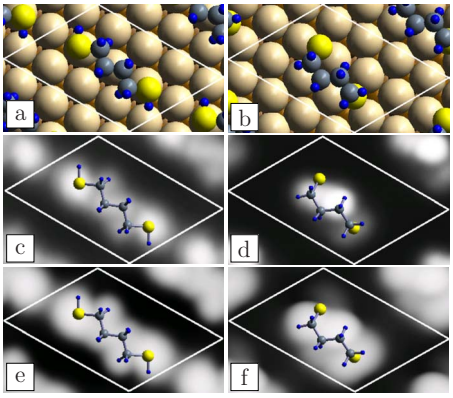

FIG. 4. (Color online) STM-images simulated within the Tersoff-Hamann model. The LDOS is integrated from the Fermi energy ε_F to ε_F+0.8 eV. The underlying adsorption geometries of BDT and BDTR are depicted in (a) and (b). STM-images of the molecule in (c) and the radical in (d) are evaluated at a constant height of $\Delta z = 7$ Å above the Au surface atoms. Simulated constant-current STM-images of BDT (e) and BDTR (f) at a contour of $\rho_0 = 1.4\times10^{-5}$ e/Å^3. The (4×3) surface unit cell is indicated by white lines. Gray scales have been chosen independently in (c)–(f).

In addition, the question arises whether BDT molecules dissociate under UHV conditions, which is difficult to assess due to the large herringbone reconstruction of the Au(111) surface. One effect of this reconstruction is a partial relaxation of the surface stress by incorporating additional gold atoms into the surface. This effectively reduces the average Au-Au distance along the $[1\bar{1}0]$ direction within the first atomic layer by approximately 4%.[102,103] We have tried to simulate this higher density of Au surface atoms within the first layer by compressing our whole slab with the unreconstructed Au(111) surface in the $[1\bar{1}0]$ direction by 4%.[110] In case of BDTR, the main effect of the smaller Au-Au distance is a reduction of the bond strength of both S-Au bonds together by approximately 0.5 eV. On the other hand, the absolute value of the binding energy of BDT decreases only by approximately 0.1 eV. At hydrogen partial pressures of less than 0.1 MPa and $T = 300$ K, adsorption of BDTR on the compressed Au(111)(1×1) model surface is energetically slightly favored.

5. Simulated STM images

STM-images of adsorbed BDT and BDTR are simulated within the Tersoff-Hamann model (Ref. 75) for the energetically most favorable configurations (see Figs. 4(a) and 4(b)). To this purpose the local density of states (LDOS) is integrated from the Fermi energy ε_F to ε_F+eU using different values for eU ranging from −1.8 to 0.8 eV. In Figs. 4(c) and 4(d) the integrated LDOS is evaluated at a constant height of $\Delta z = 7$ Å above the Au surface atoms. Constant current topographies at a contour level of $\rho_0 = 1.4\times10^{-5}$ e/Å^3 and eU=+0.8 eV are depicted in Fig. 4(e) for BDT and in Fig. 4(f) for BDTR.

The calculated constant height and constant-current images of BDT and BDTR exhibit elongated features with a major contribution originating from the alkane chain. In case

of BDT, the simulated STM image reflects the nearly symmetric conformation of the molecule at the surface. By contrast, the STM-images of adsorbed BDTR look asymmetric. This is a consequence of the two inequivalent S-Au bonds and a distortion of the alkane chain. Note that at finite temperatures the STM images might appear symmetric due to thermal averaging. Furthermore, application of Au(111)(1 $\times$1) two-dimensional space group transformations will result in isoenergetic chemisorption configurations.

Leung *et al.* have deposited 1,6-hexanedithiol molecules on the Au(111) surface and characterized the resulting adsorption geometries by low energy atom diffraction, grazing incidence x-ray diffraction, and STM measurements.[33] STM images reveal a striped phase of the adsorbed species manifested by elongated bright features which line up along high symmetry directions of the Au(111) surface.[33] The data is consistent with configurations in which the adsorbate is lying flat on the surface with the C-C-C plane approximately parallel to the substrate.[33] The alkane chain is proposed to point approximately in the $\langle 1\bar{1}0\rangle$ directions.[33] The bright features in the STM-images are suggested to originate from rows of S atoms of two adjacent molecules in the densely packed structure.[33]

A comparison to the calculated STM images appears rather difficult as we calculate shorter alkanedithiols at lower coverages. However, our data leads us to speculate that not only the S atoms but also the alkane chain contributes to the bright features observed in STM images.

B. Adsorption on Au(100)

In contrast to the close-packed Au(111) surface a more open surface such as Au(100) can lead to a stronger binding of adsorbates to surface atoms, e.g., in case of SCH_3 adsorption.[104,105] This is of particular interest, e.g., for Video-STM experiments, as stronger adsorbate-surface bonds can lead to lower diffusion rates which facilitate a direct observation of single diffusion events. In the following sections we calculate the ground-state configuration for BDT on the Au(100) surface and assess whether dissociation into BDTR and H_2 may occur.

1. Adsorption of BDT molecules on defect-free Au(100)

Local total-energy minima and the corresponding binding energies have been calculated for BDT adsorbed on the unreconstructed, but relaxed, Au(100) surface. A set of three initial configurations has been relaxed to local energy minima. In the initial configurations the BDT alkane chain is lying parallel to the surface. The molecule forms two S-Au bonds, with the S atoms located approximately atop Au surface atoms. Adsorption configurations with only a single S-Au bond are expected to be energetically unfavorable. This has been concluded without explicit computation by considering the binding energy of a single $HSCH_3$ molecule bonded atop a Au surface atom. In order to asses bonding to hollow sites, calculations were performed in which a single $HSCH_3$ molecule binds to a Au(100) hollow site. As a matter of fact, this configuration proved to be unstable. In the relaxed configuration the $HSCH_3$ molecule binds on top to a single Au surface atom. The on top binding energy E_b amounts to –0.45 eV.

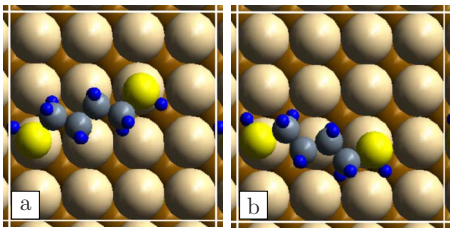

FIG. 5. (Color online) (a) BDT configuration with the largest absolute value of the binding energy per (4$\times$4) surface unit cell of the unreconstructed Au(100) surface (E_b=–0.77 eV). (b) Competing configuration shown for comparison (E_b=–0.72 eV). The surface unit cell is indicated by white lines.

The energetically most favorable adsorption geometry for one BDT per (4$\times$4) surface unit cell is shown in Fig. 5(a). Here the BDT molecule adopts a lying-down configuration in which the alkane chain is slightly bent and the C-C-C planes are oriented approximately parallel to the surface. Both sulfur atoms are close to Au on-top positions. The molecule-surface binding energy is calculated to be E_b=–0.77 eV not including zero-point energies. Structural parameters are summarized in Table III.

An energetically slightly less favorable configuration is shown in Fig. 5(b) for comparison. The energy difference with respect to the structure with the lowest calculated energy amounts to 0.05 eV in case of the (4$\times$4) surface unit cell.

TABLE III. Structural parameters and binding energies for BDT configurations on the unreconstructed Au(100) surface as depicted in Fig. 5. E_b is the DFT-PW91 binding energy per molecule defined in Eq. (1), $d_{S\text{-}S}$ is the distance between the S atoms, $d_{S\text{-}Au}$ are the S-Au bond lengths, and $d_{Au\text{-}Au}$ is the distance between the Au atoms to which the BDT binds. The value in parenthesis is the equilibrium distance between the respective Au atoms. E_b for an inclined configuration is approximated by a $HSCH_3$ molecule adsorbed atop a Au surface atom.

Configuration	Cell size	E_b (eV)	$d_{S\text{-}S}$ (Å)	$d_{S\text{-}Au}$ (Å)	$d_{Au\text{-}Au}$ (Å)
a	(4$\times$4)	–0.77	6.77	2.59, 2.59	6.63 (6.61)
b	(4$\times$4)	–0.72	6.67	2.60, 2.60	5.89 (5.91)
b	(4$\times$3)	–0.66	6.67	2.61, 2.61	5.89 (5.91)
$HSCH_3$ on top	(3$\times$3)	–0.45		2.57	
BDT (gas)			6.89		

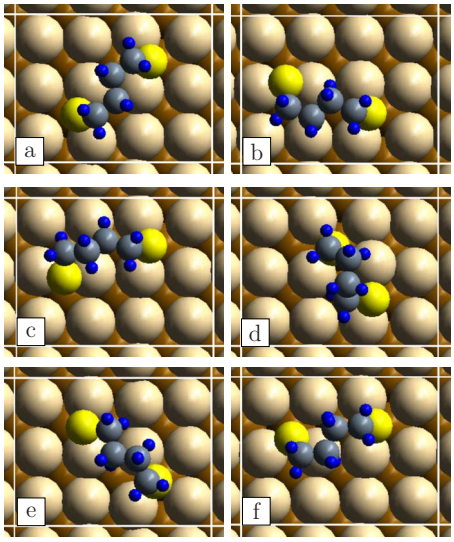

FIG. 6. (Color online) (a)–(c) BDTR configurations with the largest absolute value of the binding energy on the unreconstructed Au(100) surface. (d)–(f) Lowest energy competing configurations are shown for comparison. The surface unit cell is indicated by white lines.

Compared to adsorption on the Au(111) surface, BDT binds stronger to the Au(100) surface by approximately 0.27 eV for a coverage of one molecule per (4×4) surface unit cell. The lower binding energy on the Au(100) surface is also manifested in a shortening of the S-Au bond by approximately 0.15 Å. A weaker adsorbate-surface bond in case of denser-packed surfaces like the Au(111) surface is also observed for other adsorbates such as the SCH_3 radical (Ref. 104) or the $HSCH_3$ molecule.

2. Adsorption of BDT radicals on defect-free Au(100)

Energy minima for BDTR on the Au(100) surface were calculated by relaxing ten initial configurations to a local total-energy minimum. The initial configurations have been chosen such that both S atoms of the radical are located near hollow sites of the Au(100) substrate. Configurations in which either S atom is located atop Au surface atoms have not been taken into consideration as an initial starting geometry. Calculations for an adsorbed SCH_3 radical on the Au(100) surface reveal that on top positions of the S atom are unstable. Within this survey the alkane chain of the BDT radical has been oriented approximately parallel to the surface for all but two considered initial configurations.

Calculations for this survey have been carried through for a coverage of one BDTR per (4×3) surface unit cell. We found the adsorption geometries depicted in Figs. 6(a)–6(c) to have the lowest total energy among all other configurations. The configurations are calculated to be energetically degenerated to within 10 meV. The corresponding DFT-PW91 binding energies are $E_b=-4.01$, -4.02, and -4.01 eV, for Figs. 6(a)–6(c), respectively. The bond between BDTR and the Au surface strengthens as the coverage decreases to one radical per (4×4) surface unit cell. Thus, the binding energy decreases to $E_b=-4.11$, -4.09, and -4.07 eV for the adsorption configurations depicted in Figs. 6(a)–6(c), respectively. The small, almost coverage independent energy splitting of 10–30 meV between these configurations is not considered to be significant, see Appendix B.

TABLE IV. Structural parameters and binding energies for an excerpt of calculated configurations of BDTR on the Au(100) surface as depicted in Fig. 6. E_b is the DFT-PW91 binding energy per radical as defined in the main text, and $d_{S\text{-}S}$ refers to the distance between the S atoms.

Configuration	Cell size	E_b (eV)	$d_{S\text{-}S}$ (Å)
a	(4×3)	−4.01	5.36
b	(4×3)	−4.02	5.33
c	(4×3)	−4.01	5.45
d	(4×3)	−3.93	3.92
e	(4×3)	−3.93	5.39
f	(4×3)	−3.91	5.06

Both sulfur atoms of the BDTR bind to the Au(100) surface in between hollow and bridge sites (hollow-bridge separation equal to 1.48 Å). The S atoms are shifted from the hollow site to a nearby bridge site by 0.8 Å in Fig. 6(a), 1.2 and 0.9 Å in Fig. 6(b), as well as 1.1 and 0.9 Å in Fig. 6(c). As in the case of low-energy adsorption configurations of single SCH_3 radicals (Ref. 105), both SCH_2 groups of BDTR bind in tilted hollow-bridge like configurations to the Au(100) surface. The tilt angles with respect to the surface normal amount to 34° in Fig. 6(a), 53° and 30° in Fig. 6(b), and 53° and 41° in Fig. 6(c).

An excerpt of competing configurations for one BDTR per (4×3) surface unit cell of the Au(100) surface is depicted in Figs. 6(d)–6(f). Corresponding structural information is summarized in Table IV. Among the calculated configurations, (a)–(f) represent the four lowest-energy configurations. In all relaxed configurations both sulfur atoms bind to the substrate close to hollow- or bridgelike sites.

Our calculations again reveal the appearance of a multivalley structure of the potential energy surface. As in the case of Au(111), we find local minima which are within a range of only a few 100 meV. Notably, in case of the Au(100) surface the interplay between two S-Au bonds of the radical and the BDTR internal degrees of freedom leads to three inequivalent configurations, which are very close in energy and, within the accuracy of the calculation, represent the ground state. This result plays an important role for the diffusion characteristics of BDTR on Au(100).

3. Adsorption of BDT radicals in the presence of surface defects on Au(100)

a. Adatoms. Two stable adsorption geometries have been calculated in which both S atoms of BDTR bind to a Au adatom and atop to Au atoms of the Au(100) surface. The configurations differ in the position of the adatom with respect to the underlying substrate, which has initially been chosen as either a bridge or a hollow position. Figure 7(a) depicts the lower total-energy configuration in which the

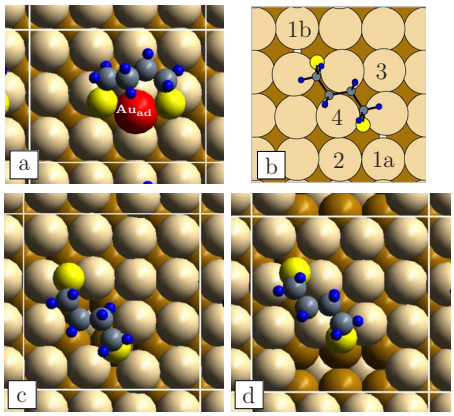

FIG. 7. (Color online) (a) Configuration involving one Au adatom (dark gray or red, $E_{b2}=-3.46$ eV). Au atoms of the first and third layer: light gray or light brown, Au atoms of the second layer: dark gray or dark brown. (b) Schematic representation of the lowest-energy BDTR configuration on the Au(100) surface. Considered defect positions are labeled 1a, 1b, 2, 3, and 4. (c) Configuration involving one surface vacancy at position 4 ($E_{b2}=-4.05$ eV). (d) Configuration involving two surface vacancies at position (1a, 2) ($E_{b2}=-3.97$ eV). The surface unit cell is indicated by white lines.

adatom is located near a bridge site. The DFT-PW91 binding energy E_{b2} with respect to the defect-free and unreconstructed Au(100) surface, defined in Eq. (4), amounts to $E_{b2}=-3.46$ eV for a coverage of one BDTR per (4×3) surface unit cell. Thus, the absolute value of the binding energy is approximately 0.56 eV smaller compared to the lowest-energy configurations on the defect-free surface with a binding energy of −4.02 eV. As a result, Au adatoms are not relevant for BDTR chemisorption on Au(100).

b. Vacancies. Adsorption configurations with one or two surface vacancies have been calculated in a (4×4) surface unit cell. The considered vacancy positions are labeled 1a, 1b, 2, 3, and 4 in Fig. 7(b). Initially the atomic coordinates of the BDT radical correspond to the lowest total-energy configuration on the defect-free Au(100) surface as depicted in Fig. 6(a).

For configurations involving a single surface vacancy one of the Au atoms labeled 1a, 3, or 4 is removed. In case of a vacancy at position 4, an alternative initial configuration of BDTR has been chosen in which both S atoms are located at the vacancy prior to relaxation. The Au atoms labeled (1a,1b) or (1a,2) have been removed for configurations involving two vacancies.

Figures 7(c) and 7(d) show the energetically most favorable configurations with one or two surface vacancies, respectively. The highest absolute value of the DFT-PW91 binding energy amounts to $E_{b2}=-4.05$ eV and occurs in case of one vacancy at position 4. We obtain $E_{b2}=-3.97$ eV in case of two vacancies at position (1a,2). In any case, the absolute value of the binding energy is at least 0.06 eV smaller compared to the lowest-energy configuration on the defect-free surface with a binding energy of −4.11 eV.

Configurations of BDTR on the unreconstructed Au(100) surface with vacancies are energetically less favorable compared to configurations without defects by at least two to three k_bT at room temperature. Based on this result, configurations with defects are expected to be of minor importance.

4. S-H bond cleavage

In the previous sections we discussed the chemisorption energetics of both BDT molecules and radicals on the unreconstructed Au(100) surface. For a coverage of one BDT per (4×4) surface unit cell we obtained DFT-PW91 binding energies for the optimum configurations of −0.77 eV in case of the molecule and −4.11 eV for the radical. As stated in Sec. III A 4, the energy needed to cleave both S-H bonds of BDT and subsequently form H_2 amounts to −2.87 eV including zero-point energy corrections. Thus, the relative abundance $p(\mathrm{BDTR})/p(\mathrm{BDT})$ of BDT radicals with respect to BDT molecules on the unreconstructed Au(100) surface is governed by the free energy difference,

$$\Delta f = -0.47\ \mathrm{eV} + \left[\mu_{H_2}(T,p) - E_{\mathrm{total}}\{H_2\} - \frac{1}{2}\hbar\omega_{H_2}\right]. \quad (9)$$

Evidently, a cleavage of both S-H bonds and subsequent H_2 formation is already energetically favored at a temperature of 0 K by approximately 0.47 eV in case of BDT adsorbed on Au(100). This distinct tendency toward dissociation into BDTR and H_2 is further assisted by entropy effects as described in Sec. III A 4.

IV. SUMMARY

Synthesis of organic molecular assemblies at surfaces and surface functionalization can be achieved by binding organic molecules to metal surfaces via thiol groups.[2] Here we present DFT calculations for the submonolayer adsorption of BDT molecules [BDT: HS-$(CH_2)_4$-SH] and BDT radicals [BDTR: ·S-$(CH_2)_4$-S·] on the (111) and (100) surfaces of gold. Dithiols on Au surfaces are an intensely studied model system for sulfur bonded organic molecules with promising perspectives in molecular electronics.[12–14,33] We adsorb the molecules on the unreconstructed Au(111) and Au(100) surfaces, which can be stabilized in an electrochemical environment.[47,48]

BDTR adsorption on Au surfaces differs fundamentally from the adsorption of mono-thiols with only a single S-Au bond. The presence of two S-Au molecule-surface bonds—together with the internal conformation degrees of freedom of the molecule—results in a complicated multivalley potential-energy surface. Identification of the adsorbed species—BDT or BDTR—and their lowest-energy adsorption configurations is an indispensable prerequisite for the study of diffusion and growth of BDT molecular films. Our results suggest a much more versatile phenomenology for adsorption and diffusion than described previously in case of the monothiols.[61]

While DFT total-energy differences come out 0.06 eV in favor of chemisorbed BDT molecules at a coverage of one molecule per (4×3) Au(111) surface unit cell, inclusion of entropic effects results in S-H bond cleavage. Thus, in equilibrium, BDT radicals are expected to be the dominant species on the unreconstructed Au(111) surface. On Au(100)

BDT radicals are found to be the energetically preferred species.

Both for Au(111) and Au(100) the BDT radicals adopt a lying-down configuration in which both sulfur atoms bond to Au surface atoms in hollow or bridgelike positions. Irrespective of the chosen surface orientation, Au(111) or Au(100), local energy minima are found to exist within a few 100 meV of the ground-state configuration. In case of Au(100) we found lowest-energy adsorption configurations, which come out energetically degenerate within the accuracy of the calculation. At a coverage of one radical per (4×4) and (6×6) surface unit cell the energy difference amounts to less than 0.03 eV.

As opposed to the adsorption of alkanethiols on Au(111), which has been observed experimentally[101] as well as theoretically[61,100,102] to become energetically more favorable in the presence of Au adatoms, we found no such energetical preference in case of BDT radicals on Au(111) or Au(100), neither for Au adatoms nor for Au surface vacancies.

Semiempirical vdW corrections to the binding energy have been evaluated. In case of the structures considered in this work, the ground-state configuration remained unaltered. In view of the absolute value of the vdW correction in comparison to experiment, however, a more sophisticated approach to vdW interactions appears to be required. Hence, plain DFT-PW91 binding energies have been quoted in this paper.

Constant current and constant height STM-images have been derived within the Tersoff-Hamann model (Ref. 75) for BDT molecules and radicals on the unreconstructed Au(111) surface. They exhibit elongated features at the position of the alkane chain, with the long axis approximately parallel to the chain. The long axis is slightly tilted with respect to the $\langle 1\bar{1}0\rangle$ directions.

ACKNOWLEDGMENTS

We thank O. Magnussen and K. Suto for helpful discussions and communication of experimental results prior to publication. We are grateful to A. Groß and K. Tonigold for stimulating discussions of their DFT results on the adsorption of dithiolates on gold surfaces. This work has been supported financially by the Deutsche Forschungsgemeinschaft (DFG) within Project No. Pe497/4-1. Calculations have been carried through at the Rechenzentrum der Universität Kiel.

APPENDIX A: ESTIMATED LOWER BOUND ON THE BDTR/AU(111) CHEMISORPTION ENERGY

In case of a complex potential energy landscape with multiple local minima it is a notoriously difficult problem to locate the global energy minimum. Our initial configurations, which we have relaxed into local potential energy minima, have been chosen by chemical intuition. Here we will try to provide an estimate for a lower bound of the binding energy per BDTR. The main contributions to the binding energy arise from the S-Au bonds, the conformational change of BDTR, the interaction of the alkane chain with the substrate, and substrate relaxation. At finite coverage, there are direct as well as substrate-mediated adsorbate-adsorbate interactions.

The energy needed to change the conformation of BDTR decreases the absolute value of the binding energy. A rather conservative approach is to omit this contribution to the binding energy. Typical energies associated with conformational changes are calculated to be order of 0.01–0.1 eV. We neglect the interaction of the alkane chain with the substrate. To obtain an approximate lower bound of the S-Au interaction, including the substrate relaxation and substrate-mediated adsorbate-adsorbate interactions, we have performed calculations for a (4×3) and (4×4) surface unit cell with two SCH_3 radicals adsorbed at the Au(111) surface. The initial position of the S atoms and the orientation of the S-C bonds have been adopted from the corresponding atoms of the BDTR ground-state configuration. Subsequently, a structural relaxation of both SCH_3 radicals and the substrate atoms was carried through. As a result, we obtain a binding energy per (4×3) and (4×4) surface unit cell for both SCH_3 radicals together of −3.47 and −3.57 eV, respectively. We take these values as a rough lower bound to the binding energy per BDTR for the respective surface unit cells. Notably, the calculated BDTR binding energies are only 0.2 and 0.1 eV above this bound. Due to the geometrical constraints in case of BDTR adsorption as opposed to the relaxation of two SCH_3 radicals, and in view of energies of the order of 0.01–0.1 eV associated with conformation changes of the free BDTR, we are confident that the calculated lowest-energy configuration in Fig. 2(a) is the ground-state configuration for submonolayer coverages of BDTR/Au(111). At worst, we expect our calculated optimum structure to be within a few k_BT of the global binding energy minimum at room temperature.

APPENDIX B: COVERAGE DEPENDENCE OF THE BDTR CHEMISORPTION ENERGY

1. Au(111)

The bond strength between BDTR and the Au(111) surface increases substantially with decreasing coverage Θ, as can been read from Table V. Due to prohibitive computational costs for calculations involving large surface unit cells we were not able to obtain the binding energy of an individual adsorbed BDTR, i.e., the limit $\Theta\rightarrow0$ could not be reached. We attribute the coverage dependence of the binding energy to strong substrate-mediated, adsorbate-adsorbate interactions. In order to corroborate this assertion, we relate the change in binding energy between the (4×3) and (4×4) surface unit cell to a quantitative measure of the change in adsorbate induced substrate relaxation. We observe that the effect of the sulfur-surface bond is an expansion of the hollow site in the vicinity of the S atom. Thus, the mutual distance $d_{i,j}$ of the neighboring three Au atoms is increased as compared to the clean substrate. We find that the expansion of the hollow sites increases as the coverage decreases.

In an effort to quantify this effect, we consider the sum of the distances between the Au atoms of the hollow sites which are closest to the S atoms for a given surface unit cell and BDTR configuration. The change of this quantity upon in-

TABLE V. Coverage dependence of structural parameters and binding energies for the configurations of BDTR/Au(111) in Fig. 2 and BDTR/Au(100) in Fig. 6. E_b is the DFT-PW91 binding energy per radical as defined in Eq. (1) and $d_{S\text{-}S}$ refers to the distance between the S atoms.

Configuration	Cell size	E_b (eV)	$d_{S\text{-}S}$ (Å)
	BDTR/Au(111)		
a	(4×3)	−3.26	4.85
a	(4×4)	−3.45	4.82
a	(4×6)	−3.63	4.83
a	(6×3)	−3.47	4.91
a	(6×6)	−3.72	4.85
b	(4×3)	−3.25	5.48
b	(4×4)	−3.31	5.50
c	(4×3)	−3.24	5.44
c	(4×4)	−3.29	5.44
d	(4×3)	−3.23	4.81
d	(4×4)	−3.31	4.86
	BDTR/Au(100)		
a	(4×3)	−4.01	5.36
a	(4×4)	−4.11	5.33
a	(6×6)	−4.18	5.33
b	(4×3)	−4.02	5.33
b	(4×4)	−4.09	5.31
b	(6×6)	−4.17	5.32
c	(4×3)	−4.01	5.45
c	(4×4)	−4.07	5.46
c	(6×6)	−4.15	5.46

TABLE VI. Convergence of the binding energy E_b for BDTR on Au(111) in the configuration depicted in Fig. 2(a). The coverage corresponds to one BDTR per (4×3) surface unit cell. Note that the values for E_b in the main part of this work have been obtained with a cutoff energy of 340 eV, nine Au layers, and 48 **k** points.

E_{cutoff} (eV)	N_{kpt}	N_{layer}	$E_{xc}[n]$	E_b (eV)
		Plane wave cutoff energy E_{cutoff}		
250	12	4	GGA	−3.34
340	12	4	GGA	−3.39
420	12	4	GGA	−3.40
520	12	4	GGA	−3.41
		Number of Au layers N_{layer}		
250	12	4	GGA	−3.34
250	12	6	GGA	−3.37
250	12	9	GGA	−3.28
250	12	12	GGA	−3.29
250	12	15	GGA	−3.25
250	12	18	GGA	−3.26
		Number of *k*-points N_{kpt}		
250	12	4	GGA	−3.34
250	48	4	GGA	−3.26
250	108	4	GGA	−3.26
		Approx. to the $E_{xc}[n]$ functional		
250	12	4	GGA	−3.34
250	12	4	LDA	−4.96

creasing the surface unit cell from (4×3) to (4×4) is defined as

$$\Delta d = \sum_{\substack{i,j=1 \\ i<j}}^{3} [d_{i,j}^{(4\times4)}(S_1) + d_{i,j}^{(4\times4)}(S_2)] - \sum_{\substack{i,j=1 \\ i<j}}^{3} [d_{i,j}^{(4\times3)}(S_1) + d_{i,j}^{(4\times3)}(S_2)] \quad \text{(B1)}$$

S_1 and S_2 refer to the sulfur atoms of BDTR. In Fig. 8 we plot the change in binding energy versus Δd for different configurations. Clearly, a correlation between the increase in binding energy and the change of adsorbate induced substrate relaxations can be observed, which corroborates our assertion.

2. Au(100)

In contrast to the Au(111) surface the coverage dependence of the binding energy is less pronounced, see Table V. The absolute value of the binding energy increases by approximately 0.16 eV if the coverage is decreased from one BDTR per (4×3) surface unit cell to one BDTR per (6×6). In case of the Au(111) surface the increase of the absolute value of the binding energy amounts to 0.46 eV. Concomitantly, we find the adsorbate induced relaxation of the Au surface atoms in the neighborhood of the S atoms to depend much more sensitively on the size of the surface unit cell in case of the densely packed Au(111) surface as opposed to the more open Au(100) surface. In view of the correlation shown in Fig. 8 this is consistent with a stronger variation of the BDTR binding energy with surface unit-cell size in case of Au(111) as opposed to Au(100).

APPENDIX C: CONVERGENCE TESTS

We report the convergence of the DFT binding energies of BDTR on the Au(111) and Au(100) surfaces with respect to computational parameters. The variation of binding energy due to an increase of the size of the surface unit cell (i.e., decrease of BDTR coverage) is discussed in Appendix B. In order to obtain an impression of the error related to the exchange-correlation functional $E_{xc}[n]$, we compare our GGA results to data calculated within the local density approximation (LDA) for $E_{xc}[n]$.[106,107]

TABLE VII. Convergence of the energy difference ΔE between different local chemisorption energy minima on the Au(111) surface.

Cell size	Config. in Fig. 2	E_{cutoff} (eV)	N_{kpt}	N_{layer}	$E_{\text{xc}}[n]$	ΔE (eV)
(4×3)	$a\leftrightarrow b$	250	12	4	GGA	0.041
(4×3)	$a\leftrightarrow b$	340	48	9	GGA	0.014
(4×3)	$a\leftrightarrow b$	250	12	4	LDA	−0.006
(4×4)	$a\leftrightarrow b$	250	9	4	GGA	0.109
(4×4)	$a\leftrightarrow b$	340	36	9	GGA	0.136
(4×3)	$a\leftrightarrow c$	250	12	4	GGA	0.047
(4×3)	$a\leftrightarrow c$	340	48	9	GGA	0.017
(4×4)	$a\leftrightarrow c$	250	9	4	GGA	0.131
(4×4)	$a\leftrightarrow c$	340	36	9	GGA	0.163
(4×3)	$a\leftrightarrow e$	250	12	4	GGA	0.073
(4×3)	$a\leftrightarrow e$	340	48	9	GGA	0.050
(4×3)	$a\leftrightarrow g$	250	12	4	GGA	0.180
(4×3)	$a\leftrightarrow g$	340	48	9	GGA	0.177
(4×3)	$a\leftrightarrow g$	250	12	4	LDA	0.226
(4×3)	$a\leftrightarrow h$	250	12	4	GGA	0.192
(4×3)	$a\leftrightarrow h$	340	48	9	GGA	0.206
(4×3)	$a\leftrightarrow h$	250	12	4	LDA	0.167

1. Au(111)

The convergence of the binding energy E_b per BDTR for the configuration depicted in Fig. 2(a) is summarized in Table VI. The error of E_b related to the cutoff energy of the plane-wave expansion, the number of Au layers in the slab, and number of **k**-points are estimated to be 0.02, 0.02, and less than 0.01 eV, respectively. An increase of the vacuum region thickness by ≈9 Å changes E_b by only 0.01 eV. As outlined in Sec. II, the relaxed positions of the Au atoms within the first three layers of the slab and the positions of the atoms of the BDT adsorbate are calculated in a slab comprising 4 layers of Au, a cutoff energy of 250 eV, and 12 special **k** points in the complete first Brillouin zone. Performing a relaxation of the atomic positions in a slab comprising 9 Au layers, a cutoff energy of 340 eV, and 48 special **k** points leads to an increase of the absolute value of E_b by less than 0.03 eV. Increasing the number of relaxed Au substrate layers from 3 to 5 changes the binding energy for one BDTR per (4×4) surface unit cell by approximately 0.01 eV

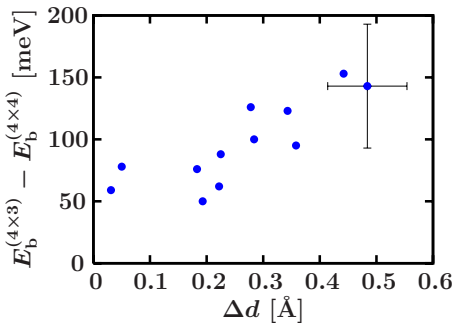

FIG. 8. (Color online) Change in binding energy E_b upon increasing the surface unit cell from (4×3) to (4×4) as a function of Δd for different configurations. Δd serves as a measure for the change in adsorbate induced substrate relaxations [see Eq. (B1)]. The data have been obtained using 250 eV for the cutoff energy, 12 **k** points in the full Brillouin zone, and 4 Au substrate layers.

TABLE VIII. Convergence of the binding energy E_b for BDTR on Au(100) in the configuration depicted in Fig. 6(b). The coverage corresponds to one BDTR per (4×3) surface unit cell. Note that the values for E_b in the main part of this work have been obtained with a cutoff energy of 340 eV, 12 Au layers, and 48 **k** points.

E_{cutoff} (eV)	N_{kpt}	N_{layer}	$E_{\text{xc}}[n]$	E_b (eV)
Number of Au layers N_{layer}				
250	12	4	GGA	−4.11
250	12	6	GGA	−4.00
250	12	10	GGA	−4.06
250	12	12	GGA	−4.03
250	12	14	GGA	−4.02
Number of k-points N_{kpt}				
250	12	4	GGA	−4.11
250	48	4	GGA	−4.07
250	108	4	GGA	−4.06
Approx. to the $E_{\text{xc}}[n]$ functional				
250	12	4	GGA	−4.11
250	12	4	LDA	−5.87

TABLE IX. Convergence of the energy difference ΔE between different (local) chemisorption energy minima on the Au(100) surface.

Cell size	Config. in Fig. 6	E_{cutoff} (eV)	N_{kpt}	N_{layer}	$E_{\text{xc}}[n]$	ΔE (eV)
(4×3)	$a\leftrightarrow b$	250	12	4	GGA	−0.018
(4×3)	$a\leftrightarrow b$	340	48	12	GGA	−0.009
(4×3)	$a\leftrightarrow b$	250	12	4	LDA	−0.069
(4×4)	$a\leftrightarrow b$	250	9	4	GGA	0.013
(4×4)	$a\leftrightarrow b$	340	36	12	GGA	0.014
(4×3)	$a\leftrightarrow c$	250	12	4	GGA	0.117
(4×3)	$a\leftrightarrow c$	340	48	12	GGA	0.084
(4×3)	$a\leftrightarrow d$	250	12	4	GGA	0.103
(4×3)	$a\leftrightarrow d$	340	48	12	GGA	0.100

(data for 250 eV cutoff energy, 12 **k** points, 9 Au layers in the slab).

Altogether, we arrive at an estimate for the absolute binding-energy error of approximately 0.10 eV not taking into account errors related to the use of the PW91-GGA exchange-correlation functional.

It is well known that the LDA for $E_{\text{xc}}[n]$ tends to overbind. Using the LDA, we obtain an absolute value of the binding energy which is 1.62 eV larger compared to PW91-GGA (see Table VI.

In Table VII the convergence of total-energy differences ΔE between different chemisorption configurations of BDTR on the Au(111) surface is summarized. The error of ΔE related to the cutoff energy, number of Au layers in the slab, and number of special **k** points is on the order of 0.03 eV.

The error of structural parameters like $d_{\text{S-S}}$ and $d_{\text{S-Au}}$ associated with a finite cutoff energy, number of Au layers in the slab, and number of special **k** points is estimated to be 0.02 Å.

2. Au(100)

The convergence of the binding energy E_{b} per BDTR for the configuration depicted in Fig. 6(b) is summarized in Table VIII. The error of E_{b} related to the number of Au layers in the slab and the number of **k**-points is estimated to be 0.01 eV each. We assume that the error of E_{b} related to the cutoff energy does not depend sensitively on surface orientation. Thus, we assume it to be equal to 0.02 eV. An increase of the vacuum region to ≈21 Å results in a change in E_{b} of 0.002 eV.

As outlined in Sec. II, the relaxed positions of the Au atoms within the first three layers of the slab and the positions of the atoms of the BDT adsorbate are calculated in a slab comprising 4 layers of Au, a cutoff energy of 250 eV, and 12 special **k** points in the complete first Brillouin zone. Performing a relaxation of the atomic positions in a slab comprising 12 Au layers, a cutoff energy of 340 eV, and 48 special **k**-points leads to a decrease of E_{b} by less than 0.03 eV.

Altogether, we arrive at an estimate for the absolute binding-energy error of approximately 0.09 eV not taking into account errors related to the use of the PW91-GGA exchange-correlation functional.

Using the LDA functional for $E_{\text{xc}}[n]$, we obtain a binding energy which is 1.77 eV lower compared to the PW91-GGA value (see Table VI).

In Table IX the convergence of the total-energy difference ΔE between different BDTR chemisorption configurations on the Au(100) surface is summarized. The error of ΔE related to the cutoff energy, number of Au layers in the slab, and number of special **k**-points amounts to ≈0.03 eV.

*franke@theo-physik.uni-kiel.de

[1] C. Joachim, J. K. Gimzewski, and A. Aviram, Nature (London) **408**, 541 (2000).
[2] F. Schreiber, J. Phys.: Condens. Matter **16**, R881 (2004).
[3] B. Baisch, D. Raffa, U. Jung, O. M. Magnussen, C. Nicolas, J. Lacour, J. Kubitschke, and R. Herges, J. Am. Chem. Soc. **131**, 442 (2009).
[4] Y. Wang, J. Kröger, R. Berndt, and W. A. Hofer, J. Am. Chem. Soc. **131**, 3639 (2009).
[5] M. Alemani, S. Selvanathan, F. Ample, M. V. Peters, K.-H. Rieder, F. Moresco, C. Joachim, S. Hecht, and L. Grill, J. Phys. Chem. C **112**, 10509 (2008).
[6] C. Dri, M. V. Peters, J. Schwarz, S. Hecht, and L. Grill, Nat. Nanotechnol. **3**, 649 (2008).
[7] A. S. Kumar, T. Ye, T. Takami, B.-C. Yu, A. K. Flatt, J. M. Tour, and P. S. Weiss, Nano Lett. **8**, 1644 (2008).
[8] M. Alemani, M. V. Peters, S. Hecht, K.-H. Rieder, F. Moresco, and L. Grill, J. Am. Chem. Soc. **128**, 14446 (2006).
[9] B.-Y. Choi, S.-J. Kahng, S. Kim, H. Kim, H. W. Kim, Y. J. Song, J. Ihm, and Y. Kuk, Phys. Rev. Lett. **96**, 156106 (2006).
[10] M. J. Comstock, N. Levy, A. Kirakosian, J. Cho, F. Lauterwasser, J. H. Harvey, D. A. Strubbe, J. M. J. Fréchet, D.

Trauner, S. G. Louie, and M. F. Crommie, Phys. Rev. Lett. **99**, 038301 (2007).
[11] J. Lahann, S. Mitragotri, T.-N. Tran, H. Kaido, J. Sundaram, I. S. Choi, S. Hoffer, G. A. Somorjai, and R. Langer, Science **299**, 371 (2003).
[12] D. L. Klein, R. Roth, A. K. L. Lim, A. P. Alivisatos, and P. L. McEuen, Nature (London) **389**, 699 (1997).
[13] M. A. Reed, C. Zhou, C. J. Muller, T. P. Burgin, and J. M. Tour, Science **278**, 252 (1997).
[14] J. G. Kushmerick, D. B. Holt, J. C. Yang, J. Naciri, M. H. Moore, and R. Shashidhar, Phys. Rev. Lett. **89**, 086802 (2002).
[15] F. Schreiber, Prog. Surf. Sci. **65**, 151 (2000).
[16] Q. Sun, A. Selloni, and G. Scoles, ChemPhysChem **6**, 1906 (2005).
[17] R. B. Pontes, F. D. Novaes, A. Fazzio, and A. J. R. da Silva, J. Am. Chem. Soc. **128**, 8996 (2006).
[18] X. D. Cui, A. Primak, X. Zarate, J. Tomfohr, O. F. Sankey, A. L. Moore, T. A. Moore, D. Gust, G. Harris, and S. M. Lindsay, Science **294**, 571 (2001).
[19] H. Akkerman, A. Kronemeijer, P. van Hal, D. de Leeuw, P. Blom, and B. de Boer, Small **4**, 100 (2008).
[20] W. Haiss, S. Martin, L. Scullion, L. Bouffier, S. Higgins, and R. Nichols, Phys. Chem. Chem. Phys. **11**, 10831 (2009).
[21] R. P. Andres, T. Bein, M. Dorogi, S. Feng, J. I. Henderson, C. P. Kubiak, W. Mahoney, R. G. Osifchin, and R. Reifenberger, Science **272**, 1323 (1996).
[22] G. Meshulam, N. Rosenberg, A. Caster, L. Burstein, M. Gozin, and S. Richter, Small **1**, 848 (2005).
[23] L. E. Harrell, T. P. Bigioni, W. G. Cullen, R. L. Whetten, and P. N. First, J. Vac. Sci. Technol. B **17**, 2411 (1999).
[24] T. Ohgi, H. Y. Sheng, and H. Nejoh, Appl. Surf. Sci. **130-132**, 919 (1998).
[25] T. Ohgi, H. Y. Sheng, Z. C. Dong, H. Nejoh, and D. Fujita, Appl. Phys. Lett. **79**, 2453 (2001).
[26] K. Bandyopadhyay and K. Vijayamohanan, Langmuir **14**, 6924 (1998).
[27] N. Vandamme, J. Snauwaert, E. Janssens, E. Vandeweert, P. Lievens, and C. V. Haesendonck, Surf. Sci. **558**, 57 (2004).
[28] T. Nakanishi, B. Ohtani, K. Shimazu, and K. Uosaki, Chem. Phys. Lett. **278**, 233 (1997).
[29] H. Noda, Y. Tai, A. Shaporenko, M. Grunze, and M. Zharnikov, J. Phys. Chem. B **109**, 22371 (2005).
[30] D. Qu and K. Uosaki, J. Phys. Chem. B **110**, 17570 (2006).
[31] T. Nakamura, H. Kondoh, M. Matsumoto, and H. Nozoye, Langmuir **12**, 5977 (1996).
[32] M. Carot, M. Esplandiu, F. Cometto, E. Patrito, and V. Macagno, J. Electroanal. Chem. **579**, 13 (2005).
[33] T. Y. B. Leung, M. C. Gerstenberg, D. J. Lavrich, G. Scoles, F. Schreiber, and G. E. Poirier, Langmuir **16**, 549 (2000).
[34] K. Kobayashi, J. Umemura, T. Horiuchi, H. Yamada, and K. Matsushige, Jpn. J. Appl. Phys., Part 1 **37**, L297 (1998).
[35] K. Kobayashi, H. Yamada, T. Horiuchi, and K. Matsushige, Appl. Surf. Sci. **144-145**, 435 (1999).
[36] J.-J. Yu, J. N. Ngunjiri, A. T. Kelley, and J. C. Garno, Langmuir **24**, 11661 (2008).
[37] M. Esplandiu, M. Carot, F. Cometto, V. Macagno, and E. Patrito, Surf. Sci. **600**, 155 (2006).
[38] J. Liang, L. G. Rosa, and G. Scoles, J. Phys. Chem. C **111**, 17275 (2007).
[39] S. W. Joo, S. W. Han, and K. Kim, J. Phys. Chem. B **104**, 6218 (2000).
[40] P. Kohli, K. K. Taylor, J. J. Harris, and G. J. Blanchard, J. Am. Chem. Soc. **120**, 11962 (1998).
[41] S. Rifai, M. Laferriere, D. Qu, D. D. M. Wayner, C. P. Wilde, and M. Morin, J. Electroanal. Chem. **531**, 111 (2002).
[42] H. Hamoudi, Z. Guo, M. Prato, C. Dablemont, W. Q. Zheng, B. Bourguignon, M. Canepa, and V. A. Esaulov, Phys. Chem. Chem. Phys. **10**, 6836 (2008).
[43] C. D. Bain, E. B. Troughton, Y. T. Tao, J. Evall, G. M. Whitesides, and R. G. Nuzzo, J. Am. Chem. Soc. **111**, 321 (1989).
[44] S. W. Joo, S. W. Han, and K. Kim, Langmuir **16**, 5391 (2000).
[45] J. M. Tour, L. Jones, D. L. Pearson, J. J. S. Lamba, T. P. Burgin, G. M. Whitesides, D. L. Allara, A. N. Parikh, and S. V. Atre, J. Am. Chem. Soc. **117**, 9529 (1995).
[46] K. Suto and O. M. Magnussen (private communication).
[47] M. A. Schneeweiss, H. Hagenström, M. J. Esplandiu, and D. M. Kolb, Appl. Phys. A: Mater. Sci. Process. **69**, 537 (1999).
[48] H. Striegler, P. Skoluda, and D. M. Kolb, J. Electroanal. Chem. **471**, 9 (1999).
[49] S. J. Stranick, M. M. Kamna, and P. S. Weiss, Science **266**, 99 (1994).
[50] J. S. Raut and K. A. Fichthorn, J. Chem. Phys. **108**, 1626 (1998).
[51] J. Weckesser, J. V. Barth, and K. Kern, J. Chem. Phys. **110**, 5351 (1999).
[52] J. V. Barth, Surf. Sci. Rep. **40**, 75 (2000).
[53] J. Weckesser, J. V. Barth, and K. Kern, Phys. Rev. B **64**, 161403(R) (2001).
[54] M. Schunack, T. R. Linderoth, F. Rosei, E. Lægsgaard, I. Stensgaard, and F. Besenbacher, Phys. Rev. Lett. **88**, 156102 (2002).
[55] R. Otero, F. Hümmelink, F. Sato, S. B. Legoas, P. Thostrup, E. Laegsgaard, I. Stensgaard, D. S. Galvao, and F. Besenbacher, Nature Mater. **3**, 779 (2004).
[56] K.-Y. Kwon, K. L. Wong, G. Pawin, L. Bartels, S. Stolbov, and T. S. Rahman, Phys. Rev. Lett. **95**, 166101 (2005).
[57] S. Subramanian and J.-C. Wang, J. Chem. Phys. **123**, 014706 (2005).
[58] J. V. Barth, Annu. Rev. Phys. Chem. **58**, 375 (2007).
[59] G. Pawin, K. L. Wong, K.-Y. Kwon, R. J. Frisbee, T. S. Rahman, and L. Bartels, J. Am. Chem. Soc. **130**, 15244 (2008).
[60] P. Maksymovych, D. C. Sorescu, and J. T. Yates, J. Phys. Chem. B **110**, 21161 (2006).
[61] A. Franke and E. Pehlke, Phys. Rev. B **79**, 235441 (2009).
[62] D. Jiang and S. Dai, J. Phys. Chem. C **113**, 3763 (2009).
[63] D. Jiang and S. Dai, Phys. Chem. Chem. Phys. **11**, 8601 (2009).
[64] G. Kresse and J. Hafner, Phys. Rev. B **47**, 558 (1993).
[65] G. Kresse and J. Hafner, Phys. Rev. B **49**, 14251 (1994).
[66] G. Kresse and J. Furthmüller, Comput. Mater. Sci. **6**, 15 (1996).
[67] G. Kresse and J. Furthmüller, Phys. Rev. B **54**, 11169 (1996).
[68] J. P. Perdew, J. A. Chevary, S. H. Vosko, K. A. Jackson, M. R. Pederson, D. J. Singh, and C. Fiolhais, Phys. Rev. B **46**, 6671 (1992).
[69] P. E. Blöchl, Phys. Rev. B **50**, 17953 (1994).
[70] G. Kresse and D. Joubert, Phys. Rev. B **59**, 1758 (1999).
[71] H. J. Monkhorst and J. D. Pack, Phys. Rev. B **13**, 5188 (1976).
[72] M. Fuchs, M. Bockstedte, E. Pehlke, and M. Scheffler, Phys. Rev. B **57**, 2134 (1998).
[73] H. Shi and C. Stampfl, Phys. Rev. B **77**, 094127 (2008).
[74] P4VASP source code available under http://cms.mpi.univie.ac.at/odubay/p4vasp_site/news.php
[75] J. Tersoff and D. R. Hamann, Phys. Rev. B **31**, 805 (1985).

[76] A. Tkatchenko and M. Scheffler, Phys. Rev. Lett. **102**, 073005 (2009).
[77] S. Grimme, J. Comput. Chem. **27**, 1787 (2006).
[78] F. Ortmann, F. Bechstedt, and W. G. Schmidt, Phys. Rev. B **73**, 205101 (2006).
[79] M. Dion, H. Rydberg, E. Schröder, D. C. Langreth, and B. I. Lundqvist, Phys. Rev. Lett. **92**, 246401 (2004).
[80] *CRC Handbook of Chemistry and Physics*, 76th ed., edited by D. R. Lide (CRC Press, Boca Raton, FL, 1995).
[81] R. Rowland and R. Taylor, J. Phys. Chem. **100**, 7384 (1996).
[82] A. Bondi, J. Phys. Chem. **68**, 441 (1964).
[83] E. McNellis, J. Meyer, and K. Reuter, Phys. Rev. B **80**, 205414 (2009).
[84] C. Vericat, M. E. Vela, G. A. Benitez, J. A. M. Gago, X. Torrelles, and R. C. Salvarezza, J. Phys.: Condens. Matter **18**, R867 (2006).
[85] I. I. Rzeznicka, J. Lee, P. Maksymovych, and J. T. Yates, J. Phys. Chem. B **109**, 15992 (2005).
[86] J.-G. Zhou and F. Hagelberg, Phys. Rev. Lett. **97**, 045505 (2006).
[87] P. Maksymovych, D. C. Sorescu, D. Dougherty, and J. T. Yates, J. Phys. Chem. B **109**, 22463 (2005).
[88] D. J. Lavrich, S. M. Wetterer, S. L. Bernasek, and G. Scoles, J. Phys. Chem. B **102**, 3456 (1998).
[89] H. Grönbeck, A. Curioni, and W. Andreoni, J. Am. Chem. Soc. **122**, 3839 (2000).
[90] M. C. Vargas, P. Giannozzi, A. Selloni, and G. Scoles, J. Phys. Chem. B **105**, 9509 (2001).
[91] Y. Yourdshahyan, H. K. Zhang, and A. M. Rappe, Phys. Rev. B **63**, 081405(R) (2001).
[92] T. Hayashi, Y. Morikawa, and H. Nozoye, J. Chem. Phys. **114**, 7615 (2001).
[93] J. Gottschalck and B. Hammer, J. Chem. Phys. **116**, 784 (2002).
[94] Y. Yourdshahyan and A. M. Rappe, J. Chem. Phys. **117**, 825 (2002).
[95] Y. Cao, Q. Ge, D. J. Dyer, and L. Wang, J. Phys. Chem. B **107**, 3803 (2003).
[96] F. P. Cometto, P. Paredes-Olivera, V. A. Macagno, and E. M. Patrito, J. Phys. Chem. B **109**, 21737 (2005).
[97] N. Gonzalez, N. Lorente, and A. Arnau, Surf. Sci. **600**, 4039 (2006).
[98] R. Mazzarello, A. Cossaro, A. Verdini, R. Rousseau, L. Casalis, M. F. Danisman, L. Floreano, S. Scandolo, A. Morgante, and G. Scoles, Phys. Rev. Lett. **98**, 016102 (2007).
[99] J. Wang and A. Selloni, J. Phys. Chem. C **111**, 12149 (2007).
[100] A. Nagoya and Y. Morikawa, J. Phys.: Condens. Matter **19**, 365245 (2007).
[101] P. Maksymovych, D. C. Sorescu, and J. T. Yates, Phys. Rev. Lett. **97**, 146103 (2006).
[102] Y. Wang, N. S. Hush, and J. R. Reimers, J. Am. Chem. Soc. **129**, 14532 (2007).
[103] Y. Wang, N. S. Hush, and J. R. Reimers, Phys. Rev. B **75**, 233416 (2007).
[104] C. Masens, M. J. Ford, and M. B. Cortie, Surf. Sci. **580**, 19 (2005).
[105] A. Franke and E. Pehlke (unpublished).
[106] D. M. Ceperley and B. J. Alder, Phys. Rev. Lett. **45**, 566 (1980).
[107] J. P. Perdew and A. Zunger, Phys. Rev. B **23**, 5048 (1981).
[108] Polarizabilities in a.u.: $\alpha_{Au}=40$, $\alpha_S=19.6$, $\alpha_C=11.9$, $\alpha_H=4.5$ and first ionization energies in a.u.: $I_{Au}=0.34$, $I_S=0.38$, $I_C=0.41$, $I_H=0.5$.
[109] vdW radii: $R_{Au}=1.66$ Å, $R_S=1.80$ Å, $R_C=1.70$ Å, $R_H=1.09$ Å.
[110] The compressed Au(111)(1×1) model surface is calculated in a rectangular $(4\times2\sqrt{3})$ surface unit cell using a plane-wave cutoff energy of 340 eV, 16 special **k** points in the complete first Brillouin zone, and a slab comprising four Au layers.

4.3 Diffusion of 1,4-butanedithiol on Au(100)-(1×1): A DFT-based master-equation approach (accepted for publication in Phys. Rev. B)

4.3.1 Synopsis

The diffusion of organic molecules on metal surface is the subject of ongoing experimental and theoretical research because it has been found that the motion of molecules may differ substantially from that of single adatoms. E.g. a large organic molecule anchored to a Cu(111) surface, mainly via two S-Au bonds, has been reported to exhibit a predominantly one dimensional motion on the surface.[158] Rotational motion on the surface is probably restricted in this case due to the rigidity of the molecule.

Here, the diffusion of a flexible organic molecule which is bonded to an unreconstructed Au(100) surface via two S-Au anchors is presented. The focus is to characterize the diffusion paths from *first-principles*, to elucidate the role of internal degrees of freedom, and to calculate diffusion properties on short and long timescales via a statistical-mechanics master-equation approach. The details complementing the following brief overview of the results can be found in the submitted manuscript, Ref. 265, which has been added to the end of this Section.

The PES of BDTR/Au(100) exhibits a multivalley topology with (local) minima. Therefore, a description of diffusion in this case is far from trivial. First of all, diffusion hops between local minima on the PES need to be calculated. In part, local minima are taken from the previously published work on BDTR/Au(100) adsorption, while other configurations relevant for diffusion have been obtained in the course of this survey. Guided by chemical intuition, MEPs between local minima have been calculated. This has been carried through for a subset of all pairs of configurations because it is computationally unfeasible to take all transitions into account. In this way an event table of 14 elementary hops has been generated which comprises hops of one of the BDTR S atoms to neighboring binding sites as well as conformational changes of BDTR on the Au(100) surface. To obtain a description of BDTR/Au(100) diffusion utilizing this event table, the BDTR configurations and elementary hops have been mapped one-to-one onto the nodes and edges of a network typically comprised of 60×60 surface unit cells. For a section of the diffusion network see Fig 4.6. On this network a master equation for the probability, $p_i(t)$, that a BDTR occupies node i has been integrated numerically. The non-trivial book keeping has been done by assigning to each node a multi-index, i, which describes the type of BDTR chemisorption configuration, the BDTR orientation on the unreconstructed Au(100) surface, and a (1×1) surface unit cell the BDTR binds to. The set of all nodes and edges is generated by applying the elements of the 2D space group *p4mm* of the Au(100)-(1×1) surface to a set of independent chemisorption configurations and the diffusion event table. Elements of the 2D space group *p4mm* are depicted in Fig. 4.6. To set up the master equation, which generates the time-evolution of the

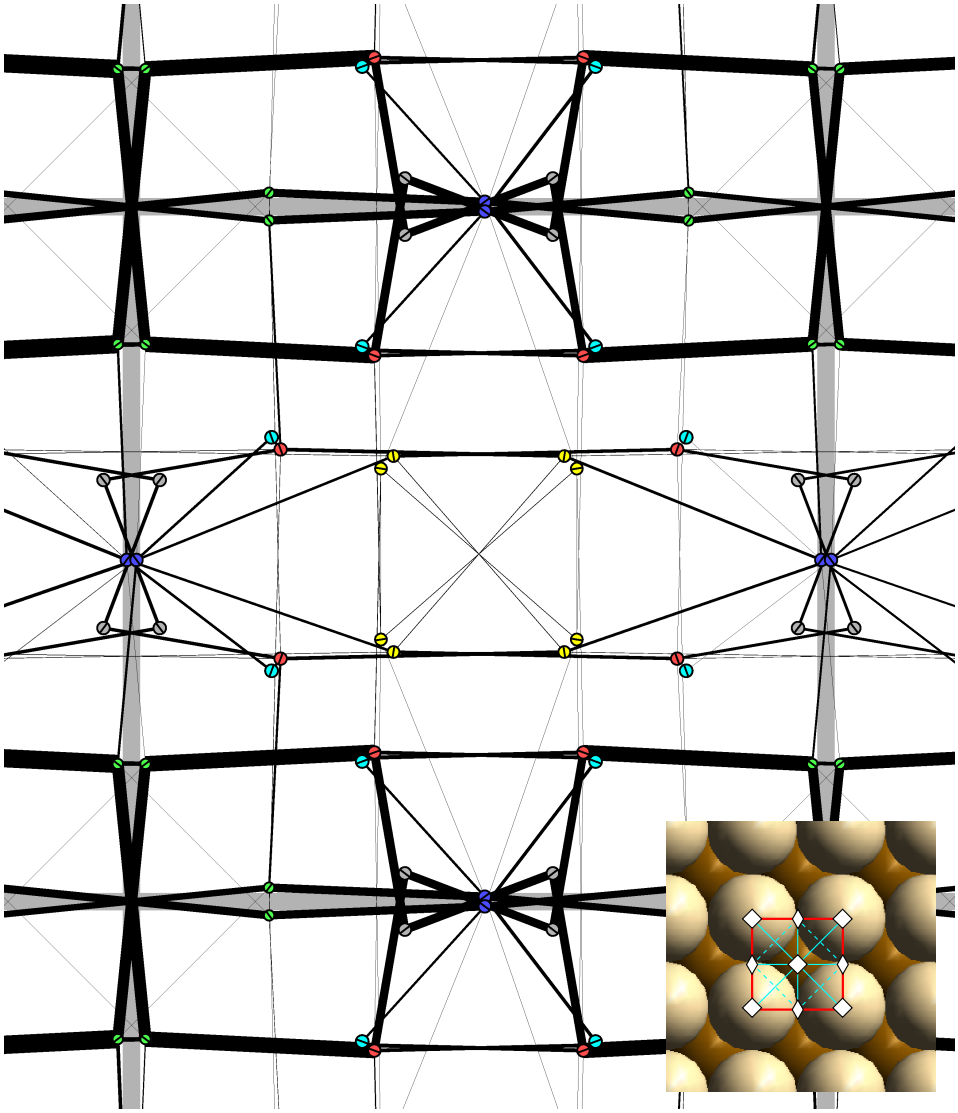

Figure 4.6: Diffusion network for BDTR/Au(100)-(1×1). The (1×1) surface unit cell is marked by thick gray lines. Filled circles denote the BDTR configurations. The position of each circle equals the center of mass of the two sulfur atoms while the color denotes the type of adsorption geometry of BDTR as detailed in the manuscript of Ref. 265. A thin line within each circle indicates the orientation of the adsorbed BDTR. Elementary diffusion paths connect the configurations (straight lines). The thickness of the line is proportional to the local probability current. A large formal temperature of $T = 1000$ K has been chosen such that all diffusion paths become visible. The Figure has been taken from Ref. 265. Inset: Illustration of the 2D space group *p4mm* of the Au(100)-(1×1) surface. Solid lines: mirror planes, broken lines: glide planes, diamonds: 180° rotational axes, and squares: 90° rotational axes.

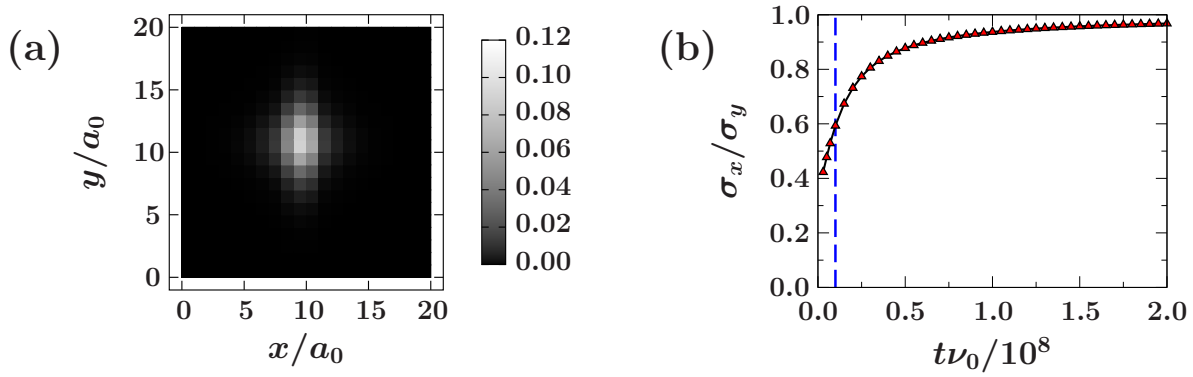

Figure 4.7: (a) Probability of finding the center of mass of the two BDTR S atoms in a given surface unit cell at scaled time $\nu_0 t = 10^7$ and a temperature of $T = 300$ K. The observed anisotropy is ascribed to short-time correlations. (b) Anisotropy of the probability at $T = 300$ K, characterized by the quotient σ_x/σ_y of the standard deviations in the x- and y-direction, versus scaled time. The broken line indicates the time for which the probability in (a) has been drawn. The Figures have been taken from the manuscript of Ref. 265.

probabilities the transition rates, $\Gamma_{i\to j}$, between two nodes i and j have been calculated within transition state theory (TST) using the DFT energy barriers from the event table. A typical value of 10^{12} s^{-1} has been assumed for the attempt frequencies of all transitions. This universal value of the attempt frequency, however, becomes irrelevant if it is absorbed into a rescaling of time and solely scaled quantities are considered. The resulting master equation for N nodes reads:

$$i = 1 \ldots N: \quad \frac{dp_i(t)}{dt} = \sum_{\substack{j=1 \\ j\neq i}}^{N} \Gamma_{j\to i}\, p_j(t) - \sum_{\substack{j=1 \\ j\neq i}}^{N} \Gamma_{i\to j}\, p_i(t). \tag{4.1}$$

The energy barriers which govern the transition rates between adjacent states cover a range from approximately 0.04 eV to 0.68 eV. Note that the smallest energy barrier, i.e. the largest transition rate, determines the time step used in the numerical integration scheme. The computational effort for a direct integration of the master equation especially at low temperatures can be considerably reduced if configurations which are only separated by a very small energy barrier are combined into a single effective configuration. E.g. let the energy barrier between node 1 and 2 and vice versa be much smaller than all other energy barriers in the network. This means that $\Gamma_{1\to 2} \gg \Gamma_{i\to j}$ and $\Gamma_{2\to 1} \gg \Gamma_{i\to j}$ for all i or j not equal to 1 or 2. The equilibration between node 1 and 2 should hence occur on a time scale which is short compared to typical time scales for other processes. Therefore, thermodynamic equilibrium between node 1 and

2 has been assumed, i.e. $\Gamma_{1\to2}\, p_1 = \Gamma_{2\to1}\, p_2$. With the definition of the joint probability $p_{\text{eff}}(t) := p_1(t) + p_2(t)$, the diffusion network can be reduced by introducing an "effective" configuration which replaces node 1 and 2. The master equation for the reduced network and the probabilities $(p_{\text{eff}}, p_3, p_4, \ldots)$ reads

$$\frac{dp_{\text{eff}}(t)}{dt} = \sum_{j=3}^{N} (\Gamma_{j\to1} + \Gamma_{j\to2})\, p_j(t) - \sum_{j=3}^{N} \frac{\Gamma_{1\to j}\Gamma_{2\to1} + \Gamma_{2\to j}\Gamma_{1\to2}}{\Gamma_{2\to1} + \Gamma_{1\to2}}\, p_{\text{eff}}(t) \tag{4.2}$$

$$\begin{aligned} i = 3 \ldots N: \quad \frac{dp_i(t)}{dt} &= \sum_{\substack{j=3 \\ j\neq i}}^{N} \Gamma_{j\to i}\, p_j(t) + \frac{\Gamma_{1\to i}\Gamma_{2\to1} + \Gamma_{2\to i}\Gamma_{1\to2}}{\Gamma_{2\to1} + \Gamma_{1\to2}}\, p_{\text{eff}}(t) \\ &\quad - \Big(\sum_{\substack{j=3 \\ j\neq i}}^{N} \Gamma_{i\to j} + \Gamma_{i\to1} + \Gamma_{i\to2}\Big)\, p_i(t). \end{aligned} \tag{4.3}$$

From an analysis of the time-evolution of the probabilities $p_i(t)$, key aspects of the BDTR diffusion have been deduced. First of all, the probability currents on the diffusion network yield information about the BDTR diffusion path and also to some extend about competing low energy pathways. This illustrates the benefits of the employed master equation approach which is capable of discovering complicated MEPs which could have otherwise been overlooked. The diffusion of BDTR/Au(100) may be thought of as a sequence of translations, conformational changes of BDTR, and rotations on the surface. Translations of BDTR to neighboring surface unit cells of the Au(100) surface occur preferentially in a certain high-symmetry direction of the substrate. The direction itself depends on the initial adsorbate orientation. The lowest total energy MEP consists of a complicated sequence of elementary hops between several intermediate local energy minima with a diffusion energy barrier of only 0.35 eV. Compared to the diffusion energy barrier for SCH_3 radicals of 0.61 eV, the result for BDTR is quite astonishing. The occurrence of such a low diffusion energy barrier for BDTR/Au(100) is suggested to originate from an intricate interplay between internal degrees of freedom of BDTR and the S-Au adsorbate-surface bonds.

The lowest energy barrier for BDTR rotations is 0.43 eV. Therefore, the order of diffusion energy barriers is $\Delta E_{\text{translation}} < \Delta E_{\text{rotation}}$, which points towards the occurrence of correlated diffusion hops on short time scales. These correlations and their time dependance have been characterized. This information may be accessible to experiments if the adsorbates can be monitored on short time scales. The anisotropy of the probability distribution has been quantified by the ratio, σ_x/σ_y, of the standard deviations in x and y directions, see Fig. 4.7. It has been observed that an initial significant anisotropy of the probability distribution decays over time. It is speculated that the time constant of the decay is related to the average time for BDTR rotations on the surface. On long time scales, the numerical results for the tracer diffusion constants follow an Arrhenius

law from which an effective diffusion energy barrier can be calculated. As a matter of fact, the numerical result for the effective diffusion energy barrier (0.36 eV) obtained by a fit to the data is in agreement to within 0.01 eV with the maximum energy barrier along the MEP for translations (0.35 eV).

Under electrochemical (EC) conditions the unreconstructed Au(100) surface can be stabilized for certain ranges of the applied external potential.[151] Interestingly, it has been reported in the literature that the mobility of adsorbates can be tuned via a change of the applied potential with respect to a reference electrode.[148,152] The predominant cause of such a potential dependant diffusion for certain systems has been attributed to a coupling of the adsorbate dipole moment to an electric field at the solid-liquid interface in the EC cell.[148,152] Hence, if the adsorbate dipole moment changes along the diffusion path, this may in turn lead to a modification of the PES. The effect of an electric field at the surface has been assessed qualitatively for BDTR/Au(100) within a rough non-self-consistent model by adding the electrostatic dipole-electric field interaction energy to the DFT total energies. Of course, the contribution of specifically adsorbed ions from the electrolyte are beyond the scope of such an approach. The data suggests that the PES topology as calculated within DFT should be significantly influenced by an electric field. Thus, the diffusion properties and, in particular, the correlations between subsequent diffusion hops are expected to be tunable via an applied external potential.

4.3.2 Manuscript (accepted for publication in Phys. Rev. B.), Copyright (2010) by the American Physical Society

Diffusion of 1,4-butanedithiol on Au(100)-(1×1): A DFT-based master-equation approach

A. Franke* and E. Pehlke
Institut für Theoretische Physik und Astrophysik
Christian-Albrechts-Universität zu Kiel, 24098 Kiel, Germany
(Dated: November 10, 2010)

The functionalization of metal surfaces via thiol-bonded molecules and the assembly of nanodevices on the surfaces should profit from a detailed atomistic understanding of the binding and diffusion properties. These differ substantially from the in-depth investigated situation of single adatoms. We report density-functional calculations for the elementary diffusion steps of 1,4 butanedithiol radicals adsorbed on a Au(100)-(1×1) surface. The elementary diffusion steps are then combined into a description of the diffusion mechanism on long time scales by integrating a master equation. The two S-Au bonds cause a multi-valley potential energy surface, which implies a complex diffusion mechanism. We identify the effect of the geometry constraints imposed by the $(CH_2)_4$-backbone on binding and diffusion. To this purpose we compare to the diffusion of a single SCH_3 radical on the same Au(100)-(1×1) surface. Altogether, the motion of the BDTR is walking-like, with the S-Atoms crossing bridge-sites of the Au surface one after the other. The lowest DFT-PW91 energy barrier for translation is 0.35 eV, while the energy barrier for rotation comes out larger, 0.43 eV. As a result of this difference there will be correlations between subsequent diffusive displacements of the molecule. The isotropic diffusion constant on long time scales is computed, and the numerical results follow an Arrhenius law.

PACS numbers: 68.43.Jk, 87.15.Vv, 64.75.Yz

I. INTRODUCTION

A promising approach towards the ultimate miniaturization in the field of nanotechnology lies in the functionalization of metal or semiconductor surfaces.[1,2] The self assembly of organic molecules with specific functional units marks a significant step towards this goal.[1,2] Prominent examples include precursors of molecular machinery[3–5] and the fabrication of switchable molecular assemblies on the surface.[6–14] A detailed insight into the binding properties and the diffusion mechanisms of the molecular building blocks on the surface should contribute to the further development of such nanostructures.

The diffusion of complex molecules has been found to differ fundamentally from the diffusion of single atoms.[15–25] For short n-alkanes on a model Pt(111) surface Raut and Fichthorn obtain directional anisotropy by molecular orientation.[17] Kwon *et al.* observed unidirectional diffusion of 9,10-dithioanthracene molecules on Cu(111) in a combined scanning tunneling microscopy (STM) and density-functional theory (DFT) study.[23] The thermally activated motion of these molecules, which form two S-Cu bonds, consists of subsequent hops of either one of the thiol groups. This resembles a "walking" motion of the molecule. From our own DFT study of the diffusion of $Au(SCH_3)_2$ complexes on the unreconstructed Au(111) surface a diffusion mechanism has emerged which is characterized by subsequent hops of the S-atoms.[16] In case of complex molecules with internal degrees of freedom on surfaces it still poses a substantial challenge for theory to calculate the elementary diffusion steps and activation energies and to combine these *ab initio* results into a statistical description of the process on various time scales.

We have chosen 1,4-butanedithiol radicals on Au(100)-(1×1) as a prominent model system. Sulfur-bonded dithiol-molecules are among the most widely studied self-assembly systems and are considered promising building blocks of future nanodevices.[2,30–47] Intense experimental research effort is devoted to further the understanding of different dithiol molecules adsorbed on the Au(111) surface under ultra high vacuum (UHV), ambient, as well as electrochemical (EC) conditions.[48–58] The existence of two thiol groups within the molecule raises the question whether dithiol molecules bind via one (upright configuration) or two (lying-down configuration) Au-S bonds to the surface. In case of the most common deposition methods either from the gas phase or from solution both upright configurations at saturation coverage (Refs.49,53,54,and 59) as well as submonolayer lying-down configurations (Refs.49–54,and 60) were observed. In a DFT study of the submonolayer adsorption of 1,4-butanedithiol [BDT: HS-$(CH_2)_4$-SH] on the unreconstructed Au(100) and Au(111) surfaces, we have found that BDT dissociates upon adsorption into adsorbed 1,4-butanedithiol radicals [BDTR: ·S-$(CH_2)_4$-S·] on the surface and H_2 in the gas phase.[61] On both surfaces the BDT radical adopts a lying-down chemisorption configuration in which two S-Au bonds are formed while the alkane chain is oriented approximately parallel to the surface plane.[61] The calculations have revealed a complicated multi-valley potential energy surface (PES) with various locally stable configurations which are within a few k_BT of the ground state. Consequently, the diffusion of the BDT radical on this surface involves many different elementary diffusion steps. To elucidate this question we

will present diffusion energy barriers for BDTR/Au(100)-(1×1) calculated from DFT. However, even when the energy barriers are known, the description of the overall diffusion process is still a formidable task due to the complexity of the network of elementary diffusion steps. We will demonstrate below how this problem can be solved by integrating the master equation.

The unreconstructed Au(100) surface is stable under certain electrochemical (EC) conditions. The quasi-hexagonal reconstruction of the Au(100) surface can be lifted leading to a stable unreconstructed Au(100)-(1×1) surface.[62] Two main mechanisms put forward to explain the lifting of the reconstruction are surface charging effects as a result of the electrode potential and specific adsorption of electrolyte ions.[63,64] An important advantage, unique to diffusion experiments at EC interfaces, is opened up by the option to vary the potential of the metal electrode with respect to a reference electrode. In this way diffusion energy barriers can be tuned. Below we will address electric field effects on diffusion barriers, albeit only within a crude non-self-consistent approach based on the dipole moment of the molecule.

Altogether, the objective of this paper is to derive the diffusion paths and energy barriers for BDTR/Au(100)-(1×1) from DFT and to elucidate the complex interplay of these elementary diffusion steps in a first-principles based statistical mechanics approach. Results will focus on correlations at short time scales as well as the diffusion constant characterizing the evolution of the probability distribution of a diffusing BDT radicals on long time scales.

II. CALCULATIONAL METHOD FOR THE POTENTIAL ENERGY SURFACE

Diffusion paths in configuration space with maximum statistical weight, so called minimum energy paths (MEP), have been calculated for the BDT radical on the Au(100)-(1×1) surface within DFT using slab geometries.

The total energy of the electronic ground state has been calculated using the Vienna *ab initio* simulation program (VASP) (Refs. 65–68) developed at the Institut für Materialphysik of the Universität Wien which is based on DFT. The generalized gradient approximation (GGA) by Perdew and Wang (PW91) (Ref. 69) is applied to the exchange-correlation functional and the electron-ion interaction is treated within the framework of Blöchl's projector augmented wave method (PAW).[70,71] The potentials for VASP from the database are used.[71]

Calculations of BDT radicals have been carried through with slabs comprising 4 layers of gold with a (4×4) surface unit cell. The size of the supercell perpendicular to the slab surface amounts to 25.1 Å such that the periodically repeated gold slabs are separated by a vacuum region. Asymmetric slabs have been chosen, i.e. the adsorbate binds to a single side of the slab only. A dipole correction is applied in order to account for the work function difference between the opposite surfaces of the slab.

The Kohn-Sham wave functions are expanded in a plane wave basis set with a cutoff energy of 250 eV. Plane waves up to an energy of 750 eV are used to represent the augmentation charges. The integrals over the Brillouin zone are approximated by sums over special **k**-points (Ref. 72) using a mesh consisting of 9 **k**-points in the complete first Brillouin zone of the (4×4) surface unit cell.

In Sec. III C we compare to the diffusion properties of SCH_3 radicals on the Au(100)-(1×1) surface, which have been calculated with slabs comprising 6 layers of gold. Calculations for SCH_3 radicals have been carried out using a cutoff energy for the Kohn-Sham wave functions of 340 eV (1000 eV for the augmentation charges). The mesh used to approximate the Brillouin zone integrals comprises 16 and 9 special **k**-points (Ref. 72) in the complete first Brillouin zone of the (3×3) and (4×4) surface unit cell, respectively.

The gold atoms in the outermost three layers on the adsorbate side of the slab as well as all adsorbate atoms are relaxed without constraints until the residual force per atom is smaller than 0.005 eV/Å. The atoms in the bottom layer of the slab are kept fixed at their ideal positions. All slabs have been set up using a theoretical lattice constant of 4.18 Å. The slight overestimate compared to the experimental value of 4.08 Å is consistent with other density functional calculations, *e. g.* for noble metals using GGA functionals.[73,74]

We have used the climbing-image nudged elastic band scheme (CI-NEB) (Refs. 75–78) to calculate MEPs in configuration space. We have chosen a linear interpolation in high dimensional configuration space between selected locally stable minima on the PES as an initial guess for the MEPs. Subsequently, all intermediate configurations are pre-converged using the conventional NEB scheme. In a second step, the CI-NEB scheme is employed, which converges the highest-energy configuration along the path to a local transition state.

The convergence with respect to cutoff energy, **k**-point sampling, total number of substrate layers, and coverage has been subject to systematic convergence tests as summarized in the Appendix. The overall error of the reported BDTR diffusion-energy barriers with respect to these convergence parameters amounts to approximately 0.02 eV. The error induced by the use of the approximate PW91 exchange-correlation energy functional is not included in this estimate, see Appendix.

To investigate the order of magnitude of van der Waals (vdW) interaction corrections to the diffusion energy barriers, we have evaluated semiempirical vdW interaction energies in Sec. III B. For the description of the empirical vdW interaction applied here and the choice of the parameters we refer the reader to our previous work on BDTR/Au.[61] The approach follows the ideas by Grimme and Ortmann, Bechstedt and

Schmidt.[79,80] Exchange-correlation functionals accounting for dispersion-interactions[81] are beyond the scope of the present paper. If not noted otherwise, energies quoted below are DFT-PW91 results.

The program *xbs* (Ref. 82) has been used to visualize the atomic configurations and the MEPs are depicted using open-source tools developed by G. Henkelman and his group.[78]

III. RESULTS AND DISCUSSION

To investigate the diffusion of BDT radicals on the Au(100)-(1×1) surface, we calculate diffusion paths on the PES. The PES exhibits several low-energy adsorption minima within a few $k_{\mathrm{B}}T$ of the ground state at room temperature. The complicated multi-valley total-energy landscape originates from the interplay between two adsorbate-surface bonds and the internal conformational degrees of freedom of the BDT radical.[61] These observations hint towards interesting yet complicated diffusion properties and require a survey of possible BDTR diffusion hops. As the Au(100)-(1×1) surface can be stabilized under EC conditions, we additionally estimate the influence of the EC environment on the calculated MEPs via coupling of the adsorbate dipole moment to the electric field in the EC interface. Finally, the calculated *ab initio* hopping rates will be used in a statistical master equation approach to bridge the gap from single diffusion events to diffusion dynamics on longer time scales.

A. Elementary diffusion hops

Diffusion hops between local adsorption-energy minima of BDT radicals on the Au(100)-(1×1) surface have been calculated by means of the NEB approach described above. As a reference, Fig. 1 summarizes the previously published lowest energy configurations.[61] Additional low energy configurations relevant for diffusion are described in this Reference. Guided by chemical intuition, we survey a subset of possible diffusion hops out of all pairs of low-energy local minima. It would be computationally prohibitive to calculate all MEPs connecting any two locally stable configurations. For a given initial and final configuration, a set of intermediate states is relaxed to a MEP starting from the straight line interpolation in configuration space. If an additional local energy minimum occurs along this path, it has to be added to the list of energy minima. Altogether, we end up with 14 elementary diffusion hops, which are summarized in Figs. 2, 3, and 4.

In this context, we call a diffusion hop *elementary* if no local minimum occurs along the calculated path except for the initial and final point. The whole set of elementary diffusion events, which we consider in this work, can be generated by applying the elements of the two dimensional space group *p4mm* of the Au(100)-(1×1) surface to the configurations in Figs. 2, 3, and 4.

In order to keep track of the diffusion processes it is instructive to categorize the results. The first category consists of elementary hops *I-VI* in which one S-atom moves from its local binding site to an adjacent one by crossing a bridge-like site. In this case, a common characteristic of the calculated transition states is that the position of the hopping S-atom can be best described as bridge or bridge-ontop like. Notably, only one of the two S-atoms passes over a low-coordinated bridge-site at a time. As the elementary hops *I-VI* are the only ones which result in a displacement of one of the sulfur atoms to a neighboring Au(100)-(1×1) surface unit cell, this puts a lower bound of 0.35 eV on the diffusion barrier for translations or rotations (starting from a BDTR prepared in the configuration Fig. 1a).

The second category is composed of elementary hops *VII-XIV* leading to a binding site or conformational change of the BDT radical in which both sulfur atoms stay within the Au(100)-(1×1) surface unit cell they initially bind to. In other words, the sulfur atoms do not pass any bridge- or ontop-like site of the substrate. The energy barriers for elementary hops *VII-XI* fall in the range of 0.04 - 0.19 eV with respect to the initial or final state, which is significantly lower compared to category one. This is ascribed to the fact that neither S-atom needs to surmount a low-coordinated bridge or bridge-ontop like site. Despite the fact that this is also true for diffusion hops *XII-XIV*, their energy barriers are somewhat larger, falling in the range of 0.24 - 0.53 eV. We suggest, that it is the energetically unfavorable conformational change of the alkane chain that contributes significantly to the diffusion barriers in case of the diffusion hops *XII-XIV*.

B. Translations and rotations on the surface

From the considerations above the following picture emerges for the diffusion of BDT radicals on the Au(100)-(1×1) surface. BDT radicals undergo diffusion events which lead to conformational changes and relocations of either S-atom to different binding sites. In order to undergo translations or rotations on the surface, the sulfur atoms need to cross over bridge-like sites on the substrate lattice. These processes (*I-VI*) are associated with larger activation-energy barriers and thus occur at lower rates compared to most conformational changes or local binding-site changes (*VII-XIV*). Based on our survey, we conjecture that the S-atoms subsequently cross over bridge-like transition states of low energy MEPs. This is indicative of a walking-like motion of BDT radicals on the surface. Previously Kwon *et al.* reported walking-like motion for a large sulfur bonded molecule with few internal degrees of freedom on the Cu(111) surface.[23] In case of BDTR/Au(100)-(1×1), however, the various internal degrees of freedom of BDTR allow for a more complicated walking motion involving conformational changes

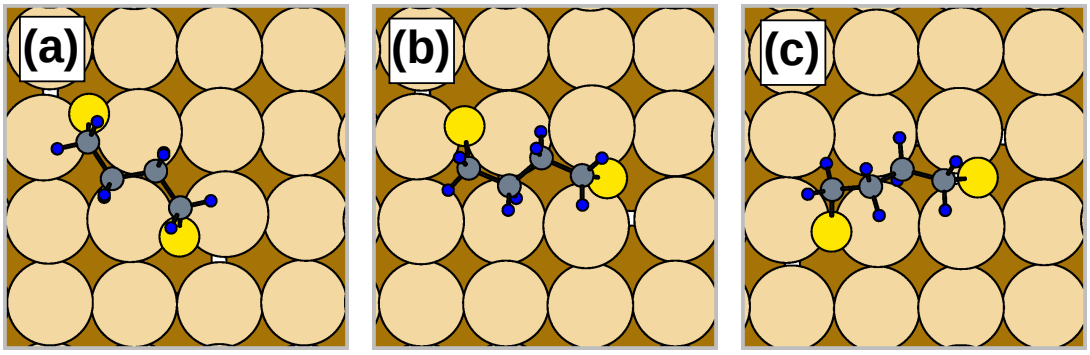

FIG. 1. (Color online) Calculated lowest-energy configurations for BDTR on the Au(100)-(1x1) surface. The binding energy with respect to the spin-polarized BDT radical in vacuum amounts to (a) -4.21 eV, (b) -4.20 eV, and (c) -4.18 eV, respectively, for a coverage of one radical per (4×4) surface unit cell. Note that these energies refer to 250 eV cutoff energy, 9 k-points in the full Brillouin zone, and 4 Au substrate layers. For 340 eV cutoff energy, 36 k-points in the full Brillouin zone, and 12 Au substrate layers the energies amount to (a) -4.11 eV, (b) -4.09 eV, and (c) -4.07 eV.[61] The tiny energy difference between the configurations is not considered to be significant. Atomic configurations are depicted schematically. Au-atoms of the first layer: large light gray or light brown circles, second layer: large dark gray or dark brown circles, S-atoms: small light gray or yellow circles, C-atoms: small gray circles, H-atoms: small black or blue circles.

as well as translations of either S-atom. It seems probable that such a complicated walking behavior could be found for a wide variety of diffusing adsorbates with two covalent bonds to the underlying substrate.

In this section we present the diffusion paths with the lowest overall activation energy barrier leading to translation and rotation of the BDTR on the Au surface. The composition of the diffusion paths from the elementary diffusion hops is not trivial due to the complexity of the paths. In fact, the diffusion paths below have been derived from integrating the master equation as described in Sec. III E.

Assuming that the BDT radical initially adopts a ground-state configuration as depicted in Fig. 1a, translation of the BDT radical by one lattice constant to an equivalent neighboring position preferentially proceeds via the MEP depicted in Fig. 5 with the corresponding atomic geometries depicted in Fig. 6. Further diffusion paths with larger overall diffusion barrier are depicted in Fig. 7 and 9. The corresponding atomic geometries are depicted in Fig. 8 and 10. The translations in Fig. 5 and 7 are composed of elementary hops *X-XIII-IX-XI-IX-I-VIII-I-XIII-X* and *II-VIII-II*, respectively, and displace the BDTR in the same direction. We consider the highest energy barrier along a path to an equivalent configuration as the corresponding diffusion barrier, which amounts to 0.35 eV in Fig. 5 and 0.43 eV in Fig. 7. Notably, translation in Fig. 5 effectively occurs via elementary hops *IX-XI-IX-I-VIII-I* with a diffusion barrie of 0.35 eV once the BDT radical has lost "memory" of its initial configuration. Here, initial and final geometry correspond to Fig. 1b. For the transition state with the largest activation energy in Fig. 5 (elementary hop I), we have carried through two subsequent unrestricted relaxations. The first relaxation has been started from the calculated approximate transition state. For the second calculation, the transition-state atomic configuration has been shifted by a small amount in the opposite direction of the previously calculated diffusion path. These two configurations relax into the two local minima from which the NEB calculation has been started. Hence, we have indeed obtained a reaction path that connects the two local minima.

Via the elementary hops *V-VII-V* as shown in Fig. 9 and 10, the BDT radical is displaced in a direction orthogonal to the translation vector in Figs. 5 and 7. The corresponding diffusion barrier is calculated to be 0.53 eV. Even though the directions associated with the considered translations are equivalent with respect to the Au(100)-(1×1) surface, the diffusion barriers differ by about 0.18 eV. This is due to the low symmetry of BDTR/Au(100)-(1×1).

Of course the translation of the BDTR in Fig. 9 could also be achieved by subsequent rotation by 90°, a translation of the type shown in Figs. 5 and 7 and a rotation by -90°. Thus, the question arises whether the preference of the molecule to move diffusively in a particular direction is preserved when such additional paths are considered.

The MEP of the lowest-energy diffusion path for rotations which we have identified is shown in Fig. 11 and the atomic geometries are shown in Fig. 12. The diffusion barrier is calculated to be 0.43 eV. The MEP is a composition of the elementary hops *X-XIII-I-II* and initial and final state of the continuous MEP are related by a space-group operation which corresponds to a 90° rotation and a vertical mirror. In fact, it turns out that BDTR translations along the diffusion path in Fig. 5 have an energy barrier which is at least 0.08 eV lower than any other combination of translation and rotation. Hence, subsequent diffusion hops are correlated, i.e. they tend to occur along the same direction (either back or forth) on the surface. This correlation is expected to decay on a time scale which roughly corresponds the the average time needed to perform a BDTR rotation. We will come

back to this issue in Sec. III E.

A semiempirical vdW correction (Ref. 79 and 80) has been evaluated for the frozen-in configurations from the PW91-MEPs discussed above. In case of translations, the MEP in Fig. 5 has the lowest diffusion energy barrier, which increases by approximately 0.09 eV when the vdW interaction-energy is included. The MEP for rotation of the BDTR is displayed in Fig. 11. In this case the diffusion energy barrier increases by 0.08 eV. Thus, when the vdW energy is *a posteriori* added to the PW91-DFT energies, the general trend is to increase the diffusion barriers for BDTR/Au(100)-(1×1). Qualitatively, however, the difference between the energy barriers for translations and rotations is preserved. In principle, one would have to go beyond the *a posteriori* correction and re-calculate the coordinates of the energy minima and diffusion paths for the PES modified by the vdW interaction energy. However, as detailed in Ref. 61, we note that the semiempirical vdW correction apparently results in an overestimate of the BDT/Au binding energy. In view of this uncertainty, we refrain from including the semiempirical vdW contribution to the MEPs in this paper.

C. Comparison to diffusion of SCH_3 - the role of BDTR conformational degrees of freedom

The DFT calculations reveal the diffusion dynamics of BDTR/Au(100), which is characterized by the elementary diffusion steps in Figs. 2, 3, and 4. Only one of the two S-atoms crosses the Au(100) bridge site at a time, resulting in a walking-like motion. In this Section we will compare this motion to the much simpler case of a single SCH_3 radical diffusing on the Au(100) surface. Can the motion of BDTR be rationalized within a simple picture of two SCH_3-legs, the motion of which is partially restrained by the $(CH_2)_4$-backbone joining the two legs? Due to the two S-Au molecule-surface bonds, the binding energy of BDTR is distinctly larger (about 1.8-1.9 eV) than the binding energy of a single SCH_3. Does this imply that diffusion is slower in case of BDTR than for SCH_3, as one might speculate at first sight? In fact, we find the opposite behavior. We will explain the reason behind this below.

SCH_3 radicals adopt an adsorption configuration on the Au(100)-(1×1) surface in which the S-atom resides in-between a hollow and bridge site of the surface, see configuration *A* in Fig. 13. The S-C bond is tilted towards the nearest bridge site by 54° with respect to the surface normal. At a coverage of one SCH_3 radical per (3×3) or (4×4) surface unit cell, the PW91-DFT binding energies $E_{\rm bind}$ amount to -2.23 and -2.27 eV, respectively (see Ref. 16 for the definition of $E_{\rm bind}$).

While $Au(SCH_3)_2$ complexes have been reported for the Au(111)-(1×1) surface [Refs. 16,83–85], our calculations suggest that on the Au(100)-(1×1) surface adsorption of single SCH_3 radicals is energetically favored. The binding energy including the energy needed to create one Au adatom amounts to -2.1 eV per SCH_3 radical of the $Au(SCH_3)_2$ complex for a (3×3) surface unit cell.

$HSCH_3$ methanethiol molecules are predicted to dissociate upon adsorption on the Au surface into SCH_3 radicals and 1/2 H_2 in the gas phase. At a coverage of one SCH_3 radical per (3×3) surface unit cell, the dissociation is energetically favored by 0.22 eV.[86] The aforementioned emphasizes that the diffusion of SCH_3/Au(100)-(1×1) is of significance beyond the model purpose it fulfills in this work.

The calculated lowest-energy diffusion-steps for SCH_3/Au(100)-(1×1) are depicted in Figs. 13 and 14. Translation to a neighboring (1×1) surface unit cell proceeds via a composition of both MEPs. At the transition state, which is 0.61 eV above the ground state configuration, the S-atom surmounts a bridge site of the Au-substrate. The energy barrier which has to be surmounted in order to change the adsorption site within a single surface unit cell is much smaller. It has been calculated to be 0.22 eV.

The calculations of the ground state and transition state reveal characteristic similarities between the diffusion paths of BDTR and the SCH_3 radical. This corroborates the proposed picture that the BDTR can be thought of as two SCH_3 radicals linked by a butane-like chain. For both adsorbates, the S-atoms adopt a ground state position in-between the hollow and bridge site of the Au-substrate in conjunction with a tilt of the S-C bond towards a bridge site. However, due to the coupling via the alkane chain, the PES of the BDTR exhibits various local minima within a range of a few 100 meV of the ground state.[61] In the lowest total-energy configuration of BDTR depicted in Fig. 1a the S-C tilt angles amount to approximately 34°, compared to a value of 54°in case of SCH_3. At the transition state, one S-atom of the BDTR is located near a bridge site of the Au-substrate. This geometry resembles the SCH_3 transition state. In particular, for the transition state ε in Fig. 6 (also see elementary hop *I*) the S-Au distances of the hopping S-atom to the two nearest Au bridge atoms amounts to 2.41 Å. The respective S-Au distances in case of SCH_3 amount to 2.41 and 2.43 Å. The S-C tilt angles with respect to the surface normal amount to 26° for the SCH_3 radical and 11°for the BDTR. Moreover, the S-C tilt angle of the quasi-stationary S-atom of the BDTR increases with respect to the ground state to 50°which is closer to the SCH_3 ground state value of 54°.

As stated at the beginning of this Section, we obtain the at first sight unexpected result that the SCH_3 diffusion barrier is almost twice as large as the diffusion barrier for the BDTR (barrier height difference 0.26 eV). This becomes plausible by considering the following two facts. While two S-Au bonds contribute to the binding energy of BDTR/Au(100), only a single S-atom is displaced at a time in case of BDTR diffusion. Thus, the diffusion barrier of BDTR/Au(100) is not much larger than the diffusion barrier of a single SCH_3 radical. Indeed, it is smaller. Due to the geometrical constraints

imposed onto the thiolate groups by the $(CH_2)_4$ backbone, neither of the two thiolate groups can aquire their optimum binding configuration. For the ground state configurations the absolute value of the binding energy of the BDTR is approximately 0.26 eV smaller than the absolute value of the binding energy of two SCH_3 radicals per (4×4) surface unit cell. This can further be illustrated by substitution of the BDTR by two SCH_3 radicals with the same atomic positions of the two S- and C_1, C_4-atoms and the same atomic coordinates of the Au-substrate. The H-atom positions are either taken from the BDTR or assumed to lie on the C_1-C_2 or C_4-C_3 bonds. If this configuration is relaxed, 0.27 eV is gained, which is very close to the energy difference of 0.26 eV quoted above. Furthermore, if the coordinates of the BDTR transition states are utilized, we obtain an energy approximately 0.61 eV above the energy of two fully relaxed SCH_3 radicals adsorbed within the (4×4) surface unit cell. This is surprisingly close to the diffusion energy barrier of a single SCH_3 radical on Au(100).

Altogether, the above calculations elucidate the effect of the alkane chain of the BDT radical on its diffusion properties. Coupling of the two thiolate groups of BDTR/Au(100) effectively leads to an increased surface mobility as compared to the mobility of each individual SCH_3 radical. In addition, the variety of possible elementary diffusion events is distinctly increased as a result of the BDTR conformational degrees of freedom.

D. Tuning the energy landscape via an external potential

Under certain EC conditions the unreconstructed Au(100)-(1×1) surface can be stabilized.[62] The interaction of the metal surface with the electrolyte at the solid-liquid interface leads to a non-vanishing excess surface charge and an electric field at the interface which can be altered by applying an additional external potential.[63,64] In this Section we estimate the effect of an electric field at the solid-liquid interface on the diffusion of BDT radicals on the Au(100)-(1×1) surface. A significant influence on the PES is to be expected in case of adsorbates with an intrinsic or charge-transfer related dipole moment.[87,90] In case of S adsorbates on Cu(100) in HCl solution Tansel and Magnussen have measured the voltage dependance of the diffusion energy barrier height. They conclude that the potential dependence of the diffusion barrier primarily results from the variation of the dipole moment of adsorbed S (i.e. charge state and adsorption geometry) during the hopping process, although a a smaller contribution caused by the Cl coadsorbate is likely.[90] Likewise, from a similar more general study presented by Giesen *et al.* the importance of adsorbate dipole moments on adsorbate surface mobility can be inferred.[87] Hence, we focus on the coupling of an electric field at the solid-liquid interface to the BDTR/Au(100) dipole moment as an important mechanism which influences the adsorbate mobility. Such an approach has been suggested and employed in previous surface diffusion studies.[88,89] Solvent effects, such as adsorption site blocking, are beyond the scope of the present work. This restricts the applied external potentials to a range where the dereconstructed Au(100) surface is stable and only small amounts of electrolyte ions are specifically adsorbed on the surface. The actual range of the external potential depends on the composition of the electrolyte.

We have calculated the dipole moment in the direction perpendicular to the Au surface from the work function differences between the periodically repeated Au slabs. All calculated dipole moments refer to the BDTR/Au(100)-(1×1) surface in vacuum. The dipole moment mainly originates from both S-C bond dipoles of the BDT radical. No significant net charge-transfer between the adsorbate and the metal surface is observed, which is consistent with a previous DFT-study of the dipole moment of SCH_3/Au(111).[91] To estimate how an electric field alters the diffusion barriers, we have evaluated the change in dipole moment along the MEPs as depicted in Figs. 5, 7, 9, and 11.

The variation of the dipole moment along the diffusion paths can be understood semi-quantitatively within a simple model. The small charge transfer between the BDTR and the surface is neglected. Then the variation of the BDTR dipole moment can be approximated by taking the z-component of the the sum of the dipole moments of two dipoles oriented parallel to the two S-C bonds. The absolute value of each dipole has been set to 0.36 eÅ equal to the dipole moment of a single SCH_3 radical in vacuum. As can be seen from Figs. 5, 7, 9, and 11, this simple S-C dipole model accounts for the predominant part of the observed variation of the dipole moment.

To account for the effect of an electric field, the electrostatic energy $-p_z E_z$ has been added non-self-consistently to the DFT total-energies, see the broken line in Figs. 5, 7, 9, and 11. The electric field has been chosen as 1.6 V/Å, which roughly corresponds to a potential of 0.4 V vs. standard calomel electrode in 0.01M $HClO_4$.[63] The electric field vector points from the BDTR side of Au surface towards the middle of the vacuum region. Nonlinear effects have been neglected. To test the non-self-consistent approach, we have carried through a self-consistent DFT test calculation with an applied electric field of 1.5 V/Å for the ground-state configurations in Fig. 1 and a CI-NEB calculation for the elementary diffusion hop XIII. The size of the supercell perpendicular to the surface has been reduced to 20 Å to avoid a spurious charge accumulation in the middle of the vacuum region. The estimated error of the selected energy differences obtained within the non-self-consistent approach between the ground-state configurations and the energy barrier for diffusion hop XIII amounts to approximately 20 meV. Note that we have not simulated electric fields larger than 1.5 V/Å self-consistently due to the artificial charge accumulation in the middle of the vacuum region.

The electric field has a significant effect on the total energy along the MEPs, which have been taken from the calculation at zero electric field, see Figs. 5, 7, 9, and 11. The coupling of the adsorbate dipole moment to the electric field leads to a lifting of the near degeneracy of the ground-state configurations in Fig. 1. The energy differences between Figs. 1a and c and between Figs. 1a and b amount to 0.16 and 0.09 eV, respectively. Furthermore, the configurations between E and E' in Fig. 5 are significantly lowered in energy, becoming nearly degenerate to the ground-state configuration in Fig. 1a. The energy relative to the ground-state configuration of the transition states labeled β and γ in Fig. 5 are increased by approximately 0.2 eV and 0.1 eV, respectively.

We emphasize that the electric field severely distorts the PES and thereby alters the position of the energy minima as well as the transition geometries. The non-self-consistent approach, using the atomic coordinates from the zero electric field relaxations, is a crude approximation, which is only valid to linear order in the electric field in case of the minima and transition states. The electrostatic dipole term can be read from from Figs. 5, 7, 9, and 11. Its significant size questions the approximation, which we therefore only apply to obtain the order of magnitude of the electric field effect on the diffusion energy barriers.

As a result, we conclude that relative diffusion energy barrier heights might significantly change when the applied potential is varied. E.g., the diffusion barrier in Fig. 7 becomes lower than in Fig. 5 due to the applied electric field. Such variations of the PES can lead to different diffusion paths, composed of different elementary diffusion steps, as a function of the electric field. At zero electric field the energy barrier is smaller for the translation of the BDTR in a particular direction than for rotation. This results in a correlation of the direction of subsequent diffusion hops. If an electric field is applied such that the energetic order of both diffusion energy barriers is inverted, this correlation can be lost. Altogether, an applied electric field offers the possibility of tuning the PES, and therewith the diffusion properties of BDTR/Au(100)-(1×1) under EC conditions.

E. Short time correlations and long-time diffusion-constant

This Section is devoted to the combination of the elementary diffusion hops into a long time-scale description of the diffusion process. In particular, we are interested in short time-scale correlations (i.e., given a particular initial orientation, the molecule preferentially moves in a certain direction on the surface) and the long-time scale isotropic, or tracer, diffusion constant. To solve this problem, we propose a master equation for the probability $p_i(t)$ of the molecule to reside in a certain configuration i. Similar techniques have been applied to chemical reaction rates.[92,93]

The set of BDTR configurations is enumerated by the multi-index i. This index describes the type of adsorption geometry, the orientation of the molecule with respect to the substrate, and the lattice vector of the Au(100)-(1×1) surface unit cell the molecule binds to. There is a one-to-one mapping between index i and configuration. The set of all configurations is generated by application of the elements of the 2D space group $p4mm$ of the Au(100)-(1×1) surface to a basis set of independent initial adsorption geometries.

According to transition state theory[94] the transition rate $\Gamma_{i\to j}$ from configuration i to j is

$$\Gamma_{i\to j} = \nu_{0,i\to j} e^{-\Delta E_{i\to j}/k_{\mathrm{B}}T}. \qquad (1)$$

For $\Delta E_{i\to j}$ the calculated DFT energy barriers are taken. We approximate the attempt frequencies $\nu_{0,i\to j}$ for the transition $i \to j$ by a universal value $\nu_{0,i\to j} = \nu_0 = 10^{12}$ s^{-1}, independent of the particular elementary transition. We note that the estimate for ν_0 is arguable. For example, values of ν_0 are $4 \cdot 10^9 \mathrm{s}^{-1}$ for DTA on Cu(111) (Ref. 25), $2 \cdot 10^{12} \mathrm{s}^{-1}$ for DMDTA on Cu(111) (Ref. 25), $10^{10.3\pm0.4} \mathrm{s}^{-1}$ for PVBA/Pd(110) (Ref. 18), or of the order of kHz for anthraquinone on Cu(111) (Ref. 15). Furthermore, a survey of pre-exponential factors $a_0^2\nu_0$ of organic molecules from the literature can be found for example in Ref. 19. However, if we assume a universal attempt frequency ν_0, this frequency can be absorbed into a rescaling of the time. For this reason the particular value of ν_0 becomes irrelevant as long as values are plotted versus the rescaled time $\nu_0 t$.

The master equation reads

$$\frac{dp_i(t)}{dt} = \sum_{j\neq i} \Gamma_{j\to i} p_j(t) - \sum_{j\neq i} \Gamma_{i\to j} p_i(t) \qquad (2)$$

As initial condition we take the BDT radical to be prepared in the configuration depicted in Fig. 1a. We do not make use of the Fourier transform approach but integrate the master equation numerically on a sufficiently large grid with periodic boundary conditions. As an aside, we note that the numerical effort can be considerably reduced by combining local energy minima that are interconnected by very low diffusion energy barriers into a single effective configuration, see Fig. 16b.

The diffusion network is depicted in Fig. 15. The Au(100)-(1×1) surface unit cell is marked by thick gray lines. The BDTR configurations are given by filled circles. The position of each circle equals the center of mass of the two sulfur atoms while the color or capital letter denotes the type of adsorption geometry of BDTR, see Figs. 2, 3, and 4. A thin line within each circle indicates the orientation of the adsorbed BDTR molecule. Elementary diffusion paths are indicated by straight lines connecting the respective configurations with the thickness of the line being proportional to the local probability current. In this way, the predominant diffusion mechanism can immediately be read from the network. The cell shown in Fig. 15 is located at the position of the

small square in Fig. 16a. For the sake of presentation we have chosen a large formal temperature $T = 1000$ K, so that all diffusion paths become visible. The predominant diffusion paths resulting from this analysis have been discussed in Sec. III B.

For a formal temperature of $T = 1000$ K, the probability $P(\vec{R}_n, t)$ of finding the the center of mass of the two BDTR sulfur atoms in the surface unit cell $\vec{R}_n$ at time $\nu_0 t = 10^5$ is presented in Fig. 16a. The isotropic probability reflects the fact that initial state memory effects have decayed. In the spatial continuum limit the probability density is a two dimensional Gaussian with width $2Dt$ and the long time scale diffusion constant D:[19]

$$P(\vec{r}, t) = \frac{1}{4\pi D t}\, e^{-\frac{(\vec{r}-\vec{r}_0)^2}{4Dt}}. \qquad (3)$$

For next-neighbor hops on a two-dimensional square lattice, the diffusion constant D is related to an effective attempt frequency ν, an effective diffusion barrier ΔE, and the surface lattice constant a_0 by an Arrhenius law:

$$D = a_0^2\, \nu\, e^{-\Delta E/k_{\rm B}T} \qquad (4)$$

Fig. 16b displays a logarithmic plot of the scaled tracer diffusion constant $D/a_0^2\nu_0$ as a function of the inverse temperature for the full and reduced network in which local energy minima separated by very low energy barriers are treated as a single effective configuration. At room-temperature the scaled tracer diffusion constant amounts to $D/a_0^2\nu_0 = 0.9{\cdot}10^{-7}$ ($D = 8{\cdot}10^5$ Å^2/s). From a linear fit to the data one obtains an effective attempt frequency $\nu/\nu_0 = 0.1$ and an effective diffusion barrier $\Delta E = 0.36$ eV. As a matter of fact, the effective diffusion barrier agrees to within 10 meV with the highest energy along the MEP depicted in Fig. 5.

The reduction of the attempt frequency $\nu_0 = 10^{12}$ s^{-1} by approximately one order of magnitude is a manifestation of the complexity of the PES. There are many local potential energy minima, which are connected by elementary diffusion hops. This can result in a complicated stochastic motion of the molecule still associated with a certain surface unit cell of the Au substrate. Consequently, given the same prefactor and diffusion energy barrier, the diffusion constant will be smaller than the diffusion constant of a point particle executing nearest-neighbor hops on the same square lattice.

Much more detailed information about the diffusion dynamics can be derived from experiment, if the random walk of the molecule can be inspected on short time scales. In this case, the orientation of the molecular axis and correlations between consecutive displacements of the molecule by a surface lattice constant come into play.

To illustrate this effect, the probability for $T = 300$ K and $\nu_0 t = 10^7$ is depicted in Fig. 16c. The average number of successful translations (given by $10^{11}\, e^{-0.36{\rm eV}/k_{\rm B}T}\; t$) is roughly two orders of magnitude smaller than in Fig. 16a. The BDT radical, initially oriented as in Fig. 1a, preferentially diffuses in the y-direction via the MEP shown in Fig. 5. In addition to this directional anisotropy of diffusion, a close inspection of the data reveals that the probability is not a two dimensional Gaussian distribution and the positions x and y are not distributed independently. The anisotropy of the probability is characterized by the quotient σ_x/σ_y of the standard deviations in the x- and y-direction, see Fig 16d. This demonstrates the decaying memory of the initial orientation of the molecule on the surface. It is expected to occur on a time scale of the order of the average time for BDTR rotations, but we have not calculated the precise effective attempt frequency for rotations.

F. Summary

The pursuit of specific functionalization of metal surfaces via thiol-bonded organic molecules requires an atomistic understanding of the bonding as well as the diffusion properties of such assemblies. The motion of molecules with two or more bonds to the surface has been reported to differ substantially from simple adatom diffusion.[15–29] With this work we contribute to the understanding of this matter by presenting DFT calculations for the diffusion of BDT radicals [BDTR: ·S-$(CH_2)_4$-S·] on the unreconstructed Au(100)-(1×1) surface, which can be stabilized in an electrochemical environment.[62] At low coverage, BDTR is anchored to the surface by two S-Au bonds as reported in a previous DFT study.[61] Reaction paths for conformational changes of the alkane chain as well as hops of either of the two S atoms to neighboring (1×1) surface unit cells have been calculated. These processes constitute the elementary diffusion events.

Diffusion of BDTR proceeds via subsequent elementary diffusion events, resulting in a complicated walking like motion. The lowest energy diffusion paths for translations along perpendicular directions and in-plane rotations of BDTR on the Au(100)-(1×1) surface have been identified. A result of the calculation is that the diffusion energy barriers along orthogonal directions are different. Within DFT-PW91 they amount to $\Delta E^{(1)}_{\rm translation} = 0.35$ and $\Delta E^{(2)}_{\rm translation} = 0.53$ eV. The diffusion barrier for in-plane rotation amounts to $\Delta E_{\rm rotation} = 0.43$ eV.

To arrive at a description of the diffusion which takes all calculated transitions into account, the elementary diffusion events are combined in a master equation approach. As an approximation, a universal attempt frequency ν_0 has been assumed. As long as scaled, dimensionless rates or times are considered, results are independent of the value of ν_0. For illustration, we use a value of $\nu_0 = 10^{12}$ s^{-1}. Due to different energy barriers for translation and in-plane rotation, ($\Delta E^{(1)}_{\rm translation} < \Delta E_{\rm rotation} < \Delta E^{(2)}_{\rm translation}$), the direction of subsequent displacements of the adsorbate is correlated. On long time scales orientational memory is lost and the probability distribution becomes isotropic. The diffusion constant D obeys an Arrhenius law with an effective diffusion barrier of 0.36 eV and effective attempt frequency of $\nu/\nu_0 =$

0.1. At room-temperature the tracer diffusion constant amounts to $D/a_0^2\nu_0 = 0.9{\cdot}10^{-7}$ ($D = 8{\cdot}10^5$ Å^2/s).

By comparison to the diffusion of a single SCH_3 radical, the effect of the BDTR alkane chain on the diffusion properties is reasoned. Albeit BDTR binds significantly stronger to the Au(100) substrate (binding energy -4.11 eV) than the SCH_3 radical (binding energy -2.27 eV), the translation diffusion barrier of BDTR (0.35 eV) is lower than that of the SCH_3 radical (0.61 eV). We conjecture that this is due to geometrical constraints arising from the connection of the two S-Au anchors via the alkane chain, which affect the ground state and transition state differently. Such a mechanism could be of general importance for similar molecular adsorbate systems.

Experiments at the electrochemical solid-liquid interface offer the opportunity to tune the diffusion energy barriers by an applied electrostatic potential. To obtain a qualitative impression, this effect has been crudely estimated via the electrostatic coupling of the electric field to the BDTR/Au(100)-(1×1) dipole moment. The non-self-consistent evaluation of the electrostatic interaction reveals a significant impact on the potential energy landscape due to the variation of the BDTR/Au(100)-(1×1) dipole moment along the diffusion paths. Thus, we speculate that for certain applied electric field the energetical order of the diffusion energy barriers for translation and rotation may change, which might lead to even qualitatively different diffusion paths and loss of correlation between successive displacements of the adsorbate on the surface.

ACKNOWLEDGMENTS

This work has been supported financially by the Deutsche Forschungsgemeinschaft (DFG) within project Pe497/4-1. Calculations have been carried through at the Rechenzentrum der Universität Kiel.

Appendix: Convergence tests

We estimate the error of the BDTR/Au(100)-(1×1) DFT diffusion barriers with respect to cutoff energy, **k**-point sampling, and total number of substrate layers. The diffusion barriers have been re-calculated using frozen-in atomic coordinates calculated with the convergence parameters described in Sec. II.

Tab. I summarizes the convergence test for the MEPs depicted in Fig. 7. The cumulative error related to the cutoff energy of the plane-wave expansion, the number of Au layers in the slab, and number of **k**-points is estimated to be 0.02 eV. We note that the chemisorption energies vary more strongly with convergence parameters. The convergence of diffusion energy barriers profits from error cancellation.

Furthermore, we have attempted to estimate the dependence of the diffusion barriers on coverage. To this purpose, we compare results obtained for a (4×3) and a slightly larger (4×4) surface unit cell. The energy barriers of elementary hops III, IV, and VII change by less than 0.01 eV and energy barriers of V and VI increase by less than 0.02 eV. The largest effect was observed in case of elementary diffusion hop I, for which the energy barrier decreased by approximately 0.06 eV.

The largest uncertainty of the diffusion energy barriers is expected to be due to the approximate exchange-correlation (XC) energy functional. The contribution to total energy from the vdW interaction can of course neither be described by the LDA nor by the GGA. Nevertheless, it still makes sense to compare results from LDA and PW91-GGA to obtain an impression of the sensitivity of the energy barriers on the choice of the semi-local approximation to the XC functional.[95,96] For simplicity, the LDA energy barriers in Tab. I have been calculated for the PW91 geometries and lattice constant. Using the LDA, the maximum increase of the diffusion barriers amounts to 0.09 eV.

TABLE I. Convergence of the diffusion barrier for translations depicted in Figs. 7 and 9. Diffusion barriers have been recalculated using the relaxed atomic positions obtained with a 250 eV cutoff energy, 9 *k*-points in the full Brillouin zone, 4 Au substrate layers, and the PW91-GGA.

E_{cutoff} (eV)	N_{kpt}	N_{layer}	$E_{\text{xc}}[n]$	ΔE_{diff} (eV)
		Fig. 7		
250	9	4	GGA	0.43
340	36	12	GGA	0.44
250	9	4	LDA	0.45
		Fig. 9		
250	9	4	GGA	0.53
340	36	12	GGA	0.55
250	9	4	LDA	0.62

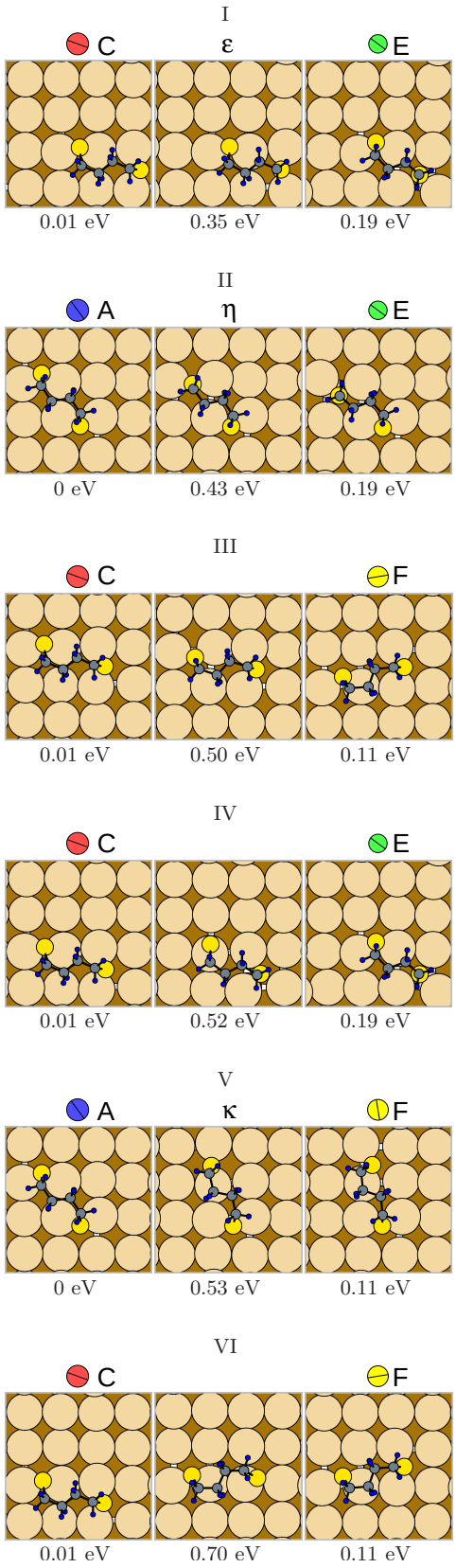

FIG. 2. (Color online) Calculated elementary diffusion hops *I*-*VI* of a BDTR on the Au(100)-(1×1) surface. The energy of the initial, final, and transition state is given below the configurations. The configuration in Fig. 1a has been chosen as the common reference energy for all elementary hops. Configurations are labelled by Roman numbers and filled circles. The capital letter or color denotes the type of adsorption geometry and the line within each circle indicates the orientation of the BDT radical. Transition states which are depicted in a figure of a MEP are tagged by Greek letters. Atomic geometries are depicted schematically according to the same scheme as in Fig. 1.

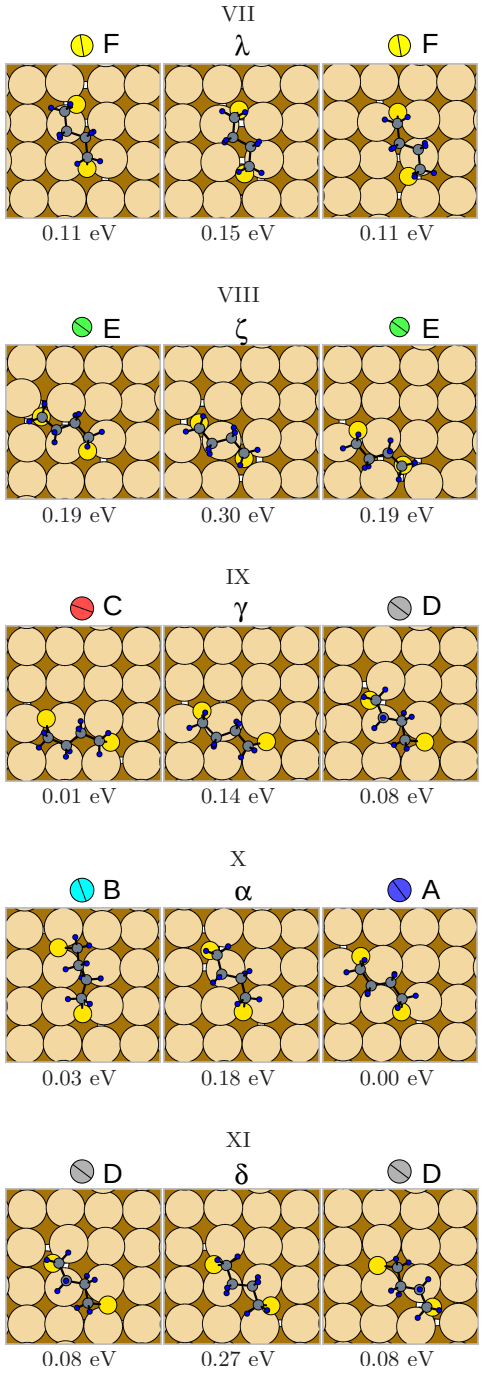

FIG. 3. (Color online) Calculated elementary diffusion hops *VII-XI* of a BDTR on the Au(100)-(1×1) surface. For an explanation of the notation see Fig. 2. Atomic geometries are depicted schematically according to the same scheme as in Fig. 1.

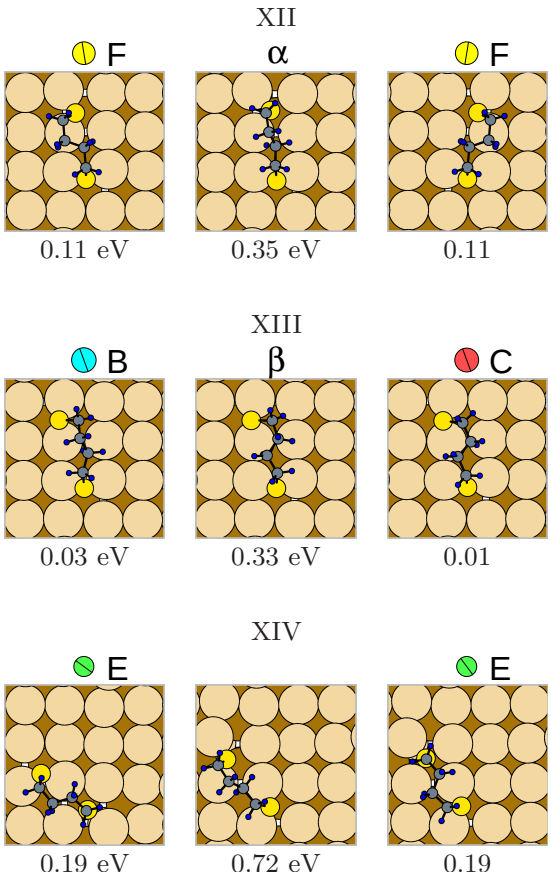

FIG. 4. (Color online) Calculated elementary diffusion hops *XII*-*XIV* of a BDTR on the Au(100)-(1×1) surface. For an explanation of the notation see Fig. 2. Atomic geometries are depicted schematically according to the same scheme as in Fig. 1.

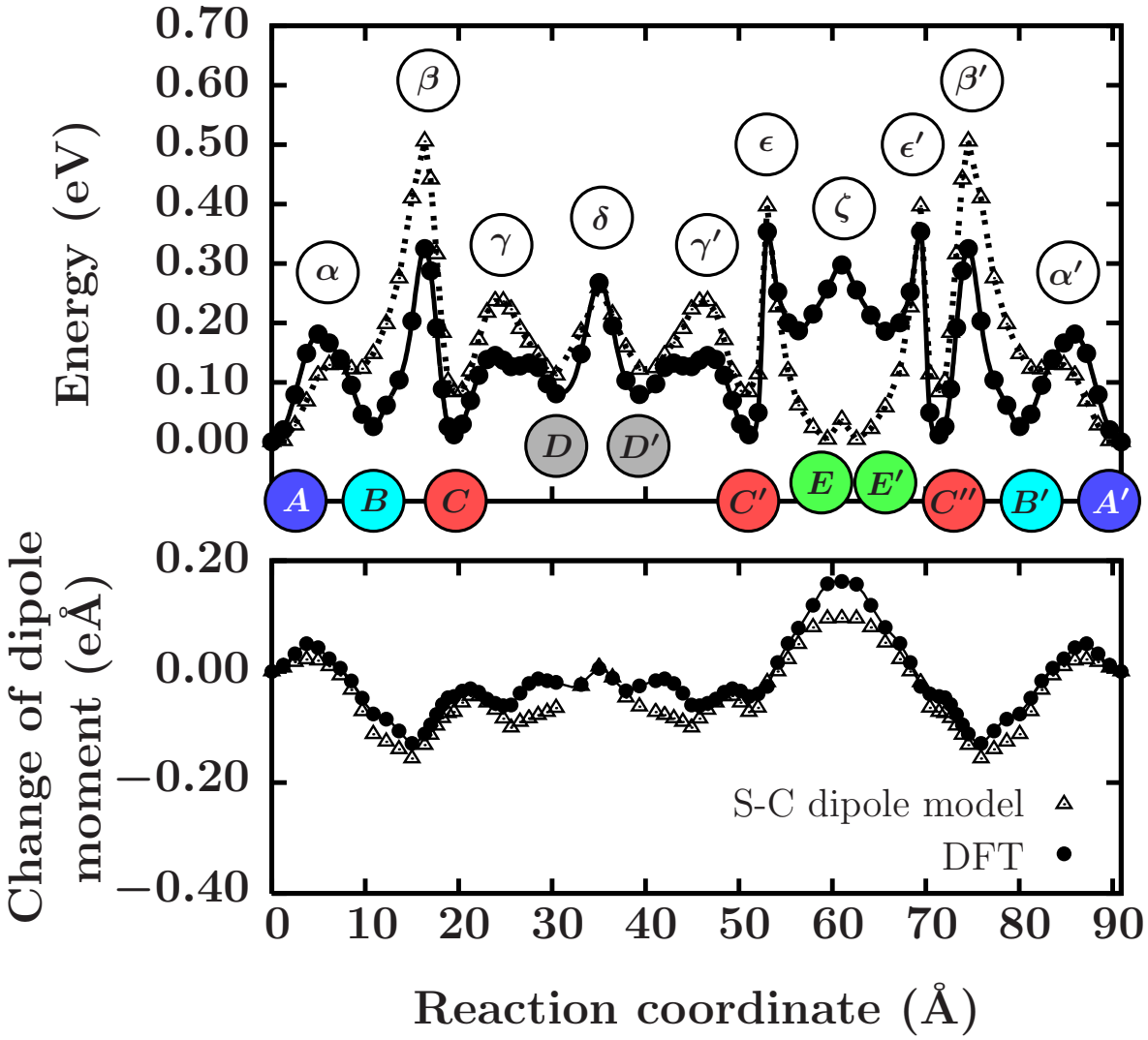

FIG. 5. (Color online) Upper panel: Lowest-barrier MEP for a translation of BDTR on the Au(100)-(1×1) surface. The MEP is a composition of individual CI-NEB runs connecting local minima. Filled circles refer to the interface to vacuum as calculated within DFT. They represent the intermediate configurations used in the DFT CI-NEB runs. Triangles are obtained by adding to the DFT energies the electrostatic energy of the BDTR dipole moment in an electric field of 1.6 V/Å. Capital letters tag (meta)stable configurations, while Greek letters tag local transition states. Geometries that merely differ by a two-dimensional space-group operation of the substrate are primed. Atomic geometries are depicted in Fig. 6. The capital letter or color of each circle denotes the different (meta)stable adsorption configurations, see Figs. 2, 3, and 4. Lower panel: Variation of the dipole moment along the MEP. Filled circles calculated within DFT. Triangles denote results from the S-C dipole model.

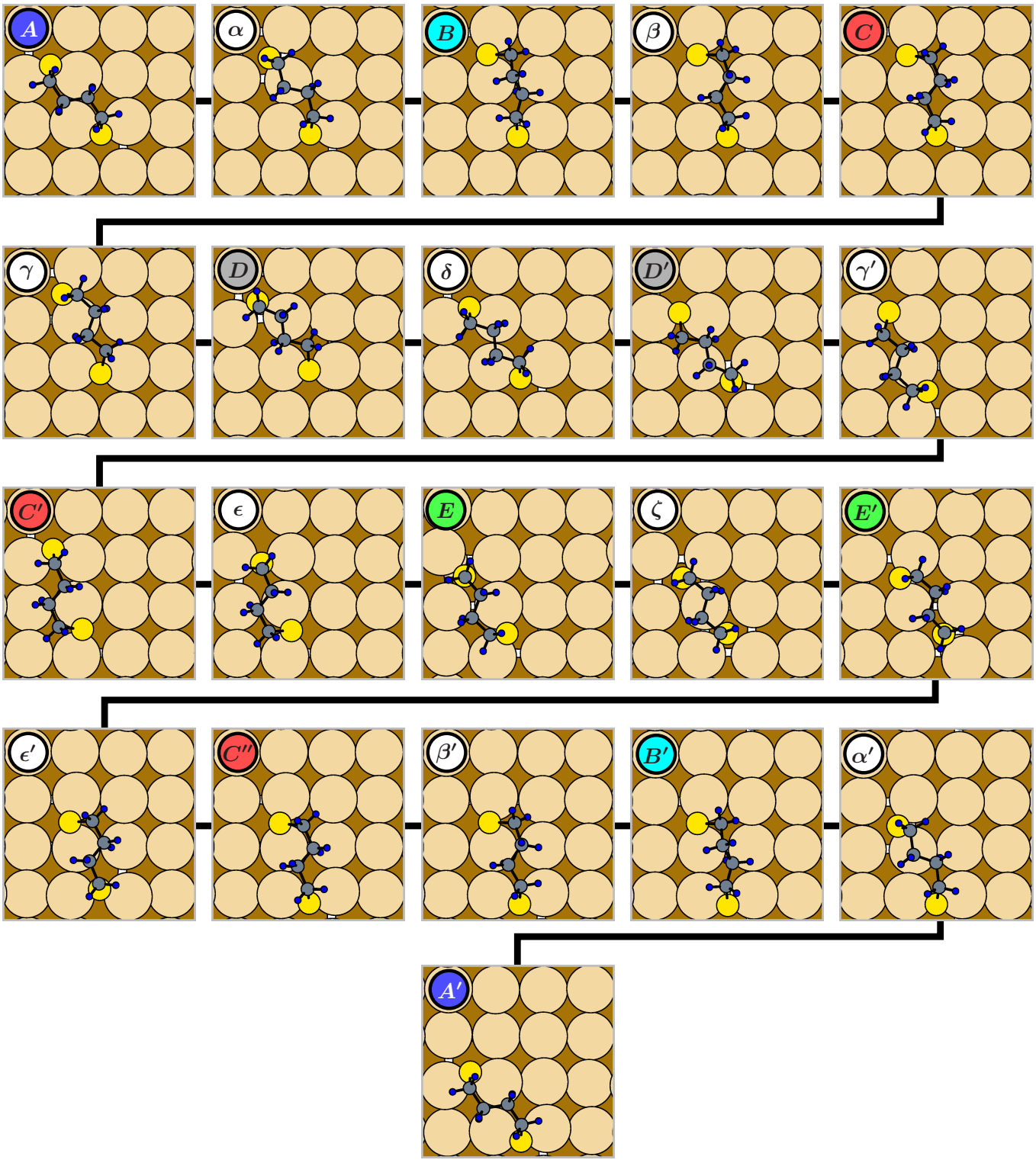

FIG. 6. (Color online) Atomic geometries of (meta)stable and transition state configurations along the lowest-barrier MEP for a translation of BDTR on the Au(100)-(1×1) surface (same path as in Fig. 5). The atomic geometries are depicted schematically according to the same scheme as in Fig. 1. The MEP is composed of elementary hops *X-XIII-IX-XI-IX-I-VIII-I-XIII-X*. Capital letters tag (meta)stable configurations, while Greek letters tag local transition states. Geometries that merely differ by a two-dimensional space-group operation of the substrate are primed.

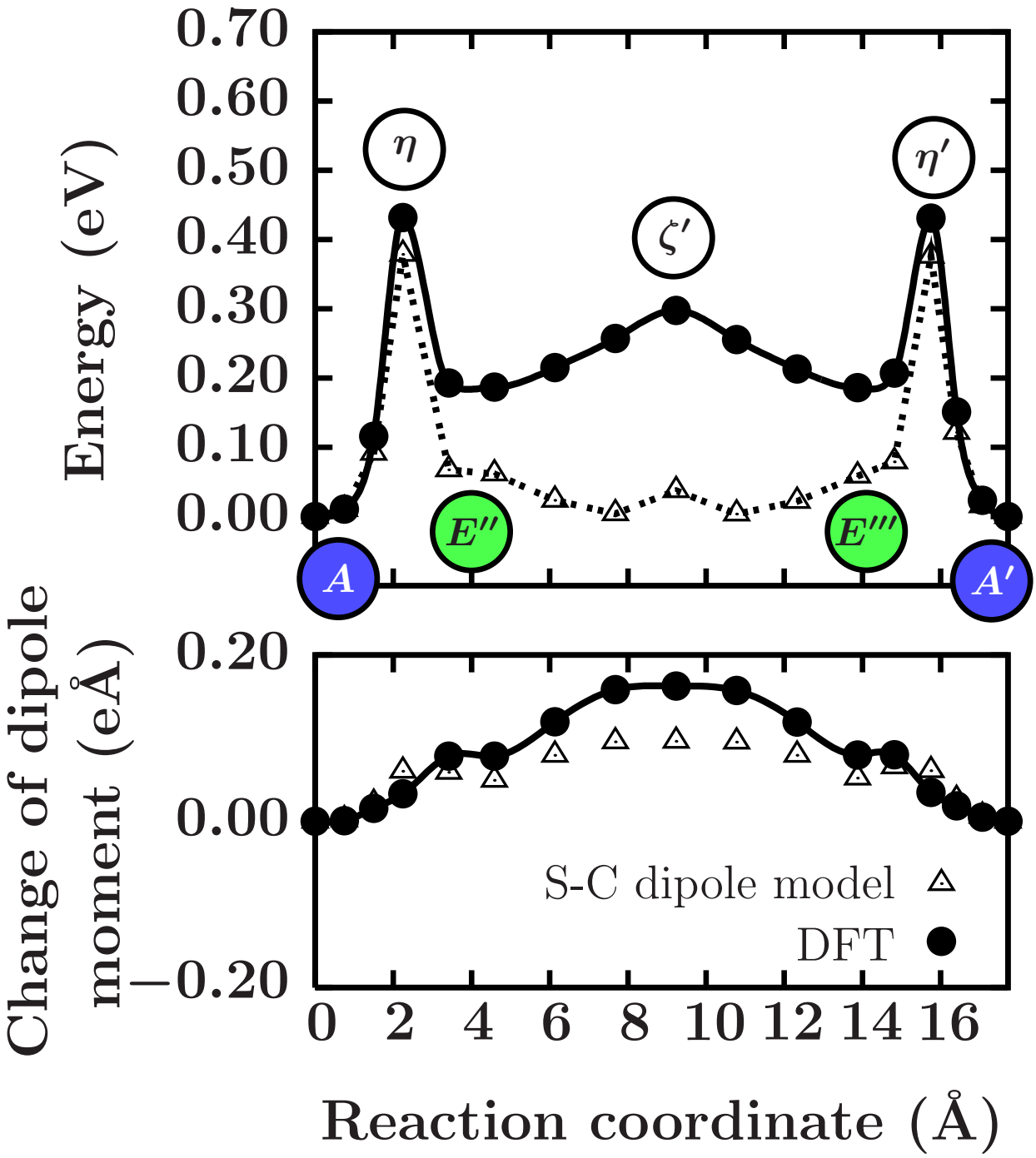

FIG. 7. (Color online) Upper panel: MEP for a translation of BDTR on the Au(100)-(1×1) surface. The energy barrier competes with the lowest energy barrier of the MEP in Fig. 5. Note that the optimum path can depend on the applied electric field. Atomic geometries are depicted in Fig. 8. Lower panel: Variation of the dipole moment along the MEP. For an explanation of the notations see Fig. 5.

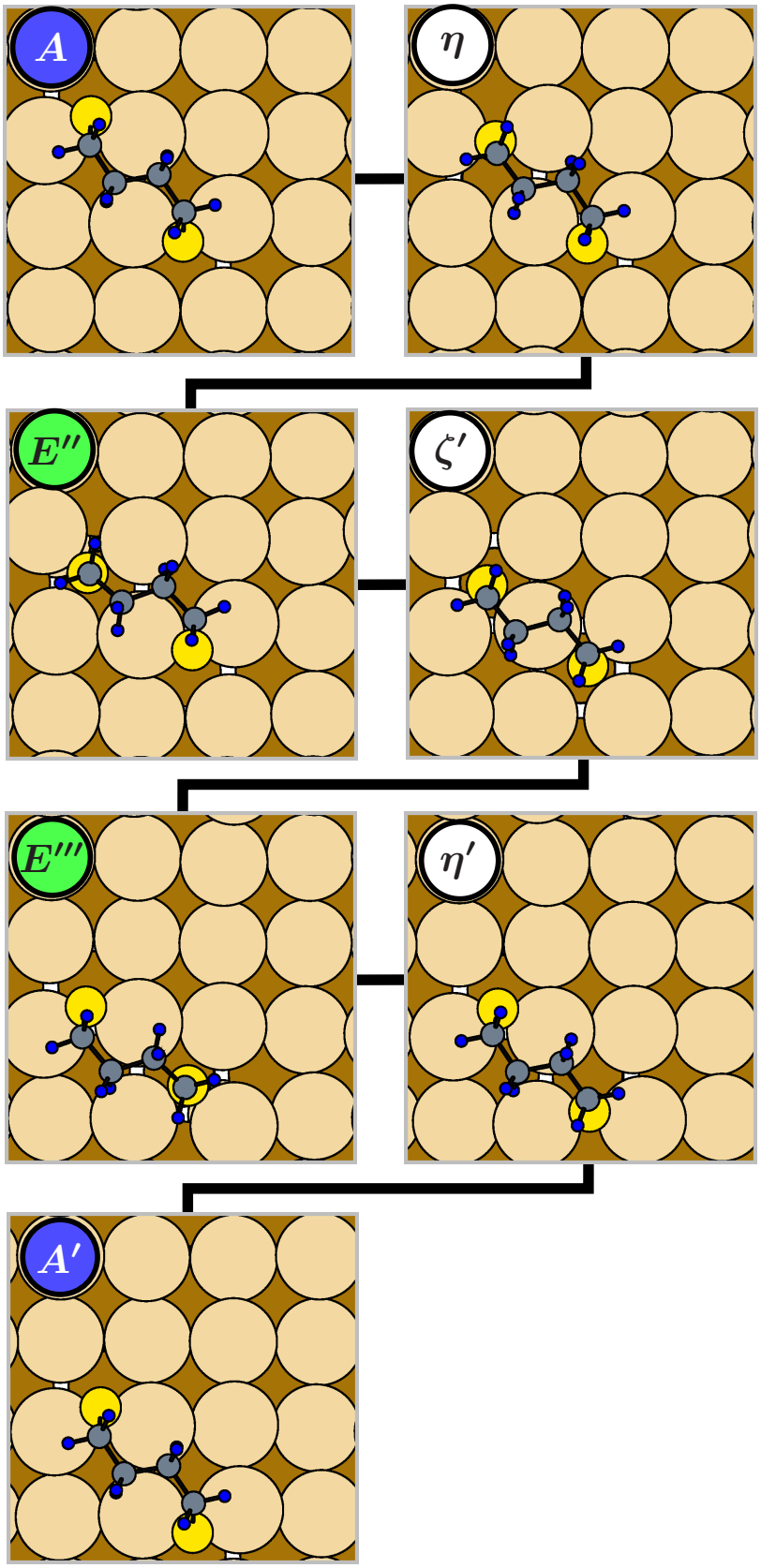

FIG. 8. (Color online) Atomic geometries of (meta)stable and transition state configurations along the MEP in Fig. 7. The MEP is composed of elementary hops *II*-*VIII*-*II*. For an explanation of the notations see Fig. 6.

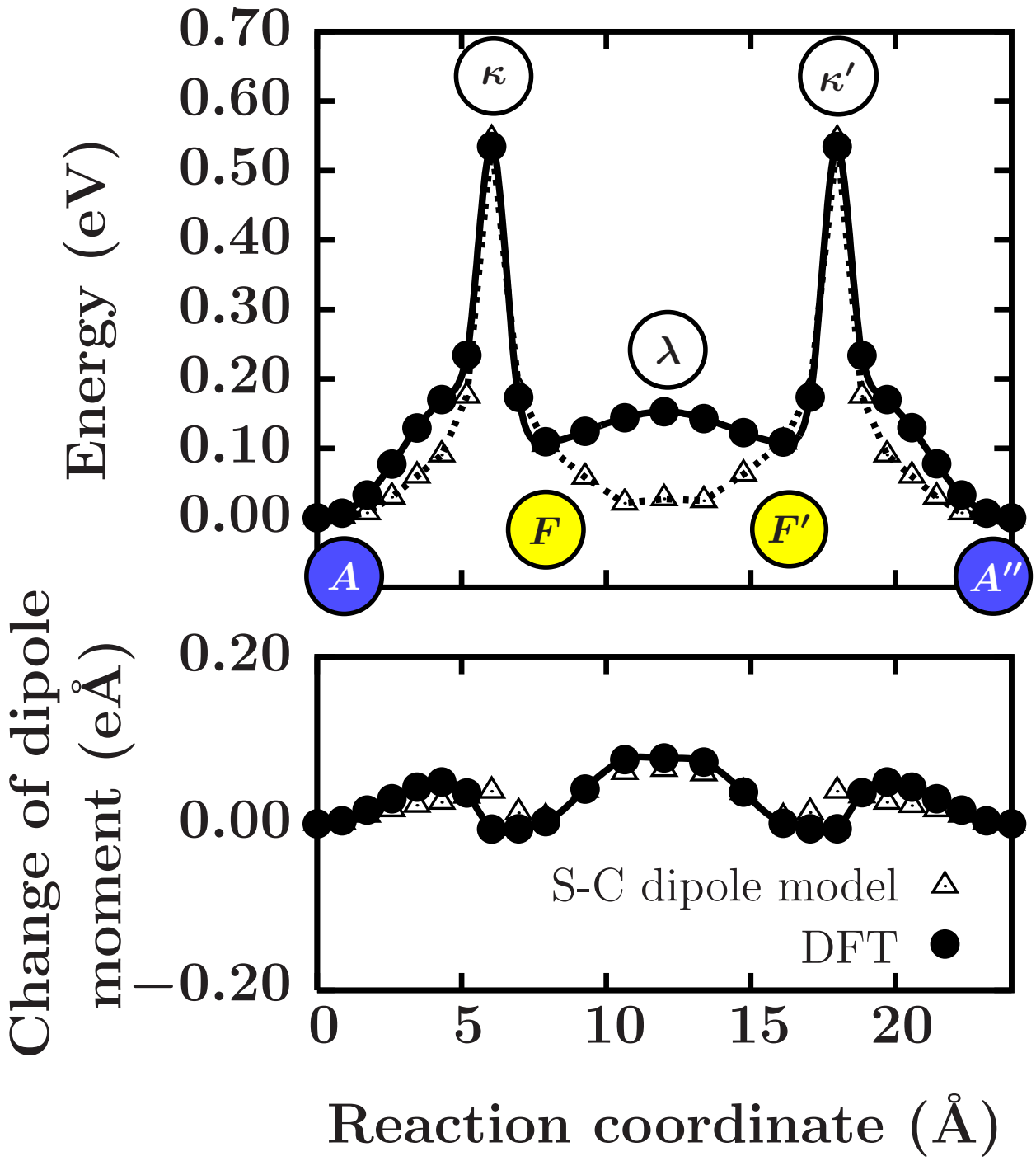

FIG. 9. (Color online) Upper panel: MEP for a translation of BDTR on the Au(100)-(1×1) surface. While the initial and final orientation of the BDTR with respect to the substrate are the same as in Figs. 5 and 7, the direction of displacement is orthogonal. Atomic geometries are depicted in Fig. 10. Lower panel: Variation of the dipole moment along the MEP. For an explanation of the notations see Fig. 5.

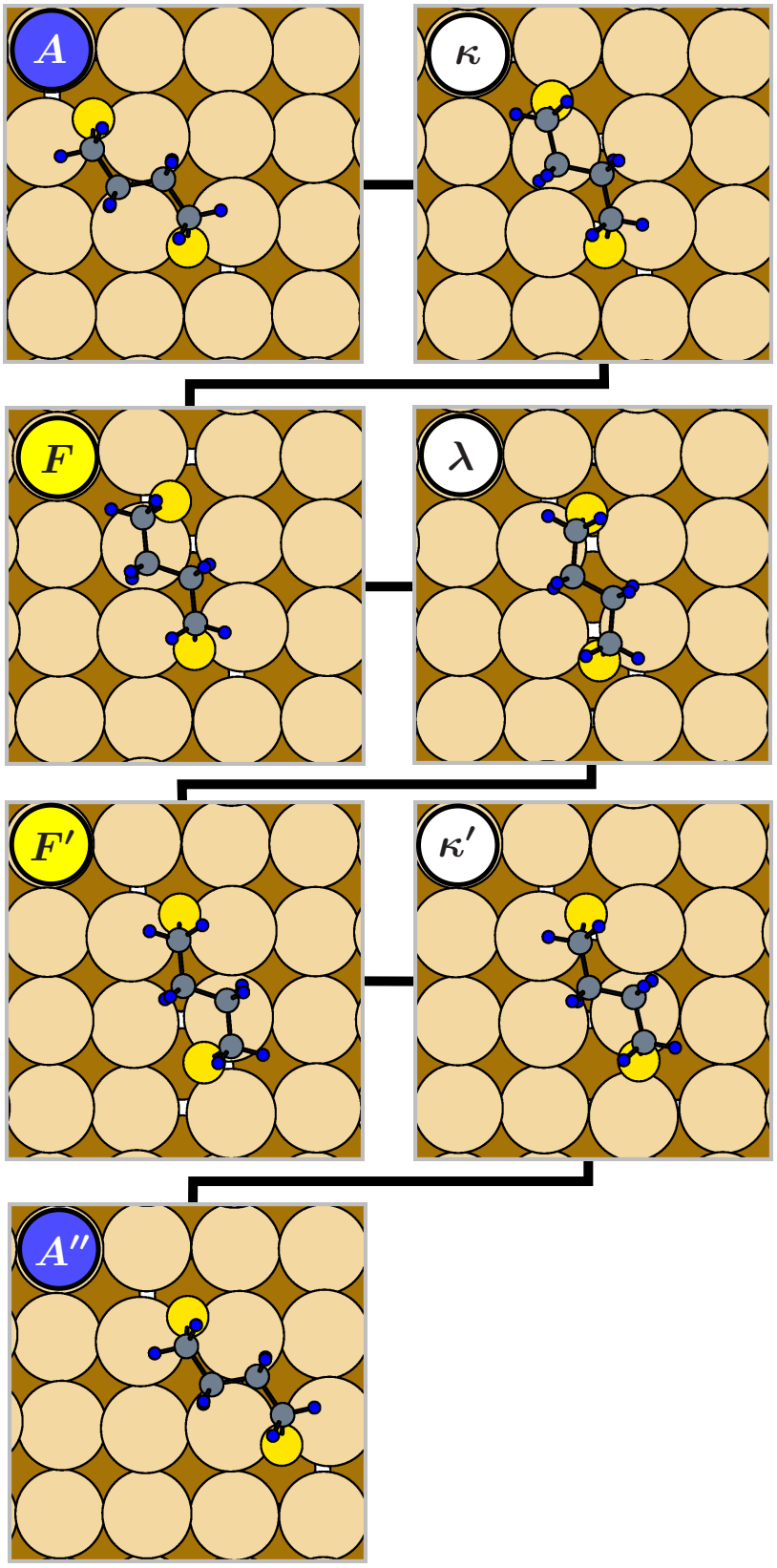

FIG. 10. (Color online) Atomic geometries of (meta)stable and transition state configurations along the MEP in Fig. 9. The MEP is composed of elementary hops *V*-*VII*-*V*. For an explanation of the notations see Fig. 6.

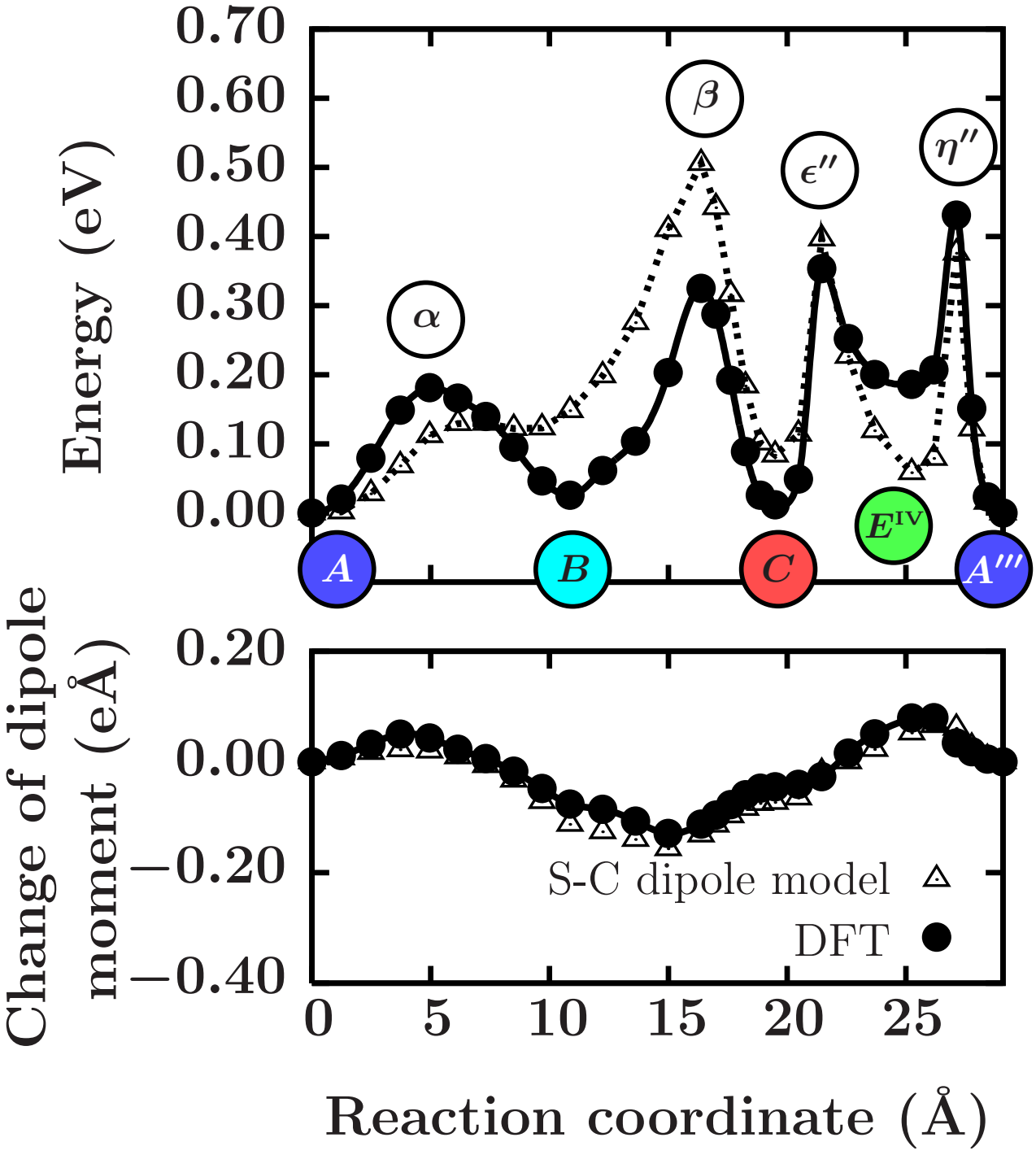

FIG. 11. (Color online) Upper panel: Lowest-barrier MEP for a rotation of BDTR on the Au(100)-(1×1) surface. Atomic geometries are depicted in Fig. 12. Lower panel: Variation of the dipole moment along the MEP. For an explanation of the notations see Fig. 5.

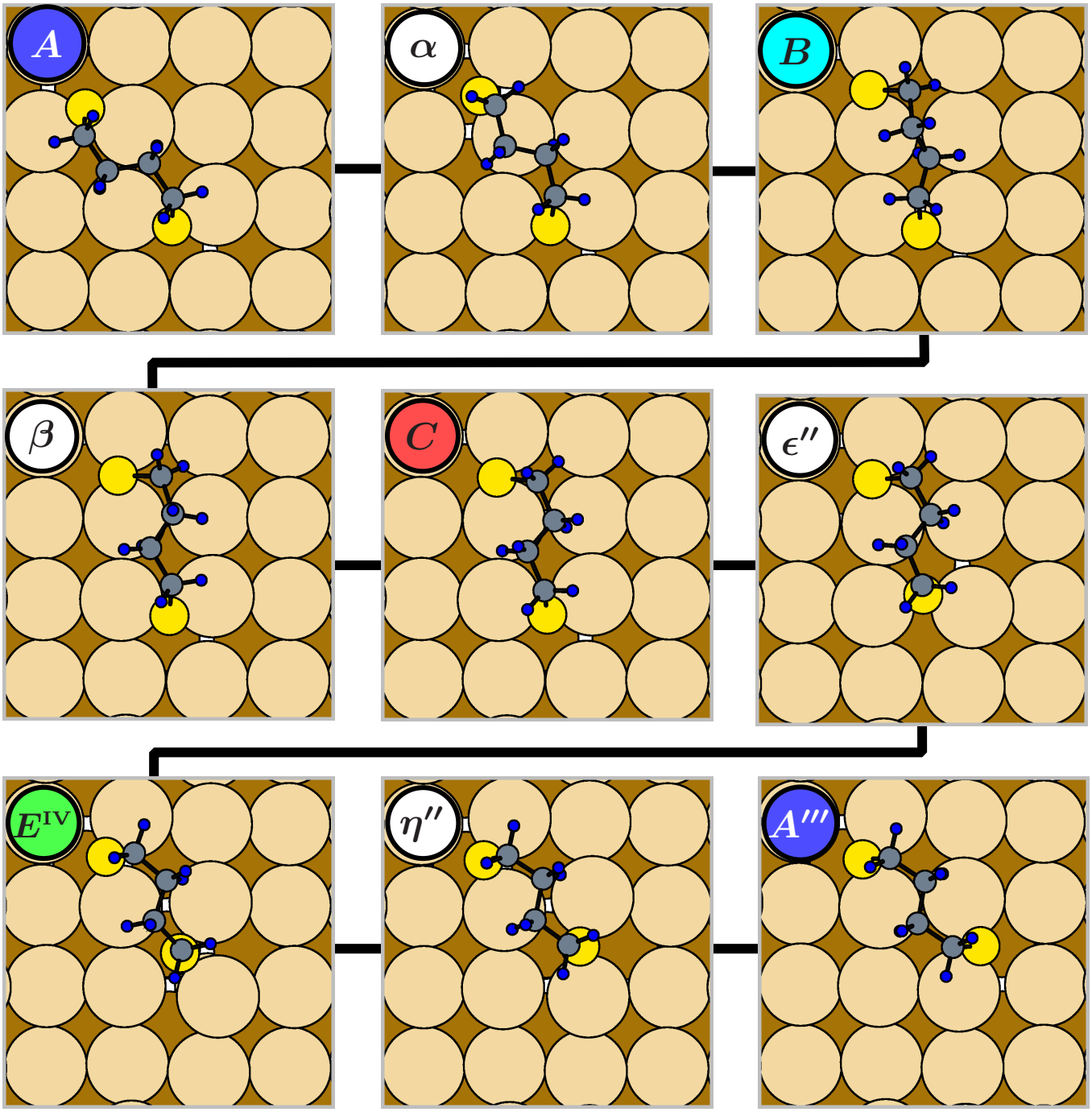

FIG. 12. (Color online) Atomic geometries of (meta)stable and transition state configurations along the MEP in Fig. 11. The MEP is composed of elementary hops *X-XIII-I-II*. For an explanation of the notations see Fig. 6.

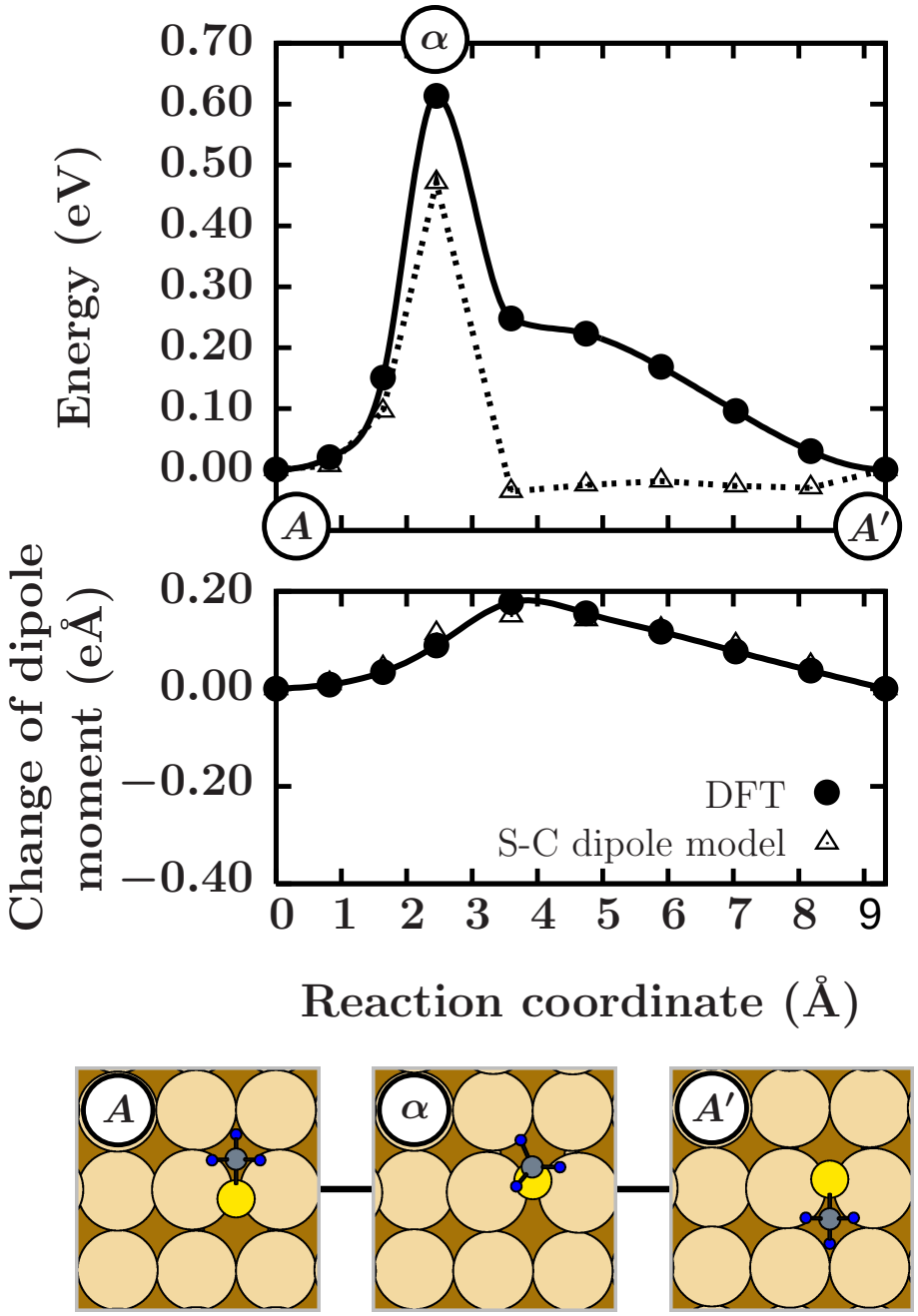

FIG. 13. (Color online) Upper panel: Lowest-barrier MEP for an SCH_3 radical crossing a bridge site of the Au(100)-(1×1) surface. Lower panel: Variation of the dipole moment along the MEP. Bottom: Atomic geometries of stable and transition-state configurations along the MEP. For an explanation of the notations see Figs. 5 and 6.

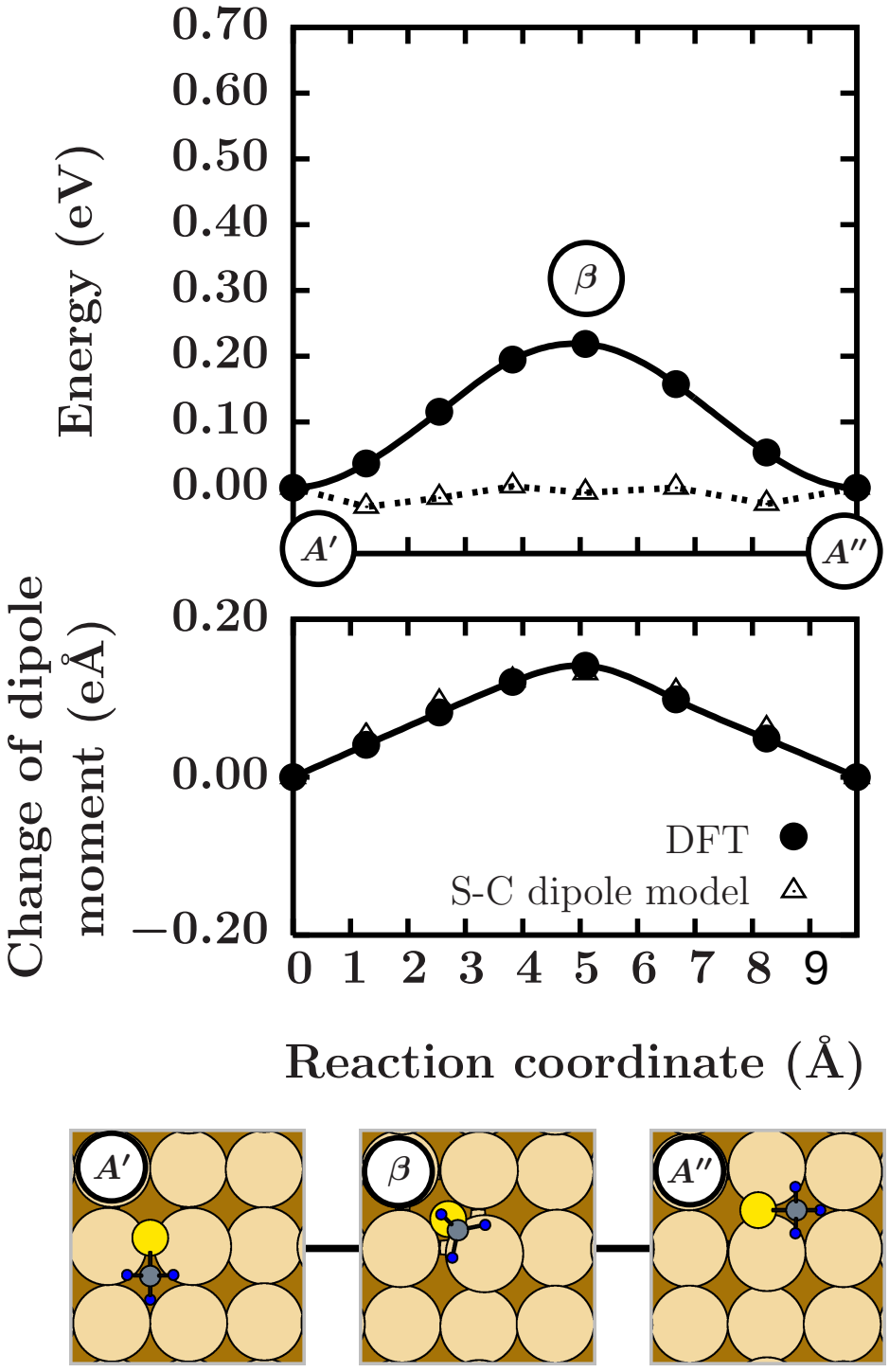

FIG. 14. (Color online) Upper panel: Lowest-barrier MEP for a 90° rotation of an SCH_3 radical on the Au(100)-(1×1) surface. After rotation, the SCH_3 radical is attached to another hollow-bridge site within the same surface unit cell. Lower panel: Variation of the dipole moment along the MEP. Bottom: Atomic geometries of stable and transition-state configurations along the MEP. For an explanation of the notations see Figs. 5 and 6.

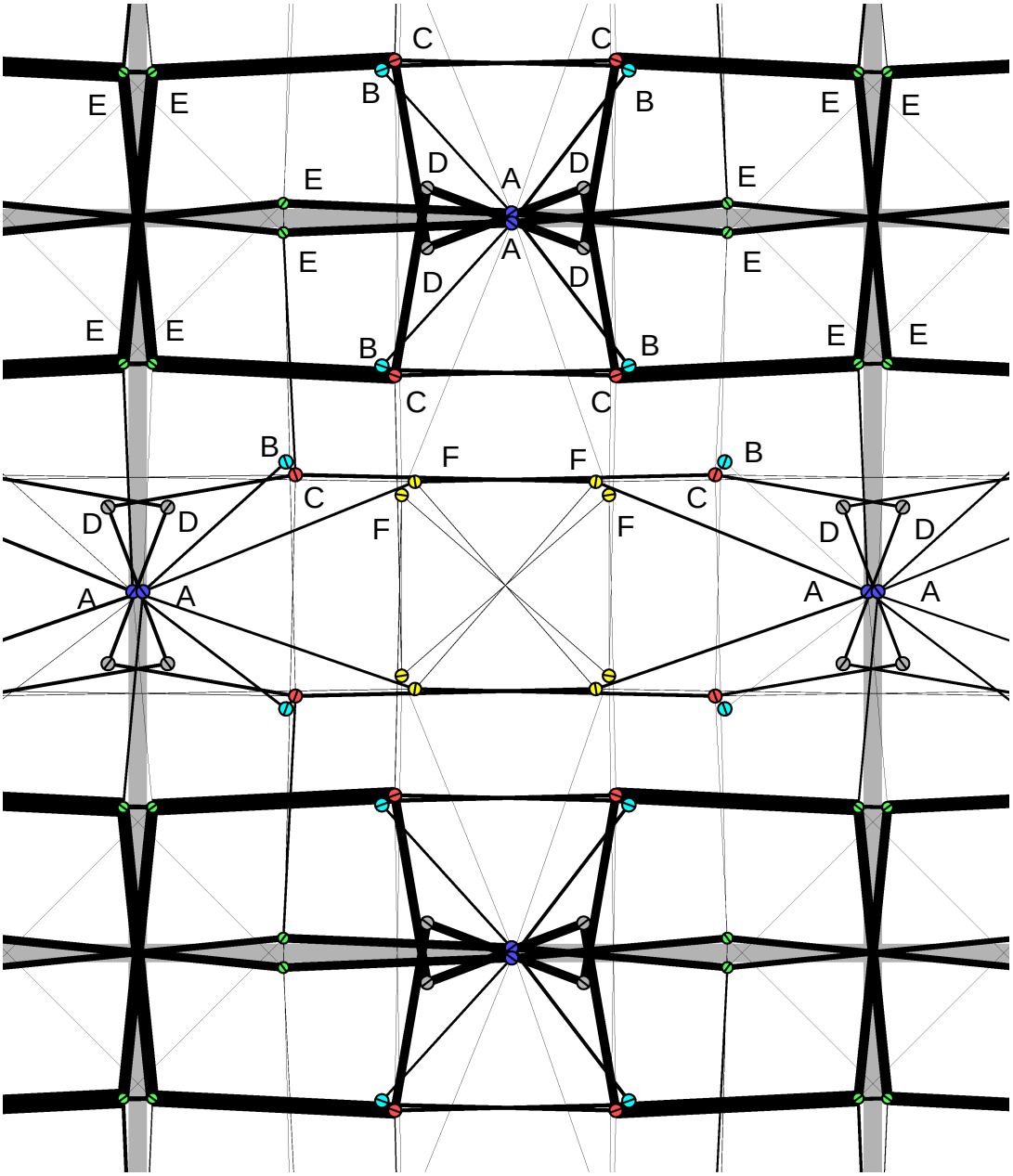

FIG. 15. (Color online) Diffusion network for BDTR/Au(100)-(1×1). The surface unit cell is marked by thick gray lines. Filled circles denote the BDTR configurations. The position of each circle equals the center of mass of the two sulfur atoms while the capital letter or color denotes the type of adsorption geometry of BDTR as in Figs. 2, 3, and 4. Capital letters have been omitted in the lower half of the figure. A thin line within each circle indicates the orientation of the adsorbed BDTR. Elementary diffusion paths connect the configurations (straight lines). The thickness of the line is proportional to the local probability current. The cell is located at the position of the small square in Fig. 16a. A large formal temperature of $T = 1000$ K has been chosen such that all diffusion paths become visible.

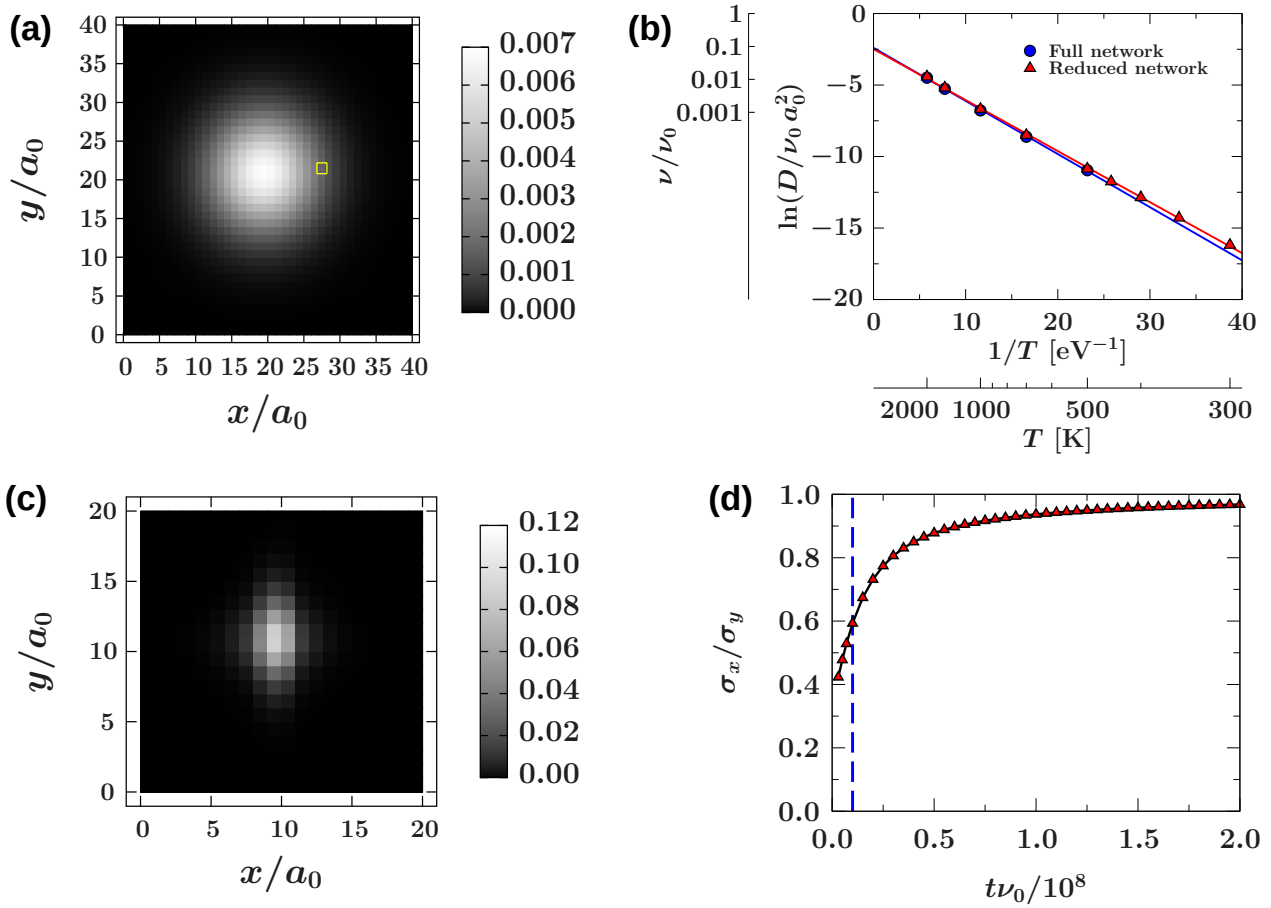

FIG. 16. (Color online) (a) Probability of finding the center of mass of the two BDTR sulfur atoms in a given surface unit cell at scaled time $\nu_0 t = 10^5$ and a formal temperature of $T = 1000$ K. The small square indicates the position at which the diffusion network and the local probability currents in Fig. 15 have been calculated. (b) Logarithmic plot of the scaled tracer diffusion constant $D/(a_0^2\nu_0)$ as a function of the inverse temperature $1/T$. The reduced network is obtained by combining energy minima separated by very low energy barriers into single effective configurations. From a linear fit to the data an effective scaled attempt frequency $\nu/\nu_0 = 0.1$ and a diffusion barrier $\Delta E = 0.36$ eV is obtained. (c) Probability of finding the center of mass of the two BDTR sulfur atoms in a given surface unit cell at scaled time $\nu_0 t = 10^7$ and a temperature of $T = 300$ K. Note that, despite the fact that $\nu_0 t$ is larger than in (a), the number of successful displacements of the BDTR is smaller than in (a) due to the lower temperature. The observed anisotropy is ascribed to short-time correlations. (d) Anisotropy of the probability at $T = 300$ K, characterized by the quotient σ_x/σ_y of the standard deviations in the x- and y-direction, versus scaled time. The broken line indicates the time for which the probability in (c) bas been drawn.

* franke@theo-physik.uni-kiel.de

[1] C. Joachim, J. K. Gimzewski, and A. Aviram, Nature **408**, 541 (2000).
[2] F. Schreiber, J. Phys.: Cond. Mat. **16**, R881 (2004).
[3] W. Browne and B. Feringa, Natur Nanotechnology **1**, 25 (2006).
[4] L. Gao, Q. Liu, Y.Y. Zhang, N. Jiang, H.G. Zhang, Z.H. Cheng, W.F. Qiu, S.X. Du, Y.Q. Liu, W.A. Hofer, and H.-J. Gao, Phys. Rev. Lett. **101**, 197209 (2008).
[5] E. R. Kay, D. A. Leigh, and F. Zerbetto, Angew. Chem. Int.Ed. **46**, 72 (2007).
[6] B. Baisch, D. Raffa, U. Jung, O. M. Magnussen, C. Nicolas, J. Lacour, J. Kubitschke, and R. Herges, J. Am. Chem. Soc. **131**, 442 (2009).
[7] Y. Wang, J. Kröger, R. Berndt, and W. A. Hofer, J. Am. Chem. Soc. **131**, 3639 (2009).
[8] M. Alemani, S. Selvanathan, F. Ample, M. V. Peters, K.-H. Rieder, F. Moresco, C. Joachim, S. Hecht, and L. Grill, J. Phys. Chem. C **112**, 10509 (2008).
[9] C. Dri, M. V. Peters, J. Schwarz, S. Hecht, and L. Grill, Nature Nanotechnology **3**, 649 (2008).
[10] A. S. Kumar, T. Ye, T. Takami, B.-C. Yu, A. K. Flatt, J. M. Tour, and P. S. Weiss, Nano Lett. **8**, 1644 (2008).
[11] M. Alemani, M. V. Peters, S. Hecht, K.-H. Rieder, F. Moresco, and L. Grill, J. Am. Chem. Soc. **128**, 14446 (2006).
[12] B.-Y. Choi, S.-J. Kahng, S. Kim, H. Kim, H. W. Kim, Y. J. Song, J. Ihm, and Y. Kuk, Physical Review Letters **96**, 156106 (2006).
[13] M. J. Comstock, N. Levy, A. Kirakosian, J. Cho, F. Lauterwasser, J. H. Harvey, D. A. Strubbe, J. M. J. Fréchet, D. Trauner, S. G. Louie, and M. F. Crommie, Physical Review Letters **99**, 038301 (2007).
[14] J. Lahann, S. Mitragotri, T.-N. Tran, H. Kaido, J. Sundaram, I. S. Choi, S. Hoffer, G. A. So morjai, and R. Langer, Science **299**, 371 (2003).
[15] K. L. Wong, G. Pawin, K.-Y. Kwon, X. Lin, T. Jiao, U. Solanki, R. H. J. Fawcett, L. Bartels, S. Stolbov, and T. S. Rahm an, Science **315**, 1391 (2007).
[16] A. Franke and E. Pehlke, Phys. Rev. B **79**, 235441 (2009).
[17] J. S. Raut and K. A. Fichthorn, J. Chem. Phys. **108**, 1626 (1998).
[18] J. Weckesser, J. V. Barth, and K. Kern, J. Chem. Phys. **110**, 5351 (1999).
[19] J. V. Barth, Surf. Sci. Rep. **40**, 75 (2000).
[20] J. Weckesser, J. V. Barth, and K. Kern, Phys. Rev. B **64**, 161403(R) (2001).
[21] M. Schunack, T. R. Linderoth, F. Rosei, E. Lægsgaard, I. Stensgaard, and F. Besenbacher, Phys. Rev. Lett. **88**, 156102 (2002).
[22] R. Otero, F. Hümmelink, F. Sato, S. B. Legoas, P. Thostrup, E. Laegsgaard, I. Stensgaard, D. S. Galvao, and F. Besenbacher, Nature Mat. **3**, 779 (2004).
[23] K.-Y. Kwon, K. L. Wong, G. Pawin, L. Bartels, S. Stolbov, and T. S. Rahman, Phy. Rev. Lett. **95**, 166101 (2005).
[24] S. Subramanian and J.-C. Wang, J. Chem. Phys. **123**, 014706 (2005).
[25] G. Pawin, K. L. Wong, K.-Y. Kwon, R. J. Frisbee, T. S. Rahman, and L. Bartels, J. Am.Chem. Soc. **130**, 15244 (2008).
[26] G. E. Poirier and E. D. Pylant, Science **272**, 1145 (1996).
[27] I. Doudevski, W. A. Hayes, and D. K. Schwartz, Phys. Rev. Lett. **81**, 4927 (1998).
[28] H. Kondoh, C. Kodama, H. Sumida, and H. Nozoye, J. Chem. Phys. **111**, 1175 (1999).
[29] D. K. Schwartz, Ann. Rev. Phys. Chem. **52**, 107 (2001).
[30] H. Song, Y. Kim, Y. H. Jang, H. Jeong, M. A. Reed, and T. Lee, Nature **462**, 1039 (2009).
[31] D. L. Klein, R. Roth, A. K. L. Lim, A. P. Alivisatos, and P. L. McEuen, Nature **389**, 699 (1997).
[32] M. A. Reed, C. Zhou, C. J. Muller, T. P. Burgin, and J. M. Tour, Science **278**, 252 (1997).
[33] J. G. Kushmerick, D. B. Holt, J. C. Yang, J. Naciri, M. H. Moore, and R. Shashidhar, Phys. Rev. Lett. **89**, 086802 (2002).
[34] F. Schreiber, Prog. Surf. Sci. **65**, 151 (2000).
[35] Q. Sun, A. Selloni, and G. Scoles, Chem. Phys. Chem. **6**, 1906 (2005).
[36] R. B. Pontes, F. D. Novaes, A. Fazzio, and A. J. R. da Silva, J. Am. Chem. Soc. **128**, 8996 (2006).
[37] X. D. Cui, A. Primak, X. Zarate, J. Tomfohr, O. F. Sankey, A. L. Moore, T. A. Moore, D. Gust, G. Harris, and S. M. Lind say, Science **294**, 571 (2001).
[38] R. P. Andres, T. Bein, M. Dorogi, S. Feng, J. I. Henderson, C. P. Kubiak, W. Mahoney, R. G. Osifch in, and R. Reifenberger, Science **272**, 1323 (1996).
[39] G. Meshulam, N. Rosenberg, A. Caster, L. Burstein, M. Gozin, and S. Richter, Small **1**, 848 (2005).
[40] L. E. Harrell, T. P. Bigioni, W. G. Cullen, R. L. Whetten, and P. N. First, J. Vac. Sci. Tech. B **17**, 2411 (1999).
[41] T. Ohgi, H. Y. Sheng, and H. Nejoh, Applied Surface Science **130-132**, 919 (1998).
[42] T. Ohgi, H. Y. Sheng, Z. C. Dong, H. Nejoh, and D. Fujita, Appl. Phys. Lett. **79**, 2453 (2001).
[43] K. Bandyopadhyay and K. Vijayamohanan, Langmuir **14**, 6924 (1998).
[44] N. Vandamme, J. Snauwaert, E. Janssens, E. Vandeweert, P. Lievens, and C. V. Haesendonck, Surf. Sci. **558**, 57 (2004).
[45] T. Nakanishi, B. Ohtani, K. Shimazu, and K. Uosaki, Chemical Physics Letters **278**, 233 (1997).
[46] H. Noda, Y. Tai, A. Shaporenko, M. Grunze, and M. Zharnikov, J. Phys. Chem. B **109**, 22371 (2005).
[47] D. Qu and K. Uosaki, J. Phys. Chem. B **110**, 17570 (2006).
[48] T. Nakamura, H. Kondoh, M. Matsumoto, and H. Nozoye, Langmuir **12**, 5977 (1996).
[49] M. Carot, M. Esplandiu, F. Cometto, E. Patrito, and V. Macagno, J. Electroanal. Chem. **579**, 13 (2005).
[50] T. Y. B. Leung, M. C. Gerstenberg, D. J. Lavrich, G. Scoles, F. Schreiber, and G. E. Poirier, Langmuir **16**, 549 (2000).
[51] K. Kobayashi, J. Umemura, T. Horiuchi, H. Yamada, and K. Matsushige, Jpn. J. Appl. Phys. **37**, 297 (1998).
[52] K. Kobayashi, H. Yamada, T. Horiuchi, and K. Matsushige, Applied Surface Science **144-145**, 435 (1999).
[53] J.-J. Yu, J. N. Ngunjiri, A. T. Kelley, and J. C. Garno, Langmuir **24**, 11661 (2008).
[54] M. Esplandiu, M. Carot, F. Cometto, V. Macagno, and E. Patrito, Surface Science **600**, 155 (2006).
[55] J. Liang, L. G. Rosa, and G. Scoles, J. Phys. Chem. C **111**, 17275 (2007).
[56] S. W. Joo, S. W. Han, and K. Kim, J. Phys. Chem. B **104**,

6218 (2000).
[57] P. Kohli, K. K. Taylor, J. J. Harris, and G. J. Blanchard, J. Am. Chem. Soc. **120**, 11962 (1998).
[58] S. Rifai, M. Laferriere, D. Qu, D. D. M. Wayner, C. P. Wilde, and M. Morin, J. Electroanal. Chem. **531**, 111 (2002).
[59] H. Hamoudi, Z. Guo, M. Prato, C. Dablemont, W. Q. Zheng, B. Bourguignon, M. Canepa, and V. A. Esaulov, Phys. Chem. Chem. Phys. **10**, 6836 (2008).
[60] C. D. Bain, E. B. Troughton, Y. T. Tao, J. Evall, G. M. Whitesides, and R. G. Nuzzo, J. Am. Chem. Soc. **111**, 321 (1989).
[61] A. Franke and E. Pehlke, Phys. Rev. B **81**, 075409 (2010).
[62] D. Kolb and J. Schneider, Electrochim. Acta **31**, 929 (1986).
[63] S. Venkatachalama, P. Kaghazchib, L. Kiblera, D. Kolb, and T. Jacob, Chem. Phys. Lett. **455**, 47 (2008).
[64] T. Jacob, Electrochim. Acta **52**, 2229 (2006).
[65] G. Kresse and J. Hafner, Phys. Rev. B **47**, 558 (1993).
[66] G. Kresse and J. Hafner, Phys. Rev. B **49**, 14251 (1994).
[67] G. Kresse and J. Furthmüller, Comp. Mat. Sci. **6**, 15 (1996).
[68] G. Kresse and J. Furthmüller, Phys. Rev. B **54**, 11169 (1996).
[69] J. P. Perdew, J. A. Chevary, S. H. Vosko, K. A. Jackson, M. R. Pederson, D. J. Singh, and C. Fiolhais, Phys. Rev. B **46**, 6671 (1992).
[70] P. E. Blöchl, Phys. Rev. B **50**, 17953 (1994).
[71] G. Kresse and D. Joubert, Phys. Rev. B **59**, 1758 (1999).
[72] H. J. Monkhorst and J. D. Pack, Phys. Rev. B **13**, 5188 (1976).
[73] M. Fuchs, M. Bockstedte, E. Pehlke, and M. Scheffler, Phys. Rev. B **57**, 2134 (1998).
[74] H. Shi and C. Stampfl, Phys. Rev. B **77**, 094127 (2008).
[75] H. Jónsson, G. Mills, and K. W. Jacobsen, "Classical and quantum dynamics in condensed phase simulations," (World Scientific Press, 1998) Chap. Nudged Elastic Band Method for Finding Minimum Energy Paths of Transitions, p. 385.
[76] G. Henkelman, B. Uberuaga, and H. Jónsson, J. Chem. Phys. **113**, 9901 (2000).
[77] G. Henkelman and H. Jónsson, J. Chem. Phys. **113**, 9978 (2000).
[78] The climbing-image NEB extension to VASP and post-processing scripts are available under `http://theory.cm.utexas.edu/henkelman`.
[79] S. Grimme, J. Comp. Chem. **27**, 1787 (2006).
[80] F. Ortmann, F. Bechstedt, and W. G. Schmidt, Phys. Rev. B **73**, 205101 (2006).
[81] M. Dion, H. Rydberg, E. Schröder, D. C. Langreth, and B. I. Lundqvist, Phys. Rev. Lett. **92**, 246401 (2004).
[82] *xbs* is available under `www.ihp-ffo.de/~msm`.
[83] P. Maksymovych, D. C. Sorescu, and J. T. Yates, Phys. Rev. Lett. **97**, 146103 (2006).
[84] Y. Wang, N. S. Hush, and J. R. Reimers, J. Am. Chem. Soc. **129**, 14532 (2007).
[85] A. Nagoya and Y. Morikawa, J. Phys.: Cond. Mat. **19**, 365245 (2007).
[86] Including zero-point energy-correction, the energy needed to dissociate $HSCH_3$ to form 1/2 H_2 and a SCH_3 radical in the gas-phase is calculated to be 1.56 eV.
[87] M. Giesen, G. Beltramo, S. Dieluweit, J. Mller, H. Ibach, and W. Schmickler, Surf. Sci. **595**, 127 (2005).
[88] J. E. Müller and H. Ibach, Phys. Rev. B **74**, 085408 (2006).
[89] K. Pötting, W. Schmickler, and T. Jacob, Chem. Phys. Chem. **11**, 1395 (2010).
[90] T. Tansel and O. M. Magnussen, Phys. Rev. Lett. **96**, 026101 (2006).
[91] P. C. Rusu and G. Brocks, Phys. Rev. B **74**, 073414 (2006).
[92] A. Maranzana, J. R. Barker, and G. Tonachini, Physical Chemistry Chemical Physics **9**, 4129 (2007).
[93] S. H. Robertson, M. J. Pilling, L. C. Jitariu, and I. H. Hillier, Physical Chemistry Chemical Physics **9**, 4085 (2007).
[94] G. H. Vineyard, J. Phys. Chem. Solids **3**, 121 (1957).
[95] P. Sony, P. Puschnig, D. Nabok, and C. Ambrosch-Draxl, Phys. Rev. Lett. **99**, 176401 (2007).
[96] E. McNellis, J. Meyer, and K. Reuter, Phys. Rev. B **80**, 205414 (2009).

4.4 Diffusion of 1,4-butanedithiol radicals on the unreconstructed Au(111) surface

In this Section the results of DFT calculations for the diffusion of BDTR on the unreconstructed Au(111)-(1 × 1) surface are presented. The Au(111) surface belongs to the most widely studied substrate surfaces for SAMs of S bonded organic molecules.[22] Under ultra high vacuum (UHV) conditions the Au(111) surface reconstructs to a higher density of atoms within the first atomic layer (herringbone reconstruction).[266] The principle part of this reconstruction can be represented as a soliton reconstruction with a very large $(22 \times \sqrt{3})$ surface unit cell.[266] Under certain EC conditions, however, the surface reconstruction can be lifted and an unreconstructed Au(111)-(1 × 1) surface can be stabilized.[151] In these cases a characterization of BDTR/Au(111)-(1 × 1) diffusion from first principles can be valuable to complement experimental data and establish a thorough atomistic understanding of the matter. *In situ* experiments, which demonstrate the assessability of diffusion properties of BDTR/Au(111)-(1 × 1) under EC conditions, have been performed by Suto and Magnussen.[171] For a brief summary see Sec. 2.2.2.

The potential energy surface of BDTR/Au(111)-(1 × 1) comprises (local) energy minima as has been detailed in Ref. 84. An assessment of the diffusion on such a complicated PES is highly non-trivial because the BDTR motion on the surface will inevitably involve several local minima along the diffusion pathway. In the following the employed strategy to find candidates for BDTR diffusion paths is outlined and results for diffusion modes which lead to translations and rotations on the Au(111)-(1 × 1) surface are presented. In part, the focus will be on the question whether short-time correlations may play a role for the diffusion characteristics of this system. As opposed to experiments for the solid-vacuum interface, the PES may be tuned via an applied external potential under EC conditions in certain cases. The influence of an electric field at the surface on the diffusion energy barriers will be estimated via an electrostatic coupling of the adsorbate dipole moment to the electric field. Despite the crudeness of such an approach, the qualitative effect of an external potential on the energy barriers is compared to preliminary experimental results. Finally, a partitioning scheme to cope with calculations of the PES for large molecules and surface unit cells has been assessed. Whenever the Au(111) surface is referred to in the following discussion, it is implicitly assumed that one deals with an unreconstructed Au(111)-(1 × 1) surface.

4.4.1 Diffusion modes

Employed diffusion-path search-strategy

Hops between local minima on the PES will be calculated within DFT using the NEB and CI-NEB algorithms. Some local minima which are relevant for diffusion have been published in Ref. 84. The search for diffusion paths starts from the ground state configuration depicted in Fig. 4.8 published in Ref. 84. Other configurations representing

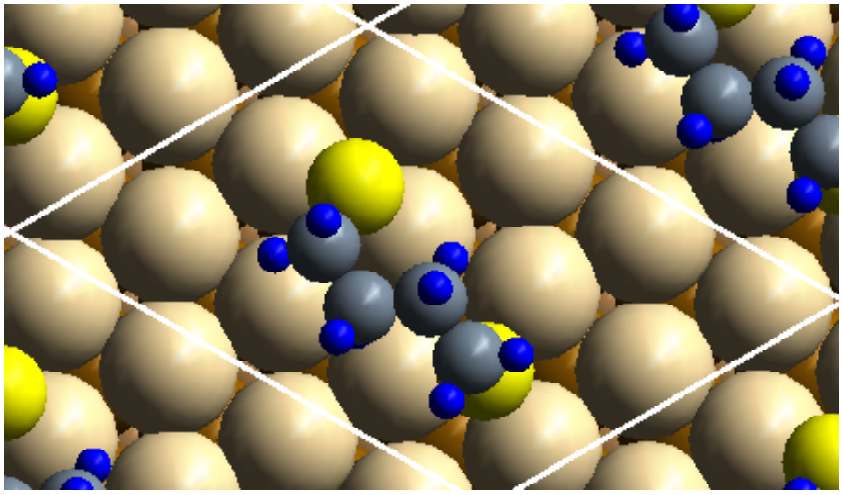

Figure 4.8: The ground state configuration of a BDTR on the unreconstructed Au(111) surface. The Figure has been taken from Ref. 84.

local minima on the PES, which are relevant for diffusion, are detailed below. Due to the very large number of local minima on the entire PES, only a subset of transitions from one configuration to the next can be included in the search. It was unfeasible to determine the complete network of interconnections between (meta)stable configurations. The choice of intermediate configurations along candidates for diffusion paths has been guided by chemical intuition and the overall goal to obtain configuration space paths leading to translations and rotations of BDTR on the Au(111) surface.

Candidates for diffusion paths for BDTR/Au(111) have been selected from five different basic diffusion modes depicted in Fig. 4.9. These basic modes comprise three inequivalent translations, $\boldsymbol{\tau}_1$, $\boldsymbol{\tau}_2$, and $\boldsymbol{\tau}_3$, of the BDTR on the Au(111) surface to nearest neighbor ground state configurations. The translations are inequivalent with respect to the BDTR geometries. In addition, two inequivalent rotations around the surface normal by 120° to symmetry equivalent ground state configurations have been calculated. A counterclockwise rotation around the surface normal is denoted as (+) and, conversely, a clockwise rotation as (−).

Having defined the basic diffusion modes brings about the task of calculating MEPs connecting the initial and final state of the described modes. The idea behind these MEP calculations has been inspired from the adsorption and diffusion properties of SCH_3 and $Au(SCH_3)_2$ on the Au(111) surface.[39] First of all, SCH_3 radicals favor bonding close to hollow or bridge sites of the Au(111) substrate surface and tend to stay in the proximity of these sites along the diffusion path. Furthermore, the diffusion of $Au(SCH_3)_2$ complexes with two S-Au bonds to the Au(111) surface proceeds via subsequent hops of one of the S atoms. It seems plausible that these basic properties should be transferable to BDTR/Au(111) diffusion and that a procedure, which embodies these principles, is likely to yield low-energy configuration space paths. Consequently, only one of the two

BDTR S atoms, which bind to the Au(111) surface, should move to the proximity of nearby hollow sites of the surface at a time. In this way, an approximate decomposition of each diffusion mode into a sequence of partial steps can be generated by hand. This sequence is taken as an initial guess for the diffusion path on which the DFT NEB calculations have been based. A multi-step procedure has been adopted to calculate MEPs along each partial step for every basic diffusion mode starting from the ground state as the initial configuration. At first a local minimum on the PES has to be identified which is in the vicinity of the end point of the first partial step. This has been accomplished by an unrestricted geometry optimization of a configuration which has been generated by hand. In a second step, a straight line interpolation between the fully relaxed initial and final atomic geometries of the partial step has been used to initialize a DFT NEB calculation. If the calculation converges to a MEP connecting the initial and final configuration of the partial step and no intermediate local minimum can be identified from an inspection of the data, the NEB calculation has been stopped. Subsequently, a CI-NEB calculation has been started from the previously obtained MEP and the highest configuration along the MEP has been converged to a local transition state. The final configuration of the converged MEP is then used as the starting point of the next partial step and the procedure starts from the beginning. On the other hand, if the MEP data suggests the existence of one or more intermediate local minima, the NEB calculation has been stopped. The employed criterion for the appearance of an intermediate local minimum is that there exists a configuration i along the MEP such that the energetical order with respect to adjacent configurations is $E_{i-1} > E_i < E_{i+1}$. An accurate localization of local minima is obviously related to the number of intermediate configurations which have been used in the NEB run. The number of configurations along each MEP has been chosen such that the distance in high dimensional configuration space between adjacent configurations is approximately 0.5-1.5 Å. An unrestricted geometry optimization has been initialized from the intermediate configuration which appears to be closest to the local minimum. The newly discovered local minimum has then been added to the list of intermediate local minima along the diffusion path and the procedure starts from the beginning. After all partial steps have been calculated, one ends up with a sequence of converged MEPs connecting local minima on the PES and a set of local transition states. These MEPs can be combined to yield a continuous configuration space path corresponding to one of the diffusion modes.

Translational and rotational diffusion on the surface

Following the strategy outlined in the previous Section, MEPs corresponding to the five considered diffusion modes shown in Fig. 4.9 have been obtained from a series of NEB and CI-NEB calculations. Each highly non-trivial MEP consists of many intermediate local minima and local transitions states, see Figs. 4.10, 4.12, 4.14, 4.16, and 4.18. The corresponding BDTR configurations of local minima and local transition states are depicted in Fig. 4.11, 4.13, 4.15, 4.17, and 4.19.

The differences between the total energy of the ground state configuration and the

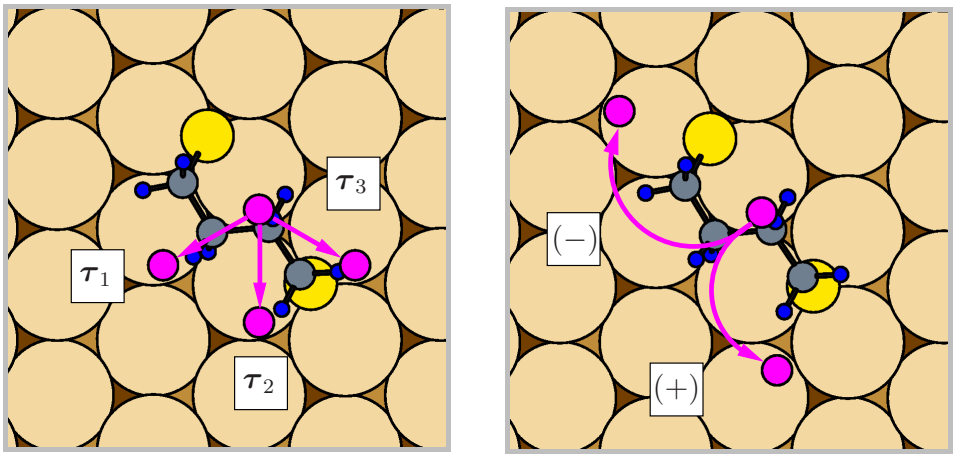

Figure 4.9: Schematic depiction of the considered BDTR/Au(111) diffusion modes. The small circles (magenta) represent the midpoints in the (x, y)-plane between the S atoms of symmetry equivalent BDTR/Au(111) ground states. The arrows indicate the BDTR translations $\boldsymbol{\tau}_1$, $\boldsymbol{\tau}_2$, and $\boldsymbol{\tau}_3$ (left panel) and the 120° BDTR rotations (+) and (−) (right panel) around different rotation axes on the Au(111) surface.

highest energy transition state along each MEP, ΔE_{max}, are summarized in Tab. 4.1 for two sizes of the surface unit cell. Starting with the pure translations of a BDTR on the Au(111) surface, the energetical order of the diffusion modes as calculated in a (4×3) surface unit cell is $\Delta E_{\mathrm{max}}(\boldsymbol{\tau}_1) < \Delta E_{\mathrm{max}}(\boldsymbol{\tau}_2) < \Delta E_{\mathrm{max}}(\boldsymbol{\tau}_3)$. The diffusion energy barrier for a translation along $\boldsymbol{\tau}_1$ amounts to 0.25 eV in case of a (4×3) surface unit cell. The maximum energy barrier which needs to be surmounted along $\boldsymbol{\tau}_1$ is at least 0.1 eV smaller compared to ΔE_{max} for $\boldsymbol{\tau}_2$ and $\boldsymbol{\tau}_3$. As a consequence, the BDTR hopping rate along $\boldsymbol{\tau}_1$ should be much larger than for translations along $\boldsymbol{\tau}_2$ and $\boldsymbol{\tau}_3$ by approximately a factor of at least 55 at room temperature assuming equal effective attempt frequencies. The precise cause of the preference for $\boldsymbol{\tau}_1$ is difficult to assess quantitatively. However, the trend appears to be plausible on qualitative grounds. Generally, the total energy of a BDTR/Au(111) configuration may increase due to the following causes: one or both of the S atoms occupy energetically unfavorable positions (e.g. near an on top site of the surface), the S-C tilt angle with respect to the surface normal is unfavorable (e.g. the partially filled BDTR HOMO/LUMO states located at the S atoms do not point towards Au surface atoms), or the BDTR alkane chain is distorted (mainly rotations around C-C bonds and bending of the alkane chain is observed). In case of the lowest total energy MEP ($\boldsymbol{\tau}_1$), the locations of the "moving" S atom for (local) transition state configurations are all close to bridge sites albeit with a shift towards near on top sites, see Fig. 4.11. In addition, the S-C bonds are tilted towards Au atoms of the surface at local transition states, and the distortion of the alkane chain is rather moderate with respect to the ground state configuration ($\approx$ 60 meV at transition state β). An

Table 4.1: Maximum energy barriers, $\Delta E_{\max}$, along the MEPs for BDTR/Au(111) translations and rotations as calculated in a (4×3) and (4×4) surface unit cell.

Mode	$\Delta E_{\max}^{(4\times3)}$ (eV)	$\Delta E_{\max}^{(4\times4)}$ (eV)	MEP see Fig.
Translation $\boldsymbol{\tau}_1$	0.25	0.35	4.10
Translation $\boldsymbol{\tau}_2$	0.35		4.12
Translation $\boldsymbol{\tau}_3$	0.40		4.14
Rotation (+)	0.30	0.40	4.16
Rotation (−)		0.43	4.18

inspection of the transition states along $\boldsymbol{\tau}_2$ and $\boldsymbol{\tau}_3$ yields a slightly different picture. The moving S atom for the two highest energy (local) transition states along $\boldsymbol{\tau}_2$, π and ρ, may be characterized as located at bridge sites of the surface. The respective S-C bond is tilted unfavorably such that the reactive BDTR orbitals do not point towards Au surface atoms. Hence, the local bonding configuration is likely to be energetically unfavorable compared to the highest energy transition state along $\boldsymbol{\tau}_1$. For translation $\boldsymbol{\tau}_3$ all of the above mentioned mechanisms, which tend to increase the total energy, come together. This indeed renders $\boldsymbol{\tau}_3$ the least favorable candidate for a diffusion path out of the three. Upon inspection of the highest energy (local) transition states, μ and ν, of $\boldsymbol{\tau}_3$, one notices that the moving S atom occupies bridge sites of the Au(111) surface in conjunction with S-C bonds tilted towards on top sites and a significant distortion of the alkane chain (≈ 0.10 meV at transition state μ).

The fact that all three translations on the Au(111) surface are inequivalent with significantly different maximum energy barriers hints towards short-time correlations between subsequent diffusion events. However, translations other than $\boldsymbol{\tau}_1$ might be a composition of low energy translations along $\boldsymbol{\tau}_1$ and low energy rotations. In this case correlations may not be able to develop. For this reason, rotations on the surface need to be considered to complement the picture. The energetical order of the diffusion modes leading to (+) and (−) rotations around the surface normal as calculated in a (4×4) surface unit cell is $\Delta E_{\max}(+) < \Delta E_{\max}(-)$. The diffusion energy barrier for the (+) rotation amounts to 0.40 eV in case of a (4×4) surface unit cell. Note, however, that the small difference between (+) and (−) amounts to only 30 meV, which comes close to

the accuracy of the calculation especially if the dependance of the energy barriers on the size of the surface unit cell is taken into account. The coverage dependance is further detailed in the paragraph "Appendix: Calculational methods and convergence tests" on page 152.

In case of the (4×4) surface unit cell, the result of the DFT calculations is that both rotations around a surface normal have a maximum energy barrier which is larger than that for the energetically favored translation $\boldsymbol{\tau}_1$. The diffusion energy barrier for a $\boldsymbol{\tau}_1$ translation is 0.05 eV smaller than the energy barrier for rotations in a (4×3) and (4×4) surface unit cell. Note that part of the MEP (configurations A through C) of rotation $(+)$ is equal to the first part of the MEP for translation $\boldsymbol{\tau}_1$. When the NEB calculations were designed, the intention was that by doing so it was likely that a MEP for rotations with a maximum energy barrier equal to that for translations could be identified. As this seemed not the case, further confidence is added to the careful conclusion that the diffusion energy barriers for translation and rotation indeed differ.

It is suggested that a significant part of the diffusion energy barrier difference between translation $\boldsymbol{\tau}_1$ and rotation $(+)$ can be traced back to different S atom positions and orientations of S-C bond angles. The energy related to the distortion of the BDTR at the transition states for $\boldsymbol{\tau}_1$ and $(+)$ is found to be almost equal. To further illustrate how the energy difference between the transition states for $\boldsymbol{\tau}_1$ and $(+)$ is related to the local S-Au bond configurations, the BDTR is substituted by two SCH_3 radicals on the Au(111) surface. The SCH_3 atomic positions are the same for the two S and C_1, C_4 atoms of the BDTR and the same atomic coordinates of the Au substrate have been used. The H atom positions are either taken from the BDTR or assumed to lie on the C_1-C_2 or C_4-C_3 bonds. Indeed, the DFT total energy of the substitute system for the highest energy transition state for rotation $(+)$ is approximately 0.08 eV larger than for translation $\boldsymbol{\tau}_1$.

The energetical order of translations and rotations is $\Delta E_{\max}(\boldsymbol{\tau}_1) < \Delta E_{\max}(+)$. Thus, the conjecture that successive diffusion hops of a BDTR on the Au(111) surface are correlated seems to be justified. Hence, diffusion hops should occur back and forth along the same direction $\boldsymbol{\tau}_1$ on the surface. These correlations are expected to decay over a period of time comparable to the average time for rotations.

When extended objects, e.g. large molecules, bind to a metal surface, a frequent matter of debate is whether van der Waals (vdW) interactions play a decisive role for the interpretation of the data.[248,267] To address this issue, a semi-empirical vdW correction[239,240] has been evaluated for the frozen-in BDTR/Au(111) configurations from the PW91-MEPs discussed above. Overall the vdW correction significantly increases the maximum energy barrier along the MEPs by as much as +0.22 eV in some cases. The energetical order of $\boldsymbol{\tau}_1$, $\boldsymbol{\tau}_2$, and $\boldsymbol{\tau}_3$ remains unaltered by the vdW correction (vdW correction $\boldsymbol{\tau}_1$: $\approx$ +0.1 eV, $\boldsymbol{\tau}_2$: $\approx$ +0.1 eV, $\boldsymbol{\tau}_3$: $\approx$ +0.2 eV). The same holds true for the considered rotations [vdW correction $(+)$: +0.1 eV, $(-)$: +0.2 eV]. Qualitatively, the difference between the energy barriers for translations and rotations is preserved. In principle, one would have to go beyond the *a posteriori* correction and re-calculate

the coordinates of the energy minima and diffusion paths for the PES modified by the vdW interaction energy.[265] However, as detailed in Ref. 84, the semi-empirical vdW correction apparently results in an overestimate of the BDT/Au binding energy and its reliability might be questioned.[265] Hence, the semi-empirical vdW correction employed here should only be taken as a rough and, maybe pessimistic, estimate of vdW induced changes of the diffusion energy barriers.

Comparison to the diffusion of SCH_3

In case of BDTR diffusion on the Au(100)-(1×1) substrate, the impact of the alkane chain on the diffusion properties is a lowering of the diffusion energy barrier compared to individual SCH_3 radicals.[265] What can be said about the diffusion of BDTR/Au(111) compared to single SCH_3 radicals? First of all, the results from the DFT calculations indicate that the diffusion energy barrier of BDTR on Au(111) [0.25 eV for a (4×3) surface unit cell] seems to be comparable to the diffusion energy barrier for a single SCH_3 radical [0.26 eV for a (3×3) surface unit cell]. For the Au(100) surface the data suggests that the constraint exerted by the BDTR alkane chain primarily raises the total energy of the BDTR ground state compared to two individual SCH_3 ground state configurations. Thus, the overall BDTR diffusion energy barrier is lower compared to SCH_3.[265] Indeed, for the Au(111) surface the alkane chain has a similar effect on the ground state. The BDTR S-Au surface anchors may not adopt their optimum geometry when the ground state configurations of two SCH_3 radicals are taken as the reference.[39] This can be illustrated by substitution of the BDTR by two SCH_3 radicals as outlined above, see page 140. If this configuration is relaxed, 0.15 eV is gained per (4×3) surface unit cell which is of the same order of magnitude as the chemisorption energy difference of approximately 0.2 eV between two SCH_3 radicals and a single BDTR [(4×3) surface unit cell]. Substitution of BDTR by two SCH_3 radicals for the BDTR transition state for translation $\boldsymbol{\tau}_1$ (configuration β) yields a 0.22 eV higher total-energy as the SCH_3 substitute system for the BDTR ground state. This is comparable to the BDTR diffusion energy barrier of 0.25 eV.

It is tempting to conclude that in case of the Au(111) surface the BDTR alkane chain constraints the SCH_3 ground state and transition state in such a way that both configurations are almost equally shifted. Hence, the diffusivity of BDTR and SCH_3 radicals would be similar. Note, however, that the BDTR diffusion energy barrier has a strong dependance on coverage which might result in a coverage dependance of the above analysis. Moreover, the analysis is seriously complicated by the fact that both BDTR S-Au anchors differ significantly between the BDTR ground state and the transition state. As a result, it is not clear what the contribution of each individual S-Au anchor to the above total-energy differences is.

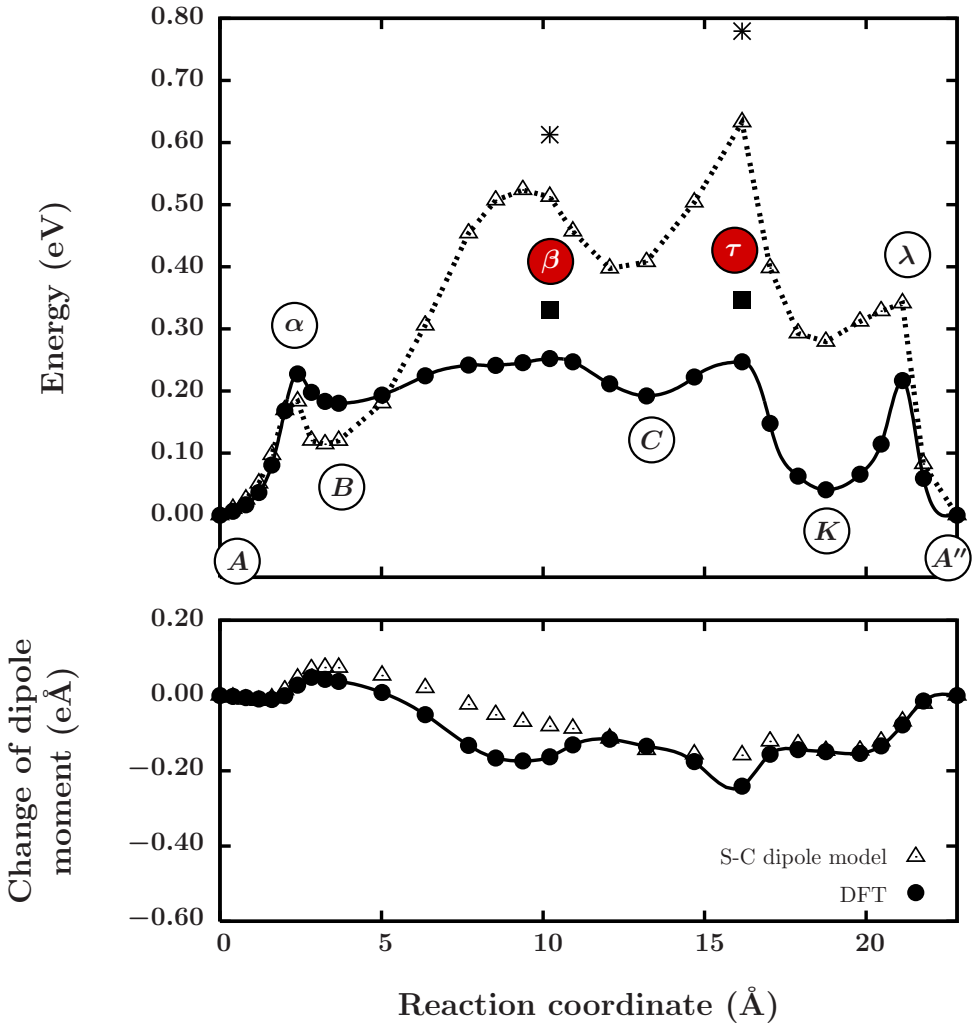

Figure 4.10: Upper panel: Lowest-barrier MEP for translation $\boldsymbol{\tau}_1$ of BDTR on the Au(111)-(1×1) surface. The MEP is a composition of individual CI-NEB runs connecting local minima. Filled circles refer to the interface to vacuum as calculated within DFT with a (4×3) surface unit cell. Filled squares are calculated with a (4×4) surface unit cell. Triangles are obtained by adding to the DFT energies [(4×3) surface unit cell] the electrostatic energy of the BDTR dipole moment in an external electric field of 1.6 V/Å. The star is obtained by adding the electrostatic energy to the DFT value for a (4×4) surface unit cell. Capital letters tag (meta)stable configurations while Greek letters tag local transition states. The highest energy transition states are marked red. Geometries that merely differ by a two-dimensional space-group operation of the substrate are primed. Atomic geometries are depicted in Fig. 4.11. Lower panel: Variation of the dipole moment along the MEP. Filled circles calculated within DFT. Triangles denote results from the S-C dipole model.

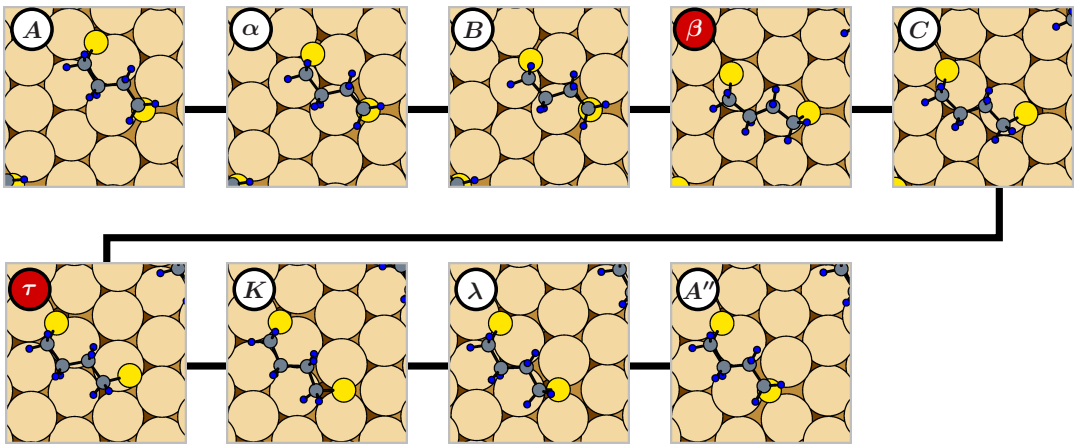

Figure 4.11: Atomic geometries of (meta)stable and transition state configurations along the lowest-barrier MEP for translation $\boldsymbol{\tau}_1$ of BDTR on the Au(111)-(1×1) surface (same path as in Fig. 4.10). Capital letters tag (meta)stable configurations while Greek letters tag local transition states. The highest energy transition states are marked red. Geometries that merely differ by a two-dimensional space-group operation of the substrate are primed. Atomic configurations are depicted schematically. Au atoms of the first layer: light brown, second layer: brown, third layer: dark brown, S atoms: yellow, C atoms: gray, H atoms: blue.

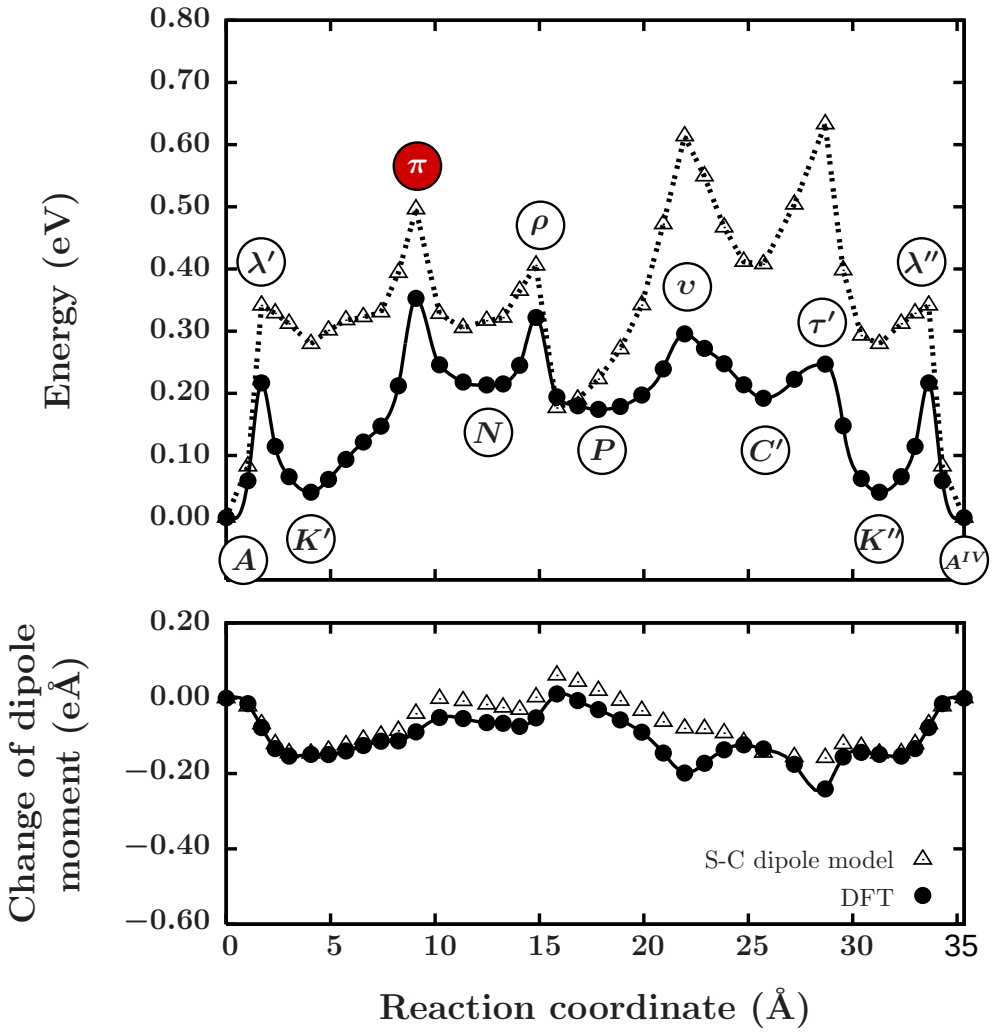

Figure 4.12: Upper panel: MEP for translation $\boldsymbol{\tau}_2$ of BDTR on the Au(111)-(1×1) surface. Atomic geometries are depicted in Fig. 4.13. The calculations have been performed in a (4×3) surface unit cell. Lower panel: Variation of the dipole moment along the MEP. For an explanation of the notations see Fig. 4.10.

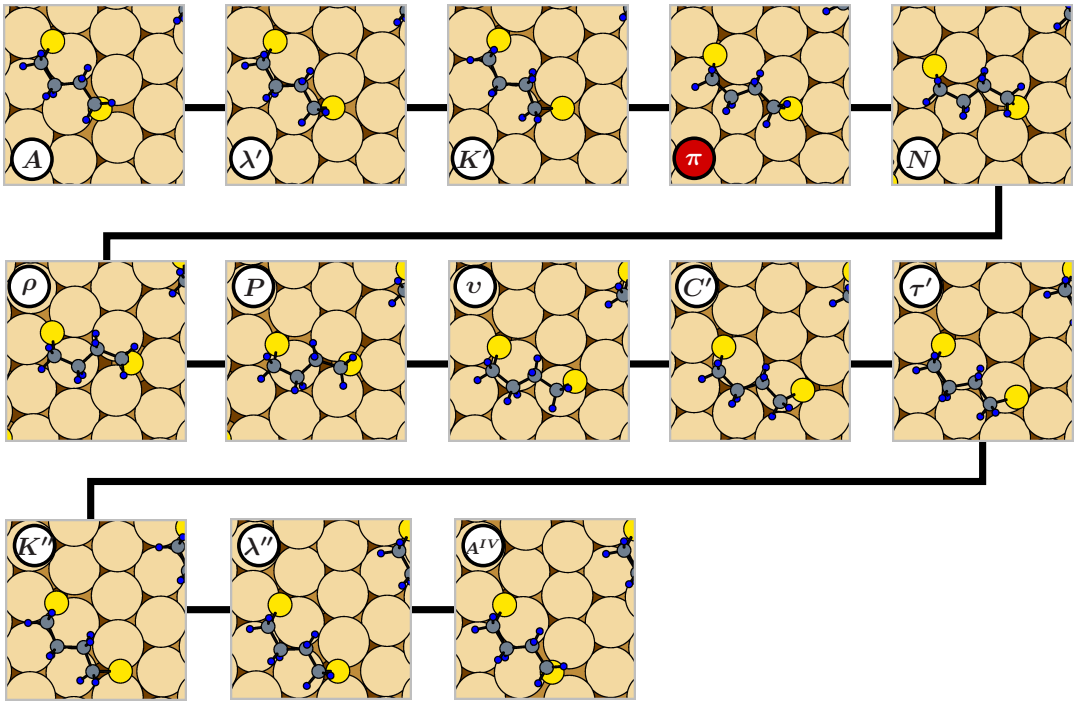

Figure 4.13: Atomic geometries of (meta)stable and transition state configurations along the MEP in Fig. 4.12. For an explanation of the notations see Fig. 4.11.

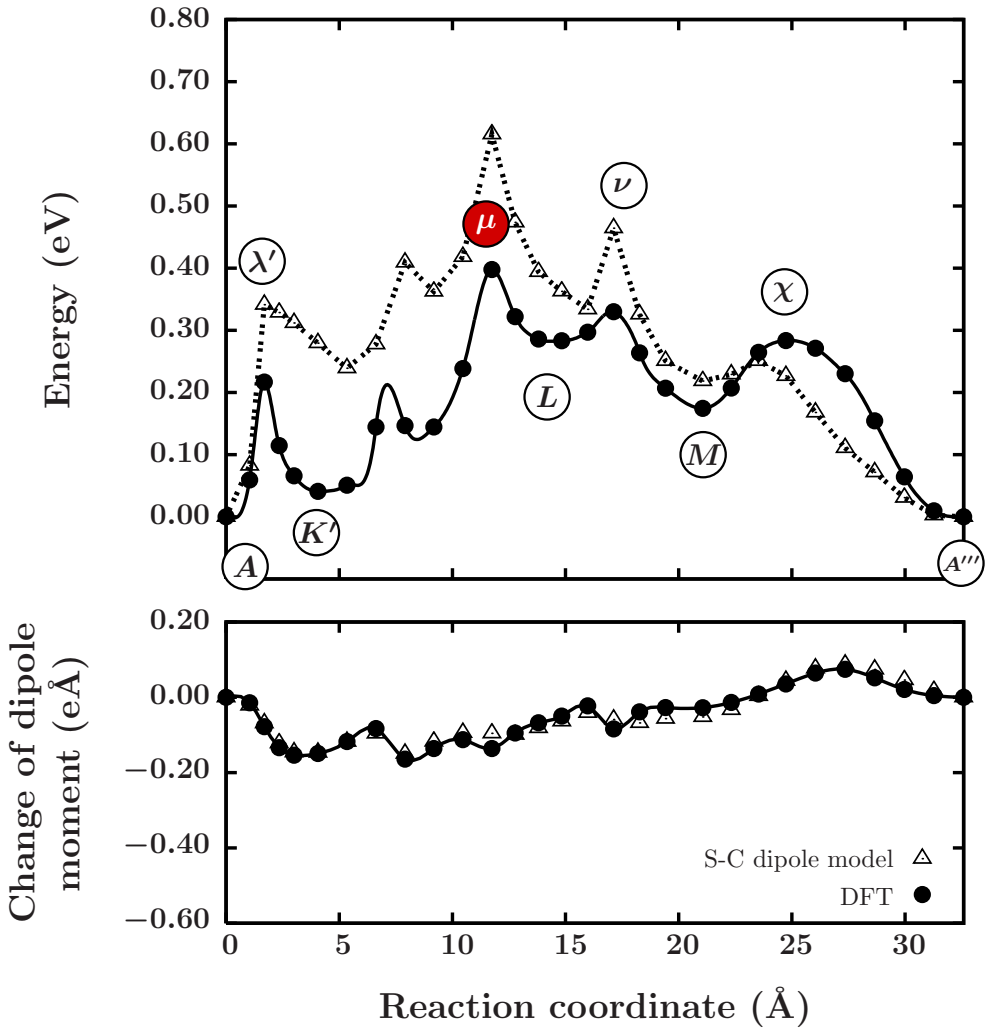

Figure 4.14: Upper panel: MEP for translation τ_3 of BDTR on the Au(111)-(1×1) surface. Atomic geometries are depicted in Fig. 4.15. The calculations have been performed in a (4×3) surface unit cell. Lower panel: Variation of the dipole moment along the MEP. For an explanation of the notations see Fig. 4.10.

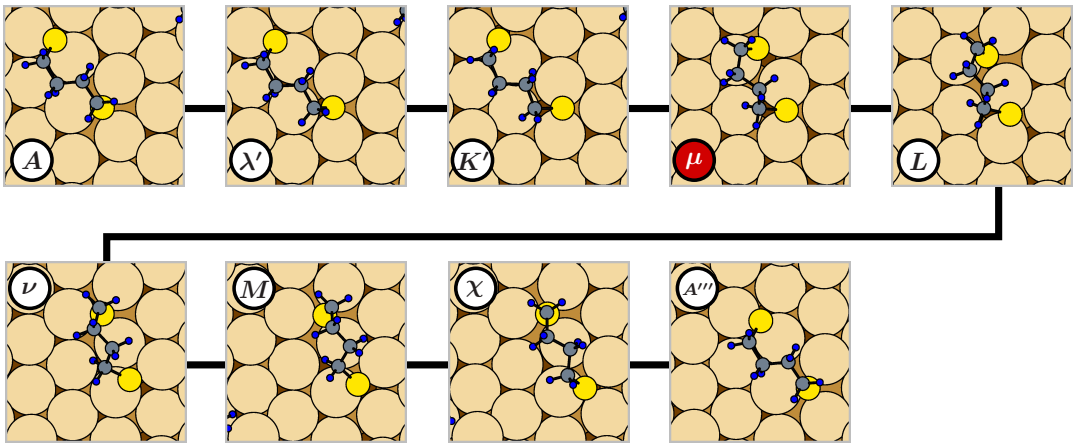

Figure 4.15: Atomic geometries of (meta)stable and transition state configurations along the MEP in Fig. 4.14. For an explanation of the notations see Fig. 4.11.

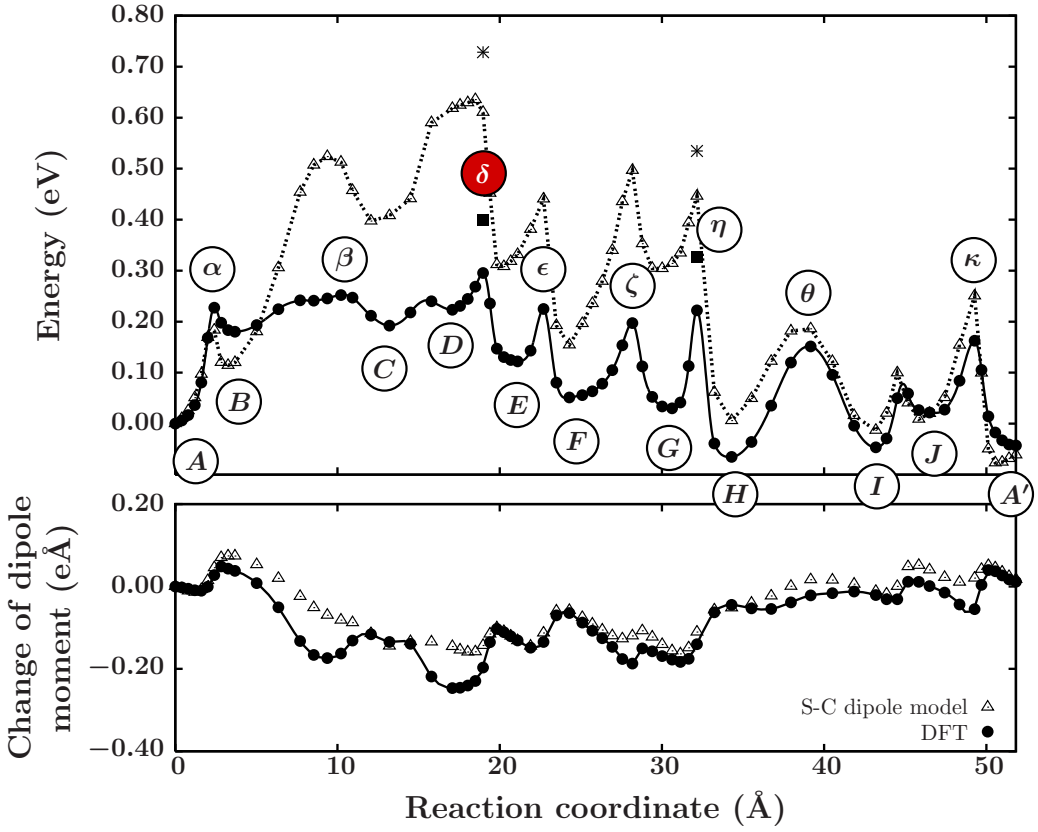

Figure 4.16: Upper panel: MEP for rotation (+) of BDTR on the Au(111)-(1×1) surface. Atomic geometries are depicted in Fig. 4.17. The calculations have been performed in a (4×3) surface unit cell in case of filled black dots and in a (4×4) surface unit cell in case of filled black squares. That configurations close to H and I have a lower total energy than A' is an artefact of the small (4×3) surface unit cell. In a (4×4) surface unit cell this artefact is not present. Lower panel: Variation of the dipole moment along the MEP. For an explanation of the notations see Fig. 4.10.

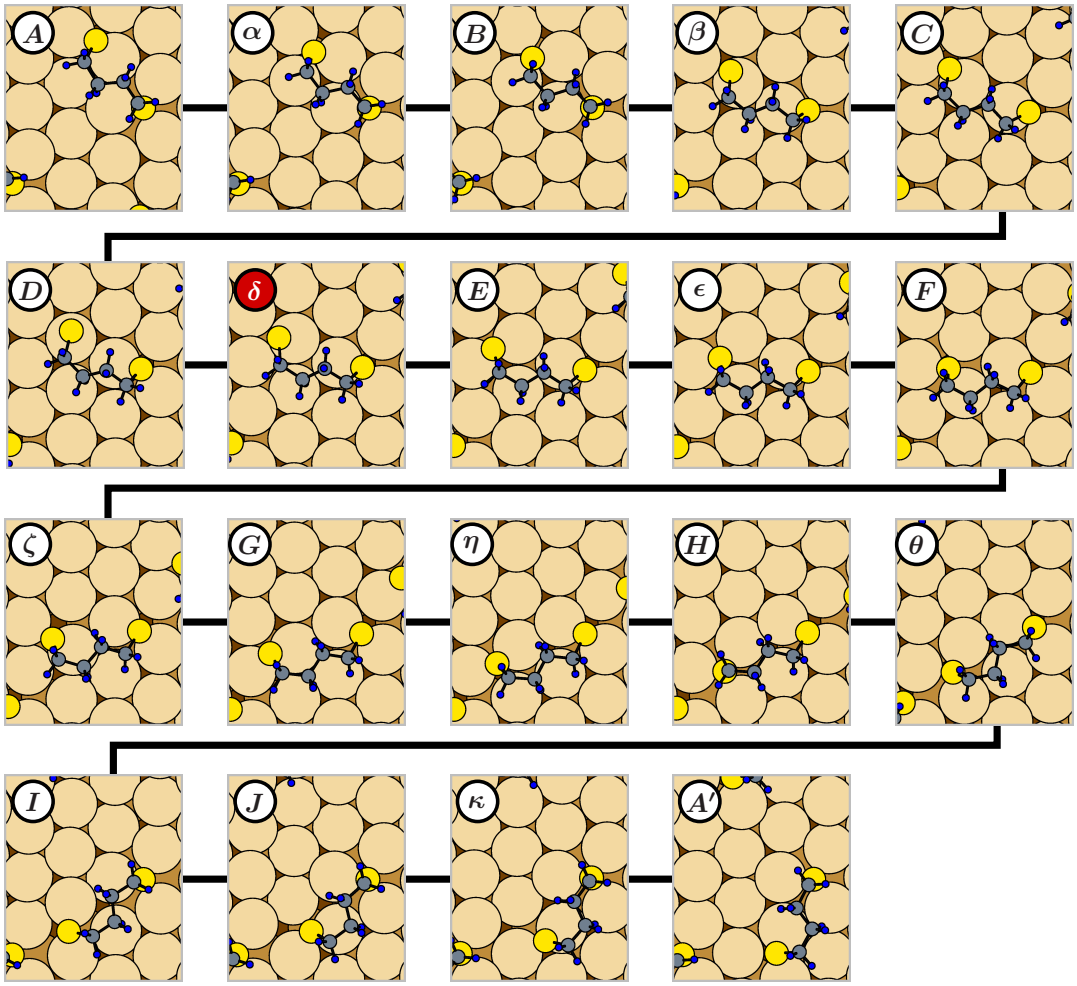

Figure 4.17: Atomic geometries of (meta)stable and transition state configurations along the MEP in Fig. 4.16. For an explanation of the notations see Fig. 4.11.

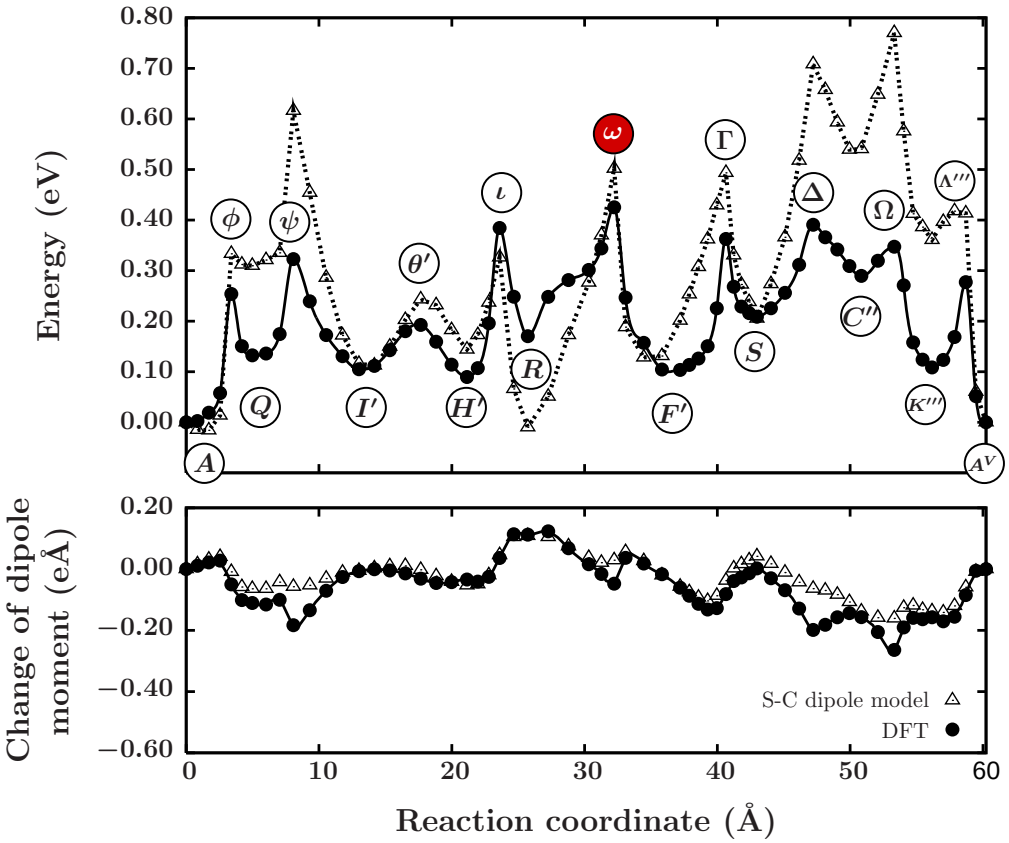

Figure 4.18: Upper panel: MEP for rotation (−) of BDTR on the Au(111)-(1×1) surface. Atomic geometries are depicted in Fig. 4.19. The calculations have been performed in a (4×4) surface unit cell. Lower panel: Variation of the dipole moment along the MEP. For an explanation of the notations see Fig. 4.10.

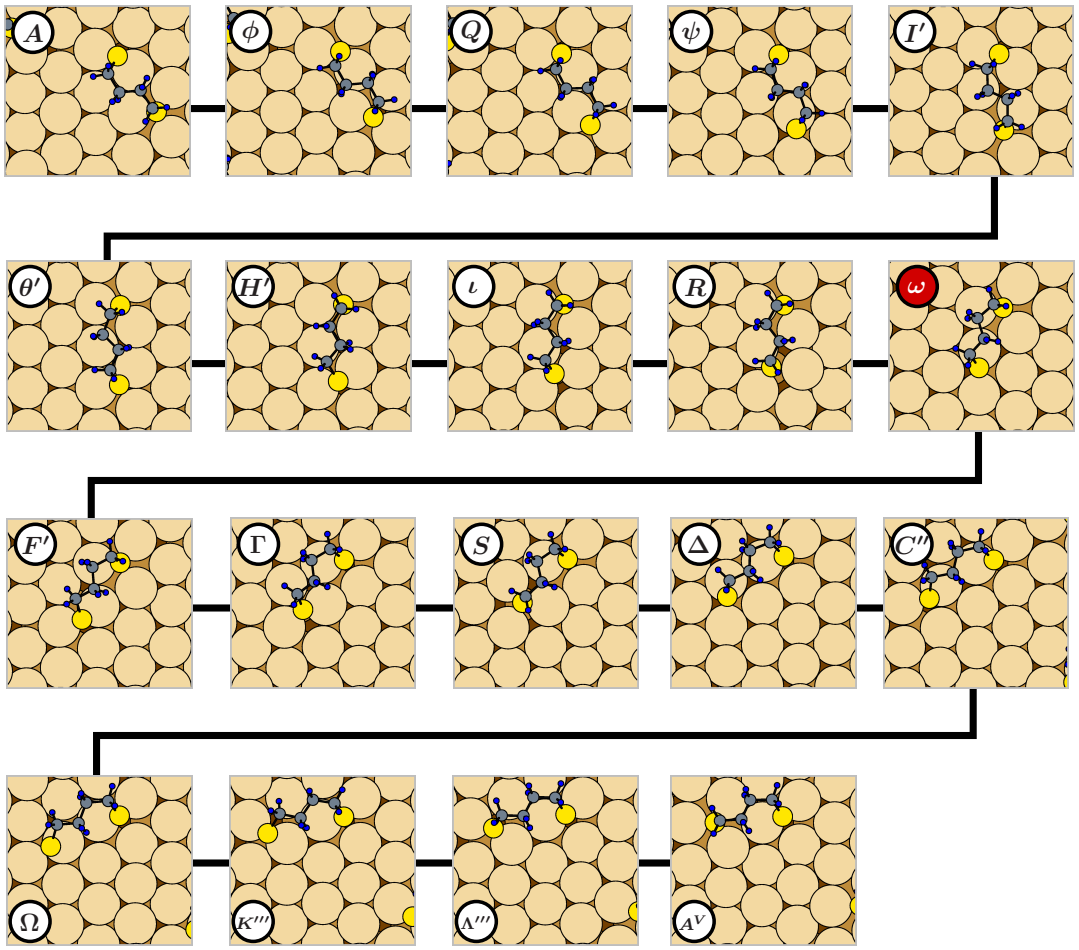

Figure 4.19: Atomic geometries of (meta)stable and transition state configurations along the MEP in Fig. 4.18. For an explanation of the notations see Fig. 4.11.

Appendix: Calculational methods and convergence tests

Most of the calculational methods (DFT, NEB, and vdW interaction corrections) used to determine the diffusion properties of BDTR/Au(111)-(1 × 1) are identical to those used in case of BDTR/Au(100)-(1 × 1). The details can be found in Ref. 265. Only the differences regarding the size of the super-cell and the number of special k-points used to calculate Brillouin zone integrals will be outlined here.

Calculations of BDTR/Au(111)-(1 × 1) have been carried through with slabs comprising 4 layers of gold with a (4 × 3) and (4 × 4) surface unit cell. The size of the super-cell perpendicular to the slab surface amounts to 24.1 Å such that the periodically repeated gold slabs are separated by a vacuum region. The integrals over the Brillouin zone are approximated by sums over special k-points[260] using a mesh consisting of 12 and 9 k-points in the complete first Brillouin zone of the (4 × 3) and (4 × 4) surface unit cell.

The error of the BDTR/Au(111)-(1×1) DFT diffusion energy barriers related to the convergence parameters cutoff energy, k-point sampling, and total number of substrate layers may be estimated from separate calculations. To this purpose, the maximum energy barriers along selected MEPs have been recalculated using frozen-in atomic coordinates obtained with the convergence parameters used for the production runs. Tab. 4.2 summarizes the convergence tests. The cumulative error related to the cutoff energy of the plane-wave expansion, the number of Au layers in the slab, and number of k-points is estimated to be 0.02 eV.

Furthermore, the dependance of the maximum energy barriers on coverage, i.e. on the size of the surface unit cell, needs to be addressed. To this purpose, results obtained for a (4 × 3), (4 × 4), and (4 × 6) surface unit cell are compared for the $\boldsymbol{\tau}_1$ MEP, see Tab. 4.2. The results for the two largest energy barriers have a strong dependance on coverage which severely complicates the interpretation of the data. Especially if the absolute size of the diffusion energy barrier is of interest, the coverage should always be quoted together with the energy barrier. However, the conclusions regarding short time correlations of subsequent diffusion hops are little affected by the coverage because different energy barriers seem to have a similar coverage dependance. The question, what the implications for a comparison to experiment are, is tough to answer. It is speculated that the DFT diffusion energy barrier in the zero-coverage limit, which could not be reached in this work, might not be the best choice for a comparison to experiments under EC conditions. Co-adsorbed ions or water molecules might play the same role in experiment as the periodically repeated BDTR in a super-cell calculation at finite coverage.

A large uncertainty of the diffusion energy barriers is also expected to arise from the use of an approximate exchange-correlation energy-functional $E_{\mathrm{xc}}[n]$. The contribution to the total energy from the vdW interaction can of course neither be described by the local density approximation (LDA) nor by the GGA.[265] It still makes sense to compare results from LDA and PW91-GGA to obtain an order of magnitude impression of the change

Table 4.2: Convergence of the diffusion energy barrier, ΔE, for translation $\boldsymbol{\tau}_1$ depicted in Fig. 4.10. For the (4×3) surface unit cell (SUC) ΔE has been recalculated using the relaxed atomic positions obtained with a 250 eV cutoff energy, 12 k-points in the full Brillouin zone, 4 Au substrate layers, and the PW91-GGA. In case of larger SUCs the atomic positions have been obtained from separate CI-NEB calculations.

Mode	Configuration	SUC	E_{xc}	E_{cutoff} (eV)	N_{kpt}	N_{lay}	ΔE (eV)
		Parameters E_{cutoff}, N_{kpt}, N_{lay}					
$\boldsymbol{\tau}_1$	β	(4×3)	GGA	250	12	4	0.25
$\boldsymbol{\tau}_1$	β	(4×3)	GGA	340	48	12	0.27
$\boldsymbol{\tau}_1$	τ	(4×3)	GGA	250	12	4	0.25
$\boldsymbol{\tau}_1$	τ	(4×3)	GGA	340	48	12	0.26
		Surface unit cell					
$\boldsymbol{\tau}_1$	β	(4×3)	GGA	250	12	4	0.25
$\boldsymbol{\tau}_1$	β	(4×4)	GGA	250	9	4	0.33
$\boldsymbol{\tau}_1$	β	(4×6)	GGA	250	6	4	0.40
$\boldsymbol{\tau}_1$	τ	(4×3)	GGA	250	12	4	0.25
$\boldsymbol{\tau}_1$	τ	(4×4)	GGA	250	9	4	0.35
$\boldsymbol{\tau}_1$	τ	(4×6)	GGA	250	6	4	0.47
		E_{xc}					
$\boldsymbol{\tau}_1$	β	(4×3)	GGA	250	12	4	0.25
$\boldsymbol{\tau}_1$	β	(4×3)	LDA[a]	250	12	4	0.30
$\boldsymbol{\tau}_1$	β	(4×3)	LDA[b]	250	12	4	0.59

[a] Using an LDA lattice constant and the LDA to calculate the atomic positions.

[b] Using the frozen-in GGA atomic positions.

of the energy barriers with the choice of the semi-local approximation to exchange-correlation energy-functional ($E_{\mathrm{xc}}[n]$).[200,267] The LDA energy barriers in Tab. 4.2 have been calculated for the PW91 as well as the LDA geometries and lattice constants. The increase of the diffusion energy barrier by 0.34 eV and 0.05 eV in case of the PW91 and LDA geometries and lattice constants, respectively, gives an impression of the energy barrier change.

4.4.2 Modification of the potential energy surface in an electrochemical environment

As mentioned in the beginning the herringbone reconstruction of the Au(111) surface is the stable reconstruction under UHV conditions. For certain EC conditions the reconstruction can be lifted and the unreconstructed Au(111)-(1×1) surface is stabilized.[151] Due to the interaction of the surface with the electrolyte ions at the solid-liquid interface under EC conditions, the Au(111) surface may exhibit a non-vanishing surface charge which causes an electric field at the interface. In addition, the electric field can be varied in an electrochemical cell by an additional external potential. In this Section it is attempted to estimate the effect of such an electric field on the diffusion of BDTR/Au(111)-(1×1).

A significant influence of an electric field on the PES is to be expected in case of adsorbates with an intrinsic or induced dipole moment.[148,152] It has been reported that the coupling of the dipole moment to the electric field may be responsible for the predominant part of the potential dependant diffusion properties via a change of the adsorbate dipole moment along the reaction path.[148,152] The focus here is on the BDTR dipole related effect on diffusion. Solvent effects, such as adsorption site blocking, are beyond the scope of the present discussion. The impact of an electric field on the PES will be estimated in a crude non-self-consistent model by simply adding the electrostatic interaction energy between an electric field perpendicular to the surface and the adsorbate dipole moment to the DFT total energy. The absolute value of the electric field has been set to 1.6 V/Å.[268] The electric field vector points away from the adsorbate covered surface. A similar approach has been suggested and employed in previous surface diffusion studies.[269,270] The technical details and restrictions of the method have been detailed previously in Ref. 84

The overall dipole moment of BDTR/Au(111) arises mainly from the two intrinsic S-C bond dipoles. An inspection of the induced surface charge density upon BDTR adsorption reveals no significant net charge transfer which is consistent with a previous study of the interface dipole of CH_3S/Au(111).[271] Keeping this in mind, the change of the dipole moment along the MEPs depicted in Figs. 4.10, 4.12, 4.14, 4.16, and 4.18 can be rationalized to originate from a change of the S-C tilt angles with respect to the surface normal along the diffusion paths. To illustrate this principle, the S-C tilt angles have been evaluated along all MEPs and the S-C bond dipole moments along the surface normal have been calculated for all configurations (data labeled *S-C dipole*

model in Figs. 4.10, 4.12, 4.14, 4.16, and 4.18). The absolute value of each S-C dipole moment has been set to that of an SCH_3 radical in vacuum (0.36 eÅ). The variation in the BDTR/Au(111) DFT dipole moment along the MEPs is in semi-quantitative agreement with the S-C dipole model. Additional calculations have revealed that the residual differences can be associated with S-Au interface effects.

The MEPs including the non-self-consistent effect of an applied electric field are shown in Figs. 4.10, 4.12, 4.14, 4.16, and 4.18 together with the original DFT data. It is apparent that the influence of the electric field on the PES is significant within the applied non-self-consistent model. The maximum energy barriers including the electrostatic energy contribution come out in the range of approximately 0.5-0.8 eV. The electric field correction to the DFT data is not small but rather approximately of the same order of magnitude as the DFT energy barriers. Moreover, the energetical order of translations and rotations has changed. E.g. the maximum energy barriers of the three translations have become almost equal in magnitude and the diffusion energy barrier of the rotation (+) comes out slightly smaller than the translational diffusion energy barrier $\Delta E(\boldsymbol{\tau}_1)$.

Compared to the range of DFT energy barriers of 0.25-0.42 eV, the employed approach to estimate the implications of an electric field leads to a near doubling of the energy barriers. It should be noted that such a large effect should be verified within a more elaborate self-consistent scheme if precise quantitative information is desired. On the other hand, the non-self-consistent model should in principle recover the main qualitative trends. Hence, the calculations suggest the following qualitative picture. First of all, the diffusion energy barrier should increase as the electric field at the interface increases, i.e. the applied external potential becomes more positive (electric field vector pointing away from the surface). In addition, the order of the energy barriers for different diffusion channels on the surface, like translations and rotations, might change for different applied external potentials. In this way correlations between successive diffusion hops might be tunable.

First results for the diffusion of BDTR on the unreconstructed Au(111) surface under EC conditions have been obtained by Suto and Magnussen.[171] As mentioned in Sec. 2.2.2 they have demonstrated that low coverages of BDTR (1-2% of a monolayer) can be prepared in 0.1 M $HClO_4$ solution and that the BDTR/Au(111) diffusion can be monitored in video-STM experiments. These preliminary experimental observations already contain valuable information about the BDTR/Au(111) diffusion characteristics. First of all, the diffusion of BDTR is sufficiently low such that the dynamics of isolated adsorbates seems to be accessible.[171] Images acquired at time intervals of 67-100 ms show protrusions of different shapes (elongated or almost circular) some of which are translated or have changed their orientation from image to image, while others can be considered stationary.[171] This might be taken as an indication of translational and rotational BDTR diffusion channels. Note, however, that under the employed experimental conditions the surface diffusivity of BDTR was high enough for the adsorbates to move during image recording which might lead to distorted protrusions and artefacts.[171] Moreover, the mean time interval between individual diffusion hops should not be many orders of magnitude smaller or larger than the time interval between subsequent images. Otherwise, nearly all or almost none of the adsorbates should have moved during

the image acquisition period. The overall picture is consistent with a diffusion energy barrier which is roughly of the order of 0.4-0.9 eV if an attempt frequency in the usual range between 10^{11}-10^{13} s^{-1} is assumed. Finally, it has been observed that the surface diffusivity of BDTR strongly decreases if the applied potential is increased. These qualitative impressions appear to be in agreement with the results of the presented DFT calculations, which is an encouraging result.

4.4.3 Approximate calculations for the potential energy surface

In general the computer time for DFT calculations scales super-linearly with the size of the system. This makes calculations for extended systems with many electrons and large super-cells unfeasible. Many of the calculations presented in this work have been carried through at the limit of what can be achieved today even on high-performance supercomputers like the NEC-SX9 at the Rechenzentrum of the University of Kiel. In addition to the computational power needed for a single DFT run, structural investigations and reaction path calculations usually involve a large number of individual DFT runs. To significantly reduce the required computer time or even to be able to perform certain calculations at all, partitioning schemes for high-level first principles calculations have been envisioned and applied in the literature.[272–274] Most of these schemes follow a similar logic. The entire system is split into a certain number of smaller overlapping subsystems, which can be calculated individually. The results for these subsystems are then combined in a suitable way to yield the total energy of the original systems. A crucial role in this type of calculation is the termination of the individual subsystems to confine the perturbance induced by the partitioning of the large system. This may be done, e.g. by introducing single link atoms or even groups of atoms at the edges of each subsystem. A further performance improvement can be achieved if the subsystems are treated at different accuracy levels, e.g. by using highly-accurate quantum-chemical or DFT methods for the regions of interest, while the rest of the system is calculated using less accurate molecular-mechanical force field methods (QM-MM schemes).

A simple partitioning scheme for BDTR/Au(111), which uses DFT calculations for all subsystems, has been evaluated in this work. It will thus be referred to as a quantum-mechanical-quantum-mechanical (QM-QM) scheme. The main goal was to explore whether an improved performance in terms of computer time can be achieved without significant loss of calculational accuracy. Such a scheme could then be used to speed up MEP calculations for even larger systems. Within the employed scheme the total energy of a BDTR chemisorbed on a Au(111) surface is approximated as

$$\begin{aligned} E_{\text{QM-QM}}(\text{Au}_n\text{–SCH}_2\text{-(CH}_2)_2\text{-CH}_2\text{S–Au}_n) = \\ E_{\text{DFT}}(\text{Au}_n\text{–SCH}_2\text{-H} + \text{H-CH}_2\text{S–Au}_n) \\ + E_{\text{DFT}}(\text{SCH}_2\text{-(CH}_2)_2\text{-CH}_2\text{S}) - E_{\text{DFT}}(\text{SCH}_2\text{-H} + \text{H-CH}_2\text{S}). \end{aligned} \tag{4.4}$$

In this expression the individual terms are defined as follows.

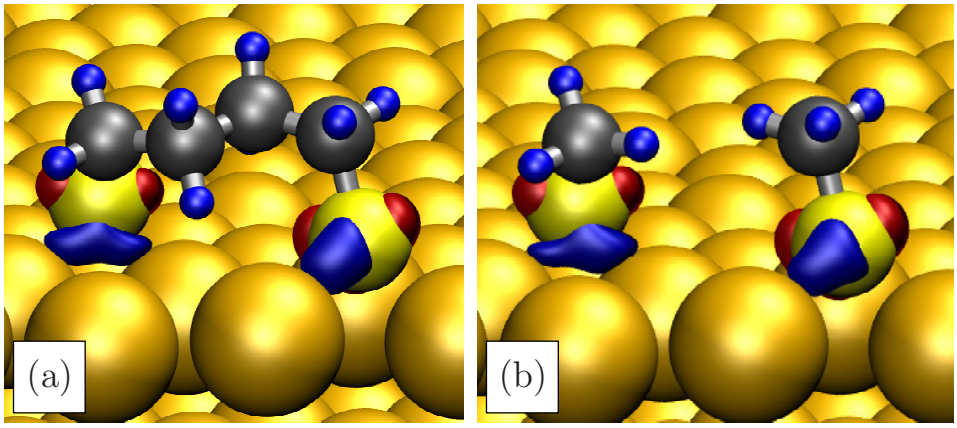

Figure 4.20: Contour surface of constant induced charge densities of the BDTR/Au(111) ground state (a) and the respective CH_3S/Au(111) substitute system (b) defined in the main text. The induced charge density is defined as $\Delta\rho_{\mathrm{BDTR}} = \rho_{\mathrm{BDTR/Au(111)}} - \rho_{\mathrm{Au(111)}} - \rho_{\mathrm{BDTR}}$ and analogous for the substitute system. Blue contour: $\Delta\rho > 0$, red contour: $\Delta\rho < 0$.

$E_{\mathrm{DFT}}(\mathrm{Au}_n{-}\mathrm{SCH_2\text{-}H} + \mathrm{H\text{-}CH_2S}{-}\mathrm{Au}_n)$ is the total energy of two chemisorbed SCH_3 radicals on the Au(111) surface. The SCH_3 atomic coordinates correspond to those of chemisorbed BDTR (for both S and the C_1, C_4 atoms), while the additional H atoms have been placed at a typical C-H bond length in the direction of the BDTR C_2 and C_3 atoms. $E_{\mathrm{DFT}}(\mathrm{SCH_2\text{-}H} + \mathrm{H\text{-}CH_2S})$ is the total energy of the aforementioned SCH_3 radicals in vacuum and $E_{\mathrm{DFT}}(\mathrm{SCH_2\text{-}(CH_2)_2\text{-}CH_2S})$ is the total energy of the BDTR in vacuum. The philosophy behind Eq. 4.4 is to separate the total energy contributions from the S-Au bonds and the distortion of the alkane chain. Hence, the S-C "legs" of BDTR are described as chemisorbed SCH_3 radicals on the Au(111) surface and the distortions of the alkane chain backbone are treated in vacuum neglecting any direct interaction with the Au surface. This point of view seems to be justified because the predominant BDTR-Au coupling is mediated through the S-Au bonds. A comparison of the induced charge densities of BDTR/Au(111) and the CH_3S/Au(111) substitute system illustrates this, see Fig. 4.20.

To get an impression of the accuracy of the above partitioning scheme, three main questions have been addressed. First, does Eq. 4.4 reproduce the DFT total energy of the BDTR chemisorption minimum? Second, are DFT total energy differences along the diffusion path for translations, $\boldsymbol{\tau}_1$, described accurately? And third, is the BDTR chemisorption configuration of the DFT PES also a minimum of the QM-QM PES? To answer the first two questions, the expression for the QM-QM total energy has been evaluated for all configurations along the MEP of $\boldsymbol{\tau}_1$, see Fig. 4.21. The QM-QM value of the total energy of the chemisorption minimum comes out 30 meV smaller than the DFT value. Total energy differences along the MEP for translation $\boldsymbol{\tau}_1$ are reproduced

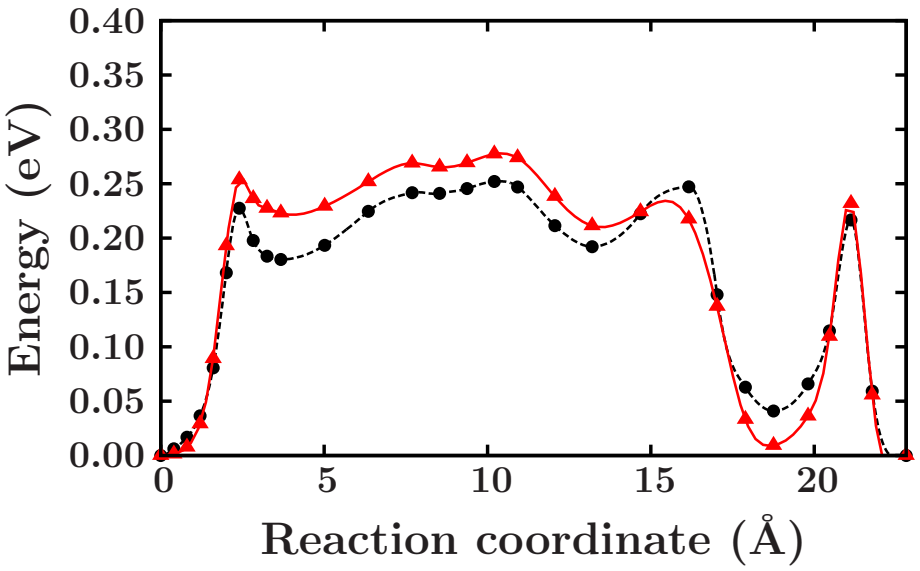

Figure 4.21: MEP for the translation $\boldsymbol{\tau}_1$ of BDTR on the unreconstructed Au(111) surface calculated within DFT using the CI-NEB method (black dots). The evaluation of the QM-QM scheme for the DFT geometries yields energy differences marked by triangles (red). In both cases the energy zero is set to the total energy obtained for the initial configuration. The solid and broken lines are guides to the eyes.

by the employed QM-QM scheme to within approximately 50 meV with respect to the DFT chemisorption minimum. A steepest-descend relaxation with variable step size has been carried through for the atomic coordinates of the BDTR chemisorption minimum to address question three. The QM-QM forces on the atoms have been calculated from Eq. 4.4 using the DFT forces obtained for the individual subsystems. The relaxation yields a significant displacement of the atomic coordinates of the chemisorption minimum and a lowering of the QM-QM total energy by at least 30 meV. Note that the QM-QM total energy minimum has not been obtained because the calculation has been terminated before convergence could be reached. It has been confirmed through an additional DFT calculation that the "updated" QM-QM atomic coordinates do not lead to a lowering of the DFT total energy. As a matter of fact, the DFT total energy increases by approximately 60 meV.

The results of the employed QM-QM partitioning scheme suggest that it is unfortunately not accurate enough for the intended purpose of efficiently sampling the BDTR/Au(111) PES. The total error of such a sampling procedure, for which relaxations of the atomic coordinates are essential, appears to be too large in view of the weakly corrugated multivalley PES of BDTR/Au(111). It seems quite uncertain that the presented QM-QM scheme would have led to a speed-up of the transition state search for BDTR/Au(111). Hence, the partitioning scheme has not been utilized any further. Note, however, that partitioning schemes work for other systems.[272–274]

4.5 Reversal of chloride-induced Cu(001) subsurface buckling in the electrochemical environment: An in situ surface x-ray diffraction and density functional theory study (published)

4.5.1 Synopsis

The unreconstructed Au(100) and Au(111) surfaces, which have been considered in the surface diffusion study of SCH_3 and BDTR, can only be stabilized in an EC environment.[151] In principle, one has to include the effect of the EC solid-liquid interface on the diffusion properties obtained through a DFT calculation for the interface to vacuum. As a first step into this direction, the influence of an electric field on the PES via an electrostatic coupling to the adsorbate dipole moment has been treated within a non-self-consistent model as outline in the previous Sections. In an EC cell consisting of working, counter, and reference electrodes in an electrolyte, an electric field in front of the working electrode surface arises from the interaction with the electrolyte. A unique feature of experiments under these conditions is that the electrode potential with respect to a reference electrode and with it the electric field can be varied via an external voltage source. The important point to note is that the working electrode is held at constant potential not at constant charge. Hence, the thermodynamic potential, γ, required for a description of the electrode surface in an EC cell with applied external potential ϕ reads $\gamma(T,\phi) = f_s(T,\sigma) - \phi\sigma$. $f_s(T,\sigma)$ is the free energy per unit surface area of the solid-liquid interface which includes the electrode surface with surface charge σ, the electrolyte and the "configurations" of electrolyte ions at the interface, e.g. being specifically adsorbed or solvated. The mean distribution of the electrolyte ions near the solid-liquid interface is such that the total charge on the electrode (σ + the charge of specifically adsorbed ions) is screened far from the electrode surface (Gouy-Chapman model).[275] It can be shown that the diffusion energy barrier for an adsorbate on the electrode surface is approximately $\Delta E_d(\phi) = \Delta E_d^0 - 4\pi(\mu_{\rm ts} - \mu_{\rm gs})\sigma_{\rm gs}(\phi)$.[152] In this expression $\Delta E_d^0 = \gamma_{\rm ts}(T,\phi_{\rm pzc,ts}) - \gamma_{\rm ts}(T,\phi_{\rm pzc,gs})$ is the diffusion energy barrier at the potential of zero-charge, $\phi_{\rm pzc}$, of the transition state and the ground state configuration, respectively. $\phi_{\rm pzc}$ is defined as the potential at which the electrode is uncharged (σ + the charge due to specifically adsorbed ions is zero). In the model by which the influence of the EC environment has been estimated in the previous Sections, ΔE_d^0 has been approximated by the DFT result for the energy barriers at the interface to vacuum. A typical value (1.6 V/Å) has been chosen for the quantity $4\pi\sigma_{\rm gs}(\phi)$.[268]

A description of the solid-liquid interface under EC conditions beyond this simple approach is, however, far from trivial. Different calculational schemes have been proposed in the literature to model the solid-liquid interface in an EC cell.[276–278] Here, DFT calculations have been carried through to investigate the c(2x2) Cl adlayer formed on a Cu(100) surface at an EC interface. The results have been published in Ref. 279. Gründer *et al.* have studied the c(2x2) Cl adlayer formed on a Cu(100) electrode in 10 mM

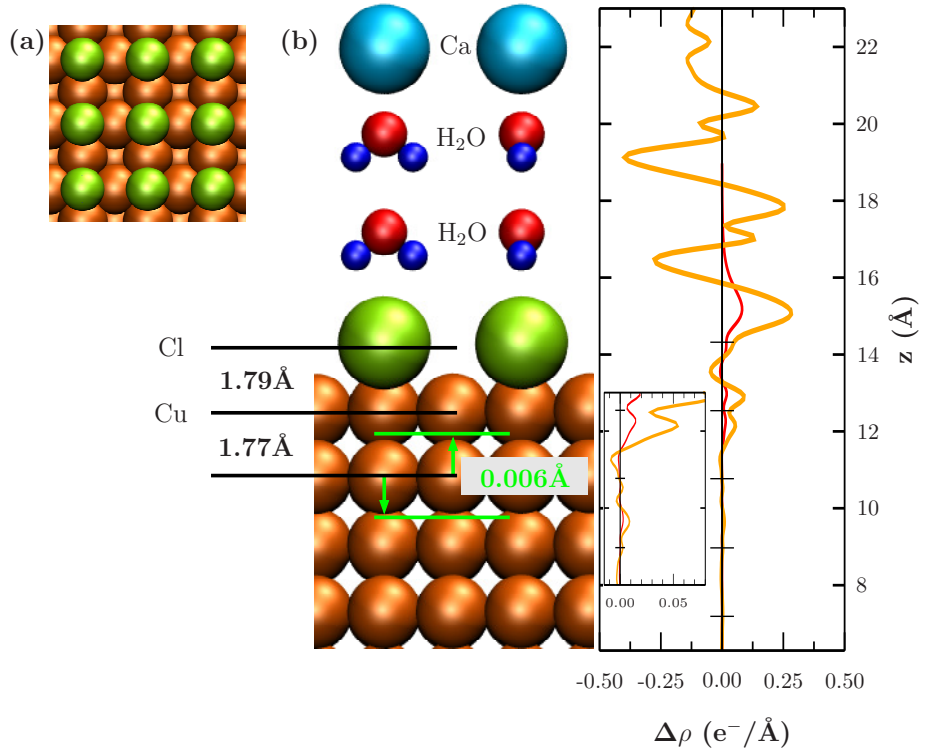

Figure 4.22: (a) Top view of the c(2 × 2) Cl adlayer on a Cu(100) surface. Cl atoms: green, Cu atoms: brown. (b) The Ca/H_2O set-up used to investigate the c(2 × 2) Cl adlayer on a Cu(100) surface under EC conditions (middle panel). The black lines have been placed at the average Cl or Cu vertical positions. The second layer buckling of the Cu atoms is indicated by the green arrows. The right panel depicts the induced charge density, $\Delta\rho$, along the surface normal (z direction) averaged over the xy plane (orange: Ca/H_2O set-up, red: electric field 0.9 V/Å without Ca/H_2O). The tick marks along the zero $\Delta\rho$ axis have bee drawn at the (average) vertical positions of the atomic layers. In the inset $\Delta\rho$ has been drawn to a larger scale.

HCl solution by *in situ* surface x-ray diffraction (SXRD).[279] Distinct differences compared to the interface to vacuum have been discovered. The Cl adatoms of the c(2x2) adlayer occupy 50% of the hollow sites of the Cu(100) surface. Therefore, a Cu atom of the second atomic layer of the surface is either located directly below a Cl adatom (Cl site) or not (empty site), see Fig. 4.22. At the c(2x2)-Cl/Cu(100) interface to vacuum, the second layer Cu atoms exhibit a small buckling such that the Cu atoms below the Cl sites are closer to the Cu(100) surface plane as the Cu atoms below the empty sites. The value of the buckling amplitude at the interface to vacuum amounts to -0.012 Å (see Ref. 279 and references therein). From their experimental data, Gründer *et al.* have educed

that the second layer Cu buckling is reversed for the employed EC conditions at -0.20 V electrode potential versus the reference. In this case the second layer Cu buckling of c(2x2)-Cl/Cu(100) amounts to +0.025 Å. It is argued that this intriguing difference between the two interfaces can be reproduced by DFT calculations. Two simple approaches have been used to model the solid-liquid interface: (i) a homogenous electric field has been applied perpendicular to the slab to mimic the electric field in front of the electrode surface[277] and (ii) two Ca atoms have been placed in the middle of the vacuum region which donate electrons to the interface such that an electric field develops between the surface and the positively charged Ca ions, see Fig. 4.22. In addition, four water molecules have been added to the simulation cell, which are placed in between the Cl adatoms and the Ca atoms to simulate the dielectric medium (solution). This set-up was inspired by the work of Filhol and Neurock[276] and has been used to model the Cu(100)/halogen/electrolyte interface by Saracino *et al.*[280]

DFT calculations carried through by Stremme for the interface to vacuum yield a second layer Cu buckling of -0.006±0.004 Å compatible with an experiment by Tolentino *et al.* (-0.012±0.003 Å).[140] If an electric field is applied to the c(2x2)-Cl/Cu(100) slab (electric field vector pointing towards the surface), a negative surface charge is induced and the second layer Cu buckling is slightly reduced to -0.005 Å and -0.004 Å for an electric field strength of 0.3 V/Å and 0.9 V/Å. However, the induced surface charges are not sufficient to reverse the buckling. In addition to a reduction of the Cu buckling, the distance between the Cl and Cu atoms of the first surface layer increases if an electric field is applied in the calculation. This is compatible with a comparison based on experimental data for the interface to vacuum and the EC interface. Hence, the qualitative trends observed in experiment have been reproduced albeit the effect comes out too small.

Introducing the water molecules and the Ca atoms to the vacuum region leads to a charge transfer and a surface charge which is substantially larger compared to the electric field effect (roughly a factor of four), see Fig. 4.22. For one this leads to a further significant increase of the distance between the Cl-Cu atoms of the adlayer and the first atomic layer of the Cu(100) surface (DFT: +7%, experiment: +17%). Moreover, the corrugation of the second layer Cu atoms is indeed reversed and comes out to be +0.006 Å (experiment: +0.025 Å). The larger effects might be related to the larger charge transfer induced by the Ca/H_2O set-up compared to the applied electric field case. An inspection of the induced charge density, $\Delta\rho = \rho_{\mathrm{Cl/Cu(100)}} - \rho_{\mathrm{H_2O}} - \rho_{\mathrm{Ca}}$, unfortunately does not reveal the precise mechanism behind the reversal of the buckling. Note that the second layer buckling effect is very small compared to the Cl-Cu relaxations taking place upon introducing the Ca atoms and the H_2O molecules to the calculations. This seems to mask the origin of buckling reversal.

The qualitative agreement between the DFT calculations and the crystallographic experiment is encouraging. Such a comparison might provide the ground to test and advance the highly active research field concerned with theoretical models for EC interfaces. If such improved descriptions become available, *first-principles* calculations of diffusion at an electrode-electrolyte interface should certainly benefit.

4.5.2 Publication Physical Review B 81, 174114 (2010), Copyright (2010) by the American Physical Society

Reversal of chloride-induced Cu(001) subsurface buckling in the electrochemical environment: An *in situ* surface x-ray diffraction and density functional theory study

Y. Gründer, D. Kaminski,* F. Golks, K. Krug, J. Stettner, and O. M. Magnussen
Institut für Experimentelle und Angewandte Physik, Universität Kiel, Olshausenstr. 40, 24098 Kiel, Germany

A. Franke, J. Stremme, and E. Pehlke
Institut für Theoretische Physik und Astrophysik, Universität Kiel, Olshausenstr. 40, 24098 Kiel, Germany
(Received 20 October 2009; published 20 May 2010)

The interface of Cu(001) electrode surfaces in 10 mM HCl solution was studied by *in situ* surface x-ray diffraction and density functional theory, focusing on the precise structure of the $c(2\times2)$ Cl adlayer formed at positive potentials. Crystal truncation rod measurements in this adsorbate phase at a potential of −0.20 $V_{Ag/AgCl}$ reveal distinct differences to corresponding data by Tolentino *et al.* [Surf. Sci. **601**, 2962 (2007)] for the $c(2\times2)$ Cl structure formed at the Cu(001)-vacuum interface. Although in both environments, the atoms in the second Cu layer exhibit a small vertical corrugation, the sign of this corrugation is reversed. Furthermore, also the Cu-Cl bond distance and the average Cu interlayer spacings at the surface differ. *Ab initio* calculations performed for this adsorbate system reproduce these effects—specifically the reversal of the subsurface second-layer buckling caused in the presence of coadsorbed water molecules and cations in the outer part of the electrochemical double layer. In addition, studies at more negative potentials reveal a continuous surface phase transition to a disordered Cl adlayer at −0.62 $V_{Ag/AgCl}$, but indicate a substantial Cl coverage even at the onset of hydrogen evolution.

DOI: 10.1103/PhysRevB.81.174114 PACS number(s): 61.05.cf, 68.08.−p, 68.43.−h, 71.15.Mb

I. INTRODUCTION

The atomic-scale structure of the metal-electrolyte interface is a topic of central importance to interfacial electrochemistry and has been studied extensively by electrochemical measurements, structure-sensitive *in situ* techniques, as well as by theoretical methods. In particular, adsorbate layers of strongly chemically bound ("specifically adsorbed") anions, such as halide or sulfate, have been investigated in great detail, revealing a complex, potential-dependent two-dimensional (2D) phase behavior, which can significantly affect electrochemical reactions such as galvanic deposition, etching, corrosion, and electrocatalytic processes.[1] Often very similar superstructures are observed as those found in studies under ultrahigh vacuum (UHV) conditions after adsorption of the corresponding gaseous species from the gas phase. Nevertheless, complete structural agreement is not expected since in electrochemical environment the presence of physisorbed species in the so-called diffuse double layer—notably coadsorbed water and cations—leads to pronounced changes in the electrostatic potential drop at the interface, as revealed by UHV model studies on simulated double layers.[2,3] The precise influence of these effects on the interface structure is still unclear. Specifically, up to now only a few studies have presented detailed measurements of the bond lengths at electrochemical interfaces that could be directly compared to structural data on corresponding anionic adlayer structures under UHV conditions.[4–9] Such comparative studies allow to clarify how the presence of the outer part of the double layer alters the chemical bonding of the chemisorbed inner adsorbate layer to the surface and the near surface structure of the metal electrode, which in turn may throw light on the interplay among the interactions of the various species at the interface, the charge distribution, and the interface structure. Here we present a combined surface x-ray diffraction (SXRD) and density-functional theory (DFT) study of Cu(001) in hydrochloric acid which reveals that the presence of water and cations in the outer double layer not only introduces relaxations in the spacing of the chemisorbed chloride and the first metal layers but also a reversal of a subsurface lattice modulation as compared to that observed in UHV. For better understanding of the structural differences in UHV and in electrochemical environment, we estimate the difference of the work function introduced by the electrolyte and discuss its influence on the structure of the adsorbate complex.[10]

Halide adlayers in electrochemical environment[1] as well as the corresponding halogen adlayers formed in the gas phase[11] adsorb on the (001) surface of most fcc metals in form of a simple low-order commensurate $c(2\times2)$ structure with $P4mm$ symmetry, where the adsorbates reside in the energetically strongly preferred fourfold-hollow sites of the metal substrate lattice.[12–15] A prototypical system for halide adsorption on fcc(001) surfaces and for which the adsorption process has been studied by SXRD and by electrochemical methods is Br on Ag(001).[10,16,17] For increasing potential a second-order phase transition from a lattice gas to an ordered $c(2\times2)$ structure has been found for the bromine adlayer. Also the adsorption of Cl on Cu(001) is an important, well-studied example of this $c(2\times2)$ adlayer. It has been reported for chlorine adlayers under UHV conditions[18–25] as well as in chloride-containing electrolytes.[6,7,26–31] However, at the electrochemical interface the $c(2\times2)$ structure was observed only positive of a critical potential (−0.4 $V_{Ag/AgCl}$ at a Cl concentration of 10^{-3} M) by *in situ* STM, whereas at more negative potentials the (1×1) substrate lattice was visible, suggesting a potential-induced order-disorder phase transition into a dilute adlayer of highly mobile chloride.[28,30] More

recently, the surface-normal interface structure of the $c(2\times2)$ adlayers of Cl and Br on Cu(001) was studied by *in situ* SXRD, focusing on the halide-copper interlayer spacing.[6,7] Specifically, the dependence of the Br adlayer spacing on potential was found to be stronger than that of the Cl adlayer, which was attributed to a more ionic character of the Cl and an almost discharged Br adsorbate, respectively. Similar SXRD measurements of Cl on Cu(001) surfaces under UHV conditions by Tolentino *et al.*[18] as well as earlier angle-resolved photoemission studies by Wang *et al.*[32] indicated that the $c(2\times2)$ superstructure extends to the second atomic copper layer in form of a small subsurface buckling, an effect that was also reported for the $c(2\times2)$ Br adlayer in the *in situ* SXRD study by Saracino *et al.*[6,7]

In this work we present detailed *in situ* SXRD and complementary DFT results on the adsorption behavior and interface structure of Cu(001) electrodes in chloride-containing electrolyte, focusing on the buckling in the second Cu layer. These studies allow to directly compare the Cu surface structure in the presence of the $c(2\times2)$ Cl adlayer and after disordering and partial desorption of the Cl with corresponding data for Cl-covered and clean Cu(001) surfaces under UHV conditions, respectively. In particular, the influence of the electrochemical environment on the copper subsurface buckling will be discussed. As reference for the surface structure of the $c(2\times2)$ Cl adlayer at the Cu(001)-vacuum interface we will use the recent SXRD study by Tolentino *et al.*[18] SXRD provides direct, highly accurate structural data that can be modeled on the basis of simple kinematic diffraction theory. Results by this technique therefore seem more reliable than those obtained by electron diffraction methods, where more complex modeling by dynamic scattering theory is required.

II. EXPERIMENTAL

A. Surface x-ray diffraction

The x-ray scattering experiments were performed at the ID 32 beamline of the European Synchrotron Radiation Facility in Grenoble using a photon energy of 22.5 keV and a grazing incidence angle of 0.44°. The Cu(001) single-crystal sample (Mateck, 99.999%, 4 mm diameter, miscut $<0.1°$) was prepared prior to the experiments by electropolishing in 70% orthophosphoric acid. Subsequently, the sample was covered by a droplet of milli-Q water and mounted into the electrochemical hanging meniscus cell described in Ref. 33. In all experiments 10 mM HCl solution prepared from suprapur hydrochloric acid (Merck) and milli-Q water was used as electrolyte. All potentials were measured versus a Ag/AgCl (3 M KCl) reference electrode. During the measurements the liquid meniscus in contact with the surface was kept under high-purity nitrogen (air liquid, 99.999%) to remove dissolved oxygen from the electrolyte.

In the crystal truncation rod (CTR) studies the integrated intensities $|F_{hkl}|^2$ (where F_{hkl} is the structure factor) of different reflections (hkl) were measured in z axis geometry by rotating the sample about its surface normal. The background-subtracted integrated intensities were corrected for the Lorentz factor, polarization factor, active sample area, and the rod interception appropriate for the z axis geometry.[34] Since the specular rod was recorded in $(\theta\text{-}2\theta)$ geometry, for which different corrections for the active sample area and the rod interception have to be applied than for the nonspecular CTRs, its intensity distribution had to be corrected by an additional scaling factor. Errors due to photon statistics and systematic errors in data acquisition are taken into account. The latter was estimated from deviation of measured integrated intensities of symmetry equivalent reflections to 20% and is the dominating contribution. The structure was determined by a fit of the simulated square of the structure factors to the experimental ones and a χ^2 minimization using the code "fit" (Ref. 35) which allows a three dimensional structural refinement of the SXRD data.[36–38] *The parameter error* Δx *of the best fit value* x *is determined by* $\chi^2(x+\Delta x)=\chi^2(x)+1$.

Standard bulk coordinates of the Cu(0 0 1) surface ($a_1=a_2=a_3=3.615$ Å, $\alpha=\beta=\gamma=90°$) are used in the following. The momentum-transfer vector is then defined by $Q=Hb_1+Kb_2+Lb_3$ with $a_ib_i=2\pi\delta_{ij}$ where H, K, L, are the diffraction indices. The index L is along the direction perpendicular to the surface. The indices of the crystal truncation rods are given by $(H+K=2n)$ and the ones for rods from the reconstructed surface are determined by $(H+K=2n+1)$.

B. Density functional theory

The density functional theory (DFT) calculations were performed using the Vienna *ab initio* simulation program (VASP) developed at the Institut für Materialphysik of the Universität Wien.[39–42] The generalized gradient approximation by Perdew and Wang (PW91-GGA) (Ref. 43) is applied to the exchange-correlation energy-functional. All atoms except Ca are described by projector augmented wave (PAW) pseudopotentials as introduced by Blöchl *et al.*[44] Ca atoms are described by ultrasoft pseudopotentials. The potentials for VASP from the database are used.[45]

The Cu(001) surface is simulated by a slab geometry with a supercell containing 15 Cu layers and a $p(2\times2)$ surface unit cell. The theoretical lattice constant for Cu of $c=3.636$ Å is assumed, which is slightly larger than the experimental lattice constant $c=3.615$ Å. The Cl atoms are adsorbed on both sides of the slab forming a $c(2\times2)$ superstructure, with the Cl atoms occupying hollow positions of the Cu(001) surface. The kinetic-energy cutoff of the plane-wave basis set has been chosen equal to 280 eV, and the integrals over the Brillouin zone are approximated by sums over special **k** points. We use a 6×6 Monkhorst-Pack set of equidistant **k** points[46] parallel to the surface. Atomic positions were relaxed until the residual forces acting on the Cu and Cl atoms are less than 1 meV/Å. The maximum allowed residual force has been chosen rather small because the atomic displacements of interest in this work are only of the order of few mÅ. In this way, the surface structure under UHV conditions can be calculated.

The Cu(001)-$c(2\times2)$ Cl surface becomes much more difficult to describe when in contact with an electrolyte. Different approaches to simulate electrochemical interfaces have been developed and are described in the literature.[7,47–52] Here

we follow two different simple approaches in order to obtain a qualitative impression of the effects on the Cu surface relaxation induced by the presence of the electrolyte: (i) a homogeneous electric field of the order of 0.3–0.9 V/Å is applied perpendicular to the slab[53] to simulate the electric field in the Helmholtz layer. In the bulk the electric field is screened by the induced surface charge density. The electrostatic potential has a discontinuity in the middle of the vacuum region. In this way the perturbing potential can be taken to be periodic. We monitor the additional displacement of the Cl and the Cu atoms induced by the electric field together with its induced screening charge density. (ii) Following the method described (and already applied to Cu(001)/halogen/electrolyte interfaces) by Saracino *et al.*,[7] two Ca atoms are placed in the middle of the vacuum region within each supercell. They are located atop the two Cl atoms in the $p(2\times2)$ surface unit cell, but in view of the large separation between the Ca and the surface atoms we expect displacement of the Ca atoms parallel to the surface to be of only minor importance for the effects investigated here. Electrons are transferred from the Ca atomic layer to the metal-halogen slab. This charge transfer results in an electric field in front of the metal. Furthermore, two pairs of water molecules, located on top of each other, have been added to each side of the slab. As in Ref. 7, the H-atoms point toward the surface, and the O atoms lie above the Cl atoms. During the subsequent relaxation, the Cl atoms and the Cu atoms in the outermost six layers of the slab as well as the H and O atoms of the water molecule are allowed to move, with each O-atom being restricted to an axis perpendicular to the surface. The residual forces acting on the water molecules are less than 3 meV/Å. In order to control the pressure exerted on the surface, calculations have been carried through for different thickness of the region between the slabs.

III. RESULTS

A. Surface x-ray diffraction

In the initial phase of the experiments the Cu(001) surface was characterized by cyclic voltammetry, recorded in the SXRD cell, and parallel measurements of the scattered x-ray intensity at selected positions along the substrate's CTRs and $c(2\times2)$ superstructure rods (Fig. 1). Specifically, the potential-dependent intensity at (1, 0, 0.1) and (1, 1, 0.1), i.e., the $c(2\times2)$ superstructure rod and the anti-Bragg position of the lowest-order Cu(001) CTR, was monitored. The intensity measured at (1, 0, 0.1) is proportional to the square of the coverage of the Cl induced $c(2\times2)$ superstructure, whereas data monitored at the anti-Bragg position (1, 1, 0.1) is sensitive to the coverage of all Cu-hollow sites occupied with Cl atoms, independent of the degree of order.[17] Recording the potential dependent intensity of both the superstructure rod and the anti-Bragg position is therefore indispensable to determine independently the coverages for both adlayer phases, the two-dimensional lattice gas as well as the Cl $c(2\times2)$ superstructure. In the voltammogram, Cl adsorption and desorption manifests in form of broad peaks between ≈−0.35 V and the onset of hydrogen evolution near −0.70 V (the additional cathodic current in this potential

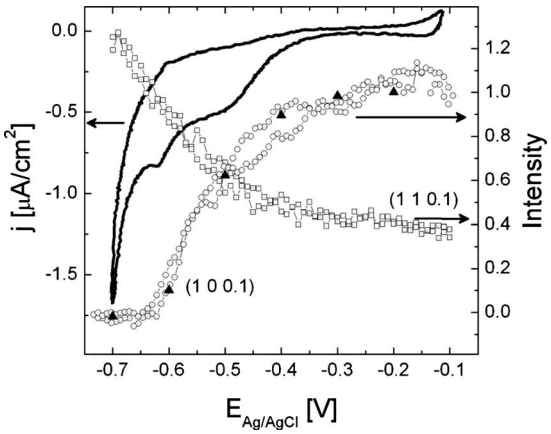

FIG. 1. Cyclic voltammogram (scan rate 10mV/s) of Cu(001) in 10 mM HCl (solid line) as well as potential-dependent intensity of the Cl superstructure rod at (1, 0, 0.1) and the Cu CTR at (1, 1, 0.1). In addition, the intensities measured after a step from −0.2 V to different potentials are indicated (filled triangles).

range may be related to the reduction of small amounts of residual oxygen in the cell). During the chloride adsorption process the intensity at the anti-Bragg position decreases while the intensity at the superstructure rod increases from zero at the negative potential limit to a saturation value at potentials positive of ≈−0.35 V. Potential-step experiments show that the intensity change occurs on time scales shorter than the time resolution of the SXRD experiments (0.5 s) and is highly reversible (as also seen in the potential-sweep experiment in Fig. 1). Such a behavior can only be attributed to the desorption and disordering of the chloride adlayer, whereas other structural changes such as potential-induced variations in the surface roughness can be excluded. Furthermore, no evidence of other ordered Cl adlayer structures was found in in-plane scans along high-symmetry directions. The latter as well as the absence of potential-induced surface roughening is in excellent agreement with the extensive previous *in situ* STM studies of this system.

According to these measurements, residual $c(2\times2)$ ordering exists down to potentials close to the onset of hydrogen evolution and only completely disappears at −0.62 V. This $c(2\times2)\leftrightarrow(1\times1)$ transition manifests in form of small peaks in the cyclic voltammogram and occurs at substantially more negative potentials than those where the $c(2\times2)$ structure was observed by *in situ* STM.[28,30] The latter most likely is caused by a high adsorbate mobility in the potential regime where the surface is only partially covered by the ordered adlayer structure, inducing rapid fluctuations in the $c(2\times2)$ domain network on time scales beyond the temporal resolution in the earlier STM studies. Indeed, in very recent *in situ* video-STM observations positional changes of the Cl adsorbates at domain boundaries faster than 10^{-4} s were inferred.[54] The intensity curves at (1, 0, 0.1) and (1, 1, 0.1) are identical for potential sweeps in positive and in negative direction, indicating a highly reversible process as expected for anion adsorption. Furthermore, in potential jump experiments the same steady-state intensities were obtained after the potential step (Fig. 1, filled triangles), typically faster than the experimental time resolution (1 s). Consequently,

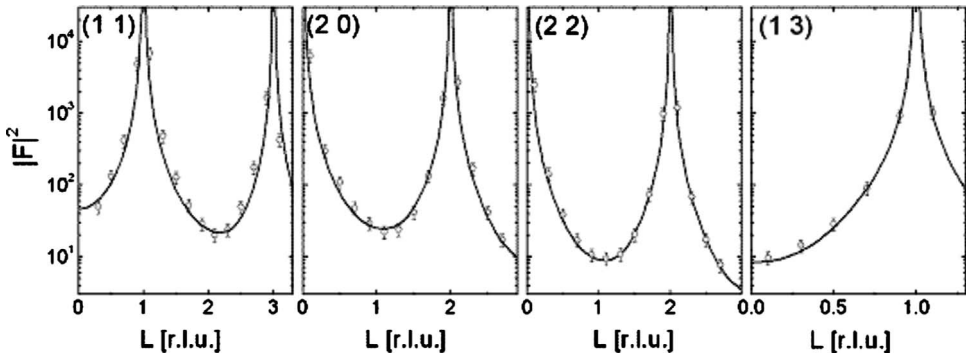

FIG. 2. Experimental crystal truncation rods of Cu(001) in 10 mM HCl at −0.70 V (circles) and best fit based on a relaxed bulk like structure (lines).

the curves in Fig. 1 represent the potential-dependent equilibrium state of this adsorbate system.

These results are at variance with recent SXRD experiments on Cu(001) in Br-containing solution by Saracino *et al.*[7] In that study the intensity at (1, 0, 0.1) on the superstructure rod was found to be nearly constant over the entire double layer potential range, even at negative potentials, where the corresponding voltammogram exhibited similar Br adsorption and desorption peaks as visible in Fig. 1. The reason for this discrepancy, not only to our SXRD results but also to the electrochemical and previous *in situ* STM data,[28] is currently unclear. However, the behavior observed in this study is almost identical to that found by *in situ* SXRD for bromide and chloride adsorption on Ag(001) electrodes, where likewise a continuous order-disorder transition to a $c(2\times2)$ phase with very similar x-ray intensity curves was reported.[10,16,17] Specifically, for Br on Ag(001) the intensity at (1, 1, 0.1) was found to increase toward more negative potentials, as in the system studied here, reaching a saturation value only 300 mV negative of the potential where the $c(2\times2)$ superstructure peak disappeared. This behavior was attributed to the presence of a disordered 2D lattice gas of adsorbates which partly occupy fourfold hollow and partly other adsorption sites. Also for Cl on Cu(001) an analogous lattice gas most likely exists negative of the phase transition potential, although the complete desorption of the anion adlayer apparently only occurs deep within the hydrogen evolution regime and hence was not accessible in the SXRD experiments. The chloride desorption process on Cu(001) with a remaining $c(2\times2)$ structure is stretched over a range of 300 mV, whereas the Br desorption process on Ag(001) with a remaining $c(2\times2)$ structure only takes place over a potential range of 200 mV. This indicates that the desorption process is slower for Cl on Cu(001) than for Br on Ag(001) which can be explained by the less noble character of the copper substrate compared to silver and the higher ionicity of the chloride compared to bromide inducing a stronger binding with larger attractive interaction between the substrate and adsorbate.

Detailed studies of the interface structure were performed at −0.20 V, where the surface is fully covered by the $c(2\times2)$ Cl superstructure (Fig. 2), and at −0.70 V, i.e., ≈100 mV negative of the order-disorder phase transition potential (Fig. 3). At both potentials we measured the (1, 1, *L*), (2, 0, *L*), (2, 2, *L*) and (1, 3, *L*) CTRs and obtained a set of 48 nonequivalent reflections. At −0.20 V in addition the specular rod and the (1, 0, *L*) and (1, 2, *L*) superstructure rods were recorded, with in total 44 integrated intensities $|F_{hkl}|^2$ at nonequivalent reciprocal space positions (hkl). The *L* dependent diffuse background of the (1, 0, *L*) superstructure rod was determined carefully and subtracted. Due to the errors associated with this procedure, the errors of the integrated intensities of the (1, 0, *L*) rod increase at lower *L*. The integrated intensities of the rods recorded at the two different potentials were taken in the same geometry on the same sample. The CTR data at both potentials is fully consistent with the potential dependence of the x-ray intensity shown in Fig. 1.

The CTRs obtained at −0.70 V were fitted to a structural model assuming a Cu(001)-(1×1) surface and a relaxation of the layer spacing d_{12} between the copper surface layer and the underlying bulk lattice (for all following Cu layers the Cu bulk spacing was used). In addition, the anisotropic Debye-Waller factors for the first two Cu layers, an isotropic Debye-Waller factor for the third layer and an overall scale factor were optimized in the fit. In analogy to the Br/Ag(001) adsorbate system[10,16] a partial occupation of the fourfold-hollow sites with Cl adsorbates was assumed to model the disordered 2D lattice gas of chloride. Models without this disordered Cl adlayer also provided good fits of the experimental data and resulted in very similar vertical relaxations, but led to unusually small Debye-Waller factors of the Cu surface layer. The parameters for the best fit ($\chi^2=2.37$), which describes well the measured CTRs (Fig. 2, solid lines), are shown in Table I, together with the parameters obtained in SXRD measurements by Mironets *et al.* for a bare Cu(001) surface in UHV.[55] The Cl coverage 80 mV negative of the order-disorder transition is 0.15 ML which is in good agreement with the values found for Br on Ag(001) (Refs. 10 and 16) at corresponding potentials, i.e., 55 mV negative of the order-disorder transition taking into account the broader desorption regime of the chloride. However, this observation differs strongly from the zero coverage reported by Huemann *et al.* for the same system at the negative end of the double layer regime.[6] In the latter study a decrease rather than an increase in the intensity at (2, 0, *L*) was found toward negative potentials, contrary to our experimental data. This is probably the main cause of the different results in that study.

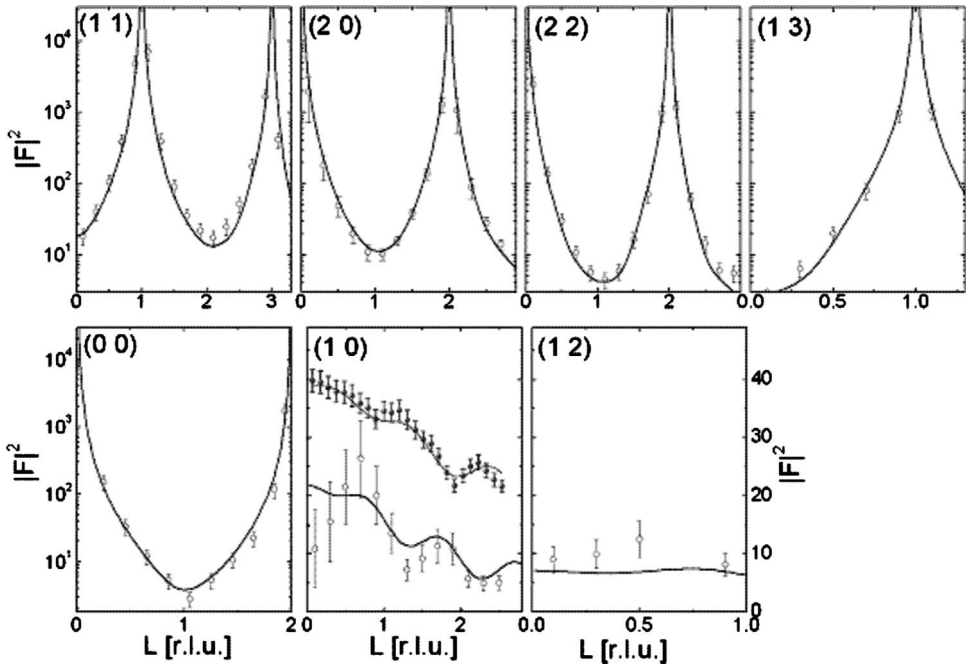

FIG. 3. Experimental crystal truncation rods and the lowest-order $c(2\times2)$ superstructure rod for Cu(001) in 10 mM HCl at −0.20 V (circles), together with the best fit based on the structural model described in the text (lines). Shown in the figures are also the measured (1, 0, L) superstructure rod of the $c(2\times2)$ Cl structure in UHV (from Ref. 18, filled symbols), which is antiphase shifted relative to the data obtained in electrochemical environment.

Unfortunately, only the (2, 0, L) CTR was measured at the negative limit, prohibiting a more detailed comparison. For the first layer a slight inward relaxation of 1.0% is found in our analysis, which directly manifests in the experimental data as a shift of the CTRs minima toward higher L. Within the experimental errors this relaxation is identical to that obtained for clean copper in UHV.[55]

Fits of the data measured at −0.20 V employed a model of a $c(2\times2)$ Cl adlayer as confirmed by STM measurements in chloride containing electrolytes[6,25–28] and supported by in-plane scans along high-symmetry directions of the Cu(001) surface. The spacing between the Cl adlayer and the Cu surface layer d_{Cl} as well as the topmost two layer spacings in the Cu substrate d_{12} and d_{23} were allowed to relax (see also Fig. 4). Furthermore due to the presence of distinct intensity oscillations in the (1, 0, L) superstructure rod (see Fig. 3) we allow in the second Cu layer different vertical positions for atoms directly below the Cl adsorbate atoms and the Cu atoms in between those. This small subsurface buckling of amplitude Δ_2 will be the focus of the following section. Qualitatively speaking, the intensity oscillations in the (1, 0, L) rod are caused by the interference of waves scattered at atomic layers, which are parallel to the surface plane and have a defined vertical distance as well as a phase difference between each other. The lateral periodicity within these layers has to be identical to that of the superstructure, with the Cl adsorbates on top of the Cu(001) forming the upper layer. The second layer has to result from a subsurface modulation with the same $c(2\times2)$ symmetry. It can be unambiguously identified as the buckling of the second layer, as the period of the oscillations of the superstructure rod is approximately one reciprocal lattice unit (see Fig. 3), corresponding to a vertical distance of 3.615 Å. This model is additionally sup-

TABLE I. Fit parameters for Cu(001)-(1×1) in 10 mM HCl at −0.70 V (this work) and under UHV conditions at 160 K (from Ref. 55). The values were given in Ref. 55 as rms vibrational amplitudes in Å and converted to Debye-Waller factors via $\langle u_s^2\rangle = B_j/(16\pi^2)$.

	(1×1) at −0.70 V	(1×1) in UHV (Ref. 55)
d_{Cl}(Å)	1.782 ± 0.030	
d_{12}(Å)	1.785 ± 0.020	1.777 ± 0.028
d_{23}(Å)	1.808 ± 0.020	1.806 ± 0.026
d_{34}(Å)	1.808 ± 0.020	1.809 ± 0.026
d_{45}(Å)	1.808 ± 0.020	1.807 ± 0.018
DW(Cl)	2.8 ± 0.1	
DW($Cu_{1\parallel}$)	1.75 ± 0.05	1.876 ± 0.036
DW($Cu_{1\perp}$)	1.18 ± 0.11	2.052 ± 0.098
DW($Cu_{2\parallel}$)	0.74 ± 0.08	1.087 ± 0.010

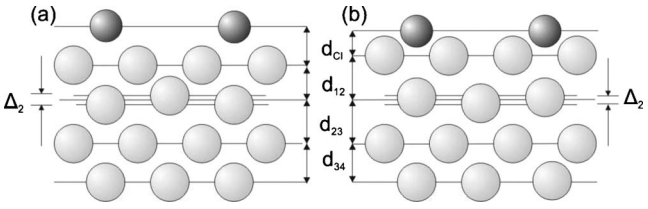

FIG. 4. Side view of the structural model for the $c(2\times2)$ Cl adlayer on Cu(001) in (a) electrochemical environment and (b) at the metal-vacuum interface, illustrating schematically the lattice relaxation and the buckling of the second Cu layer.

TABLE II. Fit parameters for $c(2\times2)$ Cl-covered Cu(001) in 10 mM HCl at −0.20 V (this work) and under UHV conditions (Ref. 18).

	$c(2\times2)$ at −0.20 V	$c(2\times2)$ in UHV (Ref. 18)
d_{Cl}(Å)	1.856 ± 0.015	1.585 ± 0.006
d_{12}(Å)	1.794 ± 0.015	1.839 ± 0.005
d_{23}(Å)	1.822 ± 0.025	1.825 ± 0.003
Δ_2(Å)	+0.025 ± 0.0070	−0.012 ± 0.003
DW($Cl_{\parallel}$)	2.39 ± 0.17	2.61
DW($Cl_{\perp}$)	2.05 ± 0.19	0.44
DW($Cu_{1\parallel}$)	1.64 ± 0.03	1.39
DW($Cu_{1\perp}$)	0.35 ± 0.06	
DW(Cu_2)	0.70 ± 0.03	0.7

ported by symmetry arguments: the $c(2\times2)$ superstructure exhibits *p4mm* symmetry with two perpendicular mirror planes crossing at the free hollow site of the Cu(001) bulk unit cell and a fourfold rotation axis also located at the free hollow site. All atoms of the unit cell are located at high-symmetry positions and therefore lateral displacements are forbidden by the symmetry. In addition all copper atoms of the first (or in fact any odd) Cu layer are equivalent and therefore a buckling in those layers is forbidden. Additional free fit parameters were anisotropic Debye-Waller factors for the first two Cu layers, an isotropic Debye-Waller factor for the third Cu layer, and the overall scale factor. The latter was found to be within 2% of the scale factor determined by the fit of the data at −0.70 V, indicating a consistent fit of the two surface structures. Table II summarized the parameters of the best fit ($\chi^2=2.85$) together with those obtained by Tolentino *et al.* for this adsorbate system under UHV conditions;[18] the corresponding calculated CTRs and superstructure rods are included in Fig. 3 (solid lines) and obviously provide a good quantitative description of the experimental data. The structural parameters of the $c(2\times2)$ Cl superstructure in the two environments strongly differ, as will be discussed in more detail in the following sections. Specifically, the second-layer Cu atoms located directly below the Cl adsorbates are at lower vertical positions than the atoms in between the adsorbed Cl, opposite to the observations at the metal-vacuum interface.[18]

The presence and qualitative behavior of this subsurface buckling can be directly seen in the experimental data. As shown in Fig. 3, the (1, 0, *L*) superstructure rods measured in vacuum and electrochemical environment exhibit a clear difference, namely, a phase shift of the oscillations relative to each other by 0.5 reciprocal lattice units. In the following we will show that this phase shift is the direct result of a reversal in the second Cu layer buckling at the electrochemical interface as compared to that found in UHV. The intensity of the superstructure rod is due only to scattering from atoms obeying the symmetry of the superstructure, i.e., the adsorbate layer and the second copper layer within our model. Placing these atoms at $\vec{r}_{Cu\ a}=\binom{0}{\Delta_2/2}$, $\vec{r}_{Cu\ b}=\binom{a_1/\sqrt{2}}{-\Delta_2/2}$ and $\vec{r}_{Cl}=\binom{0}{d}$, where $d=d_{Cl}+d_{12}$ is the vertical distance of the chloride adlayer to the average vertical positions of the second-layer Cu atoms and the buckling amplitude Δ_2 is positive if the copper atom beneath the chloride atom is lifted, the intensity distribution along the (1, 0, *L*) rod is given by

$$I \propto |f_{Cl}e^{i\cdot q_z\cdot d} + f_{Cu}(e^{iq_z\Delta_2/2} + e^{i\pi}e^{-iq_z\Delta_2/2})|^2$$
$$\approx f_{Cl}^2 + f_{Cu}^2(q_z\Delta_2)^2 + 2f_{Cu}f_{Cl}q_z\Delta_2\sin(q_zd). \quad (1)$$

Here the Debye-Waller factor is included in the structure factors for chloride (f_{Cl}) and copper (f_{Cu}) and Δ_2 is assumed to be much smaller than *d*. The oscillations of the intensity of the superstructure rod are represented by the third summand in Eq. (1), which includes the term $\sin(d\ q_z)$. This simple calculation in kinematical approximation shows clearly that exclusively the buckling amplitude Δ_2 and the vertical distance d between the second Cu layer and the Cl adlayer affect the amplitude and the period, respectively, of the intensity oscillation of the superstructure rod. This implies especially that a significant correlation between the parameter pair (Δ_2 *d*) and the remaining structural parameters can be excluded. For that reason, this small effect can be unambiguously detected, although the buckling amplitude is similar to the errors in the interlayer spacings. The above consideration also confirms the assumed model: the extension of the superstructure to another Cu layer than the second would affect the oscillation period and an additional layer would result in additional oscillations with different period. Reversal of the buckling, i.e., inversion of the sign of Δ_2, causes an antiphase shift in the oscillations. Hence, the two central qualitative observations for the (1, 0, *L*) rod—the extension of the $c(2\times2)$ to the second Cu layer and the different sign of the buckling in UHV and electrochemical environment—can already be deduced from this simplified analysis. In addition, the CTR analysis indicates a 17% expansion of the Cl-Cu interlayer spacing as compared to that found in UHV,[18] in agreement with the *in situ* SXRD results by Huemann *et al.*[6]

B. Calculation of second-layer Cu-atom buckling

In this section we argue that the reversal of the sign of the corrugation of the second-layer Cu atoms at the electrochemical interface, as opposed to UHV, can be reproduced by density functional calculations. DFT calculations for this system have been carried through by Saracino *et al.*,[7] who mentions a small buckling to result from their calculations. Here we focus on this subsurface buckling, which was not quantified explicitly in the previous DFT work. In order to relate to literature we will also quote our calculated Cl-Cu and Cu-Cu interlayer separations. Initial calculations for the clean Cl-free Cu(001) surface yield an interlayer separation of the two topmost Cu layers of 1.76 Å, which corresponds to a 3% contraction with respect to the bulk value. This agrees within the error bars with previous theoretical (GGA or LDA) results,[14,56] and it is consistent with the experimental SXRD results for a clean Cu(001) surface under UHV conditions[55] and in 10 mM HCl at −0.70 V (see Table I). For the $c(2\times2)$ Cl covered Cu(001) surface in the absence of external electric fields or additional species, i.e., the surface under UHV conditions, we obtain a Cl-Cu interlayer separation $d_{Cl}=1.667\pm0.012$ Å in agreement with Ref. 7 and an average spacing between the two topmost Cu layers d_{12}

TABLE III. Calculated surface atomic geometry of $c(2\times2)$ Cl-covered Cu(001) in the presence of external applied electric fields, additional water molecules, and water and Ca counter ions. For the latter case also the height L_z of the supercell is given. Vac denotes a vacuum layer. The estimated error of the second Cu layer corrugation is 0.004 Å.

	L_z (Å)	d_{Cl} (Å)	d_{12} (Å)	Δ_2 (Å)
$c(2\times2)$-Cl at 0 V/Å	Vac	1.67	1.82	−0.006
$c(2\times2)$-Cl at 0.3 V/Å	Vac	1.68	1.82	−0.005
$c(2\times2)$-Cl at 0.9 V/Å	Vac	1.71	1.82	−0.004
$c(2\times2)$-Cl+H_2O	44.27	1.70	1.80	−0.002
$c(2\times2)$-Cl+H_2O+Ca	44.27	1.79	1.77	+0.006
$c(2\times2)$-Cl+H_2O+Ca	45.27	1.81	1.79	+0.0034
$c(2\times2)$-Cl+H_2O+Ca	46.27	1.82	1.81	+0.0026

$=1.817\pm0.01$ Å. Saracino *et al.* have reported a first Cu-Cu layer spacing 0.6% larger than the bulk value,[7] which is within the error bar of our calculation. The 3% contraction of the interlayer separation between the topmost two Cu layers of the clean Cu(001) surface vanishes upon Cl adsorption, which is ascribed to the charge transfer from the Cu surface to the negatively charged Cl ions.[57] The buckling amplitude of the second Cu layer is $\Delta_2=-0.006$ Å, with a convergence error of about ±0.004 Å estimated from additional calculations with different number of Cu layers, vacuum thickness, *k*-point sets, and cutoff energy. This value is compatible with the experimental corrugation under UHV conditions found in the SXRD measurements by Tolentino *et al.*,[18] taking the errors in the experimental and DFT studies into account.

In a first approach, the effect of the outer part of the electrochemical double layer on the Cu surface relaxation was simulated by applying a homogeneous electric field to the $c(2\times2)$ Cl slab. The electric field vector is parallel to the surface normal and points toward the Cu surface. This corresponds to an induced negative screening charge at that surface. In response to the applied electric field the corrugation of the second-layer Cu atoms decreases, as can be seen in Table III. However, the applied fields in the range of 0.3 V/Å–0.9 V/Å are not sufficiently strong to reverse the buckling. The average interlayer separation between the two first metal layers d_{12} decreases only insignificantly as the electric field is switched on, while the Cl-Cu separation increases in agreement with the trend reported in Ref. 7. The qualitative trends are thus the same as derived from the comparison of the present SXRD experiments with the data by Tolentino *et al.*[18] but the effect is too small, at least for the electric field strengths considered here.

In all following DFT calculations the electrochemical interface was modeled by additionally introducing species of the outer Helmholtz layer—specifically water and counter ions—into the supercell, whose height was chosen equal to 44.27 Å. If solely water molecules are added to the system the corrugation decreases to $\Delta_2=-0.002$ Å while the Cl-Cu interlayer separation increases (in comparison to the surface in UHV) to $d_{Cl}=1.70$ Å and the topmost Cu interlayer separation contracts to $d_{12}=1.80$ Å. This trend fits to the conception that the Cl ion is partially screened by the water dipoles, thereby weakening the Cl-Cu bond and strengthening the attractive interaction between the two topmost Cu layers.[50]

Finally, we have added both the water molecules and Ca atoms into the vacuum region between the slabs. For this system occurs a charge transfer from the Ca atoms to the slab, which results in an electric field in the electrolyte region. Upon structural optimization of the $c(2\times2)$ Cl surface as described above (see Sec. II B), the relaxation pattern changes distinctly more pronounced than in the calculations where the electric field was directly applied. The results are summarized in Table III for different size L_z of the supercell in the direction perpendicular to the surface. We note that the total energy adopts a minimum between $L_z=45$ and 46 Å, corresponding to the condition of zero pressure. Additional calculations at different L_z but frozen position of the top layer Cu and Cl atomic positions corroborate the interpretation that a significant part of the variation in Δ_2 in Table III is related to the different amount of charge transfer as a function of L_z. The largest effect on the Cu corrugation Δ_2 can be observed for $L_z=44.27$ Å (for which, however, the pressure does not vanish). In this case, the Cl-Cu interlayer separation further increases to $d_{Cl}=1.79$ Å whereas the average spacing between the first two Cu layers decreases. Most notably, the corrugation of the second-layer Cu atoms reverses its sign as compared to the surface under UHV conditions and becomes $\Delta_2=0.006$ Å. Hence, our DFT calculations reproduce the intriguing effect of the electrolyte on the subsurface buckling of the second Cu layer. To relate this result for $L_z=44.27$ Å to the relaxations caused by an electric field (Table III, top 3 rows) we note that the screening charge density at the Cu surface atoms is roughly a factor of four larger than in case of the 0.9[V/ Å] electric field. The larger effect may therefore be a consequence of the larger induced charge density.

IV. DISCUSSION

As already discussed in the previous studies by Huemann *et al.*[6] and Saracino *et al.*,[7] the interface structures of the $c(2\times2)$ Cl adlayer on Cu(001) in electrochemical environment and at the metal-vacuum interface exhibit notable differences, which can be attributed to the presence of the outer Helmholtz layer. They are schematically indicated in the structural models shown in Figs. 4(a) and 4(b). In agreement with the previous *in situ* SXRD results[6] the Cu-Cl interlayer spacing of 1.856 Å and the corresponding Cu-Cl bond length of 2.59 ± 0.01 Å are 17% larger than that observed in UHV.[18] As already pointed out by Huemann[6] the spacing in electrochemical environment is close to that expected for ionic bonding (2.58 Å),[58] whereas the bond-length deduced from the SXRD data in UHV is closer to the bond-length expected for a covalent bonding (2.35 Å).[59] Furthermore, also the out-of-plane Debye-Waller factor of the chloride layers, corresponding to the chloride's vibrations perpendicular to the surface, is clearly increased at the electrochemical interface, whereas all other vibrational amplitudes are comparable in the two environments. Both effects can be attributed to a reduced binding of the Cl layer in the presence of the

electrolyte solution, caused by the solvation of the anionic adsorbates and the presence of counter ions in the diffuse layer.

Of particular interest in the present study is the small, but clearly detectable corrugation of the second copper layer. Under UHV conditions the Cu atoms below the Cl atoms are displaced toward the surface and those without Cl on top are closer to the Cu bulk [Fig. 4(b)].[18] This was explained by a partial charge transfer between the copper atoms in the first copper layer and the chloride atoms, resulting in an ionic bond between the chloride and the second-layer copper atoms underneath those adsorbates. In contrast, for the $c(2\times2)$ structure at the electrochemical interface our *in situ* SXRD data unambiguously indicates an upward displacement of the second-layer Cu atoms situated between the Cl adsorbate positions [Fig. 4(a)], i.e., a reversal of this subsurface buckling. A buckling of the same type as in our study and with similar corrugation amplitude (0.004–0.008 Å, depending on the potential) was also found by Saracino *et al.* for the $c(2\times2)$ structure of bromide on Cu(001).[7] Our DFT calculations strongly suggest that the corrugation reversal is a clear consequence of the presence of the electrolyte and apparently requires both the solvation of the Cl adsorbates by coadsorbed water as well as the electric field generated by cations in the outer Helmholtz layer. These effects modify the charge distribution in the chemisorbed adlayer and the adjacent Cu surface, which in turn may influence the structural relaxation of the top copper layers.

To better understand the relationship of $c(2\times2)$ Cl on Cu(001) in UHV and in electrochemical environment we estimate the potential shift introduced by the electrolyte. The potential of the metal electrode E_{Me} is given by[60]

$$E_{\mathrm{Me}} = \Phi_{\mathrm{Me}}/e - E_{\mathrm{ref}} + E_{\mathrm{sol}}. \tag{2}$$

Here Φ_{Me} is the electron work function of the metal in UHV and E_{ref} is the "absolute potential" of the reference electrode. The absolute potential of the standard hydrogen electrode is approximately $E_{\mathrm{SHE}}=4.5$ eV,[61,62] which corresponds to an "absolute potential" of the Ag/AgCl electrode of $E_{\mathrm{Ag/AgCl}}=4.7$ eV. The term E_{sol} contains potential shifts due to the contact of the electrode with electrolyte solution, which are (i) the modification of the work function when the electrode is brought in contact with the solution, (ii) the contribution of any preferentially oriented solvent molecules, and (iii) the potential drop due to the presence of free charges close to the interface. The work function of the bare Cu(001) surface is $\Phi_{001}=4.48$ eV, however, the adsorption of Cl into a $c(2\times2)$ superstructure introduces a work function shift of $\Delta\Phi_{c(2\times2)}=+1.1$ eV.[63] Consequently, the difference between the Cu(001) electrode in 10 mM HCl at an applied potential of −0.2 V and the $c(2\times2)$ Cl in UHV corresponds to

$$E_{\mathrm{sol}} = E_{\mathrm{Me}} - (\phi_{001} + \Delta\phi_{c(2\times2)})/e + E_{\mathrm{Ag/AgCl}} = -1.1\ \mathrm{V}. \tag{3}$$

Hence, the Cu(001)-$c(2\times2)$ surface in HCl solution is substantially negatively charged as compared to the $c(2\times2)$ Cl structure in UHV. This charge on the electrode side is compensated by a corresponding charge formed by cations in the outer Helmholtz layer and results in an electric field toward the Cu surface, as introduced in the calculations. Assuming the additional negative charge of the Cu(001)-$c(2\times2)$ in the electrochemical environment to be located on the Cl adlayer, this would correspond to a more ionic character of halide, resulting from the electrostatic screening of the chemisorbed Cl by the coadsorbed water and cations, which is supported by the consideration of the difference in bond lengths above. A higher ionicity of adsorbed halide ions under these conditions was already proposed in previous studies[6–9] to explain the expanded halide-copper bond at electrochemical interfaces. Furthermore, Saracino *et al.* suggested a less ionic character of $c(2\times2)$ Br on Cu(001),[7] which by analog reasoning as above can be attributed to the smaller work function shift [$\Delta\Phi_{c(2\times2)}=+0.9$ eV (Ref. 64)] induced by the Br adlayer.

Finally, we compare the structural data for the $c(2\times2)$ Cl-covered Cu surface at −0.20 V and the Cu(001)-(1×1) surface at −0.70 V, where the Cl adlayer is disordered. In both cases we find very similar values for the first Cu interlayer spacing, specifically an ≈1% inward relaxation. This agrees well with the relaxation of the clean Cu(001) surface,[55] but clearly differs from that of the Cu(001)-$c(2\times2)$ Cl in UHV,[18] which points again to pronounced changes in the nature of the adsorbate's bond as suggested previously.[6–9] The Cl vibration amplitudes at −0.70 V are increased in comparison to those at −0.20 V, in agreement with a disordering of the adlayer at negative potentials. The Cu-Cl spacing at −0.70 V appears smaller than that at −0.20 V, suggesting a slight change in the metal-halide bond. This is not unexpected since already under UHV conditions the adsorbate's coverage influences its charge state. For adsorbates in electrochemical environment this effect is even stronger due to the different hydration of the adsorbates in the low coverage phases at negative potentials as compared to that in the close-packed structures at more positive potentials, where the solvent is largely displaced from the metal surface and the adlayer is partly discharged.[1,10] However, following the arguments given previously,[6,7] the Cl-Cu bond length should increase at more negative potentials, where the adsorbate is expected to be more ionic, or be potential independent, assuming that the Cl adsorbate on Cu(001) is largely ionic even in the $c(2\times2)$ phase.[6,7] A similar effect was observed for Cl adsorption on Au(111), where the existence of a weaker bond with a longer distance at more negative potentials was revealed by x-ray absorption fine structure.[65]

V. CONCLUSION

In this work we have presented detailed structural results obtained by *in situ* SXRD measurements and DFT calculations for the chloride adlayer on Cu(001) as well as discussed those data in relationship to previous studies of this and related adsorbate systems. Although Cl adsorption at the electrochemical interfaces and Cl_2 adsorption under UHV conditions result in the same $c(2\times2)$ superstructure, the presence of the electrolyte induces a corrugation reversal in the buckling of the second Cu layer. The subsurface struc-

tural reversal can be reproduced in the calculations by taking the outer part of the electrochemical double layer into account. The estimation of the difference in work function in electrochemical and UHV environment points toward a more negatively charged Cu(001)-$c(2\times2)$ surface in solution and consequently to a more ionic bonding.

In addition, potential dependent x-ray scattering measurements reveal that the $c(2\times2)$ structure exists down to potentials close to the onset of hydrogen evolution, where a phase transition from the $c(2\times2)$ structure to a disordered 2D lattice gas of chloride is observed. The disordered Cl adlayer was found to exhibit a substantial coverage even at potentials as negative as 0.7 V vs Ag/AgCl. This behavior is analogous to that of Cl and Br on Ag(001) electrodes, where a qualitatively identical continuous order-disorder transition was reported.[10,16,17]

In general, the $c(2\times2)$ phases of anionic adsorbates on (001)-oriented metal surfaces represent particularly simple, but important cases and therefore are well suited as model systems to further a true quantum theoretical understanding of electrochemical interfaces and their relationship to surfaces under UHV conditions. Detailed surface crystallographic studies as presented here as well as in a few previous publications[6–9] provide experimental data that can be directly compared to calculations, thus allowing to test and guide the development of *ab initio* theories for the description of electrochemical phase boundaries.

ACKNOWLEDGMENTS

We thank the Deutsche Forschungsgemeinschaft for financial support via Grant No. Ma 1618/13. Calculations have been carried through at the Rechenzentrum der Universität Kiel. We acknowledge the ESRF for providing synchrotron radiation facilities and thank the ID 32 beamline staff for the technical support.

*Present address: University of Life Sciences in Lublin, Faculty of Food Science and Biotechnology, Skromna 8, 20-704 Lublin, Poland.

[1] O. M. Magnussen, Chem. Rev. **102**, 679 (2002).
[2] J. K. Sass and K. Bange, in *Electrochemical Surface Science*, edited by M. P. Soriaga (American Chemical Society, Washington, 1988), Chap. 4, p. 54.
[3] J. K. Sass, D. Lackey, J. Schott, and B. Straehler, Surf. Sci. **247**, 239 (1991).
[4] J. Wang, B. M. Ocko, A. J. Davenport, and H. S. Isaacs, Phys. Rev. B **46**, 10321 (1992).
[5] C. A. Lucas, N. M. Markovic, and P. N. Ross, Phys. Rev. B **55**, 7964 (1997).
[6] S. Huemann, N. T. M. Hai, P. Broekmann, and K. Wandelt, J. Phys. Chem. B **110**, 24955 (2006).
[7] M. Saracino, P. Broekmann, K. Gentz, M. Becker, H. Keller, F. Janetzko, T. Bredow, K. Wandelt, and H. Dosch, Phys. Rev. B **79**, 115448 (2009).
[8] O. Endo, M. Kiguchia, T. Yokoyamaa, M. Ito, and T. Ohta, J. Electroanal. Chem. **473**, 19 (1999).
[9] O. Endo, H. Kondoh, Y. Yonamoto, T. Yokoyama, and T. Ohta, Surf. Sci. **463**, 135 (2000).
[10] Th. Wandlowski, J. X. Wang, and B. M. Ocko, J. Electroanal. Chem. **500**, 418 (2001).
[11] P. A. Dowben, CRC Crit. Rev. Solid State Mater. Sci. **13**, 191 (1987).
[12] T. Kramar, D. Vogtenhuber, R. Podloucky, and A. Neckel, Electrochim. Acta **40**, 43 (1995).
[13] A. Ignaczak and J. A. N. F. Gomes, J. Electroanal. Chem. **420**, 71 (1997).
[14] A. Migani, C. Sousa, and F. Illas, Surf. Sci. **574**, 297 (2005).
[15] A. Migani and F. Illas, J. Phys. Chem. B **110**, 11894 (2006).
[16] B. M. Ocko, J. X. Wang, and T. Wandlowski, Phys. Rev. Lett. **79**, 1511 (1997).
[17] J. X. Wang, T. Wandlowski, and B. M. Ocko, in *Proceedings of the Symposium on the Electrochemical Double Layer*, edited by C. Korzeniewski and B. E. Conway (The Electrochemical Society, Pennington, NJ, 1997), p. 293.
[18] H. C. N. Tolentino, M. De Santis, Y. Gauthier, and V. Langlais, Surf. Sci. **601**, 2962 (2007).
[19] D. Westphal and A. Goldmann, Solid State Commun. **35**, 437 (1980).
[20] D. Westphal, A. Goldmann, F. Jona, and P. M. Marcus, Solid State Commun. **44**, 685 (1982).
[21] K. N. Eltsov *et al.*, JETP Lett. **62**, 444 (1995).
[22] M. Galeotti, B. Cortigiani, M. Torrini, U. Bardi, B. Andryushechkin, A. Klimov, and K. Eltsov, Surf. Sci. **349**, L164 (1996).
[23] M. Kiguchi, T. Yokoyama, S. Terada, M. Sakano, Y. Okamoto, T. Ohta, Y. Kitajima, and H. Kuroda, Phys. Rev. B **56**, 1561 (1997).
[24] C. Y. Nakakura, V. M. Phanse, and E. I. Altman, Surf. Sci. **370**, L149 (1997).
[25] C. Y. Nakakura, G. Zheng, and E. I. Altman, Surf. Sci. **401**, 173 (1998).
[26] I. Villegas, C. B. Ehlers, and J. L. Stickney, J. Electrochem. Soc. **137**, 3143 (1990).
[27] D. W. Suggs and A. J. Bard, J. Phys. Chem. **99**, 8349 (1995).
[28] M. R. Vogt, F. A. Möller, C. M. Schilz, O. M. Magnussen, and R. J. Behm, Surf. Sci. **367**, L33 (1996).
[29] T. P. Moffat, J. Phys. Chem. B **102**, 10020 (1998).
[30] M. R. Vogt, A. Lachenwitzer, O. M. Magnussen, and R. J. Behm, Surf. Sci. **399**, 49 (1998).
[31] O. M. Magnussen, L. Zitzler, B. Gleich, M. R. Vogt, and R. J. Behm, Electrochim. Acta **46**, 3725 (2001).
[32] L.-Q. Wang, A. E. Schach von Wittenau, Z. G. Ji, L. S. Wang, Z. Q. Huang, and D. A. Shirley, Phys. Rev. B **44**, 1292 (1991).
[33] O. M. Magnussen, K. Krug, A. H. Ayyad, and J. Stettner, Electrochim. Acta **53**, 3449 (2008).
[34] E. Vlieg, J. Appl. Crystallogr. **30**, 532 (1997).
[35] http://www.sub.uni-hamburg.de/opus/volltexte/1999/99/
[36] C. Kumpf, A. Müller, W. Weigand, E. Umbach, J. Wagner, V. Wagner, S. Gundel, L. Hansen, J. Geurts, J. H. Zeysing, F. Wu, and R. L. Johnson, Phys. Rev. B **68**, 035339 (2003).
[37] R. Herger, P. R. Willmott, O. Bunk, C. M. Schlepütz, B. D.

Patterson, B. Delley, V. L. Shneerson, P. F. Lyman, and D. K. Saldin, Phys. Rev. B **76**, 195435 (2007).
[38] A. Hirnet, K. Schroeder, S. Blügel, X. Torrelles, M. Albrecht, B. Jenichen, M. Gierer, and W. Moritz, Phys. Rev. Lett. **88**, 226102 (2002).
[39] G. Kresse and J. Hafner, Phys. Rev. B **47**, 558 (1993).
[40] G. Kresse and J. Hafner, Phys. Rev. B **49**, 14251 (1994).
[41] G. Kresse and J. Furthmuller, Comput. Mater. Sci. **6**, 15 (1996).
[42] G. Kresse and J. Furthmuller, Phys. Rev. B **54**, 11169 (1996).
[43] J. P. Perdew, J. A. Chevary, S. H. Vosko, K. A. Jackson, M. R. Pederson, D. J. Singh, and C. Fiolhais, Phys. Rev. B **46**, 6671 (1992).
[44] P. E. Blöchl, Phys. Rev. B **50**, 17953 (1994).
[45] G. Kresse and D. Joubert, Phys. Rev. B **59**, 1758 (1999).
[46] H. J. Monkhorst and J. D. Pack, Phys. Rev. B **13**, 5188 (1976).
[47] A. Y. Lozovoi, A. Alavi, J. Kohanoff, and R. M. Lynden-Bell, J. Chem. Phys. **115**, 1661 (2001).
[48] S. Venkatachalam, P. Kaghazchi, L. A. Kibler, D. M. Kolb, and T. Jacob, Chem. Phys. Lett. **455**, 47 (2008).
[49] E. Skúlason, G. S. Karlberg, J. Rossmeisl, T. Bligaard, J. Greeley, H. Jónsson, and J. K. Nørskov, Phys. Chem. Chem. Phys. **9**, 3241 (2007).
[50] J. Rossmeisl, E. Skúlasona, M. E. Björketuna, V. Tripkovica, and J. K. Nørskova, Chem. Phys. Lett. **466**, 68 (2008).
[51] J. S. Filhol and M. Neurock, Angew. Chem. Int. Ed. **45**, 402 (2006).
[52] C. D. Taylor, S. A. Wasileski, J. S. Filhol, and M. Neurock, Phys. Rev. B **73**, 165402 (2006).
[53] J. Neugebauer and M. Scheffler, Phys. Rev. B **46**, 16067 (1992).
[54] T. Tansel, A. Taranovskyy, and O. M. Magnussen, Studies of Adsorbate Dynamics by In Situ Video-STM: Surface Diffusion, Adsorbate-Adsorbate Interactions, and Interactions with Defects, 2008.
[55] O. Mironets, H. L. Meyerheim, C. Tusche, P. Zschack, H. Hong, N. Jeutter, R. Felici, and J. Kirschner, Phys. Rev. B **78**, 153401 (2008).
[56] R. Pentcheva and M. Scheffler, Phys. Rev. B **61**, 2211 (2000).
[57] F. Sette, T. Hashizume, F. Comin, A. A. MacDowell, and P. H. Citrin, Phys. Rev. Lett. **61**, 1384 (1988).
[58] J. C. Slater, J. Chem. Phys. **41**, 3199 (1964).
[59] R. D. Shannon, Acta Crystallogr., Sect. A: Cryst. Phys., Diffr., Theor. Gen. Crystallogr. **32**, 751 (1976).
[60] S. Trasatti, J. Electroanal. Chem. **150**, 1 (1983).
[61] W. Schmickler, Chem. Rev. **96**, 3177 (1996).
[62] W. Schmickler, *Interfacial Electrochemistry* (Oxford University Press, New York; Oxford, 1996).
[63] D. Westphal and A. Goldmann, Surf. Sci. **131**, 113 (1983).
[64] N. V. Richardson and J. K. Sass, Surf. Sci. **103**, 496 (1981).
[65] O. Endo, D. Matsumura, K. Kohdate, M. Kiguchi, T. Yokoyama, and T. Ohta, J. Electroanal. Chem. **494**, 121 (2000).

5 Electronic structure of Ag adatoms and clusters on the Ag(111) surface

5.1 Synopsis

Besides characterization of a solid surface at the atomic scale, a STM can be used to manipulate single atoms on a solid surface with very high precision, and it can be used to characterize the resulting structures. The manipulation capabilities allow for tailored atomic structures on surfaces from single atoms to large clusters of various geometries.[281,282] Such atomic geometries composed of metal atom clusters on metal surfaces have drawn a lot of attention because they are considered model systems for nanostructures on surfaces. Moreover, a controllable size selection of metal clusters may provide a way of tuning their physical and catalytic properties.[283] The electronic structure of single metal adatoms and metal clusters adsorbed on a metal substrate surface can be studied via scanning tunneling microscopy or scanning tunneling spectroscopy experiments. A multi-faceted physical phenomenology has been observed and studied through these systems. E.g. the Kondo effect of single magnetic adatoms and magnetic atoms incorporated into metal clusters on metal surfaces has been studied in detail.[284,285] In case of substrate surfaces with a surface state in the gap of the surface projected bulk band-structure [like Ag(111), Cu(111)], the scattering of a quasi 2D electron gas at adatoms and clusters can lead, e.g. to the appearance of a localized state at the adatom[286,287] and to long range interactions and ordering of adatoms on the surface due to Friedel oscillations.[126] Furthermore, a STM offers the possibility to study electron transport through single atoms, molecules, or junctions comprised of atomic chains by establishing a direct contact via the STM tip.[11,288]

Here, unoccupied electronic states and resonances of Ag adatoms, dimers, and clusters of different size and shape on the Ag(111) surface have been characterized (Ref. 289 and Ref. 283) through STM experiments conducted by A. Sperl *et al.* , DFT calculations, and tight-binding model calculations. Ref. 289 focuses on unoccupied resonances of single Ag adatoms and size-selected Ag clusters on the Ag(111) surface. STM experiments have been performed for linear and compact Ag_n clusters ($n = 1 \ldots 5$) and for a linear cluster containing approximately 160 Ag adatoms. The STM data, acquired on top of a single Ag adatom, shows a resonance 2.9 eV above the Fermi energy, ε_F. For larger

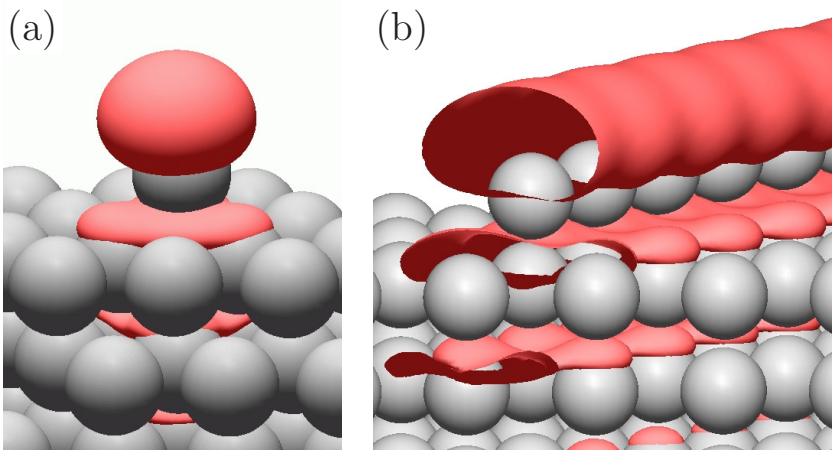

Figure 5.1: Contour plots of the absolute square of the Kohn-Sham wave function at $\bar{\Gamma}$ for the Ag monomer (a) and the Ag chain (b). The corresponding Kohn-Sham eigenenergies relative to the Fermi level are 2.66 eV for the Ag monomer and 1.37 eV for the Ag chain. The Figure has been taken from Ref. 289.

clusters the observed resonances shift towards the Fermi energy as the cluster size is increased. In case of linear clusters the resonance shifts to approximately ε_F + 1.5 eV for the 160 Ag adatom linear cluster.

DFT calculations have been carried through for a Ag monomer, dimer, and an infinitely long linear Ag chain. The DFT resonance energy of the Ag monomer (2.3 eV) agrees with the experimental value to within 0.6 eV. An inspection of the Kohn-Sham wave functions has revealed that the unoccupied resonance mainly derives from Ag $5p_z$ orbitals with some $5s$ admixtures and Ag substrate states, see Fig. 5.1. The maximum of the local density of states as calculated within DFT in case of the infinitely long Ag chain is located at approximately 1.5-1.6 eV above ε_F in agreement with STM experiments (ε_F + 1.5 eV). As for the monomer resonance, the corresponding Kohn-Sham wave functions mainly derive from Ag $5p_z$ orbitals hybridized with Ag(111) substrate states, see Fig. 5.1.

The experimentally observed tendency of the unoccupied resonance to shift towards ε_F is more pronounced in case of compact clusters compared to linear clusters. As the computational cost associated with a DFT calculation for compact clusters is prohibitive, the resonance eigenenergies have been estimated within a simple tight-binding model to explain the experimentally observed trends. The tight-binding parameters have been consistently derived from the DFT results for the monomer and the Ag(111) surface state energies. These two values represent the limiting cases for the smallest cluster, i.e. the monomer, and an infinite 2D cluster corresponding to a complete monolayer of Ag adatoms. Notably, it has been assumed that the unoccupied resonance develops into the Ag(111) surface state for the infinite 2D cluster. This is consistent with a clear p_z

orbital character of the Ag(111) surface state and with the findings of Lagoute *et al.* for Cu(111). Despite the simplicity of the employed tight-binding model, all qualitative trends observed in experiment are provided by the tight-binding frame work.

In Ref. 283 the unoccupied resonance of the Ag dimer adsorbed on the Ag(111) surface has been studied in more detail. The question which has been addressed regards the coupling of two unoccupied Ag $5p_z$ derived monomer resonances as the Ag-Ag separation is decreased from not too large separations to the ground state dimer bond length on the Ag(111) substrate surface. Upon decreasing the Ag-Ag adatom separation the monomer resonances interact, which leads to bonding and anti-bonding combinations of the Ag $5p_z$ derived resonance wave functions. From a comparison of STM experiments to DFT calculations and a simple tight-binding model for different Ag-Ag intra-dimer separations, it is suggested that the coupling is mainly direct, i.e. not predominantly mediated by the surface, at not too large Ag-Ag separations. Note that a dominant coupling via the substrate has been reported previously for Au dimers on NiAl(110) by Nilius *et al.* which is most probably related to the different electronic structure of NiAl(110) compared to Ag(111). In addition to the direct coupling of the unoccupied Ag $5p_z$ resonances of two monomers, there is also a contribution from the substrate. The direct and indirect contributions can be estimated within a minimum tight-binding model for a simple cubic lattice of atoms with only one orbital and two adatoms at on top positions. The Green's function matrix of the adatoms reads

$$G_{AA}(\varepsilon) = \begin{pmatrix} \frac{1}{\varepsilon-(\varepsilon_0+\Sigma+t+G_{12}^0|v|^2)} & 0 \\ 0 & \frac{1}{\varepsilon-(\varepsilon_0+\Sigma-t-G_{12}^0|v|^2)} \end{pmatrix} \tag{5.1}$$

where ε_0 is the eigenenergy of the Ag monomer, Σ is the self-energy, t is the transfer matrix element between the adatoms, v denotes the next-neighbor transfer matrix between an adatom and the substrate, and G_{12}^0 is the matrix element of the Green's function of the substrate with respect to the adsorption sites. The contribution to the coupling from direct interactions leads to an energy splitting of the monomer resonances of $2t$ (equals that of two Ag atoms in vacuum). The contribution from the substrate to the energy splitting of the adatom states is $2\mathrm{Re}(G_{12}^0|v|^2)$. A comparison to the orbital energy splitting for a free Ag dimer and calculations of the matrix element G_{12}^0 for two next-neighbor sites based on DFT predict that the interaction via the substrate is smaller than the direct coupling at not too large Ag-Ag separations.

Summing up, from a comparison of STM experiments to state-of-the-art DFT, and tight-binding calculations the electronic structure of unoccupied resonance states of Ag clusters on the Ag(111) surface has been characterized. The calculations provided all qualitative trends observed in experiment for the resonance energies and significantly contributed to further the understanding of the nature of the resonances and their coupling in case of an Ag adatom dimer on the Ag(111) surface.

5.2 Publication Physical Review B 77, 085422 (2009), Copyright (2009) by the American Physical Society

Unoccupied states of individual silver clusters and chains on Ag(111)

A. Sperl, J. Kröger,* N. Néel, H. Jensen, and R. Berndt
Institut für Experimentelle und Angewandte Physik, Christian-Albrechts-Universität zu Kiel, D-24098 Kiel, Germany

A. Franke and E. Pehlke
Institut für Theoretische Physik und Astrophysik, Christian-Albrechts-Universität zu Kiel, D-24098 Kiel, Germany
(Received 18 September 2007; revised manuscript received 4 December 2007; published 20 February 2008)

Size-selected silver clusters on Ag(111) were fabricated with the tip of a scanning tunneling microscope. Unoccupied electron resonances give rise to image contrast and spectral features which shift toward the Fermi level with increasing cluster size. Linear assemblies exhibit higher resonance energies than equally sized compact assemblies. Density functional calculations reproduce the observed energies within 0.6 eV and enable an assignment of the resonances to hybridized atomic $5s$ and $5p_z$ orbitals with silver substrate states.

DOI: 10.1103/PhysRevB.77.085422 PACS number(s): 68.37.Ef, 68.47.De, 73.20.At, 73.22.−f

I. INTRODUCTION

Metal clusters at the nanometer scale which are supported by surfaces or thin films are currently of significant interest. Transport properties,[1] catalytic efficiency[2] and selectivity,[3] as well as magnetic response[4] depend strongly on the size of these assemblies. Moreover, understanding the influence of the substrate on the electronic structure of clusters[5] is important for new cluster-based materials with tailored optical, catalytic, or magnetic properties. To this end, clusters may be decoupled from a metal surface by introducing an oxide thin film between the substrate and the deposited clusters.[6–10]

The preparation of clusters with a given size on a surface is not an easy task. The approaches used so far include the deposition of size-selected clusters directly onto surfaces,[11] onto layers of noble gas atoms,[12,13] and the aggregation of clusters in buffer layers.[14] An alternative approach to controlling the size and shape of clusters on a surface is to use atom manipulation with the tip of a scanning tunneling microscope. This technique was applied in a variety of investigations, for instance, manganese, iron, and cobalt dimers on NiAl(110),[15] nickel dimers[16] and chromium trimers[17] on Au(111), copper chains on Cu(111),[18] and manganese monomers to tetramers on Ag(111).[19] Quantum confinement of electronic states to chains and islands was also revealed for homogeneous metallic systems.[18,20–25]

Here, we report on studies of electronic properties of silver clusters fabricated by single-atom manipulation on Ag(111) using the tip of a low-temperature scanning tunneling microscope. As key results, we obtain that unoccupied resonances exhibit energies whose actual values depend on the size and the shape of the adatom clusters. In particular, linear and monatomically wide chains exhibit higher resonance energies than their equally sized compact counterparts. Moreover, confinement of the unoccupied resonance states to the linear assemblies is found. The energies of unoccupied resonances of monomers, dimers, and a long silver chain are in agreement with density functional theory calculations.

II. EXPERIMENT

Measurements were performed with a custom-built scanning tunneling microscope operated in ultrahigh vacuum at a base pressure of 10^{-9} Pa and at 7 K. The Ag(111) surface and chemically etched tungsten tips were cleaned by argon ion bombardment and annealing. Individual silver atoms were deposited onto the sample surface by controlled tip-surface contacts as previously described in Ref. 26. Clusters with sizes ranging from one to eight atoms were fabricated by single-atom manipulation. For tunneling resistances of $\approx 10^5\ \Omega$, dragging of single silver atoms was feasible. Coalescence of adsorbed atoms (adatoms) to dimers up to octamers was accomplished by moving single adatoms close enough to the coalescence partner ($\approx$ one nearest-neighbor distance). We notice a propensity of silver adatoms to coalesce into compact assemblies rather than into linear clusters. For instance, adding an adatom to an already existing dimer in most cases resulted in a compact trimer rather than in a three-adatom chain. Silver chains containing more than 100 atoms were prepared by moving the tip toward the surface by 3–5 nm. Various surface dislocations were observed to result from this procedure. In particular, extraordinarily long and monatomically wide chains were found several hundreds of nanometers apart from the indentation area. Spectra of the differential conductance (dI/dV) were acquired by superimposing a sinusoidal voltage signal (root-mean-square amplitude of 1 mV and frequency of 10 kHz) onto the tunneling voltage and by measuring the current response with a lock-in amplifier. Prior to and in between spectroscopy of the clusters, the tip status was monitored by spectroscopy of the Ag(111) surface state band edge. Tips were prepared by controlled indentation into the substrate. Due to this treatment, we expect the tip apex to be covered with substrate material. All scanning tunneling microscopy (STM) images were acquired in the constant current mode, with the voltage applied to the sample.

III. THEORY

The total energy of the electronic ground state and the Kohn-Sham eigenenergies have been calculated for the silver monomer and dimer configurations on Ag(111) using the Vienna *ab initio* simulation package (VASP).[27–29] Moreover, the Ag chain on Ag(111) has been calculated using the total energy package FHI96MD.[30] Both program packages are based

on density functional theory with the generalized gradient approximation (GGA) (monomer and dimer: PW91;[31] chain: PBE[32]) applied to the exchange correlation functional. These GGAs are expected to yield comparable results. For the monomer and dimer configurations, the electron-ion interaction is treated within the framework of Bloechl's projector augmented wave (PAW) method.[33,34] For the calculation of the Ag chain, a Troullier-Martins pseudopotential has been generated with the FHI98PP (Ref. 35) program. The monomer and dimer configurations have been modeled in a slab geometry comprising 14 layers of silver and a (4×4) or (5×4) surface unit cell, respectively. For the chain configuration, the slab geometry consisted of 14 silver layers and a (9×1) surface unit cell. Perpendicular to the surface, the periodically repeated silver slabs are separated by a vacuum region of approximately 1.7 nm, which has been the subject of convergence tests and proved to be sufficient. In all calculations presented here, symmetric slabs were chosen such that the adsorption geometry is the same on both sides of the slab. The Kohn-Sham wave functions are expanded in a plane wave basis set, with a cutoff energy of 250 eV being sufficient in the case of the PAW potential. A larger cutoff energy of 544 eV had to be used for the norm conserving Troullier-Martins pseudopotential. The integrals over the Brillouin zone are approximated by sums over special k points[36] using meshes consisting of 16, 9, and 6 k points in the complete first Brillouin zone for the monomer, dimer, and chain, respectively. The local density of states (LDOS) has been calculated using the latter k point meshes in the case of the monomer and dimer. Additionally, to accurately sample the dispersion of the unoccupied state close to the lower one-dimensional band edge, a mesh of 144 special k points[36] in the first Brillouin zone has been used for the Ag chain. The Kohn-Sham wave functions at these additional k points have been calculated via so-called band structure runs, which are carried out at a frozen electron density from a previous self-consistent relaxation. The densities of states have been convoluted with a Lorentzian with a full width at half maximum of 150 meV. Convergence tests for the silver monomer using an eight layer slab show that upon increasing the cutoff energy to 300 eV, the calculated Kohn-Sham eigenenergies change by less than 15 meV. Increasing the number of k points for the dimer calculation to 16 leads to a change in the Kohn-Sham eigenenergies at $\bar{\Gamma}$ of less than 10 meV (in a test calculation for an eight layer slab).

Using the norm conserving pseudopotential and the PBE-GGA for exchange and correlation, the equilibrium lattice constant of silver is calculated to be 0.419 nm. The result is very similar (0.417 nm) when the PAW pseudopotential is used together with the PW91-GGA for exchange and correlation. These values are slightly larger than the experimental lattice constant of 0.409 nm, but the slight overestimate is consistent with other density functional calculations, e.g, for noble metals using GGA functionals.[37] The slabs were set up using the respective theoretical lattice constants. The silver atoms of the outermost three layers on both sides of the slab as well as the adatoms were allowed to relax without constraints until the residual forces per atom were smaller than 7×10^{-4} hartree/bohr. The remaining layers of the slab were kept fixed at their ideal bulk positions. For the calculation of the monomer, one silver adatom is relaxed above the face-centered cubic (fcc) hollow site on both sides of the slab, corresponding to a coverage of one adatom per 16 surface atoms. For the dimer calculation, two silver adatoms are relaxed above adjacent fcc hollow sites on both sides of the slab, corresponding to a coverage of one dimer per 20 surface atoms. The chain geometry consists of silver atoms adsorbed at next-neighbor fcc hollow sites in the direction of the chain.

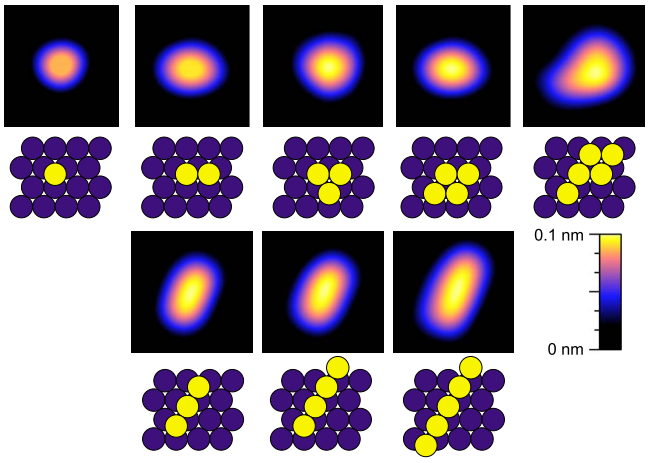

FIG. 1. (Color online) STM images of silver monomer, dimer, trimer, tetramer, and pentamer (from left to right) together with sketches of the proposed atomic arrangements (dark and bright circles depict substrate atoms and adsorbed atoms, respectively). Sample voltage and tunneling current were $V=100$ mV and $I=0.1$ nA. Image sizes: 2.1×2.1 nm^2 for $Ag_1,\ldots,Ag_5$ and 3×3 nm^2 for the linear tetramer and pentamer.

IV. RESULTS AND DISCUSSION

A. Compact and linear silver clusters: From monomer to octamer

Compact as well as linear assemblies were produced up to sizes of five and eight, respectively. STM images of single clusters are presented in Fig. 1 along with schematic models of their atomic arrangements. In these models, silver adatoms are placed at threefold coordinated fcc sites of the Ag(111) lattice. Table I compares apparent heights and full widths at half maximum (FWHMs) of linear assemblies with sizes ranging from a monomer to an octamer. Cross-sectional profiles of STM images were evaluated to this end. Per additional silver atom, the length of the chains increases by 0.28 nm on average, which is in good agreement with the nearest-neighbor distance of Ag(111). Starting from the trimer, the apparent height is 0.10 nm for all subsequent silver assemblies.

We notice that the silver dimer appears elongated in STM images (axes ≈1.28 nm and ≈1.06 nm). The orientation of the dimers is stable on the time scale of the experiment. These observations are in some contrast to previous results for Cu dimers on Cu(111),[38] where Cu_2 appeared nearly circular in STM images. This observation was attributed to in-

TABLE I. Apparent heights and FWHMs of silver clusters extracted from cross-sectional profiles of STM images. The FWHM refers to the longest lateral dimension of linear assemblies. All apparent heights and full widths at half maximum were measured at 0.1 V and 0.1 nA.

Cluster	Height (nm)	FWHM (nm)
Ag_1	0.06	1.1
Ag_2	0.08	1.3
Ag_3	0.10	1.6
Ag_4	0.10	1.7
Ag_5	0.10	2.1
Ag_6	0.10	2.3
Ag_7	0.10	2.7
Ag_8	0.10	3.0

tracell diffusion, i.e., the dimer moved within a cell of adjacent hexagonal close-packed and fcc sites centered around an on-top site.

Next we focus on unoccupied electronic states of the silver assemblies. Figure 2 shows a series of normalized dI/dV spectra acquired with the tip positioned above the center of compact clusters. The tunneling gap for spectroscopy was

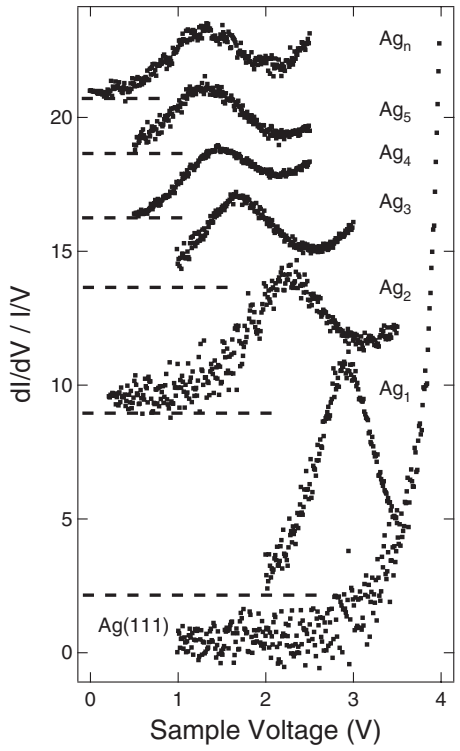

FIG. 2. Normalized spectra of dI/dV acquired on clean Ag(111), monomers (Ag_1), dimers (Ag_2), trimers (Ag_3), tetramers (Ag_4), and pentamers (Ag_5). A compact silver assembly (Ag_n) with probably $n \approx 10$ was also analyzed. The tunneling gap for the spectra was set at 1 nA and 3.5 V (Ag_1 and Ag_2), 3.0 V (Ag_3), and 2.5 V (Ag_4, Ag_5, and Ag_n). Spectra of Ag_n ($n \geqslant 1$) are vertically offset for clarity. The dashed lines indicate the respective zero of the spectra.

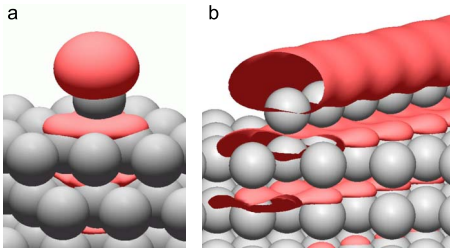

FIG. 3. (Color online) Contour plots of the absolute square of the Kohn-Sham wave function at $\bar{\Gamma}$ for (a) the silver monomer and (b) the silver chain. The corresponding Kohn-Sham eigenenergies relative to the Fermi level are 2.66 eV for the Ag monomer and 1.37 eV for the Ag chain.

stabilized at 1 nA and 3.5 V for Ag_1, Ag_2, 3.0 V for Ag_3, and 2.5 V for Ag_4, Ag_5, and Ag_n. Due to different tip-cluster distances for the various spectra, we normalized the dI/dV data sets by the conductance I/V according to Refs. 39–41. The spectrum of clean Ag(111) is featureless up to ≈3.5 eV. A steady increase at higher sample voltages is attributed to field emission resonances.[42,43] The spectrum of the Ag adatom exhibits a pronounced peak slightly below 3 eV. Spectra from the vicinity of and above the single atom revealed that spatial extension of the monomer resonance is comparable to the size of the atom in STM images. These results suggest that the silver monomer exhibits a quasiatomic resonance. This interpretation is in accordance with observations for single Au atoms on NiAl(110) (Ref. 1) and for Pd monomers on Al_2O_3 layers.[44] Thus, the enhanced normalized differential conductance can be attributed to resonant tunneling into an empty state of the Ag atom. Indeed, our calculations reveal that this state is of *sp* character arising from the hybridizaton of atomic Ag $5p_z$ orbitals with $5s$ admixtures localized at the adsorbate and silver substrate states. A typical wave function is shown in Fig. 3(a).

Spectra acquired on compact and linear clusters containing a higher number of atoms likewise exhibit a peak whose energy shifts to lower values with increasing cluster size.[45] Figure 4 summarizes the resonance energies for compact (triangles) and linear (circles) silver clusters of different sizes. The spectra were acquired atop the center of the assemblies. The resonance energies for compact clusters are lower than those for their equally sized linear counterparts. From Fig. 4, we further infer that for both cluster types, the change of the resonance energy becomes less pronounced with increasing cluster size. For instance, the energy of the compact pentamer resonance is at ≈1.5 eV, which already comes close to a compact assembly denoted Ag_n ($n \approx 10$) in Fig. 2. Lagoute *et al.*[21] investigated triangular Cu islands containing up to 15 atoms on Cu(111) and found an evolution of quasiatomic resonances to the two-dimensional Shockley-type surface state. In our case, the resonance energies of linear clusters clearly exceed the Ag(111) surface state energy (−70 meV) in the limit of large cluster sizes and are found to approach an asymptotic value of approximately 1.5 eV. This resonance energy is observed for a very long silver chain, which will be discussed in the following section. The situation for compact clusters is different. Our experimental data were measured

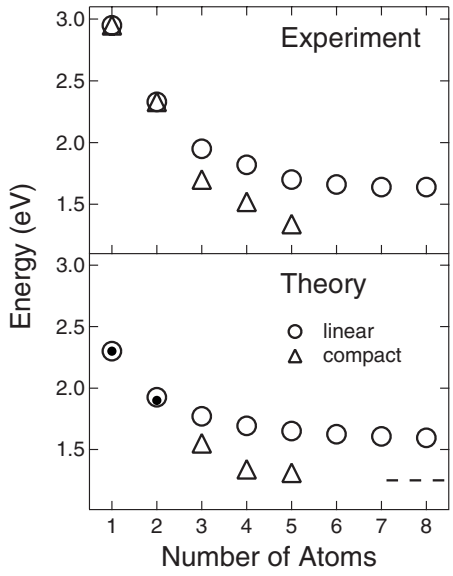

FIG. 4. Experimentally determined and calculated energies of unoccupied resonances as a function of cluster size. Resonance energies for compact (triangles) and linear (circles) assemblies are presented. Error margins for experimental energies ($\approx \pm 0.05$ eV) are the standard deviation resulting from a statistical analysis of spectra of a variety of clusters. Theoretical values calculated within a tight-binding model described in the text (open circles and triangles) are compared to *ab initio* Kohn-Sham eigenenergies (filled circles). The dashed line denotes the lower band edge of the dispersion of the chain states as obtained from density functional calculations. For each geometry, the lowest tight-binding eigenenergy is given. The island configurations refer to those displayed in Fig. 1. The compact islands enfold the trimer, the tetramer, and the pentamer.

on very small clusters and, we believe, it is not appropriate to extrapolate it to infinite cluster size. However, a close inspection of the density functional theory (DFT) results for the Kohn-Sham wave function of the Ag(111) surface state reveals its dominant p_z character similar to the resonance displayed in Fig. 3. This finding is complemented by the Ag $5p_z$ projected density of states at the Ag(111) surface which resembles a step function at the onset of the surface state. Our tight-binding interpolation is consistent with a convergence of the lowest-energy cluster eigenstate toward the lower band edge of the surface state with increasing size of the compact clusters. Thus, our interpretation is consistent with the findings of Lagoute *et al.* for the Cu(111) surface state in Ref. 21.

B. Monatomically wide silver chains

Here, we focus on electronic properties of monatomically wide silver chains. Figure 5 shows spatially resolved dI/dV spectra acquired at different sites on a linear pentamer (see inset of Fig. 5). The dI/dV spectrum taken atop the center of the assembly exhibits a single peak at $\approx$1.6 eV (to be compared also with Fig. 4). By performing spatially resolved spectroscopy along the linear cluster (spectra 2–8), a gradual trade of spectral weight from the resonance peak at $\approx$1.6 eV

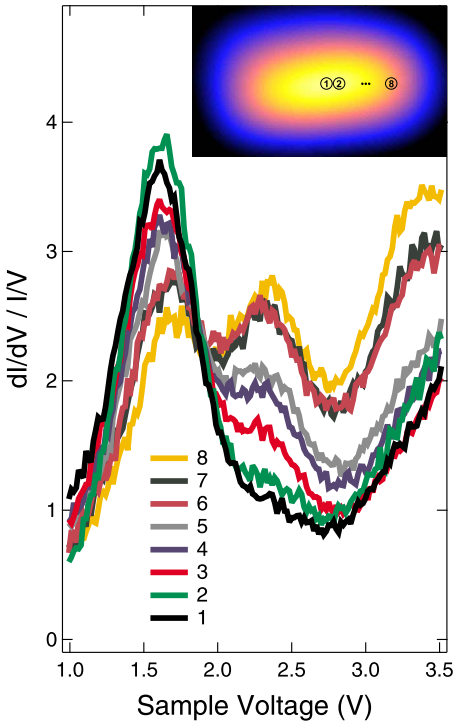

FIG. 5. (Color online) dI/dV spectra acquired at indicated (1,2,…,8) positions of a linear pentamer. Inset: STM image of linear pentamer showing the positions at which spectra were taken. The tunneling gap was set at 1 nA and 3.5 V.

to an additional peak at $\approx$2.3 eV is observed. Moreover, compared to the resonance energy of $\approx$1.6 eV observed atop the middle of the chain, at its ends this energy has shifted up to $\approx$1.7 eV. By analyzing the dependence of the first and second peaks on the length of the chains, we found (not shown) that these peaks may be well described within a simple particle-in-a-box model. Similar confinement effects for unoccupied resonances were observed for Au chains on NiAl(110) (Ref. 1) and for Cu chains on Cu(111).[18]

How does the confinement evolve for chains containing a very large number of atoms? Starting from the linear octamer, it became difficult to resolve confinement-related peaks in dI/dV spectra, which may be related to overlap of neighboring peaks. Nevertheless, confinement was evidenced by localization of density of states at the ends of a very long chain, to be discussed next. The length of the chain is $\approx$45 nm and follows a close-packed direction of the hosting Ag(111) lattice. Consequently, the number of silver atoms is approximately 160. Figure 6 shows a normalized dI/dV spectrum of the resonance in the middle of the chain. We extract an energy of $\approx$1.5 eV for the resonance position. Our DFT calculations reproduce the energy of the peak in the case of an infinitely long chain [see an illustration of the wave function in Fig. 3(b) and compare Figs. 6 and 8].

In addition to the unoccupied resonance, STM images and spatial maps of dI/dV acquired at different voltages evidence confinement of the resonance within the chain. In Fig. 7(a), spatially resolved dI/dV data acquired along the chain at the indicated voltages are presented. At voltages exceeding 1.6 V, the differential conductance increases toward the ends

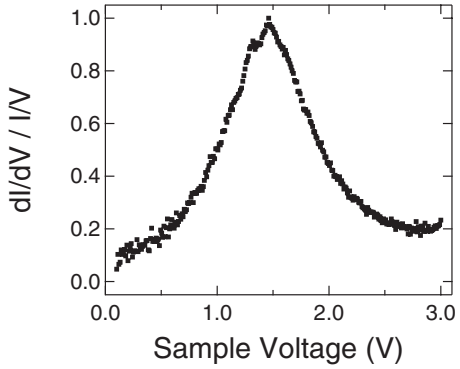

FIG. 6. Normalized spectrum of dI/dV at the center of an ≈45 nm long and monatomically wide silver chain. The tunneling gap was set at 0.6 nA and 3 V.

of the chain. Figures 7(b) and 7(c) show the evolution of the apparent height and the width (FWHM) of the chain (taken close to the middle of the chain) as a function of the applied voltage. A monotonous increase is observed for the apparent height as well as for the FWHM. At sample voltages between ≈1.5 and ≈1.7 V, height and width increase more rapidly than at other voltages. We attribute these observations to tunneling into the chain resonance.

C. Theoretical results

To compare experimental resonance energies with calculated results, we evaluated the LDOS at a position of ≈0.25 nm atop the adsorbed Ag atom for the monomer and the chain. For the dimer configuration, the LDOS was computed at approximately the same height atop the center of the dimer. The results are presented in Fig. 8. A similar LDOS for Cu chains on Cu(111) has been calculated by Stepanyuk *et al.*[46]

In case of the monomer, a resonance predominantly derived from Ag sp_z orbitals occurs at ≈2.3 eV above the Fermi energy [see Fig. 3(a)]. In case of the silver dimer, with Ag atoms occupying neighboring fcc sites, this resonance splits into a p_z bonding resonance at ≈1.9 eV and a p_z antibonding resonance.[47] The LDOS of the Ag chain is characterized by a one-dimensional band formed from an uncoccupied p_z-like resonance as shown in Fig. 3(b). The lower band edge of this one-dimensional band is located at ≈1.3 eV above the Fermi energy E_F (as derived from the electronic eigenenergies at $\bar{\Gamma}$). A peak arises at around 1.5–1.6 eV. No upper band edge of the one-dimensional band was observed for energies below the work function of silver. Table II summarizes experimental and calculated resonance energies. Owing to the agreement between experiment and theory, we interpret peaks in the dI/dV spectra as the signature of sp_z- or p_z-like Ag adsorbate resonances and their electronic interaction with silver substrate states.

We did not perform *ab initio* calculations for silver clusters of sizes larger than two atoms due to the large computational costs arising from the increasing size of the surface unit cell. However, we provide estimates for the electronic eigenenergies of larger clusters by means of a simple tight-

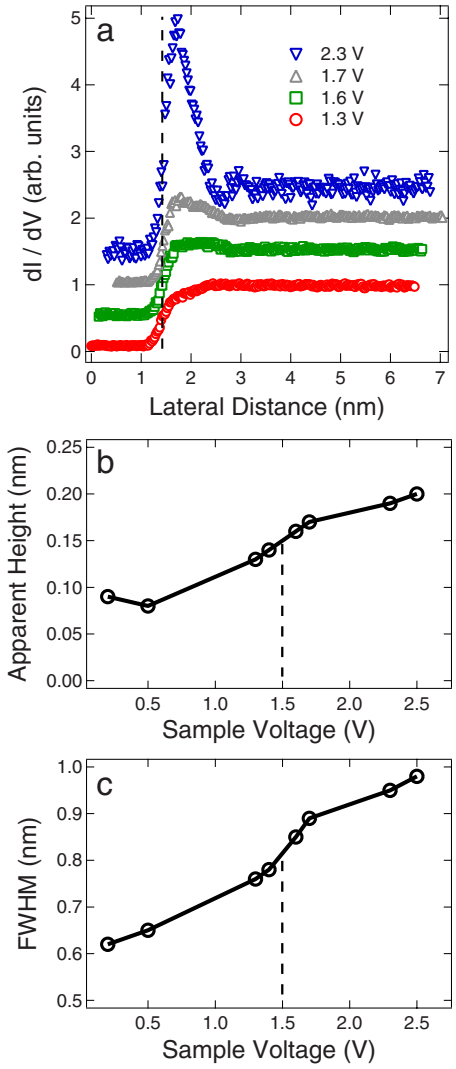

FIG. 7. (Color online) (a) Cross-sectional profiles in a map of dI/dV taken at the indicated voltages along the middle axis of the chain showing the increase of the signal at the end of the chain at a lateral displacement of ≈1.5 nm. The profiles acquired at voltages ⩾1.6 V are vertically offset for clarity. (b) Apparent height of the chain as a function of the applied voltage. (c) Like (b) for the full width at half maximum of the chain. Dashed lines in (b) and (c) indicate the chain resonance energy. Apparent heights and widths were taken close to the middle of the chain.

binding model.[21] The purpose of this estimate is to explain the energy shifts observed by tunneling spectroscopy semiquantitatively. In our tight-binding approach, the substrate is not considered explicitly, i.e., the islands are represented by freestanding two-dimensional clusters. We include one Ag sp_z orbital per atom. There are only two free tight-binding parameters: the orbital energy ε_0 and the next-neighbor transfer matrix element t, which accounts for the direct interaction between nearest-neighbor Ag atoms and, implicitly, part of the interaction via the Ag substrate. All further interactions with respect to more distant atoms are neglected, as is the variation of the crystal-field energy shift of the orbital energy for different geometrical environments. As usual, orbital overlaps are not accounted for explicitly.

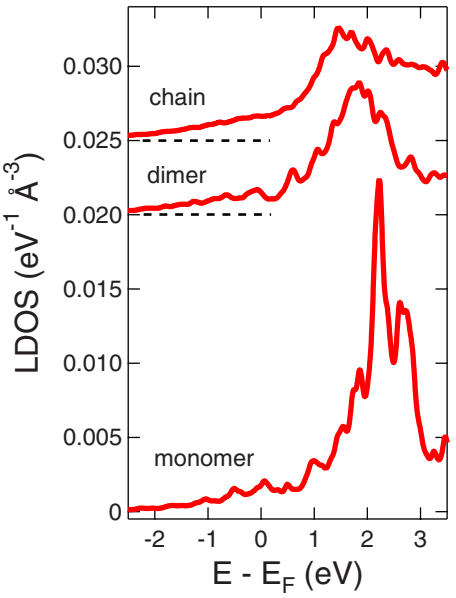

FIG. 8. (Color online) Calculated LDOS for a silver monomer (bottom), a silver dimer (middle), and an infinitely long silver chain (top) on Ag(111). Resonance energies inferred from these calculations are 2.3 eV, 1.9 eV, and 1.5–1.6 eV, respectively. The LDOS has been computed atop a silver adatom in the case of the monomer and the chain, and atop the center of the silver dimer. The dimer and chain LDOS were shifted vertically, with dashed lines indicating the respective zero LDOS.

The tight-binding parameters are consistently derived from our DFT results, i.e., the resonance energy of the monomer ε_0=2.3 eV (experimental value 2.9 eV) and the binding energy of the Ag(111) surface state at $\bar{\Gamma}$, $\varepsilon_0+6t=+0.05$ eV (experimental value ≈ -0.07 eV,[48] which is in agreement with earlier work),[49,50] are reproduced by the tight-binding model. The quality of the tight-binding results can be estimated from comparison with the DFT Kohn-Sham eigenenergies of the dimer and the chain shown in Fig. 4(b). The lowest-energy eigenvalue is given for each configuration. For further evaluation of the quality of the tight-binding model, we notice that for the effective mass m^* of the surface state, we obtain $0.8m_e$ (m_e is the free electron mass) from tight-binding calculations to be compared with a DFT value of $0.39m_e$ and an experimental value of $(0.42\pm0.02)m_e$ obtained by scanning tunneling spectroscopy.[48] The effective mass of the sp_z resonance at the one-dimensional Ag chain is $1.2m_e$ in our tight-binding approach to be compared with a value of about $0.6m_e$ derived from the dispersion of the Kohn-Sham eigenenergies close to $\bar{\Gamma}$. Most probably, the overestimate of the effective mass by a factor of 2 in both cases may partially be due to the fact that no parameter describing the crystal-field energy shift is included in the tight-binding Hamiltonion operator, giving rise to an inaccurate value of the transfer parameter.

TABLE II. Comparison of experimental (expt) and calculated (calc) energies (E) of unoccupied resonances.

Cluster	E^{expt} (eV)	E^{calc} (eV)
Monomer	2.9	2.3
Dimer	2.3	1.9
Chain	1.5	1.5–1.6

Nevertheless, the simple tight-binding approach provides all qualitative trends for the cluster eigenenergies [see Fig. 4(b)]. Compact clusters have lower eigenenergies than equally sized linear assemblies, and the trimer exhibits a lowest electronic eigenenergy which is close to the lower band edge of the infinite chain.

V. SUMMARY

Size-selected silver clusters were fabricated by tip-assisted single-atom manipulation on Ag(111). Unoccupied electronic resonances exhibit energies which are characteristic of the size and shape of the silver assemblies. In particular, the resonances of linear clusters have higher energies than the resonances of equally sized compact clusters. For both types of clusters, the resonance energy shifts toward the Fermi energy with increasing cluster size. Similar to the findings in Ref. 21, these observations are in qualitative agreement with a tight-binding model of the clusters. Calculations based on density functional theory model the energies of monomers, dimers, and monatomically wide infinitely long chains. The resonances are of *sp* character and arise from Ag $5p_z$ orbitals (with $5s$ admixtures) which are localized at the adsorbate atom and hybridize with silver substrate states.

ACKNOWLEDGMENT

Funding of this work by the Deutsche Forschungsgemeinschaft through SPP 1153 is gratefully acknowledged.

*kroeger@physik.uni-kiel.de

[1] N. Nilius, T. M. Wallis, and W. Ho, Science **297**, 1853 (2002).
[2] S. Abbet, A. Sanchez, U. Heiz, W.-D. Schneider, A. M. Ferrari, G. Pacchioni, and N. Rösch, J. Am. Chem. Soc. **122**, 3453 (2000).
[3] S. Abbet, A. Sanchez, U. Heiz, and W.-D. Schneider, J. Catal. **198**, 122 (2001).
[4] J. Bansmann, S. H. Baker, C. Binns, J. A. Blackman, J.-P. Bucher, J. Dorantes-Dávila, V. Dupuis, L. Favre, D. Kechrakos, A. Kleibert, K.-H. Meiwes-Broer, G. M. Pastor, A. Perez, O. Toulemonde, K. N. Trohidou, J. Touaillon, and Y. Xie, Surf. Sci. Rep. **56**, 189 (2005).
[5] A. S. Wörz, K. Judai, S. Abbet, J.-M. Antonietti, U. Heiz, A. Del Vitto, L. Giordano, and G. Pacchioni, Chem. Phys. Lett. **399**, 2666 (2004).
[6] R. M. Jaeger, H. Kuhlenbeck, H.-J. Freund, M. Wuttig, W. Hoffmann, R. Franchy, and H. Ibach, Surf. Sci. **259**, 235 (1991).
[7] U. Bardi, A. Atrei, and G. Rovida, Surf. Sci. **268**, 87 (1992).

[8] C. Becker, J. Kandler, H. Raaf, R. Linke, T. Pelster, M. Dräger, M. Tanemura, and K. Wandelt, J. Vac. Sci. Technol. A **16**, 1000 (1998).
[9] M. Bäumer and H.-J. Freund, Prog. Surf. Sci. **61**, 127 (1999).
[10] K. Hojrup Hansen, T. Worren, E. Lægsgaard, F. Besenbacher, and I. Stensgaard, Surf. Sci. **475**, 96 (2001).
[11] Y. Kuk, M. F. Jarrold, P. J. Silverman, J. E. Bower, and W. L. Brown, Phys. Rev. B **39**, 11168 (1989).
[12] K. Bromann, C. Félix, H. Brune, W. Harbich, R. Monot, J. Buttet, and K. Kern, Science **274**, 956 (1996).
[13] K.-H. Meiwes-Broer, *Metal Clusters at Surfaces*, Springer Series in Cluster Physics (Springer, Berlin, 2000).
[14] L. Huang, S. J. Chey, and J. H. Weaver, Phys. Rev. Lett. **80**, 4095 (1998).
[15] H. J. Lee, W. Ho, and M. Persson, Phys. Rev. Lett. **92**, 186802 (2004).
[16] V. Madhavan, T. Jamneala, K. Nagaoka, W. Chen, J.-L. Li, S. G. Louie, and M. F. Crommie, Phys. Rev. B **66**, 212411 (2002).
[17] T. Jamneala, V. Madhavan, and M. F. Crommie, Phys. Rev. Lett. **87**, 256804 (2001).
[18] S. Fölsch, P. Hyldgaard, R. Koch, and K. H. Ploog, Phys. Rev. Lett. **92**, 056803 (2004).
[19] J. Kliewer, R. Berndt, J. Minár, and H. Ebert, Appl. Phys. A: Mater. Sci. Process. **82**, 63 (2006).
[20] J. Li, W.-D. Schneider, R. Berndt, and S. Crampin, Phys. Rev. Lett. **80**, 3332 (1998).
[21] J. Lagoute, X. Liu, and S. Fölsch, Phys. Rev. Lett. **95**, 136801 (2005).
[22] H. Jensen, J. Kröger, R. Berndt, and S. Crampin, Phys. Rev. B **71**, 155417 (2005).
[23] S. Crampin, H. Jensen, J. Kröger, L. Limot, and R. Berndt, Phys. Rev. B **72**, 035443 (2005).
[24] J. Kröger, L. Limot, H. Jensen, R. Berndt, S. Crampin, and E. Pehlke, Prog. Surf. Sci. **80**, 26 (2005).
[25] J. Kröger, M. Becker, H. Jensen, Th. von Hofe, N. Néel, L. Limot, R. Berndt, S. Crampin, E. Pehlke, C. Corriol, V. M. Silkin, D. Sánchez-Portal, A. Arnau, E. V. Chulkov, and P. M. Echenique, Prog. Surf. Sci. **82**, 293 (2007).
[26] L. Limot, J. Kröger, R. Berndt, A. Garcia-Lekue, and W. A. Hofer, Phys. Rev. Lett. **94**, 126102 (2005).
[27] G. Kresse and J. Hafner, Pramana, J. Phys. **47**, 558 (1993).
[28] G. Kresse and J. Hafner, Comput. Mater. Sci. **6**, 15 (1996).
[29] G. Kresse and J. Furthmuller, Phys. Rev. B **54**, 11169 (1996).
[30] M. Bockstedte, A. Kley, J. Neugebauer, and M. Scheffler, Comput. Phys. Commun. **107**, 187 (1997).
[31] J. P. Perdew, J. A. Chevary, S. H. Vosko, K. A. Jackson, M. R. Pederson, D. J. Singh, and C. Fiolhais, Phys. Rev. B **46**, 6671 (1992).
[32] J. P. Perdew, K. Burke, and M. Ernzerhof, Phys. Rev. Lett. **77**, 3865 (1996).
[33] P. E. Blöchl, Phys. Rev. B **50**, 17953 (1994).
[34] G. Kresse and D. Joubert, Phys. Rev. B **59**, 1758 (1999).
[35] M. Fuchs and M. Scheffler, Comput. Phys. Commun. **116**, 1 (1999).
[36] H. J. Monkorst and J. D. Pack, Phys. Rev. B **13**, 5188 (1976).
[37] M. Fuchs, M. Bockstedte, E. Pehlke, and M. Scheffler, Phys. Rev. B **57**, 2134 (1998).
[38] J. Repp, G. Meyer, K.-H. Rieder, and P. Hyldgaard, Phys. Rev. Lett. **91**, 206102 (2003).
[39] R. M. Feenstra, J. A. Stroscio, and A. P. Fein, Surf. Sci. **181**, 295 (1987).
[40] N. D. Lang, Phys. Rev. B **34**, R5947 (1986).
[41] V. A. Ukraintsev, Phys. Rev. B **53**, 11176 (1996).
[42] R. S. Becker, J. A. Golovchenko, and B. S. Swartzentruber, Phys. Rev. Lett. **55**, 987 (1985).
[43] G. Binnig, K. H. Frank, H. Fuchs, N. Garcia, B. Reihl, H. Rohrer, F. Salvan, and A. R. Williams, Phys. Rev. Lett. **55**, 991 (1985).
[44] N. Nilius, T. M. Wallis, and W. Ho, Phys. Rev. Lett. **90**, 046808 (2003).
[45] The rapid rise of dI/dV due to the first field emission resonance (also referred to as "modified image state") dominates the spectra at higher voltages.
[46] V. S. Stepanyuk, A. N. Klavsyuk, L. Niebergall, and P. Bruno, Phys. Rev. B **72**, 153407 (2005).
[47] A. Sperl, J. Kröger, H. Jensen, R. Berndt, A. Franke, and E. Pehlke (unpublished).
[48] J. Li, W.-D. Schneider, and R. Berndt, Phys. Rev. B **56**, 7656 (1997).
[49] S. D. Kevan and R. H. Gaylord, Phys. Rev. B **36**, 5809 (1987).
[50] R. Paniago, R. Matzdorf, G. Meister, and A. Goldmann, Surf. Sci. **331-333**, 1233 (1995).

5.3 Publication New Journal of Physics 11, 06302077 (2009)

New Journal of Physics
The open-access journal for physics

Evolution of unoccupied resonance during the synthesis of a silver dimer on Ag(111)

A Sperl[1], J Kröger[1,3], R Berndt[1], A Franke[2] and E Pehlke[2]

[1] Institut für Experimentelle und Angewandte Physik, Christian-Albrechts-Universität zu Kiel, D-24098 Kiel, Germany

[2] Institut für Theoretische Physik und Astrophysik, Christian-Albrechts-Universität zu Kiel, D-24098 Kiel, Germany

E-mail: kroeger@physik.uni-kiel.de

New Journal of Physics **11** (2009) 063020 (8pp)
Received 2 February 2009
Published 12 June 2009
Online at http://www.njp.org/
doi:10.1088/1367-2630/11/6/063020

Abstract. Silver dimers were fabricated on Ag(111) by single-atom manipulation using the tip of a cryogenic scanning tunnelling microscope. An unoccupied electronic resonance was observed to shift toward the Fermi level with decreasing atom–atom distance as monitored by spatially resolved scanning tunnelling spectroscopy. Density functional calculations were used to analyse the experimental observations and revealed that the coupling between the adsorbed atoms is predominantly direct rather than indirect via the Ag(111) substrate. While the substrate influence is small owing to the surface-projected sp band gap, the direct interaction is most likely due to the large extension of the p wave functions at the adsorbate atoms contributing to the resonance.

Contents

[3] Author to whom any correspondence should be addressed.

1. Introduction

The electronic structure of adsorbed atoms (adatoms) or clusters of atoms on surfaces determines the coupling between adsorbate and substrate [1]–[4], the mutual interaction between the adatoms [5], magnetic properties [6], as well as their catalytic activity and selectivity [7, 8]. The coupling between adatoms is particularly interesting since it plays a crucial role in nucleation and is thus at the base of the microscopic understanding of thin film growth on surfaces [9]–[11]. Typically, the mutual interaction comprises direct and indirect contributions. Direct interactions result from the overlap of atomic orbitals and are responsible for the bonding of dimers in vacuum. This type of interaction has been investigated for metal dimers in the gas phase and noble-gas matrices [12]–[14]. An exponential energy splitting of bonding and antibonding states with the atom–atom separation is characteristic for direct coupling. Indirect interactions may become important for adatoms on surfaces and they depend strongly on the electronic structure of the substrate. In particular, long-ranged and oscillatory coupling between two adatoms or adsorbed molecules is mediated by quasi-two-dimensional electronic states [15]–[22].

The evolution of the electronic structure of clusters on surfaces with cluster dimensions and geometric shapes has been analysed atom by atom. For example, results from artificial gold chains [23], quantum confinement of one-dimensional electronic states to chains of copper atoms [24], unoccupied electronic resonances of silver clusters with various sizes and shapes [25], and the evolution of the Kondo effect of a single magnetic atom with the number of adjacent non-magnetic atoms in vertical [26] and lateral [27] hybridization geometries have been reported. In a recent study of Au dimers on NiAl(110) a splitting of the Au monomer resonance into bonding and antibonding states was reported as a function of the Au–Au separation [5]. The emerging picture, which may be inferred from this work, is that substrate-mediated adsorbate–adsorbate interactions weaken the direct coupling between the adsorbates. In particular, it was found in [5] that the splitting between bonding and antibonding states varies linearly with the reciprocal mutual Au distance, rather than exponentially as would be expected from a direct coupling in vacuum.

Here, in a combined experimental and theoretical study, we investigated the evolution of a Ag monomer sp_z resonance, which shifts toward the Fermi level upon approaching a second Ag atom. Our theoretical analysis indicates that, at not too large adatom–adatom distances, the interaction between the sp_z electronic states on the surface is similar to the direct interaction between the two Ag p_z orbitals in vacuum.

2. Experiment

Measurements were performed with a custom-built scanning tunnelling microscope operated at 7 K and in ultrahigh vacuum with a base pressure of 10^{-9} Pa. The Ag(111) surface and chemically etched tungsten tips were cleaned by argon ion bombardment and annealing. Individual silver atoms were deposited onto the sample surface by controlled tip–surface contacts as previously described in [28]. Using the tip of the microscope, silver dimers were fabricated by atom manipulation. Spectra of the differential conductance (dI/dV) were acquired by superimposing a sinusoidal voltage signal (root-mean-square amplitude 5 mV, frequency 4.7 kHz) onto the tunnelling voltage and by measuring the current response with a lock-in amplifier. Prior to spectroscopy of monomers and dimers the tip status was monitored using

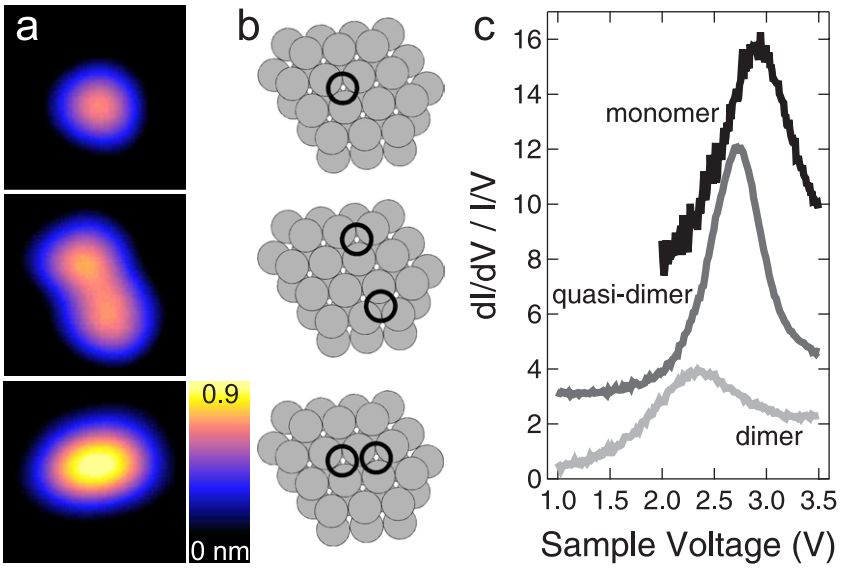

Figure 1. (a) STM images of a single Ag adatom (top), two Ag adatoms with a mutual distance of 0.58 nm, and Ag_2 on Ag(111) (sample voltage: 0.1 V, tunnelling current: 0.1 nA, image size: 2.1 nm × 2.1 nm). (b) Schematics of adsorption sites of silver adatoms (black circles) on Ag(111) lattice (grey dots). (c) Spectra of $\mathrm{d}I/\mathrm{d}V/(I/V)$ acquired with the tip placed above the centre of the assemblies in (a). The spectrum of the quasi-dimer and of the monomer have been shifted vertically by 3 and 7, respectively. Prior to spectroscopy the tip–sample distance had been set at 3.5 V and 1 nA for all spectra.

spectra of the onset of the Ag(111) surface state band edge. To obtain sharp onsets of the surface state signal and to image single adatoms with nearly circular circumference the tip was controllably indented into the substrate. Due to this *in vacuo* treatment the tip apex was most likely covered with substrate material. All scanning tunnelling microscopy (STM) images were acquired in the constant current mode with the voltage applied to the sample. We divided the $\mathrm{d}I/\mathrm{d}V$ spectra by I/V to reduce the influence of the voltage-dependent transmission of the tunnelling barrier [29].

3. Results and discussion

Figure 1(a) presents a sequence of constant-current STM images of a single Ag adatom (top) on Ag(111), two Ag adatoms (middle) with a distance of ≈ 0.58 nm, and a silver dimer (bottom). Distances between adatoms of Ag–Ag assemblies were determined from maxima positions of cross-sectional profiles taken along the connecting line between the adatoms. Together with the orientation of the assembly with respect to high-symmetry directions of the Ag(111) substrate, which was determined from dislocation lines on the surface, the extracted adatom–adatom distances agree with lattice site separations on Ag(111). The Ag dimer appears as a single entity in STM images and we assigned the nearest-neighbour distance of Ag(111) to the adatom–adatom distance of Ag_2. Our calculations indicated a slight preference of the Ag adatom to occupy the face-centred cubic (fcc) adsorption site to occupation of the metastable hexagonal close-packed (hcp) adsorption site, which is of the order of the accuracy of the

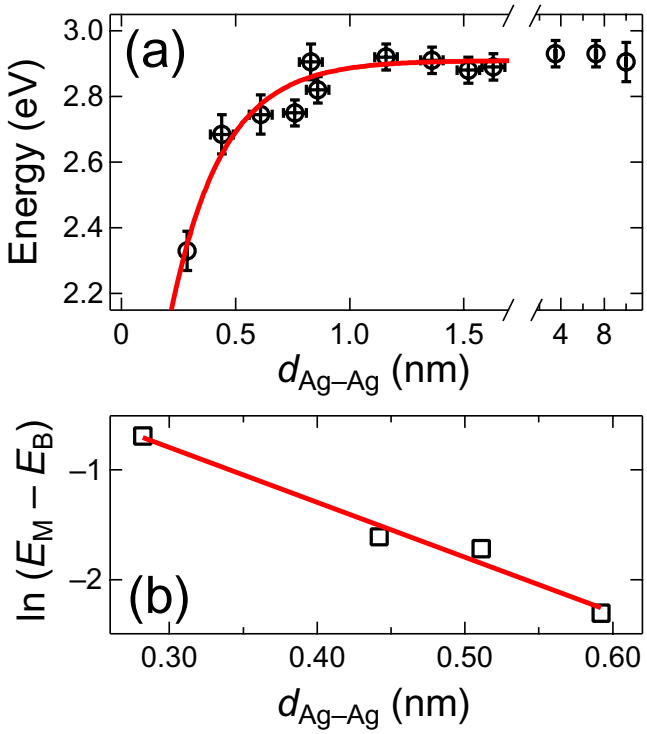

Figure 2. (a) Energy of the unoccupied resonance as a function of the Ag adatom distance, $d_{Ag–Ag}$. For distances larger than 2 nm the spectra were acquired atop the individual Ag adatoms while for smaller distances spectroscopy was performed with the tip positioned above the centre of the assembly. The solid line is a fit to the calculated data in (b). (b) Logarithm of the calculated energy difference between monomer resonance (M) and bonding resonance (B) of an Ag–Ag assembly, $\ln(E_M - E_B)$, plotted versus $d_{Ag–Ag}$. The solid line is a linear fit to the data.

calculation. We experienced that in the course of fabricating silver dimers individual Ag adatoms were also found to occupy hcp adsorption sites (see the middle STM image in figure 1(a) and the corresponding sketch in figure 1(b)). Such assemblies occurred frequently for adatom distances smaller than 0.6 nm. In the following, these assemblies are referred to as quasi-dimers. The schematics in figure 1(b) illustrate adsorption sites of individual Ag adatoms (black circles) on the hosting Ag(111) lattice (grey dots) and the orientation of the quasi-dimer and the dimer with respect to the Ag(111) crystallographic directions. Figure 1(c) shows normalized $\mathrm{d}I/\mathrm{d}V$ spectra acquired on the centre of the single Ag adatom (top), of a quasi-dimer (middle), and of the dimer (bottom). A gradual shift of the monomer-related peak from ≈ 2.9 eV via a resonance energy of ≈ 2.7 eV observed for the quasi-dimer to ≈ 2.3 eV for the dimer resonance binding energy was observed. The total shift of ≈ 0.6 eV towards the Fermi level was not induced by the electric field of the tip. Although the tip–surface distances may have differed for the spectra shown in figure 1(c), it has been shown in [30, 31] that for shifts of the order of 10 meV the tip–surface distance had to be varied by several angstroms, which was not the case here.

Figure 2(a) summarizes the resonance energies measured for a variety of Ag adatom separations, $d_{Ag–Ag}$. For $d_{Ag–Ag} > 1$ nm the shift of the resonance energy is too small to be

resolved. For separations $d_{\mathrm{Ag–Ag}} < 1$ nm a shift of the resonance energy is discernible and increases rapidly as $d_{\mathrm{Ag–Ag}}$ approaches the nearest-neighbour distance of Ag(111). The solid line in figure 2(a) is a fit to calculated data (figure 2(b)), which has been extrapolated to larger Ag–Ag distances. The calculations are discussed below. For $d_{\mathrm{Ag–Ag}} > 2$ nm, the spectra at the centre between two Ag adatoms were virtually identical with spectra of clean Ag(111) in the relevant voltage interval [25]. For this reason, the data points for $d_{\mathrm{Ag–Ag}} > 2$ nm in figure 2 were acquired atop the individual adatoms.

Using density functional theory as implemented in the Vienna *ab initio* simulation package (VASP) [32]–[34] developed at the Institut für Materialphysik der Universität Wien, we determined the electronic structure of silver dimers adsorbed on Ag(111) with increasing adatom–adatom separation. The generalized gradient approximation (GGA) PW91 by Perdew and Wang [35] was applied to the exchange correlation functional. The electron–ion interaction was treated within the framework of Blöchl's projector augmented wave (PAW) method [36]. The potentials for VASP were used from the database [37]. All configurations were modelled in a slab geometry comprising of 14 layers of Ag. Silver dimers with separations of 0.28, 0.44, 0.52 and 0.59 nm were modelled in a (5×4), (6×4), (4×4) and (6×4) surface unit cell, respectively. The surface Brillouin zone was sampled with 16, 9 and 6 k points for the (4×4), (5×4) and (6×4) unit cells, respectively. The Kohn–Sham wave functions were expanded in a plane wave basis set with a 250 eV cutoff energy.

In order to identify the orbital composition of the experimentally observed unoccupied resonance, we have calculated the projected density of states (PDOS) with respect to atomic orbitals localized at the adatom sites. In the case of the silver dimer with both atoms at neighbouring fcc sites, the maximum of the resonance was found between 1.8 and 1.9 eV above the Fermi energy [25]. This resonance can clearly be observed in the p_z PDOS (figure 3(a)), while it is absent in the s PDOS (figure 3(b)). From this we conclude a dominant p_z character, with some s admixture, of this resonance.

By projecting onto bonding and antibonding combinations of p_z orbitals located at the two Ag atoms of the dimer, we identified the centre of the bonding and antibonding p_z resonance (figure 3(c)). From this we obtained the energy splitting between the bonding (E_{B}) and the antibonding (E_{A}) state, whose logarithm is plotted as a function of the mutual Ag atom distance in figure 3(d). The results shown in figure 3(d) are consistent with an exponential variation of $E_{\mathrm{A}} - E_{\mathrm{B}}$ within the calculated range of Ag adatom distances. In order to compare to experiment, we furthermore calculated the energy shift of the bonding resonance of the Ag adatom pair with respect to the energy of the monomer resonance (E_{M}) (figure 2(b)). We found that the energy splitting between the bonding resonance with respect to the monomer resonance, $E_{\mathrm{M}} - E_{\mathrm{B}}$, quite accurately coincides with half the energy shift between the bonding and the antibonding states, $(E_{\mathrm{A}} - E_{\mathrm{B}})/2$. Thus, the splitting between bonding and antibonding states is approximately symmetric. The solid line in figure 2(a) represents a linear fit to $\ln(E_{\mathrm{M}} - E_{\mathrm{B}})$ as a function of the Ag adatom separation $d_{\mathrm{Ag–Ag}}$, which has been extrapolated to larger separations. We conclude that both experimental and theoretical data are consistent with an exponential variation of the energy splitting with $d_{\mathrm{Ag–Ag}}$. However, due to computational limitations the range of Ag–Ag distances considered here for the two Ag adatoms on the Ag substrate is too narrow to reliably distinguish between an exponential and an algebraic $(1/d)$ [5] dependence of energy splitting on adatom separation.

For comparison we have calculated the energy splitting between the $5p_z$ bonding and antibonding orbitals of a Ag dimer in vacuum. The calculated splitting of the silver $5p_z$

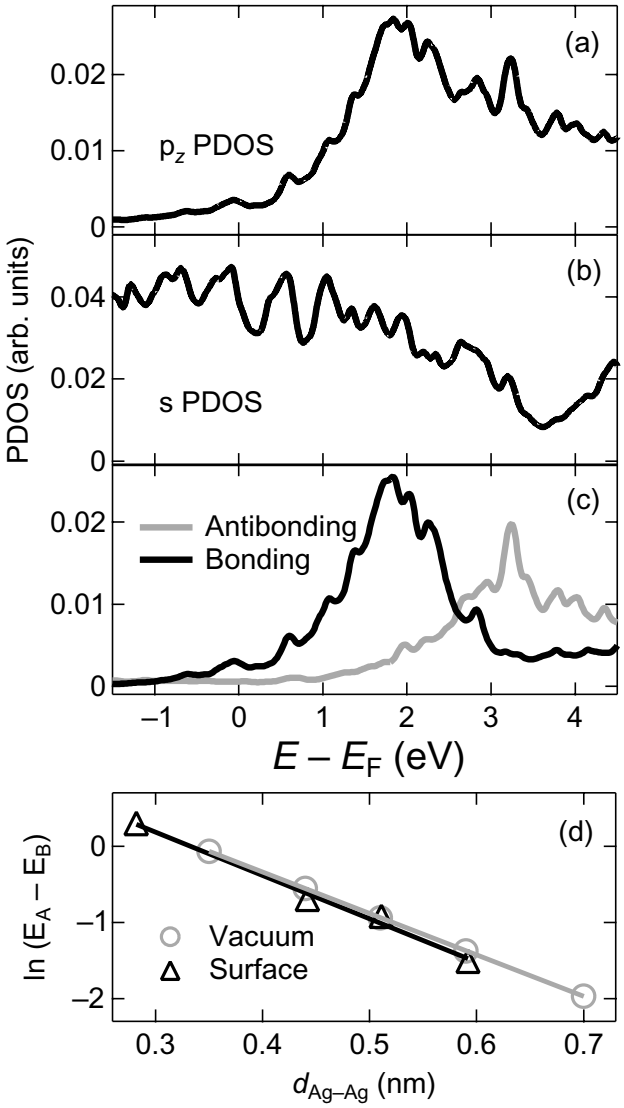

Figure 3. (a) p_z PDOS and (b) s PDOS for the silver dimer ($d_{Ag–Ag} = 0.28$ nm, both adatoms at neighbouring fcc sites). (c) Density of states projected onto bonding and antibonding p_z orbitals located at the two atoms of the Ag dimer. (d) Logarithm of the Kohn–Sham energy splitting between bonding (B) and antibonding (A) resonances as a function of Ag–Ag distance for Ag assemblies on the Ag(111) surface (triangles) and for free Ag atom pairs (circles) in the supercell. The solid lines are linear fits to the data.

bonding and antibonding orbitals varied exponentially with atom separation as expected [12, 14]. Surprisingly, as is evident from figure 3(d), the energy splitting between bonding and antibonding states for the dimer in vacuum is similar to the splitting of the dimer adsorbed on the surface for the Ag–Ag distances considered in the *ab initio* calculations.

To further analyse the interaction between adatoms on a surface we resorted to a minimum tight-binding model, which is similar to the model reported in [38]. For simplicity, we did not consider a tight-binding model of the fcc crystal and its (111) surface, but we resorted to atoms

with a single s orbital forming a simple cubic lattice, and two adatoms adsorbed at on-top sites. We found a direct contribution, $2t$, to the energy splitting between bonding and antibonding states, which is due to direct adatom interaction. The parameter t denotes the transfer integral for the two adatom states, and $2t$ is identical to the splitting occurring for the free dimer at the same adatom distance. Furthermore, there is a contribution to the splitting owing to the interaction via the substrate, $2\,\mathrm{Re}(G_{ab})\,|v|^2$, where v denotes the next-neighbour transfer integral and G_{ab} the matrix element of the Green's function of the substrate with respect to the adsorption sites. Calculations of such a matrix element of the Green's function for two next-neighbour sites on the Ag(111) surface yielded values of $\mathrm{Re}(G_{ab})(\varepsilon)$ varying between 0.05 and 0.15 eV^{-1} within the energy range of interest. For typical values of $|v|$ between 0.4 and 1 eV, the simple model also predicts that the interaction via the substrate is distinctly smaller than the observed splitting. At large adatom separations, we expect the substrate-mediated interaction to eventually dominate the direct interaction between the adatoms. In the case of Ag atom pairs on Ag(111) this appears to occur at a separation which is too large for the splitting to be resolved in experiment.

In a previous investigation of Au dimers on NiAl(110) the splitting of bonding and antibonding Au dimer states was reported for varying Au–Au distances [5]. Nilius *et al* [5] found that the variation of the splitting follows a $1/d_{\mathrm{Au-Au}}$ rather than an exponential law. This observation was argued to be due to the influence of the substrate electronic structure, which reduces the direct overlap of Au orbitals. In the case of Ag–Ag assemblies on Ag(111), however, the interaction between the individual Ag adatoms is similar to the one in vacuum (figure 3(d)). A tentative explanation for this observation involves the electronic structures of the substrates. The Ag(111) surface exhibits an extended sp band gap of surface-projected bulk electronic states in the centre of the surface Brillouin zone [39], while NiAl(110) does not [40]–[42]. Since the resonance energy of the Ag–Ag assemblies falls into the surface-projected sp band gap it is likely that the Ag(111) substrate electronic structure plays a less important role in mediating the interaction between the Ag adatoms. As a consequence, the Ag adatom assemblies on Ag(111) are subject to a substrate influence to a lesser extent than the Au adatom assemblies on NiAl(110). We suggest that the large direct interaction in case of Ag dimers on Ag(111) is also caused by the large extension of the p wave function, which dominates the resonance. This results in a slow decay of the transfer integral as a function of Ag–Ag distance.

4. Conclusion

The interaction between two Ag adatoms on Ag(111) gives rise to a shift of a sp_z resonance towards the Fermi level with decreasing mutual adatom distances. The shift was modelled by density functional calculations and is similar to the shift calculated for a Ag dimer in vacuum. This observation indicates a weak net influence of the substrate on the Ag–Ag interaction, which may originate from the surface-projected sp band gap of the substrate. We suggest that adatom–adatom interactions on surfaces with band gaps in the relevant energy interval exhibit similar behaviour. Moreover, the large extent of the p wave function favours a long range direct interaction.

Acknowledgment

Financial support by the Deutsche Forschungsgemeinschaft through SPP 1153 is acknowledged. Calculations have been carried out at the Rechenzentrum der Universität Kiel.

References

[1] Persson M 2004 *Phys. Rev.* B **70** 205420
[2] Olsson F E, Persson M, Borisov A G, Gauyacq J-P, Lagoute J and Fölsch S 2004 *Phys. Rev. Lett.* **93** 206803
[3] Limot L, Pehlke E, Kröger J and Berndt R 2005 *Phys. Rev. Lett.* **94** 036805
[4] Kröger J, Limot L, Jensen H, Berndt R, Crampin S and Pehlke E 2005 *Prog. Surf. Sci.* **80** 26
[5] Nilius N, Wallis T M, Persson M and Ho W 2003 *Phys. Rev. Lett.* **90** 196103
[6] Bansmann J *et al* 2005 *Surf. Sci. Rep.* **56** 189
[7] Abbet S, Sanchez A, Heiz U, Schneider W-D, Ferrari A M, Pacchioni G and Rösch N 2000 *J. Am. Chem. Soc.* **122** 3453
[8] Abbet S, Sanchez A, Heiz U and Schneider W-D 2001 *J. Catal.* **198** 122
[9] Lewis B and Anderson J C 1978 *Nucleation and Growth of Thin Films* (New York: Academic)
[10] Venables J A, Spiller G D T and Hanbücken M 1984 *Rep. Prog. Phys.* **47** 399
[11] Brune H 1998 *Surf. Sci. Rep.* **31** 125
[12] Fedrigo S, Harbich W and Buttet J 1993 *J. Chem. Phys.* **99** 5712
[13] Haberland H 1994 *Clusters of Atoms and Molecules* (Berlin: Springer)
[14] Rabin I, Schulze W and Ertl G 1999 *Chem. Phys. Lett.* **312** 394
[15] Lau K H and Kohn W 1978 *Surf. Sci.* **75** 69
[16] Kamna M M, Stranick S J and Weiss P S 1996 *Science* **274** 118
[17] Wahlström E, Ekvall I, Olin H and Walldén L 1998 *Appl. Phys.* A **66** S1107
[18] Repp J, Moresco F, Meyer G, Rieder K-H, Hyldgaard P and Persson M 2000 *Phys. Rev. Lett.* **85** 2981
[19] Knorr N, Brune H, Epple M, Hirstein A, Schneider M A and Kern K 2002 *Phys. Rev.* B **65** 115420
[20] Silly F, Pivetta M, Ternes M, Patthey F, Pelz J P and Schneider W-D 2004 *Phys. Rev. Lett.* **92** 016101
[21] von Hofe Th, Kröger J and Berndt R 2006 *Phys. Rev.* B **73** 245434
[22] Ziegler M, Kröger J, Berndt R, Filinov A and Bonitz M 2008 *Phys. Rev.* B **78** 245427
[23] Nilius N, Wallis T M and Ho W 2002 *Science* **297** 1853
[24] Fölsch S, Hyldgaard P, Koch R and Ploog K H 2004 *Phys. Rev. Lett.* **92** 056803
[25] Sperl A, Kröger J, Néel N, Jensen H, Berndt R, Franke A and Pehlke E 2008 *Phys. Rev.* B **77** 085422
[26] Néel N, Kröger J, Limot L, Palotas K, Hofer W A and Berndt R 2007 *Phys. Rev. Lett.* **98** 016801
[27] Néel N, Kröger J, Berndt R, Wehling T O, Lichtenstein A I and Katsnelson M I 2008 *Phys. Rev. Lett.* **101** 266803
[28] Limot L, Kröger J, Berndt R, Garcia-Lekue A and Hofer W A 2005 *Phys. Rev. Lett.* **94** 126102
[29] Stroscio J A, Feenstra R M and Fein A P 1986 *Phys. Rev. Lett.* **57** 2579
[30] Limot L, Maroutian T, Johansson P and Berndt R 2003 *Phys. Rev. Lett.* **91** 196801
[31] Kröger J, Limot L, Jensen H, Berndt R and Johansson P 2004 *Phys. Rev.* B **70** 033401
[32] Kresse G and Hafner J 1993 *Phys. Rev.* B **47** 558
Kresse G and Hafner J 1994 *Phys. Rev.* B **49** 14251
[33] Kresse G and Furthmüller J 1996 *Comput. Mater. Sci.* **6** 15
[34] Kresse G and Furthmüller J 1996 *Phys. Rev.* B **54** 11169
[35] Perdew J P, Chevary J A, Vosko S H, Jackson K A, Pederson M R, Singh D J and Fiolhais C 1992 *Phys. Rev.* B **46** 6671
[36] Blöchl P E 1994 *Phys. Rev.* B **50** 17953
[37] Kresse G and Joubert D 1999 *Phys. Rev.* B **59** 1758
[38] Klamroth T and Saalfrank P 1998 *Surf. Sci.* **410** 21
[39] Kevan S D and Gaylord R H 1987 *Phys. Rev.* B **36** 5809
[40] Lui S-C, Kang M H, Mele E J, Plummer E W and Zehner D M 1989 *Phys. Rev.* B **39** 13149
[41] Castro G R, Dürr H, Fischer R and Fauster Th 1992 *Phys. Rev.* B **45** 11989
[42] Song Z, Pascual J I, Conrad H, Horn K and Rust H-P 2001 *Appl. Phys.* A **72** S159

6 Summary

Surface functionalization via self-assembly, a focus of modern surface science, can be achieved via organic molecules chemisorbed on metal surfaces. Alkanethiol and alkanedithiol molecules bonded to Au surfaces have adopted the role of model systems in many studies. So far, however, not much information is available about adsorption geometries of alkanedithiols which bond to Au surfaces via two S-Au bonds below saturation coverage. Moreover, alkanedithiols with two S-Au bonds are a suitable model system to further the understanding of diffusion properties of molecules with two bonds to the substrate surface. It has been reported previously that diffusion of molecules can be fundamentally different from adatom diffusion or diffusion of simple molecules with only a single bond to the surface. A detailed insight into the binding properties and diffusion mechanisms should contribute to further the understanding of this important model system.

The objective of this thesis was to investigate the adsorption and diffusion of 1,4-butanedithiol molecules, HS-$(CH_2)_4$-SH (BDTs), as well as 1,4-butanedithiol radicals, $\cdot$S-$(CH_2)_4$-S$\cdot$ (BDTRs), on the unreconstructed Au(111) and Au(100) substrate surfaces by means of density-functional theory (DFT) calculations. BDT is an organic molecule with multiple internal degrees of freedom. When it comes to adsorption studies of molecules containing -SH thiol groups on Au surfaces, one important question is whether the molecules physisorb on the surface or chemisorb via S-H bond cleavage and formation of strong S-Au bonds as is frequently assumed. On both substrates BDT molecules are only weakly bonded on the surface [physisorption energy approximately -0.5 eV on Au(111) and -0.8 eV on Au(100)]. In equilibrium it has been found that both BDT S-H bonds are cleaved and BDTRs, are the predominant species chemisorbed via two S-Au bonds on the surface.

As a necessary precursor for the BDTR/Au chemisorption study, low total-energy configurations and diffusion paths of SCH_3 radicals, which mimic the BDTR S-Au bonds individually, have been analyzed on Au(111) and Au(100) surfaces. This survey has shown that energetically preferred SCH_3 configurations on both surfaces comprise those with S atoms close to bridge or hollow sites of the substrate surfaces and tilted or upright S-C bonds with respect to the surface normal. The chemisorption energy amounts to approximately -1.9 eV on Au(111) and -2.3 eV on Au(100) for a coverage of one SCH_3 radical per 16 Au surface atoms.

In case of BDTR both S-Au bonds are interconnected through an alkane chain. This results in a fundamentally different adsorption phenomenology compared to adsorption of alkanethiol radicals with only a single S-Au bond like SCH_3. As a consequence of the interplay between internal degrees of freedom of BDTR and two S-Au bonds, the

potential energy surface (PES) exhibits a complicated multivalley topology with local total-energy minima within a few 100 meV of the ground state chemisorption geometry. Both for the unreconstructed Au(111) and Au(100) surfaces BDTR adopts lying-down configurations with two S-Au bonds close to bridge or hollow-sites of the surface. The BDTR alkane chain is oriented approximately parallel to the substrate surface. At a coverage of one radical per 16 Au surface atoms the chemisorption energy amounts to approximately -3.5 eV on Au(111) and -4.1 eV on Au(100). Notably, the three lowest-energy configurations on the Au(100) surface come out energetically degenerate within the accuracy of the calculation. Besides providing valuable information concerning the chemisorption geometries of BDTR/Au, the obtained results suggest versatile BDTR diffusion properties which differ from those of molecules with only one substrate bond.

Simulated scanning tunneling microscope (STM) images within the Tersoff-Hamann model of the BDTR/Au(111) ground state geometry exhibit elongated bright features with the long axis only slightly tilted with respect to $\langle 1\bar{1}0\rangle$ directions of the surface. Leung *et al.* have observed elongated bright features in STM experiments for 1,6-hexanedithiol/Au(111) whose long axes point approximately in $\langle 1\bar{1}0\rangle$ directions. The DFT results for BDTR/Au(111) are consistent with the experimental work conducted by Leung *et al.* despite the fact that a slightly longer alkanedithiol has been considered.

The diffusion properties for BDTR on the unreconstructed Au(100) surface have been characterized from single diffusion hops to short and long time scales. Due to the complicated multivalley PES, the diffusion properties are highly non trivial. It has been shown that a characterization can be achieved by integrating a master equation for a set of elementary diffusion hops between local minima on the PES. The resulting probability currents yield low total-energy diffusion paths for translations ($\Delta E_{\mathrm{trans}}$=0.35 eV) and rotations (ΔE_{rot}=0.43 eV) of BDTR on the surface composed of a complicated sequence of elementary hops. The calculated order of the diffusion energy barriers is $\Delta E_{\mathrm{trans}} < \Delta E_{\mathrm{rot}}$, i.e. translations occur at a faster rate than rotations (energy barrier difference approximately 0.08 eV). This leads to correlations between subsequent BDTR diffusion hops in the simulation which proceed back and forth along the same high symmetry direction on the Au(100) surface. The correlations are expected to decay on time scales compatible with the average time span between BDTR rotations. If the adsorbate has lost memory of its initial configuration, i.e. on long time scales, the diffusion is isotropic on the surface. The numerical diffusion constants follow an Arrhenius law with an effective diffusion energy barrier of 0.36 eV in agreement with the highest energy barrier along the diffusion paths of $\Delta E_{\mathrm{trans}}$ = 0.35 eV. Notably, the diffusion energy barrier of BDTR/Au(100) is significantly lower than for SCH_3/Au(100) (ΔE=0.61 eV) despite the fact that BDTR is much more tightly bound to the surface by 1.8 eV. This surprising result is suggested to originate from the constraints imposed on the two S-Au bonds by the BDTR alkane chain. This is a manifestation of the important role played by internal degrees of freedom.

The diffusion of BDTR on the unreconstructed Au(111) surface has been characterized by calculating diffusion modes for translation and rotations on the surface. It has

been shown that low total-energy diffusion paths involve a complicated sequence of elementary diffusion hops between several intermediate local minima of the PES. Similar to BDTR/Au(100) the diffusion energy barrier for translations is lower than for rotations, which suggests correlations between subsequent diffusion hops (energy barrier difference approximately 0.05 eV). Notably, the diffusion energy barrier heights depend significantly on coverage. The energy barrier for translations increases from 0.25 eV in case of a coverage of one BDTR per 12 Au surface atoms to 0.47 eV for a coverage of one BDTR per 24 Au surface atoms.

A DFT diffusion study for the unreconstructed Au(111) and Au(100) surfaces is particularly relevant for experiments under certain electrochemical (EC) conditions where these surfaces can be stabilized. An experimental characterization of BDTR diffusion on electrode surfaces in an EC cell offers the unique option to vary the electric field present at a solid-liquid interface. This can be achieved through a change of the applied external potential with respect to a reference electrode. In case of the BDTR/Au systems studied in this work, a significant influence of an electric field on the diffusion properties has been discovered. The electric field effect has been estimated from the change of the adsorbate dipole moment along the diffusion paths. If the electrostatic interaction between an electric field (field vector perpendicular to the surface and pointing away from the surface) and the adsorbate dipole moment is considered in a rough non-self-consistent manner, three main effects can be witnessed: (i) the PES is significantly distorted by the electric field, (ii) the correlations between subsequent diffusion events depend on the electric field strength, and (iii) in case of BDTR/Au(111) the diffusion is predicted to slow down considerably as the electric field strength increases. This last observation is in qualitative agreement with preliminary experimental results by Suto and Magnussen.

A semi-empirical model has been evaluated to give an estimate of the impact of van der Waals (vdW) interactions on the adsorption and diffusion properties of BDTR/Au calculated within DFT using a generalized gradient approximation (GGA). In general, calculations based on a local or semi-local exchange-correlation energy-functional can not correctly account for vdW interactions. The main conclusions in this context are: (i) the BDT/Au(111) binding energy appears to be overestimated within this simple approach, (ii) the ground state BDTR adsorption configurations remain unaltered, and (iii) the main features of the calculated DFT diffusion properties are largely unaffected. To verify these statements, a more sophisticated approach using a vdW density-functional has to be applied, which is, however, computationally not feasible at present.

Beyond the adsorption and diffusion study of sulfur bonded molecules on Au surfaces, this work also contains results from two collaborations. In a combined *in situ* surface x-ray diffraction and DFT study conducted together with the group of O. M. Magnussen, the c(2x2) Cl adlayer formed on a Cu(100) surface at an EC interface has been investigated. Distinct differences compared to the interface to vacuum have been discovered regarding the relaxations of the Cl atoms and first and second Cu surface layer atoms. Excess surface charges expected to be present in experiments under EC conditions, have been taken into account in the DFT calculation by introducing water molecules and Ca

atoms as electron donors in front of the surface. The calculations have qualitatively reproduced the experimentally observed differences between the solid-vacuum and solid-liquid interface. Such a comparison might provide the ground to test and advance the research of theoretical models for EC interfaces.

Together with the group of R. Berndt the electronic structure of unoccupied resonance states of Ag adatoms and clusters on the Ag(111) surface has been characterized by means of STM experiments, DFT calculations, and tight-binding model calculations. The calculations have provided all qualitative trends observed in experiment for the cluster resonance energies, which gradually shift towards the Fermi energy as the cluster size is increased. Furthermore, the calculations have revealed the nature of the resonances which derive from Ag $5p_z$ atomic orbitals. The predominant coupling mechanism of two Ag adatom resonances at not too large adatom-adatom separations has been shown to be consistent with direct coupling as opposed to substrate mediated coupling.

Acknowledgments

At this point I would like to thank everybody who supported me during my thesis.
I would like to thank Eckhard Pehlke for giving me the opportunity to work in his group on this project and for his time and endless effort to support me with his deep understanding of physics.
I would like to show my gratitude to Richard Berndt, Jörg Kröger, and Alexander Sperl for giving me the opportunity to publish and collaborate with them.
My gratitude also goes to Olaf M. Magnussen and Yvonne Gründer for giving me the opportunity to publish and collaborate with them.
My special gratefulness and my love go to my wife Nicole and my daughter Lilly for their endless support and motivation. My gratitude also goes to my parents for their support and for giving me the opportunity to study without a care.
Last but not least, I would like to thank the Deutsche Forschungsgemeinschaft for financial support and the staff at the Rechenzentrum der Universität Kiel, where the calculations published in this work have been carried through.

Lebenslauf (CV) und Liste der Veröffentlichungen

Andreas Franke, Diplom-Physiker
geboren am 8. Juli 1978 in Kiel
verheiratet, 1 Kind

Ausbildung und Beruf

01/2006 – 01/2010	Wissenschaftlicher Mitarbeiter bei Prof. Dr. E. Pehlke, Institut für Theoretische Physik u. Astrophysik, Universität Kiel
07/2005	Diplom in Physik (*mit Auszeichnung*), Universität Kiel
05/2004 – 06/2005	Diplomarbeit in der Arbeitsgruppe von Prof. Dr. E. Pehlke: „*Dichtefunktionalrechnungen zur elektronischen Struktur der sauberen und adsorbatbedeckten Ag(111)-Oberfläche*“
08/2002 – 06/2003	Physikstudium, Pennsylvania State University (USA)
10/1999 – 07/2005	Physikstudium, Universität Kiel (Nebenfach: Chemie, Mathematik)
1998 – 1999	Grundwehrdienst in Lütjenburg / Schleswig-Holstein
1998	Allgemeine Hochschulreife, Gymnasium Kronshagen

Veröffentlichungen

„*Unoccupied states of individual silver clusters and chains on Ag(111)*“,
A. Sperl, J. Kröger, N. Neel, H. Jensen, R. Berndt, **A. Franke**, E. Pehlke,
Physical Review B 77, 085422 (2008).

„*Evolution of unoccupied resonance during the synthesis of a silver dimer on Ag(111)*“,
A. Sperl, J. Kröger, R. Berndt, **A. Franke**, E. Pehlke,
New Journal of Physics 11, 063020 (2009).

„*Adsorption and diffusion of SCH_3 radicals and $Au(SCH_3)_2$ complexes*

on the unreconstructed Au(111) surface in the submonolayer coverage regime“, **A. Franke**, E. Pehlke, Physical Review B 79, 235441 (2009) referenziert in Virtual Journal of Nanoscale Sci. & Tech. Vol. 20 (2009), Supramolecular and biochemical assembly.

„*First-principles study of 1,4-butanedithiol molecules and radicals adsorbed on unreconstructed Au(111) and Au(100)*“, **A. Franke**, E. Pehlke, Physical Review B 81, 075409 (2010) referenziert in Virtual Journal of Nanoscale Sci. & Tech. Vol. 21 (2010), Supramolecular and biochemical assembly.

„*Reversal of Chloride-induced Cu(001) Subsurface Buckling in Electrochemical Environment: An in situ Surface X-ray Diffraction and Density Functional Theory Study*“, Y. Gründer, D. Kaminski, F. Golks, K. Krug, J. Stettner, O. M. Magnussen, **A. Franke**, J. Stremme, E. Pehlke, Phys. Rev. B. 81, 174114 (2010).

„*Diffusion of 1,4-butanedithiol on Au(100)-(1×1): A DFT-based master-equation approach*“, **A. Franke**, E. Pehlke, Zur Veröffentlichung angenommen Phys. Rev. B. (2010).

Kiel, den 11. November 2010

Selbständigkeitserklärung

Ich erkläre, daß ich die vorgelegte Arbeit - abgesehen von der Beratung durch meinen Betreuer Prof. Dr. E. Pehlke - selbständig und nur unter Benutzung der angegebenen Literatur angefertigt habe. Der den Veröffentlichungen zugrunde liegende theoretische Anteil der Forschungsarbeit wurde von mir selbst durchgeführt abgesehen von der Beratung und Hilfe durch E. Pehlke. Die Veröffentlichungen wurden von mir verfasst, abgesehen von der Beratung und Hilfe durch E. Pehlke. Im Detail ist Folgendes zu ergänzen. Bei der Publikation / den Publikationen

- *Reversal of chloride-induced Cu(001) subsurface buckling in the electrochemical environment: An in situ surface x-ray diffraction and density functional theory study* habe ich die DFT Rechnungen für Cl/Cu(001) unter elektrochemischen Bedingungen durchgeführt. J. Stremme hat die DFT Rechnungen für Cl/Cu(001) gegen Vakuum durchgeführt. E. Pehlke hat die Theorieteile der Publikation verfasst. Alle übrigen Teile der Publikation wurden von Dr. Y. Gründer und Co-Autoren verfasst. Die Experimente wurden in der Gruppe von Prof. Dr. O. Magnussen durchgeführt.

- *Unoccupied states of individual silver clusters and chains on Ag(111)* und *Evolution of unoccupied resonance during the synthesis of a silver dimer on Ag(111)* habe ich die DFT Rechnungen durchgeführt und die Theorieteile der Publikationen verfasst. E. Pehlke hat die tight-binding Berechnungen konzipiert und durchgeführt. Die Teile der Publikationen, welche die Experimente betreffen, wurden von A. Sperl, Prof. Dr. J. Kröger und Prof. Dr. R. Berndt verfasst. Die Experimente wurden in der Gruppe von R. Berndt durchgeführt.

- Für alle übrigen in dieser Arbeit enthaltenen angenommenen und eingereichten Publikationen habe ich die DFT Rechnungen durchgeführt und die Manuskripte verfasst. E. Pehlke hat inhaltliche Fragen mit mir diskutiert und bei der endgültigen Formulierung der Publikationen unterstützt.

Weiterhin versichere ich, daß die vorliegende Dissertation weder ganz noch zum Teil bei einer anderen Stelle im Rahmen eines Prüfungsverfahrens vorgelegt worden ist. Die Arbeit ist unter Einhaltung der Regeln guter wissenschaftlicher Praxis entstanden. Ich habe keine früheren Promotionsversuche unternommen.

Kiel, den 11. November 2010

Bibliography

[1] R. Schaller, Spectrum, IEEE **34**, 52 (1997).

[2] R. Feynman, J. Microelectromech. Sys. **1**, 60 (1992).

[3] L. Grill, J. Phys. Condens. Mat. **20**, 053001 (2008).

[4] F. Schreiber, J. Phys. Condens. Mat. **16**, R881 (2004).

[5] F. Schreiber, Prog. Surf. Sci. **65**, 151 (2000).

[6] H. Song, Y. Kim, Y. H. Jang, H. Jeong, M. A. Reed, and T. Lee, Nature **462**, 1039 (2009).

[7] Y. Shirai, A. J. Osgood, Y. Zhao, K. F. Kelly, and J. M. Tour, Nano Lett. **5**, 2330 (2005).

[8] K. L. Wong, G. Pawin, K.-Y. Kwon, X. Lin, T. Jiao, U. Solanki, R. H. J. Fawcett, L. Bartels, S. Stolbov, and T. S. Rahman, Science **315**, 1391 (2007).

[9] F. I. Bohrer, C. N. Colesniuc, J. Park, M. E. Ruidiaz, I. K. Schuller, A. C. Kummel, and W. C. Trogler, J. Am. Chem. Soc. **131**, 478 (2009).

[10] F. Chen, J. Hihath, Z. Huang, X. Li, and N. Tao, Ann. Rev. Phys. Chem. **58**, 535 (2007).

[11] Y. F. Wang, J. Kröger, R. Berndt, H. Vázquez, M. Brandbyge, and M. Paulsson, Phys. Rev. Lett. **104**, 176802 (2010).

[12] Y. Wang, J. Kröger, R. Berndt, and W. A. Hofer, J. Am. Chem. Soc. **131**, 3639 (2009).

[13] B. Baisch, D. Raffa, U. Jung, O. M. Magnussen, C. Nicolas, J. Lacour, J. Kubitschke, and R. Herges, J. Am. Chem. Soc. **131**, 442 (2009).

[14] J. Lahann, S. Mitragotri, T.-N. Tran, H. Kaido, J. Sundaram, I. S. Choi, S. Hoffer, G. A. Somorjai, and R. Langer, Science **299**, 371 (2003).

[15] B.-Y. Choi, S.-J. Kahng, S. Kim, H. Kim, H. W. Kim, Y. J. Song, J. Ihm, and Y. Kuk, Phys. Rev. Lett. **96**, 156106 (2006).

[16] M. J. Comstock, N. Levy, A. Kirakosian, J. Cho, F. Lauterwasser, J. H. Harvey, D. A. Strubbe, J. M. J. Fréchet, D. Trauner, S. G. Louie, et al., Phys. Rev. Lett. **99**, 038301 (2007).

[17] D. L. Klein, R. Roth, A. K. L. Lim, A. P. Alivisatos, and P. L. McEuen, Nature **389**, 699 (1997).

[18] M. A. Reed, C. Zhou, C. J. Muller, T. P. Burgin, and J. M. Tour, Science **278**, 252 (1997).

[19] B. Xu and N. J. Tao, Science **301**, 1221 (2003).

[20] N. Néel, J. Kröger, L. Limot, and R. Berndt, Nano Lett. **8**, 1291 (2008).

[21] Y. Hu, Y. Zhu, H. Gao, and H. Guo, Phys. Rev. Lett. **95**, 156803 (2005).

[22] J. Love, L. Estroff, J. Kriebel, R. Nuzzo, and G. Whitesides, Chem. Rev. **105**, 1103 (2005).

[23] C. Vericat, M. E. Vela, G. Benitez, P. Carro, and R. C. Salvarezza, Chem. Soc. Rev. **39**, 1805 (2010).

[24] D. J. Lavrich, S. M. Wetterer, S. L. Bernasek, and G. Scoles, J. Phys. Chem. B **102**, 3456 (1998).

[25] A. Ulman, Chem. Rev. **96**, 1533 (1996).

[26] S. Tsuzuki, K. Honda, T. Uchimaru, and M. Mikami, J. Phys. Chem. A **108**, 10311 (2004).

[27] A. Goursot, T. Mineva, R. Kevorkyants, and D. Talbi, J. Chem. Theory Comput. **3**, 755 (2007).

[28] L. H. Dubois, B. R. Zegarski, and R. H. Nuzzo, J. Chem. Phys. **98**, 678 (1993).

[29] H. S. Kato, J. Noh, M. Hara, and M. Kawai, J. Phys. Chem. B **106**, 9655 (2002).

[30] L. Kankate, A. Turchanin, and A. Gölzhäuser, Langmuir **25**, 10435 (2009).

[31] M. G. Roper and R. G. Jones, Phys. Chem. Chem. Phys. **10**, 1336 (2008).

[32] Y. Wang, N. S. Hush, and J. R. Reimers, J. Am. Chem. Soc. **129**, 14532 (2007).

[33] I. I. Rzeznicka, J. Lee, P. Maksymovych, and J. T. Yates, J. Phys. Chem. B. **109**, 15992 (2005).

[34] R. H. Nuzzo, B. R. Zegarski, and L. H. Dubois, J. Am. Chem. Soc. **109**, 733 (1987).

[35] G. Liu, J. A. Rodriguez, J. Dvorak, J. Hrbek, and T. Jirsak, Surf. Sci. **505**, 295 (2002).

[36] P. G. Lustemberg, M. L. Martiarena, A. E. Martinez, and H. F. Busnengo, Langmuir **24**, 3274 (2008).

[37] S. Takagi, J. ichi Hoshino, H. Tomono, and K. Tsumuraya, J. Phys. Soc. Jpn. **77**, 054705 (2008).

[38] B. Hammer and J. K. N. rskov, Nature **376**, 238 (1995).

[39] A. Franke and E. Pehlke, Phys. Rev. B **79**, 235441 (2009).

[40] G. Nenchev, B. Diaconescu, F. Hagelberg, and K. Pohl, Phys. Rev. B **80**, 081401 (2009).

[41] D. P. Woodruff, Phys. Chem. Chem. Phys. **10**, 7221 (2008).

[42] H. Grönbeck, A. Curioni, and W. Andreoni, J. Am. Chem. Soc. **122**, 3839 (2000).

[43] M. C. Vargas, P. Giannozzi, A. Selloni, and G. Scoles, J. Phys. Chem. B. **105**, 9509 (2001).

[44] Y. Yourdshahyan, H. K. Zhang, and A. M. Rappe, Phys. Rev. B **63**, 081405(R) (2001).

[45] T. Hayashi, Y. Morikawa, and H. Nozoye, J. Chem. Phys. **114**, 7615 (2001).

[46] J. Gottschalck and B. Hammer, J. Chem. Phys. **116**, 784 (2002).

[47] Y. Yourdshahyan and A. M. Rappe, J. Chem. Phys. **117**, 825 (2002).

[48] F. P. Cometto, P. Paredes-Olivera, V. A. Macagno, and E. M. Patrito, J. Phys. Chem. B **109**, 21737 (2005).

[49] N. Gonzalez, N. Lorente, and A. Arnau, Surf. Sci. **600**, 4039 (2006).

[50] P. Maksymovych, D. C. Sorescu, and J. T. Yates, J. Phys. Chem. B **110**, 21161 (2006).

[51] R. Mazzarello, A. Cossaro, A. Verdini, R. Rousseau, L. Casalis, M. F. Danisman, L. Floreano, S. Scandolo, A. Morgante, and G. Scoles, Phys. Rev. Lett. **98**, 016102 (2007).

[52] J. Wang and A. Selloni, J. Phys. Chem. C Lett. **111**, 12149 (2007).

[53] A. Nagoya and Y. Morikawa, J. Phys. Condens. Mat. **19**, 365245 (2007).

[54] Y. Morikawa, C. C. Liew, and H. Nozoye, Surf. Sci. **514**, 389 (2002).

[55] L. M. Molina and B. Hammer, Chem. Phys. Lett. **360**, 264 (2002).

[56] P. Maksymovych, D. C. Sorescu, and J. T. Yates, Phys. Rev. Lett. **97**, 146103 (2006).

[57] O. Voznyy, J. J. Dubowski, J. T. Yates, and P. Maksymovych, J. Am. Chem. Soc. **131**, 12989 (2009).

[58] A. Chaudhuri, D. C. Jackson, T. J. Lerotholi, R. G. Jones, T.-L. Lee, B. Detlefs, and D. P. Woodruff, Phys. Chem. Chem. Phys. **12**, 3229 (2010).

[59] N. A. Kautz and S. A. Kandel, J. Am. Chem. Soc. **130**, 6908 (2008).

[60] F.-S. Li, W. Zhou, and Q. Guo, Phys. Rev. B **79**, 113412 (2009).

[61] M. Yu, N. Bovet, C. J. Satterley, S. Bengió, K. R. J. Lovelock, P. K. Milligan, R. G. Jones, D. P. Woodruff, and V. Dhanak, Phys. Rev. Lett. **97**, 166102 (2006).

[62] A. Chaudhuri, T. J. Lerotholi, D. C. Jackson, D. P. Woodruff, and V. Dhanak, Phys. Rev. Lett. **102**, 126101 (2009).

[63] N. C. III., P. Eisenberger, T. Y. B. Leung, P. Schwartz, G. Scoles, G. E. Poirier, and M. J. Tarlov, J. Chem. Phys. **101**, 11031 (1994).

[64] T. Nakamura, H. Kondoh, M. Matsumoto, and H. Nozoye, Langmuir **12**, 5977 (1996).

[65] M. Carot, M. Esplandiu, F. Cometto, E. Patrito, and V. Macagno, J. Electroanal. Chem. **579**, 13 (2005).

[66] T. Y. B. Leung, M. C. Gerstenberg, D. J. Lavrich, G. Scoles, F. Schreiber, and G. E. Poirier, Langmuir **16**, 549 (2000).

[67] K. Kobayashi, J. Umemura, T. Horiuchi, H. Yamada, and K. Matsushige, Jpn. J. Appl. Phys. **37**, 297 (1998).

[68] K. Kobayashi, H. Yamada, T. Horiuchi, and K. Matsushige, Appl. Surf. Sci. **144-145**, 435 (1999).

[69] J.-J. Yu, J. N. Ngunjiri, A. T. Kelley, and J. C. Garno, Langmuir **24**, 11661 (2008).

[70] M. Esplandiu, M. Carot, F. Cometto, V. Macagno, and E. Patrito, Surf. Sci. **600**, 155 (2006).

[71] J. Liang, L. G. Rosa, and G. Scoles, J. Phys. Chem. C **111**, 17275 (2007).

[72] S. W. Joo, S. W. Han, and K. Kim, J. Phys. Chem. B **104**, 6218 (2000).

[73] P. Kohli, K. K. Taylor, J. J. Harris, and G. J. Blanchard, J. Am. Chem. Soc. **120**, 11962 (1998).

[74] S. Rifai, M. Laferriere, D. Qu, D. D. M. Wayner, C. P. Wilde, and M. Morin, J. Electroanal. Chem. **531**, 111 (2002).

[75] H. Akkerman, A. Kronemeijer, P. van Hal, D. de Leeuw, P. Blom, and B. de Boer, Small **4**, 100 (2008).

[76] T. B. Creczynski-Pasa, M. A. D. Millone, M. L. Munford, V. R. de Lima, V. R. de Lima, T. O. Vieira, G. A. Benitez, A. A. Pasa, R. C. Salvarezza, and M. E. Vela, Phys. Chem. Chem. Phys. **11**, 1077 (2009).

[77] D. Qu, B.-C. Kim, C.-W. J. Lee, M. Ito, H. Noguchi, and K. Uosaki, J. Phys. Chem. C **114**, 497 (2010).

[78] H. Hamoudi, M. Prato, C. Dablemont, O. Cavalleri, M. Canepa, and V. A. E., Langmuir **26**, 7242 (2010).

[79] C. D. Bain, E. B. Troughton, Y. T. Tao, J. Evall, G. M. Whitesides, and R. G. Nuzzo, J. Am. Chem. Soc. **111**, 321 (1989).

[80] M. A. D. Millone, H. Hamoudi, L. Rodriguez, A. Rubert, G. A. Benitez, M. E. Vela, R. C. Salvarezza, J. E. Gayone, E. A. Sanchez, O. Grizzi, et al., Langmuir **25**, 12945 (2009).

[81] H. Hamoudi, Z. Guo, M. Prato, C. Dablemont, W. Q. Zheng, B. Bourguignon, M. Canepa, and V. A. Esaulov, Phys. Chem. Chem. Phys. **10**, 6836 (2008).

[82] S. W. Joo, S. W. Han, and K. Kim, Langmuir **16**, 5391 (2000).

[83] J. M. Tour, L. Jones, D. L. Pearson, J. J. S. Lamba, T. P. Burgin, G. M. Whitesides, D. L. Allara, A. N. Parikh, and S. V. Atre, J. Am. Chem. Soc. **117**, 9529 (1995).

[84] A. Franke and E. Pehlke, Phys. Rev. B **81**, 075409 (2010).

[85] P. Carro, A. H. Creus, A. Munoz, and R. C. Salvarezza, Langmuir **26**, 9589 (2010).

[86] J. V. Barth, Surf. Sci. Rep. **40**, 75 (2000).

[87] G. H. Vineyard, J. Phys. Chem. Solids **3**, 121 (1957).

[88] P. Hänggi, P. Talkner, and M. Borkovec, Rev. Mod. Phys. **62**, 251 (1990).

[89] M.-C. Marinica, C. Barreteau, D. Spanjaard, and M.-C. Desjonquères, Phys. Rev. B **72**, 115402 (2005).

[90] M. J. Gillan, Phil. Mag. A **58**, 257 (1988).

[91] G. Henkelman, A. Arnaldsson, and H. Jónsson, J. Chem. Phys. **124**, 044706 (2006).

[92] H. Jónsson, G. Mills, and K. W. Jacobsen, *Classical and Quantum Dynamics in Condensed Phase Simulations* (World Scientific Press, 1998), chap. RAW Quantum transition state theory, p. 405.

[93] C. J. Cerjan and W. H. Miller, J. Chem. Phys. **75**, 2800 (1981).

[94] R. A. Olsen, G. J. Kroes, G. Henkelman, A. Arnaldsson, and H. Jónsson, J. Chem. Phys. **121**, 9776 (2004).

[95] G. Henkelman and H. Jónsson, J. Chem. Phys. **111**, 7010 (1999).

[96] R. Malek and N. Mousseau, Phys. Rev. E. **62**, 7723 (2000).

[97] N. L. Doltsinis, *Computational Nanoscience: Do It Yourself!* (John von Neumann Institute for Computing, 2006), vol. 31 of *NIC Series*, p. 375.

[98] M. R. S. rensen and A. F. Voter, J. Chem. Phys. **112**, 9599 (2000).

[99] D. Passerone and M. Parrinello, Phys. Rev. Lett. **87**, 108302 (2001).

[100] A. Laio and M. Parrinello, P. Natl. A. Sci. USA **99**, 12562 (2002).

[101] H. J. G. Henkelman, G. Jh́annesson, *Progress on Theoretical Chemistry and Physics* (Kluwer Academic Publishers, 2000), chap. Methods for Finding Saddle Points and Minimum Energy Paths, p. 269.

[102] P. G. Bolhuis, D. Chandler, C. Dellago, and P. L. Geissler, Ann. Rev. Phys. Chem. **53**, 291 (2002).

[103] H. Jónsson, G. Mills, and K. W. Jacobsen, *Classical and Quantum Dynamics in Condensed Phase Simulations* (World Scientific Press, 1998), chap. Nudged Elastic Band Method for Finding Minimum Energy Paths of Transitions, p. 385.

[104] G. Henkelman and H. Jónsson, J. Chem. Phys. **113**, 9978 (2000).

[105] G. Henkelman, B. Uberuaga, and H. Jónsson, J. Chem. Phys. **113**, 9901 (2000).

[106] Z. Zhang and M. G. Lagally, Science **276**, 377 (1997).

[107] J. H. G. Owen, D. R. Bowler, C. M. Goringe, K. Miki, and G. A. D. Briggs, Phys. Rev. B **54**, 14153 (1996).

[108] D. R. Bowler, J. H. G. Owen, K. Miki, and G. A. D. Briggs, Phys. Rev. B **57**, 8790 (1998).

[109] G. Kellogg, Surf. Sci. Rep. **21**, 1 (1994).

[110] T. T. Tsong, Physica A **357**, 250 (2005).

[111] E. Pehlke, priv. comm.

[112] T. R. Linderoth, S. Horch, E. Lægsgaard, I. Stensgaard, and F. Besenbacher, Phys. Rev. Lett. **78**, 4978 (1997).

[113] G. Boisvert, L. J. Lewis, M. J. Puska, and R. M. Nieminen, Phys. Rev. B **52**, 9078 (1995).

[114] C. Ratsch and M. Scheffler, Phys. Rev. B **58**, 13163 (1998).

[115] C. M. Chang and C. M. Wei, Chin. J. Phys. **43**, 169 (2005).

[116] G. L. Kellogg and P. J. Feibelman, Phys. Rev. Lett. **64**, 3143 (1990).

[117] H. Yildirim and T. S. Rahman, Phys. Rev. B **80**, 235413 (2009).

[118] G. Ehrlich and F. G. Hudda, J. Phys. Chem. **44**, 1039 (1966).

[119] R. L. Schwoebel and E. J. Shipsey, J. Appl. Phys. **37**, 3682 (1966).

[120] G. Boisvert and L. J. Lewis, Phys. Rev. B **56**, 7643 (1997).

[121] M.-C. Marinica, C. Barreteau, M.-C. Desjonquères, and D. Spanjaard, Phys. Rev. B **70**, 075415 (2004).

[122] A. Karim, A. N. Al-Rawi, A. Kara, T. S. Rahman, O. Trushin, and T. Ala-Nissila, Phys. Rev. B **73**, 165411 (2006).

[123] A. Kara, O. Trushin, H. Yildirim, and T. S. Rahman, J. Phys. Condens. Mat. **21**, 084213 (2009).

[124] J. M. Wen, S. L. Chang, J. W. Burnett, J. W. Evans, and P. A. Thiel, Phys. Rev. Lett. **73**, 2591 (1994).

[125] B. Fischer, H. Brune, J. V. Barth, A. Fricke, and K. Kern, Phys. Rev. Lett. **82**, 1732 (1999).

[126] J. Repp, F. Moresco, G. Meyer, K.-H. Rieder, P. Hyldgaard, and M. Persson, Phys. Rev. Lett. **85**, 2981 (2000).

[127] U. Kürpick, Phys. Rev. B **66**, 165431 (2002).

[128] J. V. Barth, H. Brune, B. Fischer, J. Weckesser, and K. Kern, Phys. Rev. Lett. **84**, 1732 (2000).

[129] T. Michely, W. Langenkamp, H. Hansen, and C. Busse, Phys. Rev. Lett. **86**, 2695 (2001).

[130] H. Brune, K. Bromann, H. Röder, K. Kern, J. Jacobsen, P. Stoltze, K. Jacobsen, and J. No/rskov, Phys. Rev. B **52**, 14380(R) (1995).

[131] M. Bott, M. Hohage, M. Morgenstern, T. Michely, and G. Comsa, Phys. Rev. Lett. **76**, 1304 (1996).

[132] U. Kürpick, A. Kara, and T. S. Rahman, Phys. Rev. Lett. **78**, 1086 (1997).

[133] S. Ovesson, A. Bogicevic, G. Wahnström, and B. I. Lundqvist, Phys. Rev. B **64**, 125423 (2001).

[134] Y. Tiwary and K. A. Fichthorn, Phys. Rev. B **81**, 195421 (2010).

[135] G. Boisvert, L. J. Lewis, and A. Yelon, Phys. Rev. Lett. **75**, 469 (1995).

[136] K. A. Fichthorn and M. Scheffler, Phys. Rev. Lett. **84**, 5371 (2000).

[137] C. M. Chang, C. M. Wei, and J. Hafner, J. Phys. Condens. Mat. **13**, L321 (2001).

[138] U. Kürpick, Phys. Rev. B **64**, 075418 (2001).

[139] A. U. Nilekar, J. Greeley, and M. Mavrikakis, Angew. Chem. Int. Ed. **45**, 7046 (2006).

[140] J. Stremme, Diploma thesis, CAU Kiel (2009).

[141] A. Franke, unpublished.

[142] D. R. Alfonso, A. V. Cugini, and D. S. Sholl, Surf. Sci. **546**, 12 (2003).

[143] J. A. Rodriguez, J. Dvorak, T. Jirsak, G. Liu, J. Hrbek, Y. Aray, and C. Gonzalez, J. Am. Chem. Soc. **125**, 276 (2003).

[144] A. Michaelides and P. Hu, J. Chem. Phys. **115**, 8570 (2001).

[145] G. L. Kellogg, J. Chem. Phys. **83**, 852 (1985).

[146] J. G. McCarty and H. Wise, J. Chem. Phys. **72**, 6332 (1980).

[147] B. Hinch, J. Frenken, G. Zhang, and J. Toennies, Surf. Sci. **259**, 288 (1991).

[148] T. Tansel and O. M. Magnussen, Phys. Rev. Lett. **96**, 026101 (2006).

[149] J. C. Dunphy, P. Sautet, D. F. Ogletree, O. Dabbousi, and M. B. Salmeron, Phys. Rev. B **47**, 2320 (1993).

[150] D. Kelly, A. Gellman, M. Salmeron, G. Somorjai, V. Maurice, M. Huber, and J. Oudar, Surf. Sci. **204**, 1 (1988).

[151] D. M. Kolb, Prog. in Surf. Sci. **51**, 109 (1996).

[152] M. Giesen, G. Beltramo, S. Dieluweit, J. Müller, H. Ibach, and W. Schmickler, Surf. Sci. **595**, 127 (2005).

[153] T. Mitsui, M. K. Rose, E. Fomin, D. F. Ogletree, and M. Salmeron, Phys. Rev. Lett. **94**, 036101 (2005).

[154] P. Lazić, M. Alaei, N. Atodiresei, V. Caciuc, R. Brako, and S. Blügel, Phys. Rev. B **81**, 045401 (2010).

[155] M. J. Ford, R. C. Hoft, and J. D. Gale, Mol. Simulat. **32**, 1219 (2006).

[156] D. Jiang and S. Dai, J. Phys. Chem. C **113**, 3763 (2009).

[157] D. Jiang and S. Dai, Phys. Chem. Chem. Phys. **11**, 8601 (2009).

[158] K.-Y. Kwon, K. L. Wong, G. Pawin, L. Bartels, S. Stolbov, and T. S. Rahman, Phy. Rev. Lett. **95**, 166101 (2005).

[159] G. Pawin, K. L. Wong, K.-Y. Kwon, R. J. Frisbee, T. S. Rahman, and L. Bartels, J. Am.Chem. Soc. **130**, 15244 (2008).

[160] R. Otero, F. Hümmelink, F. Sato, S. B. Legoas, P. Thostrup, E. Laegsgaard, I. Stensgaard, D. S. Galvao, and F. Besenbacher, Nat. Mater. **3**, 779 (2004).

[161] J. A. Miwa, S. W. andHenkjan Gersen, F. Besenbacher, F. Rosei, and T. R. Linderoth, J. Am. Chem. Soc. **128**, 3164 (2006).

[162] M. Schunack, T. R. Linderoth, F. Rosei, E. Lægsgaard, I. Stensgaard, and F. Besenbacher, Phys. Rev. Lett. **88**, 156102 (2002).

[163] J. Weckesser, J. V. Barth, and K. Kern, Phys. Rev. B **64**, 161403(R) (2001).

[164] J. Weckesser, J. V. Barth, and K. Kern, J. Chem. Phys. **110**, 5351 (1999).

[165] J. Ikonomov, P. Bach, R. Merkel, and M. Sokolowski, Phys. Rev. B **81**, 161412 (2010).

[166] J. L. Brand, M. V. Arena, A. A. Deckert, and S. M. George, J. Chem. Phys. **92**, 5136 (1990).

[167] D. Cohen and Y. Zeiri, J. Chem. Phys. **97**, 1531 (1992).

[168] K. A. Fichthorn, P. G. Balan, and Y. Chen, Surf. Sci. **317**, 37 (1994).

[169] D. Huang, Y. Chen, and K. A. Fichthorn, J. Chem. Phys. **101**, 11021 (1994).

[170] J. S. Raut and K. A. Fichthorn, J. Chem. Phys. **108**, 1626 (1998).

[171] K. Suto and O. M. Magnussen, private communication.

[172] M. Born and R. Oppenheimer, Ann. Phys. **389**, 457 (1927).

[173] A. L. Fetter and J. D. Walecka, *Quantum Theory of Many-Particle-Systems* (Dover Publications, 2003).

[174] R. J. Needs, M. D. Towler, N. D. Drummond, and P. L. RÃos, J. Phys. Condens. Mat. **22**, 023201 (2010).

[175] D. M. Ceperley, Rev. Mod. Phys. **67**, 279 (1995).

[176] P. Hohenberg and W. Kohn, Phys. Rev. **136**, 864 (1964).

[177] R. M. Martin, *Electronic Structure* (Cambridge University Press, 2004).

[178] R. M. Dreizler and E. K. U. Gross, *Density Functional Theory* (Springer Verlag, 1990).

[179] W. Kohn and L. J. Sham, Phys. Rev. **140**, A1133 (1965).

[180] E. R. Johnson, I. D. Mackie, and G. A. DiLabio, J. Phys. Org, Chem. **22**, 1127 (2009).

[181] D. Ceperley and B. Alder, Phys. Rev. Lett. **45**, 566 (1980).

[182] J. Perdew and A. Zunger, Phys. Rev. B **23**, 5048 (1981).

[183] S. Kurth, J. P. Perdew, and P. Blaha, Int. J. Quant. Chem. **75**, 889 (1999).

[184] V. N. Staroverov, G. E. Scuseria, J. Tao, and J. P. Perdew, Phys. Rev. B **69**, 075102 (2004).

[185] M. Fuchs, M. Bockstedte, E. Pehlke, and M. Scheffler, Phys. Rev. B **57**, 2134 (1998).

[186] L. A. Curtiss, K. Raghavachari, P. C. Redfern, and J. A. Pople, J. Chem. Phys. **106**, 1063 (1997).

[187] P. Bagno, O. Jepsen, and O. Gunnarsson, Phys. Rev. B **40**, 1997 (1989).

[188] S. Kümmel and L. Kronik, Rev. Mod. Phys. **80**, 3 (2008).

[189] J. P. Perdew, J. A. Chevary, S. H. Vosko, K. A. Jackson, M. R. Pederson, D. J. Singh, and C. Fiolhais, Phys. Rev. B **46**, 6671 (1992).

[190] J. P. Perdew, K. Burke, and M. Ernzerhof, Phys. Rev. Lett. **77**, 3865 (1996).

[191] B. Hammer, L. B. Hansen, and J. K. Nørskov, Phys. Rev. B **59**, 7413 (1999).

[192] Y. Zhang and W. Yang, Phys. Rev. Lett. **80**, 890 (1998).

[193] J. P. Perdew, A. Ruzsinszky, G. I. Csonka, O. A. Vydrov, G. E. Scuseria, L. A. Constantin, X. Zhou, and K. Burke, Phys. Rev. Lett. **100**, 136406 (2008).

[194] J. H. G. Owen, D. R. Bowler, C. M. Goringe, K. Miki, and G. A. D. Briggs, Phys. Rev. B **54**, 14153 (1996).

[195] B. Hammer, M. Scheffler, K. W. Jacobsen, and J. K. Nørskov, Phys. Rev. Lett. **73**, 1400 (1994).

[196] W. Brenig and E. Pehlke, Prog. Surf. Sci. **83**, 263 (2008).

[197] A. Stroppa, K. Termentzidis, J. Paier, G. Kresse, and J. Hafner, Phys. Rev. B **76**, 195440 (2007).

[198] F. Favot, A. D. Corso, and A. Baldereschi, J. Chem. Phys. **114**, 483 (2001).

[199] F. Tran, P. Blaha, and K. Schwarz, J. Phys. Condens. Mat. **19**, 196208 (2007).

[200] P. Sony, P. Puschnig, D. Nabok, and C. Ambrosch-Draxl, Phys. Rev. Lett. **99**, 176401 (2007).

[201] J. Tao, J. P. Perdew, V. N. Staroverov, and G. E. Scuseria, Phys. Rev. Lett. **91**, 146401 (2003).

[202] J. P. Perdew, A. Ruzsinszky, J. Tao, V. N. Staroverov, G. E. Scuseria, and G. I. Csonka, J. Chem. Phys. **123**, 062201 (2005).

[203] J. P. Perdew, A. Ruzsinszky, G. I. Csonka, L. A. Constantin, and J. Sun, Phys. Rev. Lett. **103**, 026403 (2009).

[204] V. N. Staroverov, G. E. Scuseria, J. Tao, and J. P. Perdew, J. Chem. Phys. **119**, 12129 (2003).

[205] S. Ivanov, S. Hirata, and R. J. Bartlett, Phys. Rev. Lett. **83**, 5455 (1999).

[206] A. D. Becke, J. Chem. Phys. **98**, 1372 (1993).

[207] J. P. Perdew and A. Zunger, Phys. Rev. B **23**, 5048 (1981).

[208] J. Perdew, Chem. Phys. Lett. **64**, 127 (1979).

[209] V. I. Anisimov, J. Zaanen, and O. K. Andersen, Phys. Rev. B **44**, 943 (1991).

[210] M. Dion, H. Rydberg, E. Schröder, D. C. Langreth, and B. I. Lundqvist, Phys. Rev. Lett. **92**, 246401 (2004).

[211] S. Tsuzuki, K. Honda, T. Uchimaru, M. Mikami, and K. Tanabe, J. Am. Chem. Soc. **124**, 104 (2002).

[212] E. McNellis, J. Meyer, and K. Reuter, Phys. Rev. B **80**, 205414 (2009).

[213] M. Fuchs and X. Gonze, Phys. Rev. B **65**, 235109 (2002).

[214] J. Harl and G. Kresse, Phys. Rev. B **77**, 045136 (2008).

[215] J. Harl and G. Kresse, Phys. Rev. Lett. **103**, 056401 (2009).

[216] D. Lu, Y. Li, D. Rocca, and G. Galli, Phys. Rev. Lett. **102**, 206411 (2009).

[217] M. Rohlfing and T. Bredow, Phys. Rev. Lett. **101**, 266106 (2008).

[218] H.-V. Nguyen and G. Galli, J. Chem. Phys. **132**, 044109 (2010).

[219] H. Rydberg, B. I. Lundqvist, D. C. Langreth, and M. Dion, Phys. Rev. B **62**, 6997 (2000).

[220] D. C. Langreth, M. Dion, H. Rydberg, E. Schröder, P. Hyldgaard, and B. I. Lundqvist, Int. J. Quant. Chem. **101**, 599 (2005).

[221] D. C. Langreth, B. I. Lundqvist, S. D. Chakarova-Käck, V. R. Cooper, M. Dion, P. Hyldgaard, A. Kelkkanen, J. Kleis, L. Kong, S. Li, et al., J. Phys. Condens. Mat. **21**, 084203 (2009).

[222] O. A. Vydrov and T. Van Voorhis, Phys. Rev. Lett. **103**, 063004 (2009).

[223] M. Mura, A. Gulans, T. Thonhauser, and L. Kantorovich, Phys. Chem. Chem. Phy. **12**, 4759 (2010).

[224] K. Toyoda, I. Hamada, K. Lee, S. Yanagisawa, and Y. Morikawa, J. Chem. Phys. **132**, 134703 (2010).

[225] L. Romaner, D. Nabok, P. Puschnig, E. Zojer, and C. Ambrosch-Draxl, New J. Phys. **11**, 053010 (2009).

[226] M. Vanin, J. J. Mortensen, A. K. Kelkkanen, J. M. Garcia-Lastra, K. S. Thygesen, and K. W. Jacobsen, Phys. Rev. B **81**, 081408 (2010).

[227] N. Atodiresei, V. Caciuc, P. Lazić, and S. Blügel, Phys. Rev. Lett. **102**, 136809 (2009).

[228] T. Thonhauser, V. R. Cooper, S. Li, A. Puzder, P. Hyldgaard, and D. C. Langreth, Phys. Rev. B **76**, 125112 (2007).

[229] V. R. Cooper, Phys. Rev. B **81**, 161104 (2010).

[230] P. Lazic, N. Atodiresei, M. Alaei, V. Caciuc, S. Blügel, and R. Brako, Comput. Phys. Commun. **181**, 371 (2010).

[231] A. Gulans, M. J. Puska, and R. M. Nieminen, Phys. Rev. B **79**, 201105 (2009).

[232] G. Román-Pérez and J. M. Soler, Phys. Rev. Lett. **103**, 096102 (2009).

[233] C. Ambrosch-Draxl, D. Nabok, P. Puschnig, and C. Meisenbichler, New J. Phys. **11**, 125010 (2009).

[234] H. C. Longuet-Higgins, Discuss. Faraday Soc. **40**, 7 (1965).

[235] E. Zaremba and W. Kohn, Phys. Rev. B **13**, 2270 (1976).

[236] J. F. Dobson, J. Wang, B. P. Dinte, K. McLennan, and H. M. Le, Int. J. Quant. Chem. **101**, 579 (2005).

[237] R. P. Feynman, Phys. Rev. **56**, 340 (1939).

[238] A. Tkatchenko and M. Scheffler, Phys. Rev. Lett. **102**, 073005 (2009).

[239] F. Ortmann, F. Bechstedt, and W. G. Schmidt, Phys. Rev. B **73**, 205101 (2006).

[240] S. Grimme, J. Comp. Chem. **27**, 1787 (2006).

[241] S. Grimme, J. Antony, S. Ehrlich, and H. Krieg, J. Chem. Phys. **132**, 154104 (2010).

[242] S. Grimme, J. Comp. Chem. **25**, 1463 (2004).

[243] K. Tonigold and A. Groß, J. Chem. Phys. **132**, 224701 (2010).

[244] L. Goerigk and S. Grimme, J. Chem. Theo. Comp. **6**, 107 (2010).

[245] J.-H. Franke, V. Caciuc, L. F. Chi, and H. Fuchs, Phys. Rev. B **78**, 165432 (2008).

[246] M.-T. Nguyen, C. A. Pignedoli, M. Treier, R. Fasel, and D. Passerone, Phys. Chem. Chem. Phys. **12**, 992 (2010).

[247] F. Ortmann, W. G. Schmidt, and F. Bechstedt, Phys. Rev. Lett. **95**, 186101 (2005).

[248] G. Mercurio, E. R. McNellis, I. Martin, S. Hagen, F. Leyssner, S. Soubatch, J. Meyer, M. Wolf, P. Tegeder, F. S. Tautz, et al., Phys. Rev. Lett. **104**, 036102 (2010).

[249] G. Kresse and J. Hafner, Phys. Rev. B **47**, 558 (1993).

[250] G. Kresse and J. Hafner, Phys. Rev. B **49**, 14251 (1994).

[251] G. Kresse and J. Furthmüller, Comp. Mat. Sci. **6**, 15 (1996).

[252] G. Kresse and J. Furthmüller, Phys. Rev. B **54**, 11169 (1996).

[253] J. Hafner, J Comp. Chem. **29**, 2044 (2008).

[254] URL `http://cms.mpi.univie.ac.at/vasp`.

[255] G. Kresse and J. Furthmüller, Comp. Mat. Sci. **6**, 15 (1996).

[256] P. E. Blöchl, Phys. Rev. B **50**, 17953 (1994).

[257] G. Kresse and D. Joubert, Phys. Rev. B **59**, 1758 (1999).

[258] M. Marsman and G. Kresse, J. Chem. Phys. **125**, 104101 (2006).

[259] G. Kresse and D. Joubert, Phys. Rev. B **59**, 1758 (1999).

[260] H. J. Monkhorst and J. D. Pack, Phys. Rev. B **13**, 5188 (1976).

[261] M. Methfessel and A. T. Paxton, Phys. Rev. B **40**, 3616 (1989).

[262] H. Shi and C. Stampfl, Phys. Rev. B **77**, 094127 (2008).

[263] P. Maksymovych and J. T. Yates, J. Am. Chem. Soc. **130**, 7518 (2008).

[264] R. D. Johnson III, ed., *NIST Computational Chemistry Comparison and Benchmark Database, NIST Standard Reference Database Number 101, Release 15* (NIST, http://cccbdb.nist.gov, Feb. 2010).

[265] A. Franke and E. Pehlke, manuscript accepted for publication in Phys. Rev. B. (Oct. 28, 2010).

[266] C. E. Bach, M. Giesen, and H. Ibach, Phys. Rev. Lett. **78**, 4225 (1997).

[267] E. McNellis, J. Meyer, and K. Reuter, Phys. Rev. B **80**, 205414 (2009).

[268] S. Venkatachalam, P. Kaghazchib, L. Kiblera, D. Kolba, and T. Jacob, Chem. Phys. Lett. **455**, 47 (2008).

[269] J. E. Müller and H. Ibach, Phys. Rev. B **74**, 085408 (2006).

[270] K. Pötting, W. Schmickler, and T. Jacob, Chem. Phys. Chem. **11**, 1395 (2010).

[271] P. C. Rusu and G. Brocks, Phys. Rev. B **74**, 073414 (2006).

[272] J. He, C. D. Paola, and L. Kantorovich, J. Chem. Phys. **130**, 144104 (2009).

[273] Q.-M. Hu, K. Reuter, and M. Scheffler, Phys. Rev. Lett. **98**, 176103 (2007).

[274] C. Tuma and J. Sauer, Chem. Phys. Lett. **387**, 388 (2004).

[275] W. Schmickler, *Interfacial electrochemistry* (Oxford University Press, 1996).

[276] C. D. Taylor, S. A. Wasileski, J.-S. Filhol, and M. Neurock, Phys. Rev. B **73**, 165402 (2006).

[277] A. Y. Lozovoi, A. Alavi, J. Kohanoff, and R. M. Lynden-Bell, The Journal of Chemical Physics **115**, 1661 (2001).

[278] T. Jacob, Electrochim. Acta **52**, 2229 (2007).

[279] Y. Gründer, D. Kaminski, F. Golks, K. Krug, J. Stettner, O. M. Magnussen, A. Franke, J. Stremme, and E. Pehlke, Phys. Rev. B **81**, 174114 (2010).

[280] M. Saracino, P. Broekmann, K. Gentz, M. Becker, H. Keller, F. Janetzko, T. Bredow, K. Wandelt, and H. Dosch, Phys. Rev. B **79**, 115448 (2009).

[281] A. Sperl, J. Kröger, and R. Berndt, phys status solidi b **247**, 1077 (2010).

[282] J. Lagoute, X. Liu, and S. Fölsch, Phys. Rev. B **74**, 125410 (2006).

[283] A. Sperl, J. Kröger, R. Berndt, A. Franke, and E. Pehlke, New J. Phys. **11**, 063020 (2009).

[284] N. Néel, J. Kröger, R. Berndt, T. O. Wehling, A. I. Lichtenstein, and M. I. Katsnelson, Phys. Rev. Lett. **101**, 266803 (2008).

[285] P. Wahl, P. Simon, L. Diekhöner, V. S. Stepanyuk, P. Bruno, M. A. Schneider, and K. Kern, Phys. Rev. Lett. **98**, 056601 (2007).

[286] L. Limot, E. Pehlke, J. Kröger, and R. Berndt, Phys. Rev. Lett. **94**, 036805 (2005).

[287] F. E. Olsson, M. Persson, A. G. Borisov, J.-P. Gauyacq, J. Lagoute, and S. Fölsch, Phys. Rev. Lett. **93**, 206803 (2004).

[288] J. Kröger, N. Néel, and L. Limot, J. Phys. Condens. Mat. **20**, 223001 (2008).

[289] A. Sperl, J. Kröger, N. Néel, H. Jensen, R. Berndt, A. Franke, and E. Pehlke, Phys. Rev. B **77**, 085422 (2008).